Real-time Monitoring and Adaptive Control of CO_2 Laser Beam Welding

By

Hongping Gu

A thesis
presented to the University of Waterloo
in fulfillment of the
thesis requirement for the degree of
Doctor of Philosophy
in
Physics

Waterloo, Ontario, Canada, 1998

© (Hongping Gu) 1998

National Library of Canada
Acquisitions and Bibliographic Services
395 Wellington Street
Ottawa ON K1A 0N4
Canada

Bibliothèque nationale du Canada
Acquisitions et services bibliographiques
395, rue Wellington
Ottawa ON K1A 0N4
Canada

Your file Votre référence

Our file Notre référence

The author has granted a non-exclusive licence allowing the National Library of Canada to reproduce, loan, distribute or sell copies of this thesis in microform, paper or electronic formats.

L'auteur a accordé une licence non exclusive permettant à la Bibliothèque nationale du Canada de reproduire, prêter, distribuer ou vendre des copies de cette thèse sous la forme de microfiche/film, de reproduction sur papier ou sur format électronique.

The author retains ownership of the copyright in this thesis. Neither the thesis nor substantial extracts from it may be printed or otherwise reproduced without the author's permission.

L'auteur conserve la propriété du droit d'auteur qui protège cette thèse. Ni la thèse ni des extraits substantiels de celle-ci ne doivent être imprimés ou autrement reproduits sans son autorisation.

0-612-38242-7

Canada

The University of Waterloo requires the signatures of all persons using or photocopying this thesis. Please sign below, and give address and date.

Abstract

Sensor technology has been developed for real-time monitoring and adaptive control of laser beam welding in this work, which include acoustic and optical monitoring of penetration condition of welds, optical measurement of gap width, weld fault detection, as well as adaptive control of beam focal position, beam position on the seam and welding speed. Acoustic sensor is an ordinary condensed microphone. Optical sensor is a unique system of many capabilities that has been developed in this work. With this sensor, a neural fuzzy control system has been designed to improve the control action for these parameter controls.

Acoustic monitoring is based on the variation in frequency distribution of the air-borne acoustic signals. Interpretation of the acoustic signals to extract information on weld quality is not straightforward. Three approaches have been proposed to identify the weld using acoustic signals: statistical deviation, statistical pattern recognition and neural network. Each method has shown a certain degree of accuracy of prediction.

Optical monitoring is to use the as-developed multi-spot and multi-color detection technique to measure gap width, to detect weld defeats and to identify penetration condition. With optical monitoring, high sampling rate is reached. In weld fault detection, an inverse-filtering algorithm has been developed to successfully resolve information on the weld faults.

Closed loop controls of beam focal position, seam tracking and welding speed have been successfully achieved during CO_2 laser beam welding experiment. A neural fuzzy control system has been designed for adaptive control of welding speed and seam tracking using optical feedback signals. Simulation results show improvement in control action in comparison to conventional PID controller.

Acknowledgements

I am deeply indebted to my supervising professor, Dr. Walt W. Duley, for his guidance and valuable advice during this research work. Without his guidance and support, completion of this work is impossible.

I would like to thank for Dr. Robert Mueller for discussion of some of the experimental results. I also would like to thank many people in this group for their helping throughout the experimental process.

Special thanks go to my wife, Yaozhi, for her love and encouragement during my graduate work. I also would like to express my love to my daughters, Angela and Joyce, for their understanding of my hard work.

Contents

	Page No.
Author's declaration	ii
Borrower's paper	iii
Abstract	iv
Acknowledgements	v
Table of Contents	vi
List of Tables	x
List of Figures	xii
Chapter 1 Introduction and Theoretical background	1
1.1 Literature review	1
1.1.1 Laser welding technology	1
1.1.2 In-process monitoring techniques	3
1.1.2.1 Plasma charge sensor	4
1.1.2.2 Optical sensors	5
1.1.2.3 Acoustic sensor	8
1.1.3 Objective	10
1.2 Basic theory of laser beam interaction with metals	10
1.2.1 Laser keyhole welding process	10
1.2.2 Operation characteristics and weld quality	14
1.2.3 Vapor gas dynamics within the keyhole	15
1.3 Optical and acoustic emission from keyhole welding	19
1.3.1 Plasma generation	19
1.3.2 Optical emission	23
1.3.3 Sound generation	25

Chapter 2 Experimental equipment and sensing techniques 29

2.1 CO_2 laser 30

2.2 Laser head and working station 34

2.3 Motion control and data acquisition system 34

2.4 Detectors and sensing system 35

2.5 Welding materials and welding trials 37

Chapter 3 Acoustic monitoring techniques 40

3.1 Characteristics and quantization of acoustic signals 40

3.2 A simple approach to interpret acoustic signals 46

3.3 Weld classification using statistical pattern recognition 50

3.3.1 Basic theory of pattern recognition analysis 50

3.3.2 Feature selections of acoustic signals 54

3.3.3 Performance of weld classification 57

3.3.4 Discussions 62

3.4 Analysis of acoustic signals detected from different location 65

3.4.1 Features of acoustic signals 65

3.4.2 Analysis signals 71

3.4.3 Discussion 71

3.5 Weld classification using a neural network 73

3.5.1 Basic structure and learning rules of the neural network 73

3.5.2 Performance of weld classification 77

3.5.3 Discussion 78

Chapter 4 Characteristics of optical emission and detection techniques 82

4.1 Variation of optical emission 82

4.2 Statistical characteristics of emission signals 85

4.3 Running average filtering 93

4.4 Spatial distribution of plasma emission 96

4.5 Frequency domain analysis 102

4.5.1 Characteristics of FFT spectrum 102

4.5.2 Weld classification by neural network 105
4.6 Multi-spot and multi- color detection techniques 108
4.7 Inverse filtering and weld quality identifier 110

Chapter 5 Optical monitoring and optical data analysis 114
5.1 A gap detection 114
5.1.1 Gap and weld quality 114
5.1.2 Gap detection technique 115
5.1.3 Experimental data 116
5.1.4 FFT analysis of UV and IR signals 121
5.2 Weld fault detection 121
5.2.1 Nature of weld faults 121
5.2.2 Signal variation with weld quality 126
5.2.3 Implementation of inverse filtering 129
5.3 Analysis of weld quality using FFT technique 137
5.3.1 Technique of separate-signal detection 137
5.3.2 Experimental data and analysis 138

Chapter 6 Implementation of closed loop control 144
6.1 Basic concept of feedback control 144
6.2 Auto focusing system 146
6.2.1 Laser beam focusing ability and working regime 147
6.2.2 Dual-view detection technique 149
6.2.3 Signal response 151
6.2.4 Closed-loop welding 154
6.3 Seam tracking 155
6.3.1 Optical fiber sensing system 158
6.3.2 Signal response 161
6.3.3 Linear combiner and position error signal 163
6.3.4 Closed-loop seam tracking experiment 166
6.4 Adaptive speed control 171

6.4.1 Principle of sensing weld penetration 171
6.4.2 Closed loop welding with a PID controller 177

Chapter 7 Improvement of control action using a neuro-fuzzy controller 179
7.1 Structure of rule based fuzzy logic controller 179
7.2 A fuzzy logic controller for welding speed control 185
7.3 A hybrid neuro-fuzzy controller for seam tracking 190

Chapter 8 Discussion and Conclusion 199
8.1 Acoustic monitoring 200
8.2 Optical monitoring 201
8.3 Adaptive control of welding process 202

References 203

List of Tables

Page No.

3.1 Feature selection of acoustic signals detected from above-the-workpiece surface by inter-class distance measures and information measures. Highlighted data have little contribution to classification. 55

3.2 Feature selection of acoustic signals detected from under-the-workpiece surface by inter-class distance measures and information measures. 56

3.3 Performance of classification of laser welds using acoustic and optical signals. 58

3.4 Classification of laser welds by combination of acoustic and optical signals. The definition of classes is as the same as that in table 3.3 and laser power is about 1.6 kW. 63

3.5 Comparison of performances of weld classification by acoustic signals that are taken at two different sampling rates. 64

3.6 Information measures of acoustic signals from lap weld with changing welding speed. 68

3.7 Information measures of acoustic signals from lap weld of mild steel sheet with changing laser beam focal position. Welds were carried out at a power of 1.6 kW and a speed of 38.1 mm/s. 68

3.8 Acoustic classification of laser welds of mild steel sheet. The welds are produced with a constant power 1.6 kW and at changing speed. 72

3.9 Acoustic classification of lap welds of mild steel sheet. Welds were produced with a laser power 1.6 kW and welding speed of 50.8 mm/s and with changing focal position. Signals were recorded at locations: "-" refers to move-down and "+" denotes move-up. 72

3.10 Classification of welds into three classes by neural network. 79

3.11 Classification of welds into two classes by neural network. 80

3.12 Weld classification of the training data by a three-layer neural network. 81
4.1 Statistical data of emission signals from the center of the plume. 88
4.2 Separability of the emission signals from the plume. 91
4.3 Separabilities of IR signals from weld pool. 91
4.4 Results of weld classification by neural network. Input data are the optical emission spectra from plasma plume emission and IR emission from the weld pool beside the keyhole. 106
4.5 Results of weld classification by neural network. Input data are the optical emission spectra from plasma plume emission and IR emission from the weld pool behind the keyhole. 107
7.1 Control rules of a fuzzy logic controller for welding speed control. 188
7.2 Control rules of the fuzzy logic controller in a hybrid neuro-fuzzy system for seam tracking. 193
7.3 Constants of the consequent part in a Sugeno inference system after trained. 195

List of Figures

Page No.

1.1 Schematic illustration of vapor generation, vapor flow and melt flow in laser welding keyhole. 18

1.2 Illustration of acoustic generation. 26

2.1 Experimental setup for laser welding and signal detection. 29

2.2 Intensity distribution of the VFA-1700 laser beam. 32

2.3 Gaussian intensity distribution. 33

2.4 Diagrammatically illustration of the structured fiber bundle in the optical sensing system. 36

2.5 Illustration of laser beam focus on the metal surface. 37

3.1 Acoustic emission spectra during laser keyhole welding of steel sheet at three different welding speeds. 42

3.2 Normalized power spectra of acoustic emission during CO_2 laser bead-on-plate welding of mild steel at three welding speeds. 43

3.3 Photographs of cross-sections of welds from laser welding at various welding speeds. The thickness of steel sheet is 1.2 mm. 44

3.4 Total squared deviation of the AE signal. Good welds were obtained (a) near the minimum when changing speed, (b) when laser power is above a certain value. 46

3.5 Effect of focus on total squared deviation of AE signals during laser welding under different focal conditions. 47

3.6 Total squared deviation of the AE during laser welding of 1-mm thick galvanized steel sheet with laser power 1.6 kW. 48

3.7 Total squared deviation of the AE during laser lap welding of mild steel sheets of 1.1-mm thickness at a laser power of 1.7 kW. 48

3.8 Total squared deviation of AE signals from butt weld and the corresponding sections of the weld. Butt 1 is good weld, while a wide gap (butt 2 and 3) yields a high AE deviation and poor weld quality. 50

3.9. Acoustic signals in a 2-D discriminant space. The solid symbols denote the mean of each class. 58

3.10 Graphic illustration of weld classification for two welding runs using acoustic and optical signal data. Laser power is about 1.6 kW. 61

3.11 Graphic illustration of weld classification from data of combining acoustic and optical signals, which are the same set of data in Fig.3.10. 62

3.12 Schematic illustration of experimental setup for laser beam welding and multi-position acoustic detection. 66

3.13 Acoustic spectra from laser lap welding of mild steel sheet at three welding speeds. The signals were recorded above the work-piece surface with the detector at location #1. 67

3.14 Acoustic spectra from laser lap welding of mild steel sheet at three welding speeds. The signals were recorded under the work-piece surface with the detector at location #3. 67

3.15 Acoustic spectra of laser welding of mild steel sheet at fixed speed (50.8 mm/s) and laser power (1.6 kW) and with changing focal position. The detector was at location #1. 70

3.16 Acoustic spectra of laser welding of mild steel sheet at the same process condition as that in Fig.3.15, but the detector was mounted at location #2. 70

3.17. Photographs of weld cross section. The welds are produced with a laser power 1.6 kW and at speed of 50.8 mm/s. The focal position are (a) optimal position, (b) move-down 4 mm, and (c) move-up 2 mm with respect to the optimal position. 71

3.18 Structure of a feedforward neural network. 76

4.1 Physical model of plasma plume emission during laser beam interaction with metals. 85

4.2 Optical emission spectrum of the plasma plume recorded during CO_2 laser beam welding of galvannealed steel sheet. The optical sensing range of the spectrometer is 259.25-534.69 nm. 86

4.3 A typical optical emission (UV) signal of plasma plume recorded during laser beam welding of steel sheet. 87

4.4 Averaged emission signal in Fig.4.2-1. (a)The average is calculated over 10 data points. (b)The average is calculated over 50 data points, thus the overall sampling rate is reduced to 40 Hz. 88

4.5 Density distributions of the emission signals from the plasma plume. The signals were recorded by photodiodes during laser beam welding of galvannealed steel sheet (1 mm thick) at laser power 1.5 kW and at three welding speeds: v15 = 19.05 mm/s, v30 = 38.1 mm/s and v50 = 63.5 mm/s. 92

4.6 Illustration of side and top views of different detection spots. 94

4.7 Density distributions of IR radiation signals from the melt pool at two detecting spots: (a) behind the keyhole, (b) beside the keyhole. The three distributions in each plot represent welds at different welding speeds. 96

4.8 Smoothed emission signal of that in Fig. 4.3 using running average filtering. 97

4.9 Density distributions of IR signals after run-time filtering. The signal source is the same as that in Fig.4.2-6. (a) behind the keyhole, (b) beside the keyhole. 98

4.10 Schematic drawing of imaging system with a CCD camera and the horizontal view of a image of the plasma plume. 100

4.11 Images of CO_2 laser beam interaction with steel sheet. 101

4.12 Spatial distributions of plasma plume emission. (a) Signals were measured across the weld, (b) Signals were measured along the weld with the detector behind the laser head. 102

4.13 Schematic illustration of the position of the detection spot relative to the plasma plume. 103

4.14 Calculated plume radiation with changing detection spot along the weld line. 104

4.15 FFT spectra of optical emission signals of broad band emission from plasma plume (#1) and IR emission from weld pool beside the keyhole (#2). Laser power is 1.6 kW and the welding was performed on bead-on-plate. 105

4.16 FFT spectra of optical signals of broad band emission from the plume (#1) and IR emission from the weld pool behind the keyhole (#2). 106

4.17 Principle behind detection of focal position. 111

5.1 Schematic illustration of gap detection technique. 118

5.2 Emission signals acquired using twin-spot detection technique. These signals represent two welding speeds: (a) 38.1 mm/s and (b) 63.5 mm/s. 120

5.3 Emission signals detected by twin-spot technique at different laser power. The welding speed is kept at 38.1 mm/s. 121

5.4 Relative positions at which a significant IR signal was detected through the gap. 123

5.5 Emission signals corresponding to pinhole detection acquired by twin-spot detection technique. #1 signal is the UV radiation from plume. #2 signal is the IR in front of the weld pool. 124

5.6 FFT spectra of emission signals from laser beam butt welding of a wedge seam. #1 signal is UV radiation from the plume; #2 is the IR from the gap ahead of weld pool. From (a) to (c) the gap gradually opens up so that the IR signal increases. 125

5.7 Photograph of a weld produced on a seam of gradual gap. 129

5.8 Photograph of a weld with pinholes in it. 130

5.9 UV and IR radiation from laser beam butt welding of a wedge-gap seam. In (a), the IR signals are shifted to avoid overlap in the plot. (b) and (c) are subsections of signals in (a). 131

5.10 UV and IR radiation during laser beam butt welding with pinholes in the weld. The emission signals are obtained using a twin-spot detection technique. 132

5.11 Coefficient calculated by inverse filtering algorithm using the emission signals in Fig.5.9. 134

5.12 Coefficient calculated by inverse filtering algorithm. The emission signals are related to the weld in Fig.5.10. 134

5.13 (a) Photograph of a weld and the coefficient calculated from the emission signals during the corresponding laser weld process. (b) Photograph of a weld and the coefficient calculated from the emission signals during this laser welding process. 135 136

5.14 Photograph of a laser weld with defects. 137

5.15 The inverse-filtering coefficient of the UV and IR emission signals from the welding plume. A small gap is maintained in the seam so that the weld has defects in it. 139

5.16 The modified inverse-filtering coefficient of the emission signals in Fig.5.15 by shifting 5 data points. 139

5.17 (a) Coefficient of the emission signals relating to the weld in Fig.5.7. A data-shifting scheme is applied. (b) Calculated coefficient of a good weld. Data shift does not change the overall data value. 140

5.18 Schematic illustration of laser beam welding and signal detection system. 141

5.19 FFT spectra of optical emission detected by sensor #1. Laser power was 1.7 kW. At speed of 38.1 mm/s, good full penetration welds were produced on a steel sheet of 1.1 mm thick. 142

5.20 FFT spectra of the time derivative of optical emission signals detected by sensor #1. The spectra are corresponding to that in figure 3.19. 144

5.21 FFT spectra of optical emissions from laser welding plume that are detected by sensor #2. Laser power is 1.7 kW. 145

5.22 FFT spectra of the time derivative of optical signals detected by sensor #1. The welding speed was kept at 38.1 mm/s and the laser power is lowered so that partial penetration welds were produced. 146

5.23 FFT spectrum of the modulated laser beam radiation that was sensed by a pyroelectric detector. 147

5.24 FFT spectra of optical signals from modulated laser beam welding at a travel speed of 50.8 mm/s. The averaged laser power was 1.38 kW. 148

5.25 FFT spectrum of acoustic emission from modulated laser beam welding. Laser average power was 1.38 kHz while the welding speed was 50.8 mm/s. 149
6.1 Schematic diagram of computer close-loop control. 151
6.2 Measured spot size of the CO_2 laser beam as a function of vertical distance. 154
6.3 A schematic illustration of the focal position detection technique. 155
6.4 Diagram of the light-collection focus system. 156
6.5 Emission signals by two spot detection during laser welding of a slope surface. Laser power was 1.6 kW and welding speed was 50.8 mm/s. Laser beam moves in horizontal plane. 158
6.6 Differential signal intensity recorded using the dual-view technique. 159
6.7 Differential signal intensity of that in Fig.6.6 after filtered using running average filtering algorithm. 159
6.8 Weld contours tested in experiment. (a) Triangular shape, (b) Double-triangular shape. 160
6.9 Photographs of bead-on-plate welds with and without closed loop focus control. 162
6.10 Photographs of welds that were produced under closed loop control and at two speeds: (a) 63.5 mm/s and (b) 76.2 mm/s. 163
6.11 Schematic illustration of the relation between the laser spot and the center of the emission source. 165
6.12 Schematic illustration of seam position detection. 166
6.13 Relative optical signals of plume emission recorded using the multi-spot detection technique. Butt welds between different gauge metal sheets were made. The laser beam spot shifted from the thin sheet side to the thick sheet side. 167
6.14 Real-time optical emission signals detected using the multi-spot detection technique. Welds were performed on a tilted seam of butt joint of different gauge metal sheets. (a) At the start of weld the laser beam was located on the thin sheet and at the end of weld the beam shifted to the thick sheet. (b) Beam position shift in reverse direction. 168
6.15 Structure of a linear combiner. 169

6.16 Error signals of the beam position off the seam which are the output from a linear combiner. Case 1: from thin to thick; Case 2: from thick to thin. 173
6.17 Position error signals of those in Fig.6.16 after applying running average filtering. 174
6.18 Photographs of welds that were made under closed loop seam tracking. (a) A titled straight line joint, (b) and (c) bending seam. 175
6.19 Multi-spot detection technique used for adaptive speed control. 179
6.20 Optical signals detected using the multi-spot detection technique during laser beam welding at changing speed: (a) acceleration and (b) deceleration. Laser power was 1.6 kW. 180
6.21 The differential signals between IR and UV radiation from Fig.6.20. 181
6.22 Relative signal intensities of plume emission using the three-spot detection technique. All the signals were broad-band light. (a) Acceleration, (b) Deceleration. #1 and #2 spots are beside the weld pool. #3 spot is at the center of weld pool. 182
6.23 Velocity profile of bead-on-plate welding under close-loop control. Laser power was 1.5 kW. Two initial speeds are given: (a) low speed and (b) high speed. 184
7.1 Basic architecture of a fuzzy logic controller. 186
7.2 Atchitecture of an ANFIS fuzzy controller. 189
7.3 Block diagram of a PD-like fuzzy logic controller for welding speed control. 192
7.4 Input and output membership functions of a fuzzy logic controller for speed adjustment. 193
7.5 Control surface of the fuzzy logic controller for welding speed. 195
7.6 Control action of the fuzzy logic controller for speed adjustment when optical signals are presented to the system. 197
7.7 Control action incurred from a proportional controller in response to the input differential optical signal. 197
7.8 Basic structure of a hybrid neural fuzzy control system for seam tracking during laser beam welding. 198

7.9 Initial membership functions of the optical signal from the Adaline, which are constructed for the input of ANFIS controller. 200

7.10 Membership functions of figure 7.9 after parameter adjustment through a training process with the experimental data. 202

7.11 Control action of the hybrid neural fuzzy controller when three optical emission signals are presented to the system. 203

7.12 Membership functions of the consequent part of a Mandani type fuzzy controller for seam tracking in the hybrid neuro-fuzzy system. 205

7.13 Control action of the Mamdani type fuzzy controller in the hybrid neuro-fuzzy system when three optical signals are fed into the system. 206

Chapter 1

Introduction and Theoretical Background

1.1 Literature review

1.1.1 Laser welding technology

Laser beam welding is an important modern manufacturing technology. The technological core of the laser welding process is to use an intense light beam to melt the edges or surfaces to be joined, either with or without filler material. With the beam moving along the joint, the melted metal undergoes subsequent mixing, cooling and solidification. In general, melting is achieved by local heat input from a heat source. Most sources of heat are applied on the sheet surface, so heat transfer or conduction is important to achieve full penetration welding. For laser beam welding, the concentrated heat source can be applied directly inside the sheet. As a result, deep penetration weld can be achieved.

In laser welding, the heat source comes directly from photons. Photons can be focused onto a very small spot and can penetrate into the material. Furthermore, the photon beam can be directed to anywhere without contact with the work-piece. Consequently, welds can be controlled very precisely in location and a weld of very narrow bead can be produced. Moreover, the heat transferred to the surrounding material is not significant since heat transport away from the weld pool is almost entirely by

conduction. The processing time determines the energy dissipation, and thus the heat affected region.

There are two types of laser welding[1], one is deep penetration keyhole welding and the other is conduction welding. When coherently focused light is directed at the welding spot, it is absorbed in a surface layer of approximately 0.5 μm thickness[2]. If the power density is adequate, the surface is then melted and a vapor capillary occurs as the actual welding heat source to initiate keyhole welding. If the beam intensity is not high enough, heat is generated only on the surface and penetrates into the interior of the welding spot solely as a result of heat conduction.

In conventional welding, heat is generated mainly on the surface and must be propagated into the interior by thermal conduction, which occurs in three dimensions. This process mechanism based on heat conduction limits the processing speed and the heat loss can be high. As a result, the weld bead is relatively large. In contrast, during laser beam welding, the heat source can be generated in the interior of the material if the beam intensity is high enough. This situation increases efficiency and produces welds with high depth-to-width aspect ratio.

The use of a laser to supply the energy for welding has a number of advantages over conventional methods. Notably, lasers are capable of supplying high power into a very small volume. For example, weld over 10-mm deep penetration are possible in a single pass[68-69]. Laser welding can also be carried out at a high scan speed. Thus the region involved is heated and cooled very rapidly so that only a small amount of heat is deposited in the base materials. As a result, thermal distortion is much reduced. That is why the laser welding produces high quality welds with a small heat-affected zone (HAZ) and a high depth-to-width ratio for the fusion zone. In addition, laser welding is a non-contact process and it does not require any filler wire so that welds can be produced with little or no contamination. Moreover, laser welding has the ability to weld from one side in a variety of configurations. Steel blanks can be butt welded regardless of differences in alloy composition, coatings or thickness. In short, localized heating by a focused beam, deep penetration and high speed are the main advantages over traditional processes. This technique is extremely important in the automotive industry.

An important application of laser welding in industry is in the production of tailored blanks[6] in which two steel sheets of different gauges are welded together before being formed. A laser welded seam is stronger than the base material and forms a smooth joint between the two blanks and enable stamping with minimum die wear. With laser welding, the material's formability is reduced only within a narrow heat affected zone that barely alters the macroscopic formability of the whole panel. In this respect, deep drawing operations are possible. If galvanized steel is used, a narrow weld seam means little zinc depletion. Thus corrosion resistance throughout the heat-affected zone is possible.

Laser beam welding has proved to be a reliable method of joining piece-parts in high speed, automatic, large-volume production operations. As the scale of production increases, the need for in-process sensing and on-line supervisory or adaptive control of the vital process parameters is increasing, since adaptive control will ensure good quality and reliability. This results in reducing scrap rate of materials due to improper operating conditions or the unpredictable variation of material properties such as surface condition.

1.1.2 In-process monitoring techniques

In automatic machinery, the machine will go through its programmed movements without human intervention and usually the machine is self-regulating. In ordinary automation there is a sequence of operation subject to some overall control. With adaptive control or intelligent machines, the machine can be set a task and it teaches itself to do the task better and better according to some preset criteria. The start of this process is to be able to take the signal from the process while the process is running and to do so sufficiently quickly that the error detection can be made and the machine corrected before there is any considerable product waste. Fast in-process data acquisition can be realized in laser processing.

With laser processing, the welding system can be programmed in a very flexible way to direct the optical energy to the work-piece. What is more important is that there are very few side effects in delivering this optical energy. No electric or magnetic fields,

sound, light or other optical signals other than that from the laser beam itself are associated with beam delivery. In addition, there is no heat or mechanical stress resulting from the transmission process. Thus, any signal from the laser process will probably come from the interaction itself. This gives a good opportunity for in-process diagnostics.

Previous work for the in-process monitoring of laser welding process includes plasma charge sensing[4,5], optical sensing[6,7], acoustic sensing[8,9], and imaging (video camera)[10]. These approaches have a feature of obtaining one parameter that is a function of welding parameters. Plasma generation is inherent to the CO_2 laser welding process, and this plasma produces acoustic and optical emissions. Most in-process monitoring techniques use these emissions as information sources.

Acoustic and optical emission signals are closely related to plasma intensity and dynamic processes involved in plasma generation are reflected in these emission signals. Therefore, emission signals contain related diagnostic information about the welding process. Besides, emission data can be obtained with sensors away from the beam-material interaction zone. It thus makes non-contact monitoring and measurement possible.

1.1.2.1 Plasma charge sensor

The intensity and stability of the plasma are directly related to the welding process and weld quality. An unstable plasma affects the beam absorption by the work-piece and thus thermal input to the welding process, leading to variable weld quality. On the other hand, variations of process parameters or material defects during laser beam interaction with materials can cause the instability of the plasma. In general, an intense plasma indicates that sufficient laser power has been deposited on the material and converted into heat. Weak plasma signal implies a loss of beam power or poor coupling of laser power into the material, which may be caused by material defects or damage to optical components. Plasma characteristics can be measured by an plasma charge sensor[5], which uses an electrically isolated welding nozzle as a passive electric probe to detect the charge potential in the space between the nozzle and the work-piece. The charge observed

is a function of the formation of a plasma cloud in the region between the welding nozzle and the work-piece. The charge is mainly generated due to optical and thermal ionization of the vapor atoms, and the thermionic emission from the work-piece. The formation of the plasma cloud is indicative of keyhole formation. A deep or wider keyhole results in a greater number of charged particles within the plasma and a higher plasma temperature. The sensor thus can respond to the state of the weld as well as the depth of penetration.

Li *et al*[5] have demonstrated that the plasma charge sensor has the capability of detecting plasma temperature, weld penetration depth, and a wide range of weld defects such as keyhole failure, weld perforation, mild-weld disruptions, weld humping and incomplete welds. With a modified plasma charge sensor in which a ceramic laser-welding nozzle fitted with four quadrantal isolated electrodes of the plasma charge sensor, they showed the possibility of detecting laser beam position shift and mistracking by taking two differential signals from the opposing pairs of electrodes.

The plasma charge sensor requires a specially designed laser welding head and direct contact with the laser-generated plasma. This structure limits the application area, and is not usually suitable for large scale welding system.

1.1.2.2 Optical sensors

Optical sensors detect plasma emission, emission from the hot molten weld pool and reflected laser radiation. There have been many studies on the analysis of plasma emission. Plasma emission can be viewed directly, recorded through a fiber at the side, or viewed through a scraper mirror[6, 12]. Plasma radiation coming from the welding site has two basic sources. The first is the weld pool that radiates mainly in the infrared at temperatures up to the boiling point. The second one is the plasma which radiates in the visible and the ultraviolet at temperatures up to 10^4 K. Both sources have emission over a wide wavelength range. Chen *et al*[6] studied plasma radiation from welding at two wavelength bands in the UV and in the IR, and found that the signals in both wavelength bands are relatively constant under good welding conditions. From signal strength and stability, weld failure due to the deposited specific energy, focus condition and surface

defects could be identified. This study showed the predictive nature of the ultraviolet signal to certain welding faults such as incipient keyhole failure.

During penetration welding, the keyhole cannot be kept stable because of the fluid dynamic processes and variations in laser beam coupling, so that the plasma emission is not constant. A variation in the metal vapor density during welding is directly responsible for plasma emission fluctuations, so that the fluctuation spectrum can be related to weld quality. The correlation between the fluctuations of the emission of the plasma above the work-piece and the degree of full penetration was described by Maischner *at el*[10]. Their results showed that with increasing degree of full penetration higher amplitudes at high frequencies were detected. Recently, Beyer *et al*[12] used a neutral network with back-propagation algorithm to treat the plasma emission spectrum in order to correlate the penetration with emission. This technique proved to be successful in identifying full penetration welding conditions. But this technique has not yet been incorporated into an adaptive control circuit.

A quality-monitoring system employing multi-photo sensors has been reported by Miyamoto *et al*[13, 14]. In their system, two or more photodiodes were used to view the weld plasma plume at various angles. It was suggested that at large aiming angles the sensors detect the plasma behavior in the keyhole rather than the plasma above the metal surface, while at lower aiming angles the sensors mainly detect the behavior of the plasma ejected out of the keyhole. Their experimental results showed that the mean square value of the AC component of the deep red light detected by a photodiode at an angle of 75 degrees can be related to weld penetration.

Oscillations in the optical emission signal have been used to detect the presence of an excessive gap between the plates in YAG laser lap welding[15]. In their work, the light returned through the core of the delivery fiber is detected at the rear of a laser-tuning mirror, which is referred to as the core power monitor. By means of fast Fourier transform, the detected signals show a very distinct frequency peak appearing at around 3 kHz when the keyhole is completely open. This frequency peak vanishes when the keyhole closes at the bottom. The primary infrared emissions from the weld pool simply indicate the heat content of the weld since a larger heat input will result in a higher

temperature and an increase in infrared emission. The dependence of infrared emission signals on penetration depth has been studied by Sanders *et al*[16]. They obtained a nearly linear relationship between the weld monitor signal and the weld depth under partial penetration conditions. When full penetration is achieved, the weld monitor signal was found to drop.

Use of two photodiodes to detect the sagging of the melt pool due to a progressive gap between the edges and to detect the linear misalignment due to a change of slope between the edges was reported by Nava-Rudiger *et al*[17]. In their studies, the addition and subtraction of the two signals have a good correlation with the geometric defects. If the optical detection is designed in such a way that an image of the keyhole is observed through a pinhole on the focusing mirror[18], a better relation between signal intensity and the penetration depth can be reached. However, this approach raises a potential difficulty in the setup of the measuring device. An infrared sensing device has been used by Doong *et al*[19] to investigate the feasibility of measuring the surface temperature variation near the molten pool during laser beam welding. The temperature variation can be correlated to changes in welding parameters. In their study, the defects of welds such as undercut, misalignment and inadequate penetration problems can be observed from the variation in the temperature signals.

A focus control system for YAG laser welding has been reported by Haran *et al*[20], which is based on an optical sensor incorporated into the fiber delivery system to detect light generated by the welding process and uses the chromatic aberrations in the optical delivery system to separate the broadband light into two wavelength bands. These two different spectral bands of light will be imaged at different distances. As a result, maximum coupling will occur for each spectral band at a different standoff distance between the effector optics and the work-piece. However, this focal position sensing system cannot be applied to CO_2 laser welding systems.

The use of a CCD camera to record and measure the image size of the weld pool or plasma plume is another optical approach to monitor laser-welding processing. For a good weld in a specific material, there is optimum plasma plume size that is determined by the welding speed and the laser power. Kinsman and Duley[11] have successfully

achieved adaptive control on the welding speed by calculating the pixel number of the image and the deviation of the pixel number as well as with a fuzzy logic algorithm. However, in laser welding of different gauge sheet material, the technique to view the size of the plume image may have difficulty in determine the control action. This is because the beam position shifts to the thick sheet side and generates a large plume while the speed should be reduced to ensure full penetration. Direct visual inspection of the melt pool through a CCD video camera with a welding green optical filter was performed by L. Li *et al*[21]. To sample only the melt pool and the high temperature spots, they developed a real time adaptive closed loop control system for process parameters such as melt pool size, average image intensity, and work-piece standoff. However, such an image sensor and the required processing system are expensive.

1.1.2.3 Acoustic sensor

Sonic detectors are free from contamination by the dust from laser welding process and are also cheaper than optical detectors, and may be suitable for industrial applications although they are susceptible to false signals. Detection of acoustic emission can be made through an acoustic mirror, an acoustic nozzle[1], or through air-borne acoustic signals[8]. The acoustic signal that is sensed through the acoustic mirror[70] is not a direct signal and it could be influenced by the fluctuation of the laser power, while sensing through the acoustic nozzle is not straightforward so that these two techniques are not attractive for monitoring laser beam welding. Air-borne acoustic signals come directly from the welding site, and experiments indicate that air-borne acoustic signals contain information about penetration. One of the approaches of this work is to study air-borne acoustic emission during laser welding and to try to find a signature that indicates weld quality.

Acoustic emission used as a monitoring signal is a new technique, and only limited work has been done to date. In the early 1960s, Borchers *et al* detected acoustic emission during the melting and solidification of metals. During conventional welding of steel, Racko[22] and Hartbower *et al*[23] observed discernible acoustic emission which

could be an indicator of cracking along the weld. Acoustic emission from cracking in welding has a broad frequency spectrum, which spans up to 300 kHz with peak emission near 100 kHz[24]. In laser processing, Saifi *et al* [25] recorded and studied the acoustic emission using a piezoelectric crystal mounted directly to the work-piece near the weld site during welding with a high repetition rate pulse YAG laser.

In 1985, Jon[8] first reported the results of non-contact acoustic emission monitoring technique for laser beam welding. He used a piezoelectric sensor to monitor pressure changes generated by the intense vaporization produced during laser welding. In his work, the acoustic sensor was attached to a steel plate suspended above the work-piece. On the plate there was a hole through which the laser beam passed to carry out the welding. The resulting acoustic emission propagated through the air and the steel plate to reach the sonic sensor. In this way, the detector only senses the strong signal from intense vaporization. Such technique was reported to be able to detect laser misfiring, loss of power, improper focus and excess root opening. It was claimed that the technique of monitoring acoustic emission is suitable for quality control in laser welding.

The study of air-borne acoustic emission during laser welding is quite new. In 1993, J. W. Whittaker *et al* [26] found that the laser focus position was optimized when acoustic emission energy was at maximum. In the same year, studies on the power spectrum of acoustic emission during laser welding of aluminum have been carried out by the Waterloo group[27, 28]. It was observed that during full-penetration welding of aluminum there exists a dominant frequency band peaked near 6.5 kHz over the frequency range of 0 - 10 kHz. The acoustic signal of this frequency band may possibly be used as an indicator for monitoring weld quality. But no approach has been developed to deal with this signal yet.

Farson *et al* [29] reported a laser weld penetration monitoring and control system. In this research, the air-borne acoustic signal was sensed with a microphone and the signal then was filtered, digitized and Fourier-transformed by a computer. The power spectrum of the signal is then input to a neutral network algorithm to be analyzed. From the processed acoustic signals, it is capable of recognizing the state of penetration of a laser weld with about 95% accuracy. With this system, one can use a fuzzy logic

algorithm to calculate the change in welding speed necessary to maintain full weld penetration. However, this technique still cannot separate a poor weld due to partial penetration from one due to excess penetration.

In spite of the simplicity of acoustic detectors, the output of these sensors is strongly correlated to optical signals[30]. Since the plasma plume is one of the main sources to generate sound pressure signals in the vicinity of the laser material interaction site, the derivative of the optical signal may closely follow the acoustic wave intensity.

1.1.3 Objective

Monitoring of weld quality and adaptive control of the welding process are the goals of the present research work. In order to achieve these goals, developing a sensor system is the key task. In this work, several approaches to extract diagnostic information for in-process monitoring have been attempted, based on the analysis of the power spectrum of the acoustic signal over a wide frequency range (0 - 20 kHz) and correlation with corresponding welding conditions. Furthermore, an optical sensor system has been developed, which can be used for closed loop control of the laser welding process, and which is also capable of detecting various weld defects.

1.2 Basic theory of laser beam interaction with metals

1.2.1 Laser keyhole welding process

There are two methods of welding with the laser beam – the conduction limited mode and the keyhole penetration mode. Conduction limited welding occurs when the laser beam intensity is insufficient to cause significant vapor at the given welding speed. The molten metal in the weld pool circulates by the force resulting from the variation in the surface tension with temperature and density variation. During laser heating, only a

small amount of material on the surface is vaporized. Thus the optical and acoustic emission is weak.

The alternative mode is keyhole penetration welding in which the laser power density is sufficiently high ($\geq 10^6$ W/cm^2) to cause direct vaporization of the metal and a structure called the keyhole in the weld pool is formed. This keyhole is stabilized by the pressure from the vapor being generated and behaves like a black body in that the radiation enters the hole and is subject to multiple reflections before being able to escape. In consequence nearly all the incident beam is absorbed. For this reason, the energy conversion efficiency is very high in keyhole welding. Inside the keyhole there is a high density of metal vapor, which is partially absorbing and hence is capable of forming a plasma. In certain situations, the hot plasma vapor emerging from the keyhole may assist ionization of the shield gas through combined effect of laser photon absorption and electron-atom collision. The hot plasma not only is highly emitting, but also will exert a strong force on the surrounding gas thus generating acoustic emission. When the work-piece moves relative to the beam, the vapor pressure of the metal sustains the keyhole, and at the same time molten metal flows along side wall to the rear of the keyhole where it rapidly solidifies forming the weld nugget.

The metal vapor plasma is highly absorbent of the CO_2 laser beam. If it is not properly controlled or suppressed when it emerges from the keyhole, the plasma will severely attenuate the laser beam, resulting in diminished depth of penetration and perhaps a collapse of the keyhole. When the keyhole is sustained at an appropriate laser power, welding speed and plasma control, a steady state condition is attained. We then obtain a good quality deep-penetration weld with a high aspect ratio.

In keyhole welding, there are two mechanisms which determine weld quality. One is the flow structure of the molten metal around the keyhole and the other is the absorption of laser power within the keyhole. The flow structure directly affects the wave formation on the weld pool and final frozen weld bead geometry. The absorption may affect both the metal flow and entrapped porosity. In laser welding, deposition of laser beam power occurs on the boundary of the keyhole. Within the keyhole, the photon energy is absorbed partly by the mechanism of Fresnel absorption and partly by plasma

absorption and re-radiation[71,72]. Accordingly, laser power is transferred to the keyhole wall either by the plasma or by direct absorption at the wall.

When the laser beam is incident on the metal, the metal evaporates into the melt pool explosively, which is not a stable process. There always exist variations in the absorbed laser power by the material under irradiation with a moving laser beam. The variations include laser power fluctuation, change of beam coupling coefficient and the hydrodynamic instability at the boundary between the molten metal and the inside of the keyhole. The hydrodynamic instability may be driven by the convection in the liquid and the flow of vapor out of the keyhole. As a result, the keyhole oscillates and undergoes frequent collapse. Partial closure occurs. In the partial penetration case, the rapid and periodic motion of the keyhole results in a periodic change in weld depth. Every cycle of the keyhole motion can be divided into three phases: the stable oscillation period, the instability formation period and the recovery period. The change of keyhole structure due to its oscillation is associated with a complicated variation of refractive index with position in the keyhole. This in turn modifies the paths of light rays incident at grazing incidence on the keyhole wall. The Fresnel absorption coefficient[31] on the keyhole wall is $A(\theta) = 1 - R(\theta)$, which depends on the angle of incidence θ of the light on the boundary where $R(\theta)$ is the Fresnel reflection coefficient. The Fresnel absorption for light incident on a metal at grazing incidence angle shows the most dramatic rise in absorption[31]. Since the absorption depends on the incident angle and the keyhole is under dynamic oscillation, the Fresnel absorption must fluctuate from time to time. This makes the Fresnel contribution to the laser power absorbed in the keyhole very sensitive to the precise keyhole shape.

The inverse Bremsstrahlung (IB) absorption is the process in which an electron absorbs a photon in the electric field of an ion[32]. This absorption of the laser beam in the keyhole plasma depends on the temperature and electron density of the plasma. The absorbed energy is transported by heat conduction and radiative transport to a region near the boundary of the keyhole. The absorption of the CO_2 laser radiation in a plasma can be described by the absorption coefficient[32]

$$\alpha = [1.628\times10^{-32}(n_e n_i / \sqrt{T_e})\exp(\frac{h\nu}{kT}) + k_{ea}]\times[1-\exp(-\frac{h\nu}{kT})] \qquad (1.1)$$

where n_e and n_i are electron and ion densities. The first bracket contains the absorption due to the electron-ion inverse Bremsstrahlung and photorecombination, and k_{ea} denotes absorption due to the electron-atom inverse Bremsstrahlung. The second bracket contains the contribution of the stimulated emission. The absorption due to the electron-atom collisions does not exceed a few percent of the total absorption for laser generated plasma. At slow welding speeds, the IB absorption will cause the keyhole radius to be larger than the laser beam. It should be noted that the radius of the laser beam at the focus does not maintain a constant geometry since the plasma in the metallic plume above the mouth of the keyhole is hot enough to defocus the laser beam.

Keyhole oscillation during laser beam welding of quartz and aluminum has been observed by Arata[33] using X-ray photography technique. Partial closure and re-opening in a keyhole were seen in a study of CO_2 laser interaction with liquids[34-35]. In order to estimate the time scale during the keyhole partial closure and re-open, a simple energy balance model was used by Duley[28]. If the keyhole is viewed as simple cylinder[36-37], the minimum energy required to re-establish the keyhole to its equilibrium depth after collapse is

$$\Delta E = \pi a^2 d\Delta H \qquad (1.2)$$

where d is the length of keyhole that is re-established. a is the keyhole radius, and $\Delta H = \rho c(T_v - T_m) + \Delta H_v$, where ρ is the liquid density, c is the heat capacity. T_v and T_m are vaporization and melting temperatures, respectively, and ΔH_v is the latent heat of vaporization. For a partial collapse of the keyhole to a radius a_0 , the energy required becomes

$$\Delta E = \pi(a^2 - a_0^2)d\Delta H \qquad (1.3)$$

For a CW laser source, the time τ required for vaporization of this part of the keyhole is

$$\tau \equiv \frac{\Delta E}{P} = [1-(\frac{a_0}{a})^2]\frac{d\Delta H}{I} \qquad (1.4)$$

where P is laser power and $I = P/\pi a^2$ is the laser beam intensity. The diameter of the keyhole has been estimated to be very close to the diameter of the focused laser beam

based on the video observation of the molten pool during laser beam welding of steel[38]. The plasma emission area on the videotapes showed that the plasma obscured only the area that is approximately the same as that of the focused beam area. This observation also indicates that the position of the laser interaction is below the surface of the plate. In high power laser beam welding, the diameter of the laser beam depends on the power, the quality of the optics and the beam mode. The diameter can vary from 0.1 to 2 mm.

1.2.2 Operational characteristics and weld quality

Welds produced through laser keyhole welding can be classified roughly in three categories: lack of penetration, full penetration and burn through or drop out. These are determined by welding parameters, such as welding speed, laser power, and focus condition, and the type of material used as the work-piece. Suppose for a given laser power (P) with properly focusing, a good weld is produced at a welding speed (v_0). A specific energy E, defined as

$$E = \frac{P}{v} \tag{1.5}$$

is generally used to describe the deposited laser energy during welding[73]. When the welding speed is much slower than v_0, a high specific energy causes a large weld pool. In the case of welding steel sheet, the ferrostatic head is too large for surface tension to keep the pool in place and thus it drops out of the weld, leaving a hole or a depression. When the welding speed is too high, it results in a lack of penetration. In addition, the strong flow towards the center of the weld in the wake of the keyhole has no time to redistribute and so is frozen as an undercut at the sides of the weld. High speed welding also leads to pressure instabilities that cause an uneven weld bead and periodic change in weld depth[74]. Thus, it is obvious that the control of welding speed is important to obtain good welds.

In full penetration welding, the laser beam penetrates completely through the metal sheet. Within a range of the deposited laser power, the converted energy is not proportional to the deposited energy since part of the incident laser beam is lost through

the keyhole. However weld quality is not affected significantly yielding an operational range. Therefore, laser beam keyhole welding should be performed in this range, which allows consistent good welds. However, in real world, various material defects and alignment problems such as surface finish change, sheet fit up *etc* could affect final weld quality.

In general, an ideal welding process can offer the correct quantity of heat to melt welds. Excessive heat input will cause a wider pool with poor mechanical properties, large deflections and high residual stresses. Inadequate heat input will cause penetration problems and brittle structure such as fine martensite due to fast cooling rate. Therefore, processing parameters should be controlled under optimal welding condition.

The maximum welding speed for a given thickness rises with an increase in power. At high speeds the effects of lateral conduction during welding is small. Thus in the Swifthook and Gick[1] model with a moving line source, an analytical solution was obtained

$$Y = 0.483X \tag{1.6}$$

in which $Y = 2vR/\kappa$, $X = P/kdT$, $2R$ is the weld width (m), κ is the thermal diffusivity $(k/\rho c_p)$ (m^2/s), d is the thickness of the sheet (m), T is the temperature (K), $P = P_0(1-r_f)$ is the absorbed laser power (W), P_0 is the incident laser power and r_f is the reflectivity of the material. This simple equation can be used to make an approximate estimation of the maximum weld speed. However, because it has neglected latent heat, it overestimates the actual speed.

1.2.3 Vapor gas dynamics within the keyhole

The form and size of the keyhole during laser welding will adjust themselves according to the energy coupling conditions, which include laser power and welding speed for a given material. A theoretical description of keyhole dynamics is a very complex problem. Many models have been developed to calculate the geometry of the keyhole and to describe the stability behavior of a "cylindrical" keyhole[43]. With proper simplifications, each model only provides information on some aspects of keyhole

dynamics. No complete description has yet appeared. However, the only problem of interest here is in the pressure balance within the keyhole and the emerging of the vapor or plasma out of the keyhole opening.

To simplify numerical calculation, the keyhole has often been described as a cylindrical shape[39]. Under dynamical balance, the keyhole is assumed to be held open by the balance between surface tension p_γ (liquid wall), ablation pressure p_{ab} and gas pressure δp due to vapor flow out of keyhole along keyhole axis[40]. The hydrostatic and hydrodynamic pressure due to the melt can be neglected. Thus the pressure balance has the form[40]

$$p_{ab} + \delta p = p_\gamma \tag{1.7}$$

In equation (1.7), surface tension tries to close the keyhole while vapor pressure tries to keep the keyhole open.

Under irradiation with a high intensity laser beam, surface vaporization occurs. The vapor pressure at the heated surface can become much higher than the external pressure. The state of vapor close to the surface is far from thermodynamic equilibrium. A thin layer adjacent to the surface, which is called the Knudsen layer[40], is formed. Within this layer, the velocity distribution of the evaporated particles rapidly changes from a strongly non-equilibrium distribution at the surface to a local Maxwellian distribution with a speed normal to the surface. The thickness of the Knudsen layer is of the order of several mean free path lengths of the particles. At the keyhole wall, the thickness of the Knudsen layer is typically 10 μm, which is small relative to the keyhole diameter. With this simplification, Knudsen layer can be treated as a one-dimensional problem. Across the Knudsen layer, there exists an evaporation jet, which induces an ablation pressure on the surface. With conservation of momentum of the evaporating particles, the ablation pressure on the surface may be expressed as

$$p_{ab} = m(n_g u_g^2 - n_l u_l^2) \tag{1.8}$$

where n_g and u_g are density and velocity of the particles at the end of the Knudsen layer. n_l and u_l denote those at the liquid surface, and m is the mass of the evaporating particles. In considering the continuity equation of fluid flow $mnu = const$ and $n_l >> n_g$ (liquid

density is much higher than gas density), the ablation pressure can be approximated as[43]

$$p_{ab} \approx m n_g u_g^2 \tag{1.9}$$

The quantities n_g and u_g are to be evaluated at the end of the Knudsen layer where the gas is approximately in local equilibrium (local Maxwellian distribution). They could be estimated as functions of the temperature (T_s) in K at the keyhole wall and the local gas pressure (p_g) by solving the kinetic Knudsen layer equations[41]. In this calculation, the dimensionless quantities u_g/c_s, n_g/n_s were given as a function of p_s/p_g. The vapor pressure p_s is of the form[42]

$$\log p_s = -\frac{A}{T_s} - B \log T_s + C \tag{1.10}$$

where A, B, C are material constants. For steel, $A = 19710$, $B = 1.27$, and $C = 13.27$. The calculated pressure p_s is in mmHg. The local speed of sound c_s for an ideal gas can be expressed as $c_s = (5kT_s / 3m)^{1/2}$. The pressure p_s and density n_s can be related by the ideal gas equation $p_s = n_s k T_s$. The T_s at the keyhole wall may vary along the keyhole wall. To a good approximation, only the averaged surface temperature needs to be considered[43]

$$T_s = T_0 + \frac{2q_\lambda}{\rho c v} \frac{K_0(P_e)}{K_1(P_e)} I_0^2(P_e) \tag{1.11}$$

where $P_e = av / 2\kappa$ is the Péclet number, a is the keyhole radius and ρ is the density of the fluid. v is the welding speed. T_0 is the ambient temperature and $I_0(x)$, $K_0(x)$, $K_1(x)$ denote the modified Bessel functions. q_λ is the heat flux from heat conduction losses. It was estimated that the surface temperature can exceed the evaporation temperature of the metal by approximately 50 - 100 K[43]. With the surface temperature prescribed, the ablation pressure can be estimated to be ~10^4 Pa.

The pressure due to surface tension in equation (1.7) can be calculated using

$$p_\gamma = \frac{\gamma}{a} \tag{1.12}$$

where γ is the surface tension constant and a is the keyhole radius. The keyhole radius is approximately that of the radius of the laser beam at its focus. At the threshold laser power, $a \approx 1.7 r_0$ [43], and is nearly independent of the kind of metal. Beyond the laser

threshold, the keyhole radius rises rapidly with increasing laser power and decreasing translation speed. Using a typical value $\gamma = 1$ N/m for steel and $a = 10^{-4}$ m in equation (1.12) yields $p_\gamma \sim 10^4$ Pa.

It has been estimated[40] that the gas pressure within the keyhole due to the vapor flow out of the keyhole is of the same order of magnitude of p_{ab}.

When the keyhole is maintained, vapor gas flows out of the keyhole due to the pressure difference. The loss of the vapor particles is supplemented by the continuous evaporation from the keyhole wall (Fig.1.1). There is then a net mass flow from the keyhole wall to the center of the keyhole, followed by a flow out of the keyhole opening. Therefore, the vapor pressure at the center of the keyhole must be lower than that at the keyhole wall. For this reason, the pressure difference that drives the vapor flow out of the keyhole is less than the pressure p_γ (~10^4 Pa). In an experimental measurement by Miyamoto *et al*[44], it was found that the pressure difference is about 10^2 Pa. The out-flowing vapor is only a small portion of the vapor generated in the keyhole. With a moving laser beam, most of the vapor is condensed on the rear keyhole wall, forming part of the weld. The vapor profiles will initiate melt ejection primarily in the direction of the

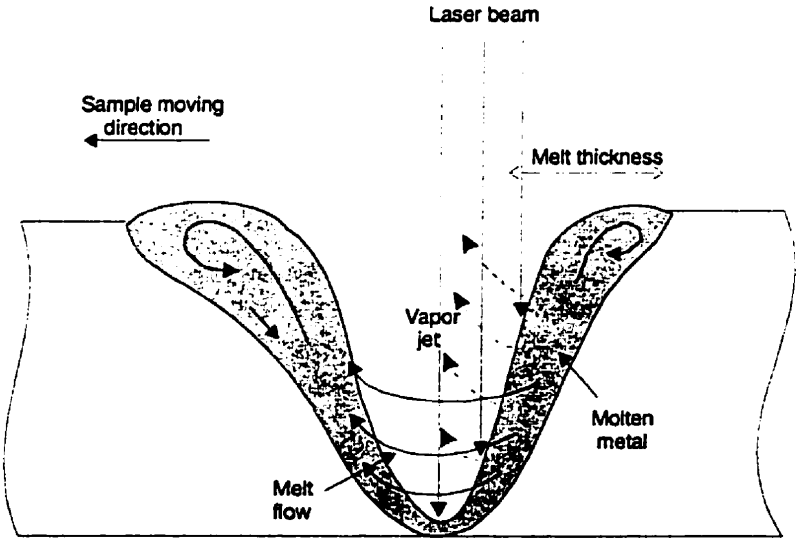


Figure 1. Schematic illustration of vapor generation, vapor flow and melt flow in laser welding keyhole.

sample translation and will create a vortex at the top of the back wall of the keyhole. The melt thickness Δ at the front side of the wall is determined by the heat diffusivity κ and the sample translation speed v since $\Delta \approx \kappa / v$.

1.3 Optical and acoustic emissions from keyhole welding

1.3.1 Plasma generation

Upon generation of a keyhole by an intense laser beam, the metal vapor within the keyhole interacts directly with the laser beam to form a plasma. This interaction involves direct photon absorption through the process of inverse Bremsstrahlung (IB). Inverse Bremsstrahlung is a process in which the plasma electrons absorb photons from the laser beam during inelastic collisions with ions, neutrals, and other electrons. The free electrons present in the metallic vapor are accelerated by inverse Bremsstrahlung until their kinetic energy is sufficient to ionize the atoms of the vapor by an avalanche process to a final density depending on the laser intensity and the loss mechanisms. The metallic plasma ejected at the keyhole opening will further induce ionization of the surrounding ambient gas atoms. The behavior of the plasma and vapor directly reflects keyhole characteristics. Studies of optical emission and acoustic emission of the expanding plasma or vapor are useful in understanding keyhole characteristics, and optical and acoustic emission also provides detection signals for in-process control.

The classical model of plasma heating and generation by microwaves can be approximately applied to the energy transfer by inverse Bremsstrahlung[45]. Using the rate equation for the electron density $n_e(t)$

$$\frac{dn_e(t)}{dt} = R_i - R_{loss} \tag{1.13}$$

where R_i is the ionization rate. $R_{loss} = R_{diff} + R_{rec}$, in which R_{diff} and R_{rec} are the loss rates by diffusion and recombination, respectively. The rate equation for the averaged electron energy $\bar{\varepsilon}$ (J)

$$n_e \frac{d\bar{\varepsilon}}{dt} = \alpha I - P_{el} - P_{loss} \tag{1.14}$$

in which α is the absorption coefficient (cm^{-1}), P_{el} is the power loss (W/cm^3) due to elastic electron-atom collisions and P_{loss} is the loss (W/cm^3) resulting from inelastic collisions. This inelastic collision loss can be written as[46]

$$P_{loss} = R_i(E_Z + \bar{\varepsilon}) - R_{ee}(E_Z + E_e + \bar{\varepsilon}) \tag{1.15}$$

where E_Z is the ionization energy and E_e is the excitation energy. n_e and $\bar{\varepsilon}$ depend on intensity. The recombination rate ($cm^{-1}t^{-1}$) [46]

$$R_{rec} = R_{ee} + R_{en} = f(n_e, \bar{\varepsilon}) n_e^3 + f(n_e, \bar{\varepsilon}) \sum_g \frac{n_g}{M_g} n_e^2 \tag{1.16}$$

originates from three-body electron recombination, where n_g is the neutral gas density of atomic mass M_g.

When in local equilibrium state, the electron density in the plasma is given approximately by the Saha equation[47]:

$$\frac{n_e n_{i,Z+1}}{n_{i,Z}} = \frac{2U_{i,Z+1}}{U_Z} \left(\frac{2\pi m_e \kappa T}{h^2}\right)^{3/2} \exp\left(-\frac{\chi_Z}{\kappa T}\right) \tag{1.17}$$

where $n_{i,Z}$ and $n_{i,Z+1}$ are the densities of the ground state atoms or ions of charge Z, $Z+1$, U_Z is the statistical weight of the ground state of an atom or ion of charge Z, and χ_Z is its ionization energy, m_e is the mass of an electron. The electron density will be strongly dependent on the plasma temperature. The population density, $n_{k,Z}$, of the vapor atoms is given by the Boltzmann law[47]

$$n_{k,Z} = \frac{n_{i,Z} g_k}{U_Z} \exp\left(\frac{E_Z - E_{k,Z}}{kT}\right) \tag{1.18}$$

where g_k and E_{kZ} are statistical weight and ionization energy of level k; $n_{i,Z}$, U_Z and E_Z are atomic (ionic) density, partition function and ionization energy, respectively.

The maximum electron density in the laser-induced plasma is related to the plasma frequency[5]

$$\omega_p = (\frac{n_e e^2}{\varepsilon_0 m_e})^{1/2} \tag{1.19}$$

where m_e is the mass of electron. When the laser beam frequency $\omega_l > \omega_p$, laser radiation is transmitted into the plasma, while for $\omega_l < \omega_p$, incident laser radiation is reflected by the plasma. The threshold intensity of a laser-induced plasma for a CW beam increases with decreasing laser power due to losses by heat flow and vaporization.

The absorption coefficient of the plasma from laser power for inverse Bremsstrahlung is strongly dependent on electron density and laser beam frequency. If the collisions between electrons and ions are the dominant process in laser generated plasma, when neglecting the effect of electron-atom IB, the absorption coefficient is given by[47]

$$\alpha = (\frac{\pi c}{\omega})^2 \frac{n_e S_0 G}{kT} (\frac{1-\exp(-h\nu / kT)}{h\nu / kT}) \tag{1.20}$$

The factor G is the Gaunt factor and the factor $n_e S_0$ is given by

$$n_e S_0 = \frac{16}{3} \frac{n_i n_e Z^2}{m^2 c^3} (\frac{e^2}{4\pi\varepsilon_0})^3 (\frac{2\pi m}{3kT})^{1/2} \tag{1.21}$$

where Z is the ionic charge and n_i the ion density. The Gaunt factor is a quantum mechanical correction to the classical theory. For an electron density which is much smaller than the critical cutoff density N_{cc}, which depends on the laser wavelength [from the above equation (1.18), $N_{cc} = 10^{21}/\lambda^2(\mu m)$], α is given by[45]

$$\alpha \cong \frac{\nu \omega_p^2}{c(\nu^2 + \omega_l^2)} \tag{1.22}$$

where ν is the electron collision frequency, c the speed of light, and ω_l and ω_p are the laser and plasma frequencies. For $\omega_l > \omega_p$ and $\omega_l > \nu$, the absorption can be approximated as

$$\alpha \approx C \frac{n_e(I) n_v(I)}{\omega_l^2} \tag{1.23}$$

in which $n_v(I)$ is the density of metal vapor and C is a constant. This absorption coefficient decreases with increasing frequency ω_l, resulting in a lowering of the threshold intensity with increasing wavelength. The plasma expansion out of the keyhole reduces the absorption.

It can be seen from the above that a plasma above the keyhole opening may attenuate the laser beam, resulting in an interruption of laser processing. Usually, a shielding gas is applied to the welding spot in order to blow off this plasma. However, breakdown in the shielding gas can also occur during laser welding through ignition of the metallic vapor. The breakdown intensity depends on the vapor density and the electron density, respectively. For example, with initial electron densities above 10^{16} cm^{-3}, the formation of a CO_2 laser-induced Ar plasma occurs at $I = 10^6$ W/cm^2. The laser-induced shielding gas plasma produces optical emission, which follows the strength of the vapor or plasma expansion out of the keyhole.

Plasma shielding is strongly dependent on shield gas. Helium is an efficient shielding gas, which minimizes breakdown and prevents blocking of the beam. This occurs since helium has a high ionization potential and good heat conductivity. Compared to other shielding gases, helium provides optimum welding results[75].

As the ionization threshold of the metal vapors is usually lower than that of the shield gas, the plasma is initiated through the ionization of metal vapor. If the growth rate of the electron energy by IB is higher than the loss due to elastic collision with neutral atoms of the gas or vapor, the necessary condition for the development of an electron avalanche in a gas leading to its ionization can be defined in the form

$$\alpha I > P_{el} = 2n_e \frac{m_e}{M} \nu \bar{\varepsilon} \tag{1.24}$$

where M is the mass (kg) of the neutral atoms of the vapor and m_e is the mass of electrons. If Δ is the first ionization potential (eV) of the vapor atom, the mean electron energy ($\bar{\varepsilon}$) initiating the ionization is estimated to be between $\Delta/8$ and $\Delta/10$[45]. Using this value of $\bar{\varepsilon}$, an intensity threshold I_i for initiating the plasma is when $\omega_i^2 >> \nu^2$

$$I_i(MW/cm^2) \approx 600 \frac{\Delta}{\lambda^2 A} \tag{1.25}$$

where A is the atomic mass number of the gas, and the wavelength λ is in μm. Because the ionization threshold decreases with Δ and depends on λ^{-2}, the ionization is facilitated at longer laser wavelength (such as at 10.6μm). In this respect, the threshold is rather low

for laser processing of metals. Therefore, a bright plasma plume is always present during laser welding.

1.3.2 Optical emission

Thermal radiation is one of the most important characteristics of the laser-generated plasma and consists of continuum radiation resulting from recombination (free-bound transitions) and Bremsstrahlung (free-free transitions) as well as line radiation (bound-bound transitions). In the plasma, local thermodynamic equilibrium is established when the electron collision rate processes dominate the processes of radiative decay and recombination. When local thermodynamic equilibrium is established in the plasma, the density in specific quantum states is the same as a system in complete thermal equilibrium having the same total density, temperature and chemical composition. In this state, radiation is not simply a blackbody spectrum at the plasma temperature. In general, the spectrum of the radiation from the plasma will have a complex structure consisting of the superposition of relatively narrow spectral lines and a continuum having a complex spectral structure.

The contribution of blackbody radiation from the weld pool at a wavelength λ and temperature T can be estimated using Planck's law[48]. The radiant emissivity $E_{b\lambda}$ (W/m^2) is given by

$$\frac{dE_{b\lambda}}{d\lambda} = \frac{c_1}{\lambda^5}\left(\exp\left(\frac{hc}{\lambda kT}\right) - 1\right)^{-1} \tag{1.26}$$

where c is the speed of light, h Planck's constant (6.626×10^{-34} J/s) and k is Boltzmann's constant (1.38×10^{-23} J/K). c_1 is a combined constant. This is an almost exponential rise in energy at a given waveband with a rise in temperature. Through integration, the total intensity in the half space E_b is obtained

$$E_b = \sigma T^4 \tag{1.27}$$

where σ is the Stefan-Boltzmann constant (5.6697×10^{-8} W/m^2K^4). For blackbody radiation, there is one wavelength λ_{max} for which the ratio $dE_{b\lambda}/d\lambda$ is a maximum for each temperature. This wavelength is defined by Wien's law:

$$\lambda_{max} T = 2897.8(\mu mK) \tag{1.28}$$

For steel with a boiling point of 3300 K and a melting point of 1800 K, the weld pool will typically radiate in a range between 0.87 – 1.6 μm. The vapor plasma has a much higher temperature, which has been measured at ~8000 K[14]. With this temperature, emission is intense with a wavelength peak in the UV range (0.36 μm).

Line radiation arises from highly excited and ionized atoms in the plasma. In the case of laser welding of steel sheet, the dominant spectral lines from the Fe ions and excited Fe atoms in the laser welding plasma are observed in the UV range. Assume the plasma is optically thin. The spectral line intensity, I_{ki}, is related to the population density of the upper level of a spectral line, $n_{k,Z}$, through[32]

$$I_{ki} = \frac{1}{4\pi}\int n_{k,Z} A_{ki} h\nu_{ki} dl \tag{1.29}$$

where A_{ki} is the atomic transition probability, $h\nu_{ki}$ the photon energy, and the integration is taken over the plasma depth that is viewed by the detector.

The radiation due to Bremsstrahlung produces continuum radiation with a Planck-function (B_ν) frequency distribution[49]:

$$E_{f\nu} = \frac{Cn_e n_i}{(2\pi\nu)^3 T^{0.5}}[1-\exp(-\frac{2\pi h\nu}{kT})]B_\nu \tag{1.30}$$

in which $E_{f\nu}$ is the radiation power emitted from the keyhole per unit volume and frequency interval, n_e and n_i are electron and ion number density, ν is the radiation frequency, k and h are Boltzmann's and Planck's constant, C is a constant. It has been estimated[50] that plume radiation accounts for more radiation output than the keyhole walls since the keyhole walls are at a lower temperature. Therefore, in spite of many radiation sources, the dominant source is the thermal radiation from the hot plasma.

In deep penetration welding, the plasma is at a high temperature. This temperature is sustained due to a complex balance between several factors, which include the

temperature of formation of the vapor, the absorption of the vapor to incoming radiation, the expansion of the plasma and the conduction losses. The absorption of the plasma to the incoming beam is dependent on the electron density. In considering the fact that the light emitted from the plasma is dependent on the temperature, any change away from this balanced state will result in a change in the plasma radiation, especially in the UV radiation. Therefore a slight change of plasma temperature will cause a noticeable change in UV signal before the keyhole collapses driven by fluid flow. Accompanying the keyhole collapse, the size of the weld pool changes, thus resulting in a change in the infrared radiation signal.

1.3.3 Sound generation

Acoustic emission is generated due to local volumetric change when a material is irradiated with a laser beam. The local volumetric change can be caused by heating at the irradiated spot and by direct vaporization of material. However, there is no sound generation if heating and vaporization are steady. Only an unsteady displacement of fluid accompanying an accelerated growth in volume or oscillation of the vapor cloud boundary gives rise to acoustic emission. Therefore, during laser welding, a potential source of sound is the unsteady flow of metal vapor out of the keyhole. The expanding hot vapor has a higher density than the ambient air, thus it displaces the surrounding air and generates sound.

The vapor expansion can be considered as a 'piston' which acts on the gas surrounding the keyhole opening. If p_g is the mean vapor pressure inside the keyhole, the pressure difference is

$$\Delta P = p_g - p_0 \tag{1.31}$$

which serves as the driving force for the vapor expansion out of the keyhole and determines the intensity of the acoustic emission, where p_0 is atmospheric pressure. Consider a small region, ΔV, adjacent to the keyhole opening, as shown in Fig.1.2. Suppose that a mass of vapor is injected into this region at a rate m per unit volume per unit time and that the newly injected mass occupies a fraction β per unit volume from

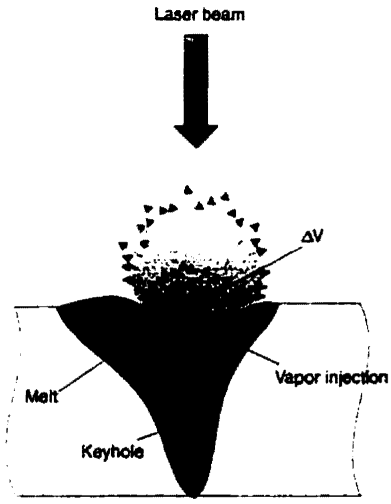


Figure 1.2 Illustration of acoustic generation.

which it has displaced the original fluid of mean density ρ_0. The mass conservation equation would be[51]

$$\frac{\partial \rho}{\partial t} + \rho_0 \nabla \cdot \mathbf{v} = m \tag{1.32}$$

where ρ is the overall density of the region above the keyhole opening, i.e. the total mass contained in unit volume, v is the vapor expansion velocity. If there were no external force, the momentum conservation equation would be

$$\rho_0 \frac{\partial \mathbf{v}}{\partial t} + \nabla p' = 0 \tag{1.33}$$

where p' is the sound field. The volumetric mass increase rate must be equal to

$$m = \frac{d}{dt}(\beta \rho_m) \tag{1.34}$$

in which ρ_m is the mass density of the injected vapor. Since the injected vapor displaces the ambient fluid, the mass density in the control volume above the keyhole is then

$$\rho = \beta \rho_m + (1-\beta)\rho_f \tag{1.35}$$

where ρ_f is the density of the ambient fluid, which is equal to ρ_0. A differential equation for sound generation can be derived from Eq.1.35

$$\frac{\partial \rho}{\partial t} = m + \frac{\partial \rho_f}{\partial t} - \frac{\partial}{\partial t}(\beta \rho_0) = m + \frac{1}{c^2}\frac{\partial p'}{\partial t} - \frac{\partial}{\partial t}(\beta \rho_0) \tag{1.36}$$

where c is the speed of sound, which is $p' = c^2 \rho'$. By differentiating the above equation with respect to time, we have

$$\frac{1}{c^2}\frac{\partial^2 p'}{\partial t^2} - \frac{\partial^2 \rho}{\partial t^2} = \frac{\partial^2}{\partial t^2}(\beta \rho_0) - \frac{\partial m}{\partial t} \tag{1.37}$$

By combining the above equations, a wave equation can be obtained

$$\frac{1}{c^2}\frac{\partial^2 p'}{\partial t^2} - \nabla^2 p' = \rho_0 \frac{\partial^2 \beta}{\partial t^2} \tag{1.38}$$

The solution to Eq.1.38 is

$$p'(\mathbf{r}, t) = \rho_0 \frac{\partial^2}{\partial t^2} \int_{V'} \frac{\beta(\mathbf{r}', t - |\mathbf{r} - \mathbf{r}'|/c)}{2\pi |\mathbf{r} - \mathbf{r}'|} d\mathbf{r}' \tag{1.39}$$

In reality, the keyhole opening is very small compared to the wavelength of the sound in ambient air and the distance of the sensor away from the source, so that the acoustic source from welding can be taken as a point. The solution for acoustic pressure at a distance r from the source can be expressed as[51]

$$p'(r, t) = \rho_0 \frac{\partial^2}{\partial t^2}\left(\frac{\beta(t - r/c)}{2\pi r}\right) \tag{1.40}$$

Therefore, sound pressure is generated by an unsteady vapor expansion, which corresponds to the time derivative of the vapor flow rate. This sound pressure decreases with distance from the plume. Furthermore, the keyhole shape, the keyhole fluctuation and degree of ionization of the vapor within the keyhole are important in determining the frequency distribution of the acoustic emission.

When considerable absorption of laser beam directly by vapor plasma occurs, unsteady heat added to the vapor will enhance the acoustic emission. Suppose the heat supplied to unit mass of vapor is $h(r, t)$ in the small volume ΔV. Then the vapor density is expressed as

$$\rho = \rho(p, h) \tag{1.41}$$

Hence

$$d\rho = \left.\frac{\partial \rho}{\partial p}\right|_h dp + \left.\frac{\partial \rho}{\partial h}\right|_p dh = \frac{1}{c^2} dp + \left.\frac{\partial \rho}{\partial h}\right|_p dh \tag{1.42}$$

Assume the vapor is a perfect gas, $\rho = p / RT$, so that

$$\left.\frac{\partial \rho}{\partial h}\right|_p = -\frac{p}{RT^2}\left.\frac{\partial T}{\partial h}\right|_p = -\frac{\rho_0(\gamma - 1)}{c^2} \tag{1.43}$$

giving

$$d\rho = \frac{1}{c^2} dp - \frac{\rho_0(\gamma - 1)}{c^2} dh \tag{1.44}$$

where $\gamma = c_p / c_v$ is a thermal constant. The unsteady heat addition provides a acoustic source term in the wave Eq.1.38, which becomes

$$\frac{1}{c^2}\frac{\partial^2 p'}{\partial t^2} - \nabla^2 p' = \rho_0 \frac{\partial^2 \beta}{\partial t^2} + \frac{\rho_0(\gamma - 1)}{c^2}\frac{\partial^2 h}{\partial t^2} \tag{1.45}$$

and acoustic emission is enhanced by the rate of change in the heat addition rate. Physically, the unsteady heating causes unsteady expansion of the vapor at essentially constant pressure. Therefore, the vapor expansion is the ultimate source of the sound emitted.

Chapter 2

Experimental Equipment and Sensing Techniques

The general equipment employed in the laser welding process and signal acquisition includes a CO_2 laser, a working table, and detectors and control boards. Figure 2.1 shows a schematic description of the system.

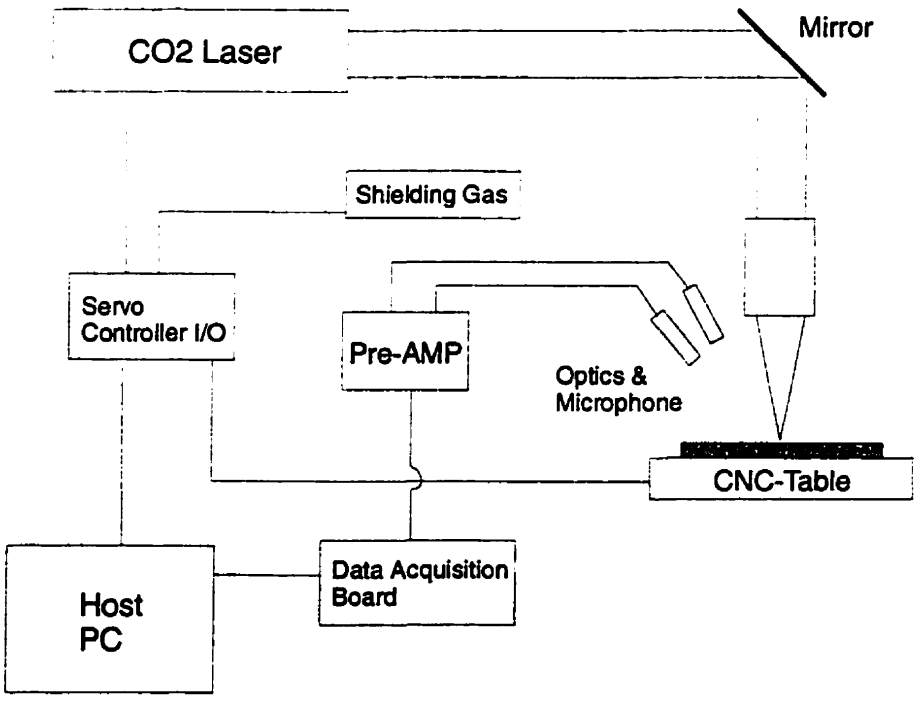


Fig. 2.1 Experimental setup for laser welding and signal detection.

2.1 CO_2 laser

The main equipment in a laser processing system is the laser. It provides the necessary heat source. CO_2 laser has a high electrical-to-optical energy transfer efficiency, and a high power generating ability. Up to now, the commercial laser with the highest output power available and high stability is the CO_2 laser. For this reason, CO_2 lasers are widely used as heat sources in the laser material processing industry.

Three basic elements are employed for generating the laser beam: an optical resonant cavity, an active lasing medium, and an excitation source. The optical cavity consists of two mirrors that are designed as a stable oscillatory cavity. For the CO_2 laser, the active lasing medium is a gas mixture consisting of Carbon Dioxide (CO_2), Nitrogen (N_2), and Helium (He). CO_2 is the principal gas. N_2 and He are added to enhance efficiency and provide the necessary electrical characteristics. The excitation is achieved by electrical discharge by means of the formation of plasma in the discharge tube. A number of technologies have been developed to make the CO_2 laser generate a high power beam. These include fast gas flow, preionization and the use of RF discharge excitation. Commercial lasers only are allowed a limited gas discharge zone. Fast gas flow technology makes the commercial laser capable of generating multi-kilowatt or even higher output. The fast flow CO_2 laser overcomes the discharge instability problem and the bottleneck effect by rapid cooling. The gas flow can be either transverse or axial. Transverse flow lasers have a simple and compact configuration, and can replace the gas in the discharge zone very quickly to generate a high power output. With axial flow lasers, an axial discharge and optical feedback favors an axially symmetric power distribution in the output beam. Such CO_2 lasers usually generate good laser beam quality at comparatively high power.

In this work, a Lumonics VFA-1700 CO_2 laser was used. This laser is a fast axial flow CO_2 laser. The fast gas flow is driven by a blower mounted below the laser head enclosure. The blower drives the lasing gas mixture at a high speed through the discharge tube where the glow discharge is carried out along the axial direction of the tube. The

heated gas flows out the chamber and into the heat exchanger. From the heat exchanger, the gas is recirculated through the resonator.

The VFA-1700 laser has dual discharge tubes that are parallel. Each discharge tube consists of multiple discharge sections. The purpose of this design is to provide a uniform discharge zone. The optical paths of these two tubes are connected together using two bending mirrors. This configuration saves a lot of space, and improves laser beam quality due to the increased length-to-aperture ratio. The rear mirror of the optical cavity has almost 100% reflectivity, allowing only a minute portion of the beam to be transmitted. This portion of beam is received by a thermopile to monitor laser power.

General parameters of the VFA-1700 CO_2 laser are as follows

Wavelength	10.6 μm
Rated output	1700 watts (CW)
Output power range	600 to 1750 watts
Output power stability	±2% deviation from set-point
Mode	TEM_{01}*
Pointing stability	±0.15 mrad, over 24 hours
Beam diameter	17 mm at $1/e^2$ points
Beam divergence	less than 3 mrad, full angle

The laser output power is obtained with a mixture having ratios CO_2:He:N_2 = 60:130:90, which are set and indicated on the gas panel. The total pressure of the gas mixture inside the cavity is 100 mbars. When required, a lower minimum power than that listed above can be reached by decreasing the CO_2 concentration in the mixture. In operation, the laser power can be adjusted by changing the discharge current. It has been found that the laser power increases almost linearly with discharge current. The overall performance of this laser is very stable, but there is a warm up period when the laser is switched on. During this initial period, the laser output increases a little since some remaining residual gas in the discharge tube is gradually replaced with lasing gas mixture. Thus, in order to achieve a stable laser output, the laser is allowed to warm up for about half an hour before use. In fact, the laser power delivered onto the work-piece is a little lower than the readings in the laser controller because of the losses due to imperfect reflection by the bending

mirrors and the reflection from the focal lens and *KCl*-protective window. The total loss is about 7 -8 %.

The laser also can be operated in a pulsed mode. By adjusting the command in a short program, the duty cycle, the repetition rates, and the modulation depth can be set. In addition, the laser output can provide different pulse shapes.

The resonator of the VFA laser supports a certain set of modes of oscillation. The idealized allowed sets of modes are Hermite-Gaussian functions, which have the spatial intensity distribution (TEM_{mn}) given by Hermite Polynomials

$$I_{mn}(x,y) = I_0\{[H_n(\frac{x\sqrt{2}}{\omega})H_m(\frac{y\sqrt{2}}{\omega})]\exp(-\frac{x^2+y^2}{\omega^2})\}^2 \qquad (2.1)$$

where H_m and H_n are the Hermite polynomials of order m and n, respectively. ω is the spot size of the beam which is defined as the radius where the intensity drops to $1/e^2$ of the value at the center. The lowest order of these modes is the TEM_{00} mode, which has the greatest peak intensity and lowest divergence. This mode actually has a simple Gaussian intensity distribution

$$I(r) = I_0 \exp(-\frac{r^2}{\omega^2}) \qquad (2.2)$$

in which I_0 is the intensity at the beam center. However, lasers do not always oscillate in only one mode but emit in a superposition of several modes. In addition, individual modes are not purely Gaussian because of the presence of finite apertures. For the VFA-1700 laser, the laser beam is in the TEM_{01}* mode which is a combination of the TEM_{00} mode and the TEM_{01} mode. The laser beam of this mode is preferred for welding

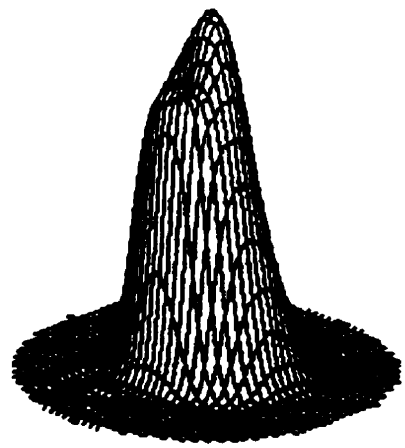


Figure 2.2 Intensity distribution of the VFA-1700 laser beam.

applications since it can create appropriate melting isotherms[52]. Fig.2.2 shows the intensity distribution of the VFA-1700 CO_2 laser beam. This intensity distribution was measured using a Prometec laser beam analyzer. For comparison, the Gaussian intensity distribution is given in Fig.2.3. It can be seen that the laser beam intensity distribution is very close to a Gaussian distribution.

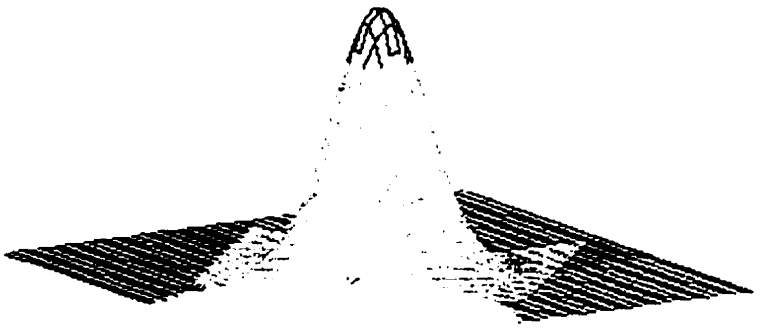


Figure 2.3 Gaussian intensity distribution.

The diffraction of light has several effects on the laser beam. First, the actual mode shape changes radically with distance so that the final mode shape can only be attained in the far-field region. Secondly, substantial fringing exists in the beam in the near-field region but it gradually disappears as the far-field region is approached. Finally, the laser diverges non-linearly in the near-field region while in the far-field region the spread with distance is constant. For these reasons, the laser beam is used at a large distance from the output mirror. In our setting, the delivering distance from the output mirror to the processing point is about 2 - 3 meters.

The diameter of the focal spot of a laser beam can be determined by $d = f \cdot \theta_d$, in which f is the focal length and θ_d is the full divergence angle of the laser beam. If a lens of shorter focal length is used, a smaller focal spot can be obtained and so can a higher laser beam intensity.

2.2 Laser head and working station

The laser head contains a *ZnSe* focusing lens, a *KCl* window and a gas nozzle and can be moved vertically to change the focal position on the work-piece. For laser welding, the *ZnSe* lens has a 5-inch focal length. This lens can focus the CO_2 laser beam down to a spot a few hundreds of micrometers in diameter.

The *KCl* window protects the *ZnSe* lens from contamination by dust or spatter from the welding site. The *KCl* window can easily be damaged by heat during welding. A damaged window will distort the laser beam so that the focusing condition will be altered. For this reason, the *KCl* window needs to be checked frequently.

The gas nozzle in the laser head supplies an axial shielding gas. This shielding gas also protects the lens system from spatter during laser welding and serves as cooling gas for the laser head. There is a side nozzle pointing to the weld site along the weld direction. Its function is to suppress the laser-induced plasma and to provide shielding for the welds.

The working table is a computer-numerically-controlled (CNC) table, which can be programmed for the desired motion including speed, direction, travel distance and a non-linear trajectory. In addition, the start and end points of the movement of the table and the firing of the laser beam can be timed sequentially. On the working table there is a slot or groove which is parallel with one of the axes of the movement. Laser welding is performed along this groove. During welding, metal sheets were kept firmly on the working table by clamps.

2.3 Motion control and Data acquisition system

Two motion control boards (Galil DMC-1000 and DMC-400 controller) are used to control XY 2-D motion and Z-axis motion separately. Three brush type servomotors are used to drive the welding table and the vertical motion of the laser head.

The data acquisition boards are a Microstar DSP 2400 data processor (DAP) and a Uei data acquisition board. The Microstar processor itself is a complete microcomputer

with its own CPU, RAM, ROM, analog and digital output, input control and timing circuits, and direct memory access controller. The DAP also contains a Motorola 56001 digital signal processor (DSP), which facilitates digital signal processing at high speed. The Uei data acquisition board has the capability of acquiring data simultaneously from 8 channels at a sampling rate of 10 MHz.

The input signal can be acquired directly by the DSP board and then transferred to the host computer for storage. These data give the signal in the time domain. When the frequency spectrum is desired, the input signal is first processed with a fast Fourier transform (FFT) by the DSP and then sent to the host computer. The frequency spectrum thus given finally was composed of 512-data points. In order to get a spectrum over the frequency range of 0 - 20 kHz, the FFT was carried out at a sampling rate of 4×10^4 samples per second. This sampling rate prevents aliasing from occurring in our data. Basically, aliasing is a phenomenon in which a high-frequency component is represented by a lower-frequency component, thus resulting in an incorrect description of the spectral distribution of the signal.

With the Uei board, it can be operated in the direct memory access (DMA) mode. In this mode, the acquired data can be accessed directly by the CPU, thus eliminating data transfer, which offers much fast processing. This board is used to acquire multi-channel optical emission data.

2.4 Detectors and sensing system

Acoustic signals are detected by an Omni-directional condenser microphone (Electret 33-1063) with a flat frequency response between 50 Hz - 20 kHz. Above 20 kHz, the response drops sharply so that it is not possible that the higher frequency components from acoustic emission would affect our FFT results through aliasing. This microphone can be easily mounted around the laser head. In this experiment, the microphone was attached to the laser head and pointed toward the welding spot. The microphone should be mounted close to the welding site and directly aimed at it since the

reflection from the nearby objects could affect the response of the microphone to the acoustic emission.

A pyroelectric detector (Molectron model P3-01) has been used to monitor the laser pulse. The CO_2 light was scraped using a beam splitter before the focusing lens. This detector could also be mounted over the weld surface beside the laser head. In this way, it could be used to record reflected CO_2 laser radiation from the welding spot. It views the weld pool at an angle of about 45 degrees normal to the surface. The pyroelectric detector has a response over a wide wavelength range which extends to the far infrared. The rise time of this detector depends on the load resistors. In our case, the detector was set to high responsitivity so that the typical rise time was about 0.5 ms. A narrow band filter with a transmission window at the wavelength of the CO_2 laser emission was put in front of the detector window so that it only allows the detector to sense the laser radiation reflected from the weld pool.

An optical sensing system was also developed in this work, which has the ability of sensing a change in focal position, beam position and relative weld pool size. This system offers the possibility of adaptive control of the laser welding process. This sensing system consists of a light focusing and collecting unit, a structured fiber bundle and a photodiode array and pre-amplifiers. The output electric signals from this system are directly fed into the data acquisition board.

The focusing unit is an optical system that contains two focusing lenses, and images the plume onto the fiber bundle. Commercially available photodiodes are used to construct the photodiode array. In the connector between the fiber output and the photodiodes, various filters are inserted, which allows multi-wavelength detection.

The structured fiber bundle is the basis of this system, and is not available as a

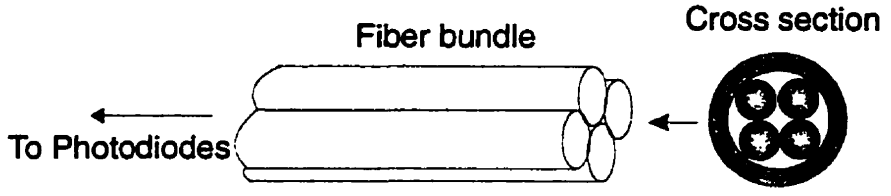


Figure 2.4 Diagrammatically illustration of the structured fiber bundle in the optical sensing system.

commercial product. The bundle is configured in such a way that each fiber collects the desired portion of the light emitted in the plasma plume and the weld pool. A typical structure of the fiber bundle used in this work is shown in Fig.2.4. Here, standard optical fiber connectors were used to make the device, and the unit is very compact and easy to use.

2.5 Welding materials and welding trials

During laser welding, the laser beam focal position must be adjusted properly to obtain an optimum condition since the focal position affects the formation of the weld and the weld geometry. The laser beam can be focused either below the surface or above it, as shown in Fig.2.5. Usually, to get a good quality weld the focal position is adjusted to be slightly below the metal surface. This setting optimizes the formation and stability of the keyhole. Experience shows that for welding thick metal sheet, a focus about 0.5 ~ 1 mm below the surface yields higher penetration, while for thin sheet, focusing on the surface is acceptable. In this study, sheet thickness is around 1 mm so that the focus either on the surface or slightly below the surface gives good results. However, the generated acoustic signals for these two focus conditions may be different, and such differences can be used to monitor the focusing condition by acoustic emission. Optical emission signals also show a dependence on focal positions.

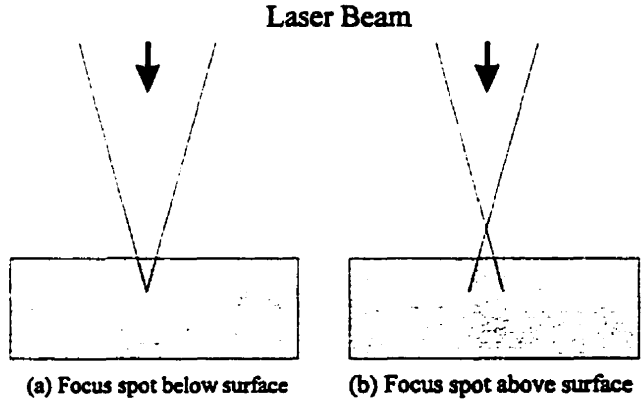


Figure 2.5 Illustration of laser beam focus on the metal surface.

Mild steel, galvanized and galvannealed steel sheets were used in this study. Mild steel is an ordinary cold rolled steel, while galvanized and galvannealed steels have a zinc coating. Mild steel has a good absorptivity for CO_2 laser radiation, and can be easily welded. The zinc coating on the galvanized steel sheet behaves as a lubricant and prolongs the life of press tools, and the coating also protects the steel from rust. This coating does not materially affect weldability for butt welds, however the vaporization of the zinc coating does have some effects on the welding process. Depending on the deposited laser power and the scanning speed, the weld surface appearance can range from a continuous coating remaining on the weld surface to a black zone from which all the zinc has been vaporized. During welding, the weld pool can be very turbulent owing to the escape of zinc vapor, and sometimes spatter appears. The high temperature during welding causes the formation of zinc oxide vapor and with primers the breakdown products can include H_2, CO_2 and water vapor. These vapors and gases can cause porosity in the weld. In butt welding, coated steel sheet can be welded easily without treatment on the cutting edge. In lap welding, a channel must be provided to allow Zn vapor to escape, or the welds will be porous.

Steel sheets with thicknesses from 0.8 mm to 1.6 mm were used. Helium, argon and nitrogen were used as shielding gases in laser beam keyhole welding. Since only thin metal sheets (less than 2 mm) are welded in this experiment, the plasma blocking of the laser beam is not a significant problem in this case, and different kinds of shielding gas have little effect on the welding process.

Bead-on-plate, butt as well as lap welds were carried out, and welds were made in a single pass. Butt weld was performed between sheets with the same or different thickness. Samples were prepared by cutting the metal sheet using a shear. No careful cleaning of samples is required except for wiping off grease since grease can change surface absorptivity. In order to generate weld defects and analyze the relation of the signals to weld faults, defects were purposely introduced.

Laser welding is usually carried out at a relatively high speed. But at initiation, the laser beam needs to dwell a while to start the weld for some metals. This initiation time also depends on the thickness of metal, and in our experiments usually ten microseconds

were used. A series of welds have been done under various welding conditions including changing laser power, welding speed, focal position, and seam gap *etc*. These processing conditions yield welds of various qualities so that the relation between weld quality and welding parameters can be determined. All the welding processes and recording of the signals were controlled by a computer and results were found to be reproducible.

The general appearance of the welds can be seen immediately after welding, so that weld quality can be roughly judged by visual inspection of the weld bead. Detailed examination of the welds was carried out through analyzing weld cross section. In doing so, welds were first cut with a diamond wheel saw perpendicular to the direction of welding, and then the weld cross sections were polished and etched with nital. The dimensions of the weld zone were observed and measured under a stereo optical microscope or with a digital micrometer. Structures of the welds were photographed using a digital camera attached to the optical microscope. The final weld quality was assessed according to the weld width and depth, the smoothness of the weld bead and the presence of defects that included holes and cracks in the welds.

In order to test the developed weld fault detecting technique, artificial weld defects were generated via creating gap, mismatch and damage on the edge of sheet. Pinhole is a common weld defect occurring in production line and it is created during laser beam interaction with metal or in solidification of the molten pool. If there is a damage on the joining edge or mismatch, beam interaction will be interrupted and less metal will be melted to fill the joint thus causing pinhole formation. On the other hand, improper melt metal flow pattern, drop out of liquid metal or foreign element in the melt pool will result in pinhole formation during solidification phase. It should be pointed out that monitoring emission signal during laser beam welding could only detect the pinholes created during laser beam interaction. Detection of pinholes formed during solidification phase needs different sensing technique.

Chapter 3

Acoustic Monitoring Techniques

3.1 Characteristics and quantization of acoustic signals

Acoustic monitoring is one of the approaches that have been adopted in developing an efficient and fast-response in-process monitoring technique for laser beam welding. This technique is attractive because of its simplicity and its low price as well as its fast response. However, the reliability of this technique is questionable due to the fact that acoustic sensors are susceptible to interference in production environments. Up to now acoustic monitoring remains a topic of academic interest. Air-borne acoustic signals are mainly generated by unsteady expansion of the vapor or plasma plume during laser beam interaction with the metal. The unsteadiness is governed by the keyhole oscillation and rate of vapor generation. It is intuitive that the sound level and the energy distribution among the frequency components would vary under different welding conditions because a keyhole and weld pool of different size is produced.

A set of spectra of acoustic emission (AE) is given in Fig.3.1. This set of data was acquired from welding steel sheet with a 1.65 kW CO_2-laser beam at different speeds. Speeds were chosen in such a way that welds of various qualities were produced. Welds with different quality can be related to these acoustic spectra. For all of the keyhole welds, acoustic components cover the entire frequency range 0 – 20 kHz, but there are two distinct regions that can be identified. One is the low frequency region below 5 kHz while the other is the region of frequency above 5 kHz. A relatively strong narrow band

of frequency components in the region of 3-5 kHz is apparent, which originates from the keyhole oscillation. Many components in the low frequency range can be seen when welding at low speed, which corresponds to a wide weld bead. At high speed, high frequency components are relatively strong. In this case, the weld has only partial penetration. At moderate welding speeds, yielding good welds, the narrow band is much stronger in comparison with the background. The dominance of this band of frequency components produces a distinct tone that can be heard during the welding process. In contrast, frequency components in the high frequency region generate a harsh background sound.

Plasma plume expansion is a highly fluctuating process during laser welding and this affects the acoustic signal significantly. As a result, a particular component at a given frequency has no clear physical meaning. In order to interpret these signals and facilitate a numerical comparison between acoustic signals under different welding conditions, normalization of the FFT spectra is applied. In this approach, the spectrum was divided into 20 blocks of sub-frequency with each one having 1 kHz bandwidth. The intensity in each 1 kHz band was then integrated and expressed as a fraction of total acoustic power. These acoustic blocks can be conveniently expressed as a vector in a 20-dimension space:

$$\mathbf{I} = [I_1, I_2, \cdots, I_k]^T \tag{3.1}$$

in which $I_k\{k=1, 2,...,20\}$ are individual block frequency components of the acoustic signals.

The normalized acoustic spectra in Fig.3.1 are shown in Fig.3.2, and give a clearer mathematical description of the energy distribution. It is apparent that welding at intermediate speed results in an enhancement in AE intensity in the frequency blocks at 4 and 5 kHz. At higher and lower welding speed, the dominant frequency components lie in the 12-17 kHz range. AE in this frequency range are related to instabilities in the keyhole[53] and accompany welds when the resulting structure (such as penetration condition) deviates from that obtained under optimized conditions. This variation in weld morphology can be seen in weld cross-sections shown in Fig.3.3.

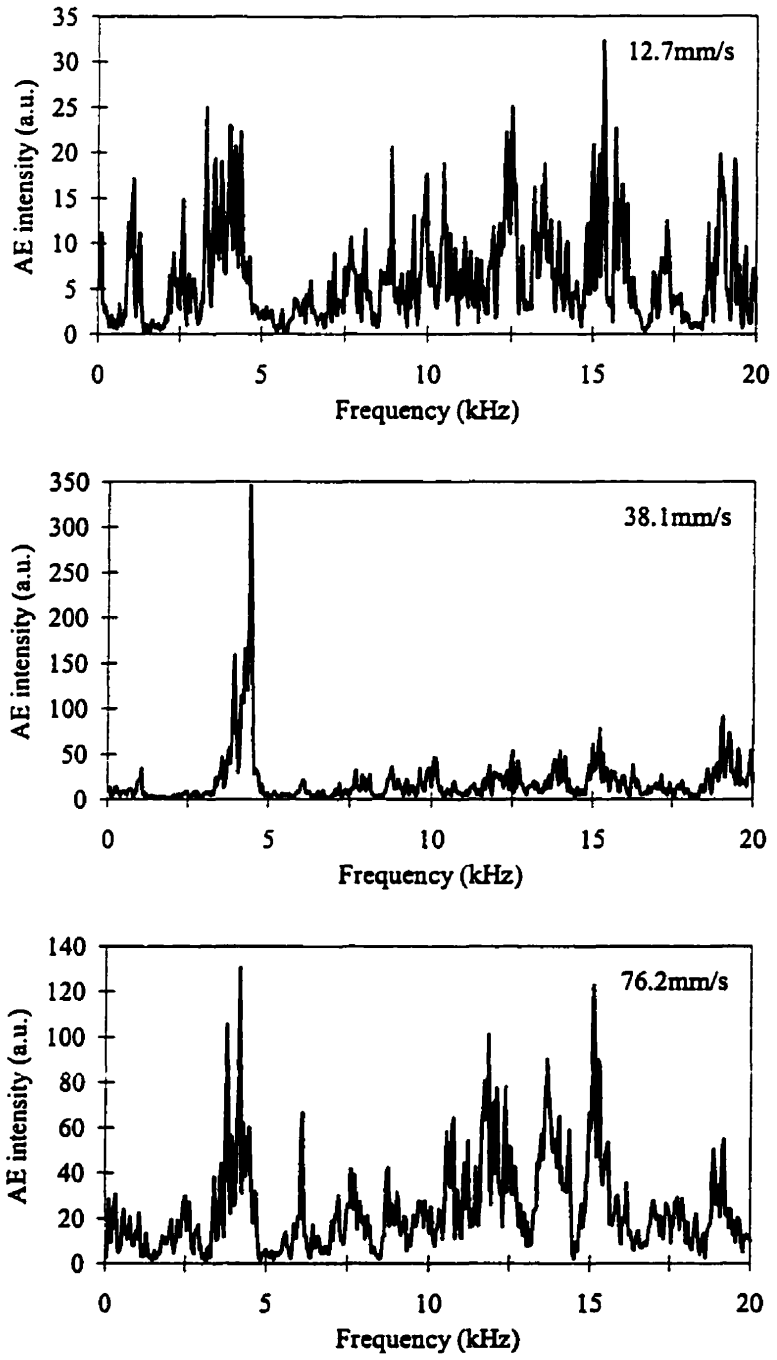


Figure 3.1 Acoustic emission spectra during laser keyhole welding of steel sheet at three different welding speeds.

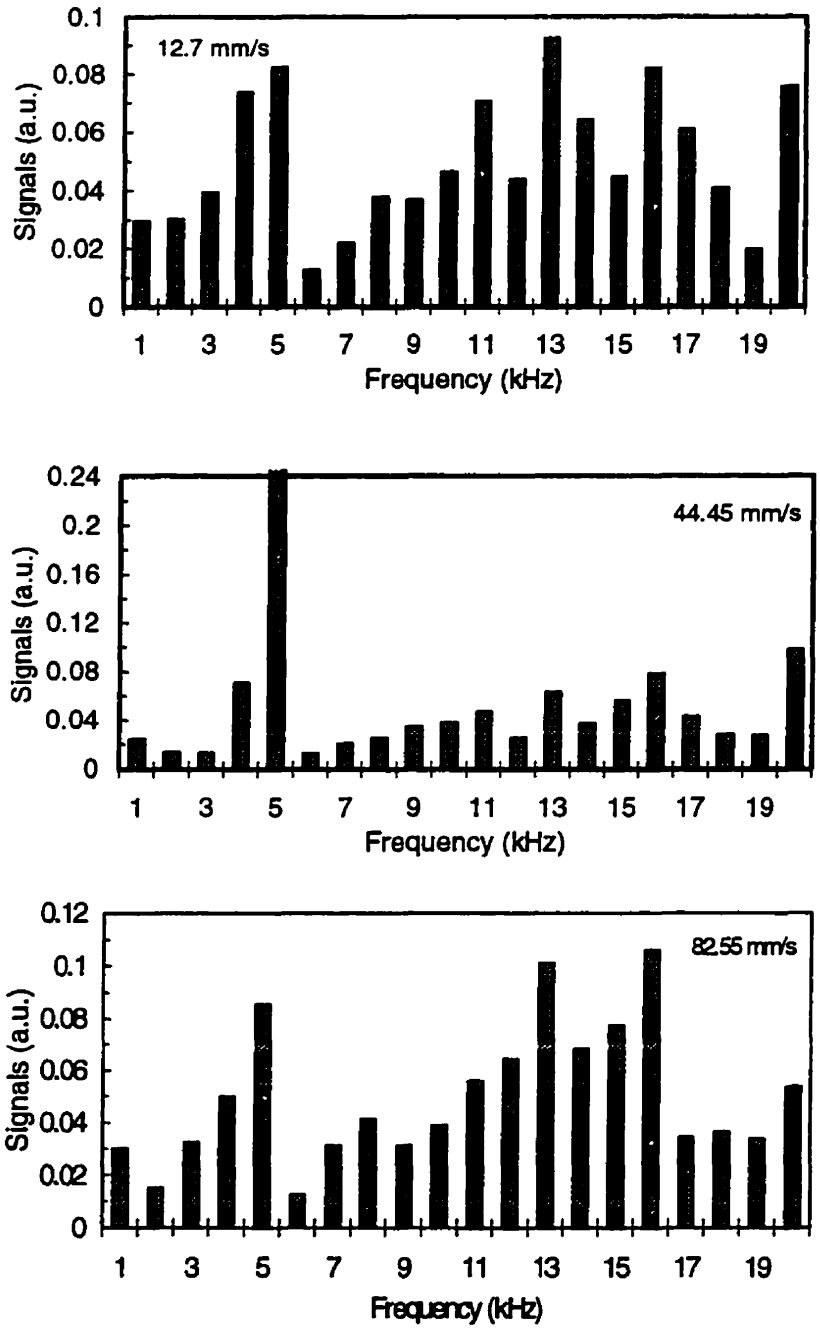
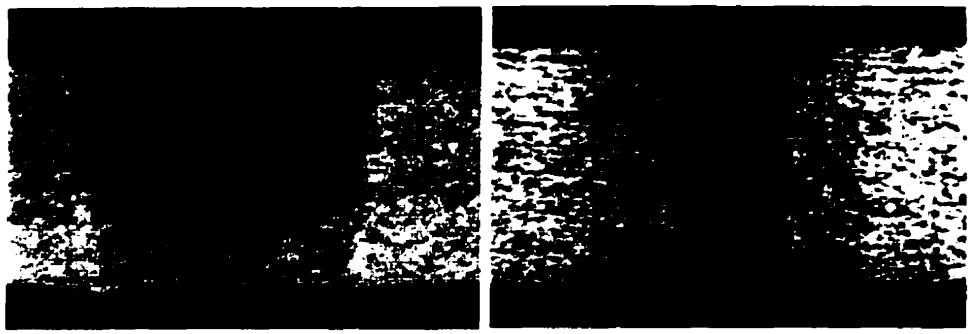
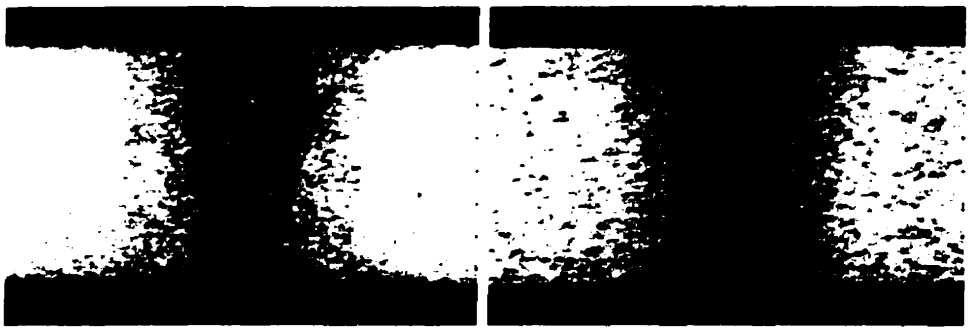


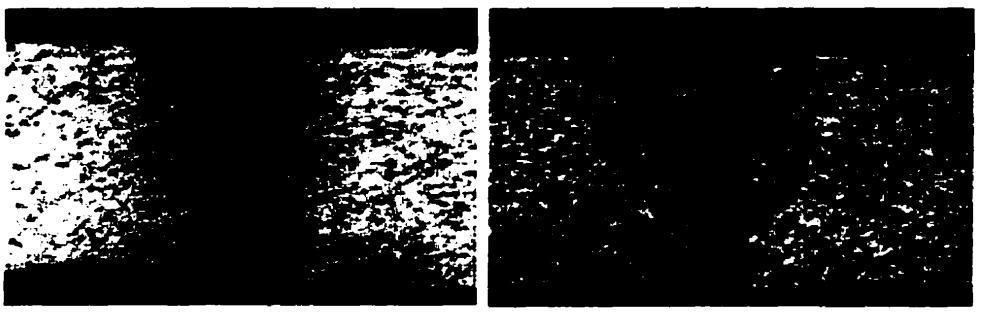
Figure.3.2 Normalized power spectrum of acoustic emission during CO_2 laser bead-on-plate welding of mild steel at three welding speeds.



(a) 12.7 mm/s (b) 25.4 mm/s

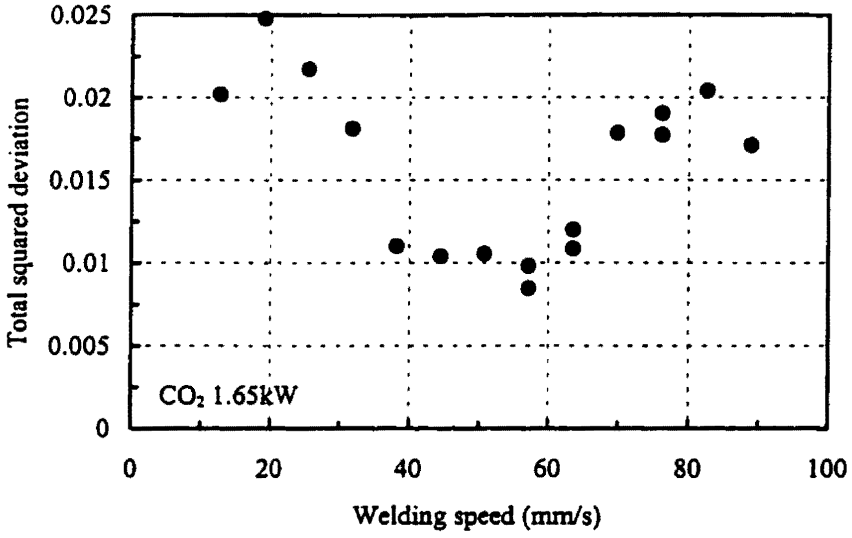


(c) 38.1 mm/s (d) 50.8 mm/s

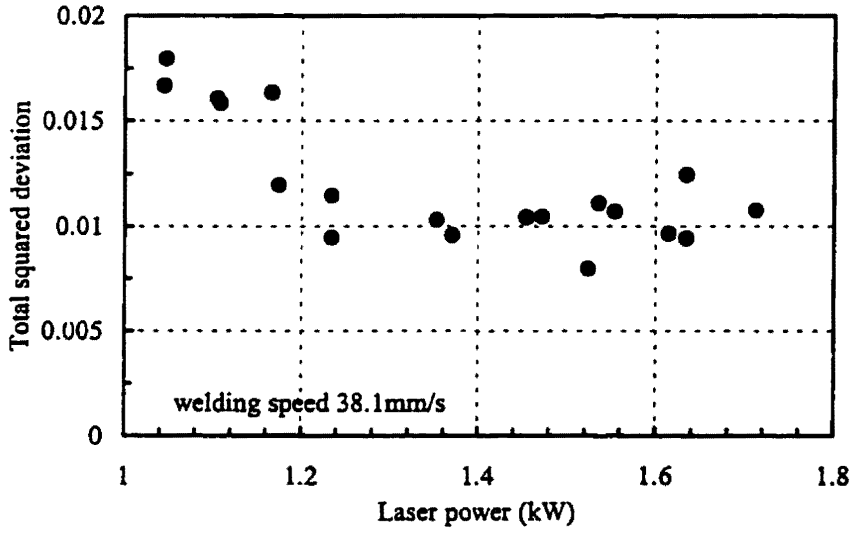


(e) 76.2 mm/s (f) 88.9 mm/s

Figure 3.3 Photographs of cross-sections of welds from laser welding at various welding speeds.



(a)



(b)

Figure 3.4 Total squared deviation of the AE signal. Good welds were obtained (a) near the minimum when changing speed, (b) when laser power is above a certain value.

3.2 A simple approach to interpret acoustic signals

To quantify the dependence of weld characteristics on AE spectra, one can identify AE FFT component intensities I_k^0 obtained under optimized welding condition at frequency k and compare them to measured values I_k. A quantitative comparison between these two spectra is given by the total squared standard deviation

$$D = \sum_{k=1}^{N} (I_k - I_k^0)^2 \tag{3.2a}$$

where N is the total number of components used for calculation (since the maximum number of components is 20, so that $N \leq 20$). Thus a small value of D is obtained under conditions for which the AE spectrum is closest to the preferred distribution.

Values of D obtained for bead-on-plate welds in mild steel sheet are plotted as a function of weld speed as well as laser power in Fig.3.4. As expected, low values of D are obtained for a relatively narrow range of welding conditions under which the weld is characterized by full penetration and small heat-affected zone (HAZ). With regard to laser power, only small deviation is observed at laser powers above the value at which

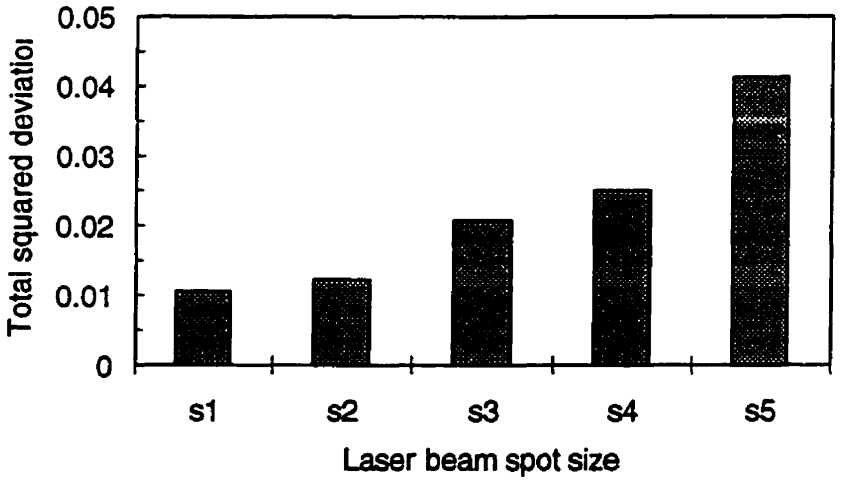


Figure 3.5 Effect of focus on total squared deviation of AE signals during laser welding under different focal conditions.

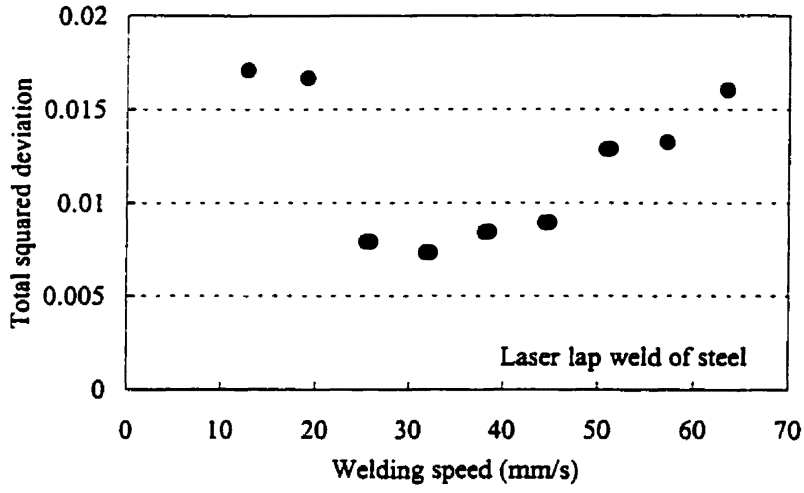


Figure 3.6 Total squared deviation of the AE during laser welding of 1-mm thick galvanized steel sheet with laser power 1.6 kW.

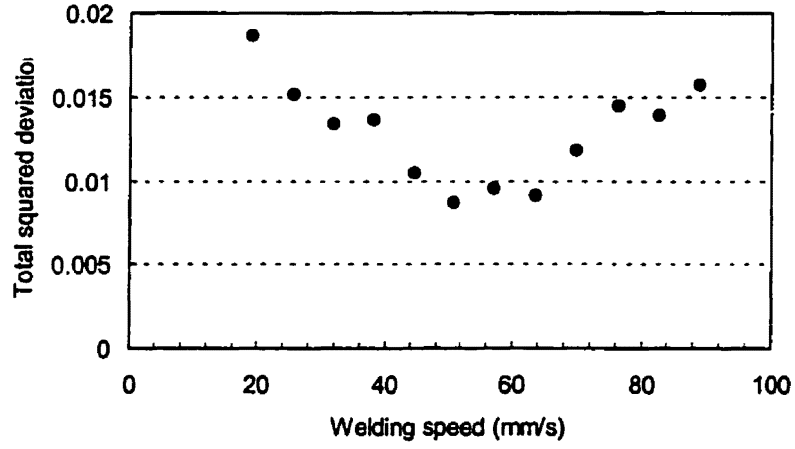


Figure 3.7 Total squared deviation of the AE during laser lap welding of mild steel sheets of 1.1-mm thickness at a laser power of 1.7 kW.

full penetration welding occurs.

This effect is also seen when the position of the laser beam focus is changed relative to the steel surface. As shown in Fig.3.5, full penetration welds with a high aspect ratio and small HAZ were obtained at S_1 and S_2, whereas only partial penetration was observed at S_3 and S_4 with changed focal positions. S_4 was an extreme example of a poorly penetrated weld.

The frequency distribution of AE intensity during bead-on-plate welding of galvanized steel differs from that obtained when welding mild steel under the same conditions. The difference is characterized by an enhancement of high-frequency acoustic components, and probably arises from the vaporization of the Zn coating. Selective emission at high frequencies attributable to vaporization of a surface layer has previously been observed[28]. To increase sensitivity, values of I_k and I_k^0 in the range 11-20 kHz were weighted differently from those at lower frequencies. A modified expression is

$$D = \sum_{k=1}^{N} \alpha_k (I_k - I_k^0)^2 \qquad (3.2b)$$

in which α_k is a weight factor. In this way, the resulting values of D are plotted as a function of weld speed and laser intensity in Fig.3.6. A reduction in D is again observed under optimized welding conditions.

Welding of 1-mm mild steel under lap joint conditions shows a similar behavior to that for bead-on-plate welding, but the speed at which D is minimized is shifted to lower values, as shown in Fig.3.7. The distribution of I_k and I_k^0 is also different from that obtained under bead-on-plate conditions.

For butt welding of steel sheets, a strong correlation between D and gap width is found, which is shown in Fig.3.8. When optimized welding conditions are used to define a spectrum I_k^0, small changes in gap separation are accompanied by a dramatic change in I_k and a large variation in D. Photographs of cross sections through the welded seam (Fig.3.8) confirm this dependence. This suggests that variability in joint fit up may be detectable from selected components in the acoustic spectrum.

AE spectra contain components in the 20 Hz to 20 kHz range that appear to be diagnostic of various aspects of the laser welding process as whole. It is not possible at

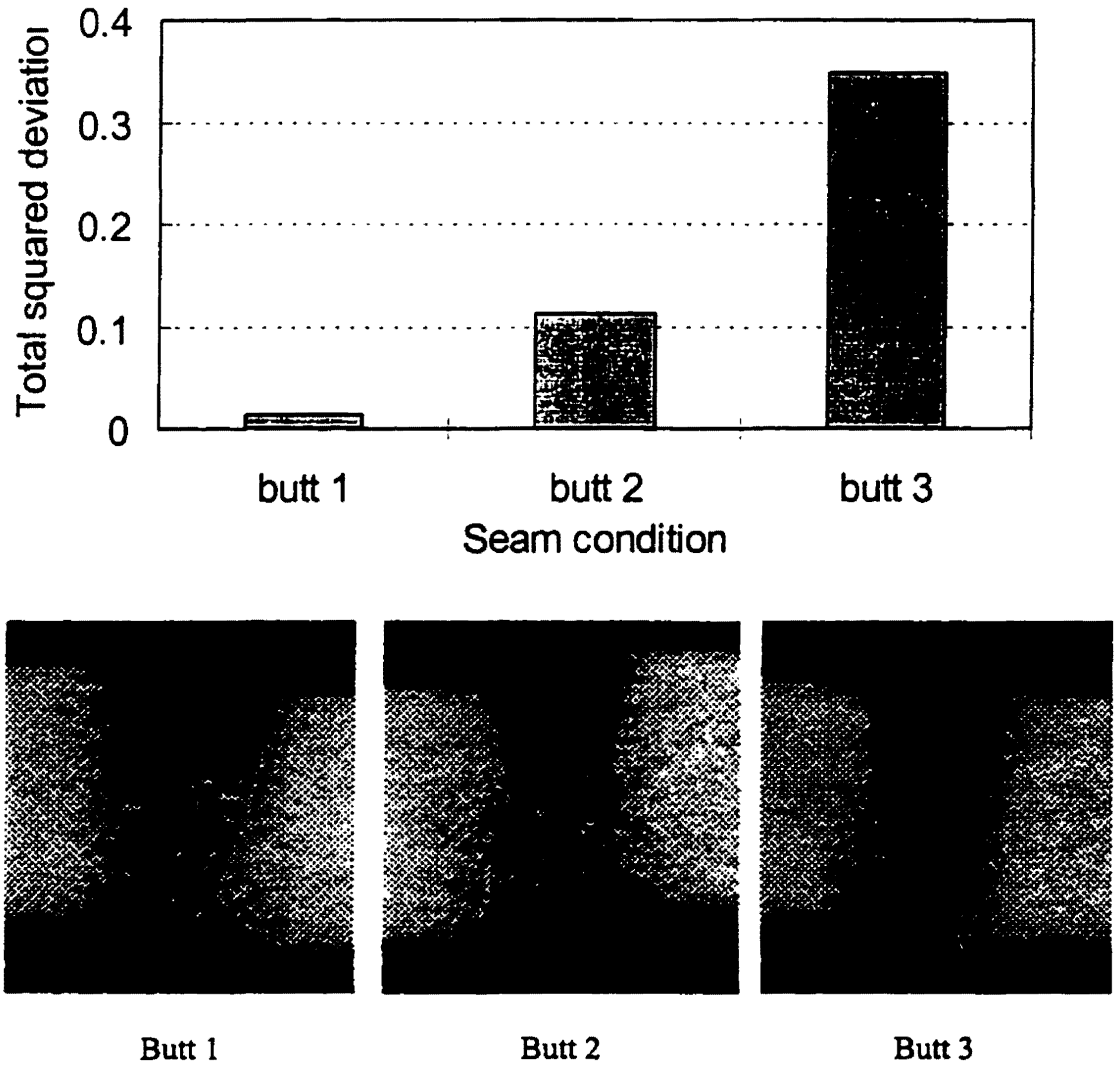


Figure 3.8 Total squared deviation of AE signals from butt weld and the corresponding sections of the weld. Butt 1 is good weld, while a wide gap (butt 2 and 3) yields a high AE deviation and poor weld quality.

present to assign specific frequency components to particular aspects of the physical interactions involved in converting incident laser radiation to heat and a well-formed weld, but the spectrum contains sufficient diagnostic information to distinguish acceptable welds from those with various defects. This effect is manifested in a simple way through the squared standard deviation D. Values of D are observed to change in response to laser welding conditions in a way which is simply related to incident laser intensity, focal position and joint fit up. This offers the possibility that AE treated in this way may be useful for weld monitoring or for inclusion in a control loop.

3.3 Weld classification using statistical pattern recognition

Pattern recognition is a signal analysis technique that can be applied to acoustic and optical signals to extract information about weld characteristics.

3.3.1 Basic theory of pattern recognition analysis

Implementing a pattern recognition system requires three essential steps:

(1) Sampling the input signals to produce the pattern space.

(2) Extraction or selection of the features, which sometimes involves transformation of the signals from the pattern space to the feature space, from which one can obtain useful information and then make subsequent reduction of data size.

(3) Classification of the feature space to identify the individual signal classes.

The Bayesian decision rule forms the basis for the design of optimum classifiers. However, it requires the full knowledge of the underlying probability distribution of the data and leads in general to a non-linear model. This classifier requires a lot of calculation time and is not practical for real-time classification. It is reasonable to examine the applicability of a linear discriminant function, simplifying the process of

classification. Unfortunately, most real-world data are not normally distributed, and for these cases, sub-optimal linear classifiers can be designed using the Minimum Squared Error approach. In reality, if the data are close to the normal distribution, we still can approximate the classifier by a linear discriminant function, however, the approximation may result in the classification accuracy of less than 100%.

The digitized and integrated signal spectrum can be rewritten as a vector in a *N*-dimension space:

$$\mathbf{X} = [x_1, x_2, \ldots x_k]^T \tag{3.3}$$

in which X_1, X_2, ... X_N are frequency components of the emission signals. The superscript *T* signifies the transverse of the data vector. At a sampling rate of 40 kHz, we have a total of *N=20* components (which are called features). The number of features used for classification is important since in addition to reducing computation efficiency a high dimensionality requires a large number of experimental data sets for training the classifier. If a set of signals is representative of separate different welds, they must have particular features which contain key information about class membership. Two feature selection schemes could be considered: (a) inter-class distance measure and (b) information measure.

Inter-class distance measure actually measures the separation of two data sets in the feature space. Large inter-class distribution should contribute to better classification. For each feature, the inter-class distance is defined as

$$d_{i,AB} = \frac{m_{iA} - m_{iB}}{\sigma_{iA} + \sigma_{iB}} \tag{3.4}$$

where m_{iA}, m_{iB} are the means for the *ith* feature of the two classes *A* and *B*, σ_{iA} and σ_{iB} are the corresponding standard deviations of each class. For laser welds, they contain 3 classes (full penetration, poor penetration and overheated), there should be three pairwise inter-class distances. The squared sum of all the pairwise distances for every feature is used as the selection criterion.

Quantitative measures of information have been developed in communication theory and can be applied here to the analysis of acoustic signals. Information measure[54] calculates the mutual information between features x_i and class c_i, and is a

measure of how well feature x_i resolves the uncertainty about class c_j. The mutual information is defined as

$$I(c_i, x_i) = \log \frac{P(c_i|x_i)}{P(c_i)} \tag{3.5}$$

where $P(c_i)$ is the *priori* probability of class c_i and $P(c_i/x_i)$ is a conditional probability of c_i for a given feature x_i. To evaluate the information contained in a feature, an average of the mutual information over the set of classes can be used. In practice, feature x_i takes continuous values from zero to a certain number. For the convenience of calculation, the feature x_i can be partitioned into a manageable number of intervals and the following expression can be used

$$I(c, x_i) = \sum_k P_k \sum_{c_j} P(k|c_j) \log P(k|c_j) - \sum_{c_j} P(c_j) \log P(c_j) \tag{3.6}$$

in which x_i is the *ith* feature of class (c_j). $P(k/c_j)$ is the conditional probability that a sample from class c_j will have the value of x_i fall within the *kth* interval of its partition. P_k is the probability that x_i falls in the *kth* interval regardless of class. With this definition, the larger the average mutual information, the more distinctive is the set of signals to identify classes.

Two algorithms can be employed to build a linear disciminant for classification of laser beam welds.

(1) Minimum squared error (MSE) algorithm[55]

In a k-dimension space (Eq. 3.3), a point represents the data of an acoustic spectrum of weld that is detected at a particular time. A collection of signals, which are acquired from the different welds or from the same weld but at different times, forms a point distribution in the k-D space. If the signal is able to distinguish varieties of welds, the points should be located in different region in this space. In this case, a hyper-plane can be found to separate the regions between two clusters of weld points. This hyper-plane is called a linear discriminant function. Mathematically, the linear discriminant function can be written

$$g(\mathbf{x}) = \mathbf{w}^T \mathbf{x} + w_0 \tag{3.7}$$

where $\mathbf{x}$ is the signal vector.

By the MSE algorithm, the vector w^T and the constant w_0 can be determined using a set of training data. If we use $\mathbf{a}=[\mathbf{w}^T, w_0]^T$, and $\mathbf{y}=[\mathbf{x}^T, 1]^T$, the linear discriminant function can be expressed as

$$g(\mathbf{y}_i)=\mathbf{a}^T\mathbf{y}_i \tag{3.8}$$

The MSE algorithm is to find a vector $\mathbf{a}$ to minimize the squared error

$$E(\mathbf{a})=\sum_{i=1}^{N}(\mathbf{a}^T\mathbf{y}_i-b_i)^2 \tag{3.9}$$

Minimization of $E(\mathbf{a})$ yields the results:

$$\mathbf{a}=\mathbf{R}^{-1}\frac{1}{N}\sum_{i=1}^{N}b_i\mathbf{y}_i \tag{3.10}$$

where $\mathbf{R}=\frac{1}{N}\sum_{i=1}^{N}\mathbf{y}_i\mathbf{y}_i^T$.

For classification of three classes, linear discriminants of three pairwise functions can be found. The decision rule is

$$\mathbf{x}\in c_i \quad \text{if } g(\mathbf{x})>0$$
$$\mathbf{x}\in c_j \quad \text{otherwise} \tag{3.11}$$

For each signal data, it goes three times through the above procedures.

In constructing the classifier, no assumption was made, so this method applies for all data distributions.

(2) Fisher's linear discriminant[56]

In high dimensional space, one cannot visually inspect the data distribution. When a Fisher's linear discriminant is constructed, the data vector x can be projected on lines specified by vector w along which the distances between classes are maximized. For a K-class problem, K-1 vectors can be found. The inter-class distance measure is defined as the sample between-class matrix B divided by the sample within-class matrix S_w. Therefore, the problem is to find the vectors w to maximize

$$J(\mathbf{w})=\frac{\mathbf{w}^T\mathbf{B}\mathbf{w}}{\mathbf{w}^T\mathbf{S}_w\mathbf{w}} \tag{3.12}$$

where $\mathbf{B}=\sum_{c_i}(\mathbf{x}_i-\bar{\mathbf{x}})(\mathbf{x}_i-\bar{\mathbf{x}})^T$ is the sample between-class matrix, and

$$\mathbf{S}_w = \sum_{c_i} N_i \mathbf{S}_i = \sum_{c_i} \sum_{k=1}^{N_i} (\mathbf{x}_{ik} - \bar{\mathbf{x}}_i)(\mathbf{x}_{ik} - \bar{\mathbf{x}}_i)^T \tag{3.13}$$

is the sample within-class matrix. It can be proved[56] that when w takes the eigenvectors of $\mathbf{S}_w^{-1}\mathbf{B}$, $J(w)$ is maximized. Thus, for this approach, we first need to find the eigenvectors e_j $(j = 1, 2, ..., K-1)$ of $\mathbf{S}_w^{-1}\mathbf{B}$, and then construct the discriminants

$$g_j = \mathbf{e}_j^T \mathbf{x}_i \tag{3.14}$$

In a classification, the decision rule is to assign the sample to the class (measured by its class mean) to which it is closest in the $K-1$ dimensional discriminant space. For laser welding, the signal data can be classified into three classes ($K=3$). Accordingly, two eigenvectors can be obtained. From these vectors, each signal spectrum can be represented as a point (g_1, g_2) in a two-dimension space. Under each class, the training data has a mean point $(\bar{g}_{1j}, \bar{g}_{2j})$ where $j=1$, 2, and 3 denoting 3 classes. These three mean points define the centers of each class. Weld classification is based on the appropriate measure of the squared distance from (g_1, g_2) to $(\bar{g}_{1j}, \bar{g}_{2j})$, that is, a signal is assigned to the class which has a minimum distance.

In this study, both classifiers have been used. They give approximately the same result. In the following section, we don't specify which algorithm is used to yield the results.

3.3.2 Feature selections of acoustic signals

Table 3.1 and 3.2 list the calculated results for AE signals at two locations based on inter-class distance and information measures. According to the feature selection criterion, each feature makes a different contribution to weld classification. Those features with low values from both measures should not be included in classifying calculation. The results indicate that the four highest frequency components, which are highlighted in the table, contribute little to the classification. In the analysis below, 16 features are selected with frequency bands from 1 to 16 kHz. For the optical signal, there

Table 3.1. Feature selection by inter-class distance measures and information measures. Highlighted data have little contribution to classification.

Features	Inter-class distances	Information measures
1	1.3933	0.3354
2	0.8488	0.4214
3	0.2656	0.4362
4	0.1591	0.6050
5	0.7317	0.2984
6	0.3990	0.2278
7	0.5154	0.3353
8	0.5798	0.4581
9	0.1314	0.2912
10	0.2855	0.1661
11	0.1104	0.1476
12	0.3518	0.2679
13	0.0437	0.3867
14	0.0484	0.4610
15	0.1850	0.4125
16	0.5026	0.2954
17	0.2206	0.1899
18	0.1928	0.1435
19	0.0697	0.1010
20	0.0544	0.1058

Note: Acoustic signals was detected from above-the-workpiece surface.

Table 3.2. Feature selection by inter-class distance measures and information measures.

Features	Inter-class distances	Information measures
1	1.2639	0.3951
2	1.0079	0.3899
3	1.1799	0.1595
4	0.8779	0.2803
5	0.0147	0.3225
6	0.1834	0.3375
7	0.0467	0.5270
8	0.0127	0.5056
9	0.0880	0.5746
10	0.1786	0.4951
11	0.0071	0.5129
12	0.1258	0.5052
13	0.5466	0.3844
14	0.0581	0.3348
15	0.2627	0.3736
16	0.3066	0.2282
17	0.0487	0.2259
18	0.0155	0.1692
19	0.0602	0.2149
20	0.4697	0.3153

Note: Acoustic signals was detected from under-the-workpiece surface.

is actually a very low signal intensity below 10 kHz, and only 10 features need to be considered.

Another way of reducing features of the acoustic signal is to combine two or more frequency blocks into one. The applicability of this method only can be tested after checking the classification results.

3.3.3 Performance of weld classification

When the welding speed is varied, three classes of welds are produced. At a speed lower than 30 mm/s, the welds produced are considered as overheated, that is, they are fully penetrated but have too wide a heat affected zone (defined as class 2). Those performed at speeds greater than 80 mm/s are classified as partial penetration welds (class 3). The optimal welds, full penetration weld (class 1), are produced at speeds around 50 mm/s. According to the weld classification definition, a graphic representation of the classification results from acoustic signals is plotted in Fig.3.9. In this figure, the full symbols denote the center of each population. The points for this set of experimental

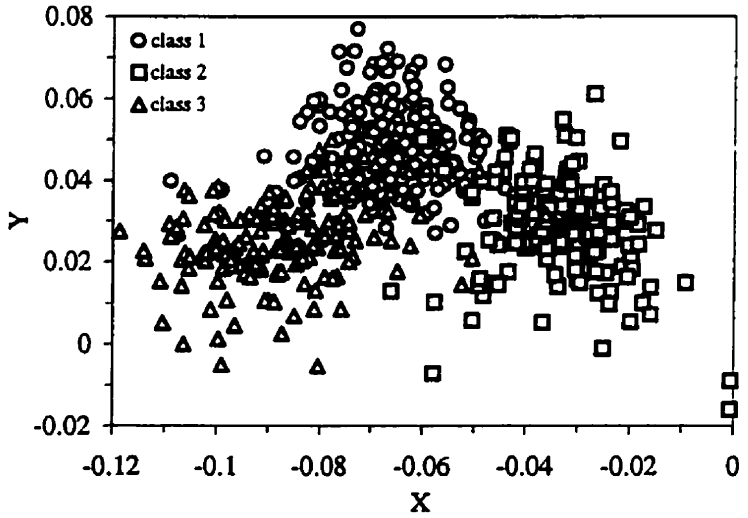


Figure 3.9. Acoustic signals in a 2-D discriminant space. The solid symbols denote the mean of each class.
class 1: full penetration; class 2: overheated; class 3: partial penetration.

Acoustic Signal					
	class 1	class 2	class 3	Total	Accuracy(%)
Overheated	78	156	6	240	65.00
Full penetration	207	25	8	240	86.25
Partial penetration	56	8	336	400	84.00
Optical Signals					
	class 1	class 2	class 3	Total	Accuracy(%)
Overheated	19	214	7	240	89.17
Full penetration	158	30	52	240	65.83
Partial penetration	130	3	267	400	66.75

Table 3.3 Performance of classification of laser welds using acoustic and optical signals. The reference classes are defined as:

Class 1 : 50 – 57.15 mm/s

Class 2 : 19.05 – 25.4 mm/s

Class 3 : 82.5 – 88.9 mm/s

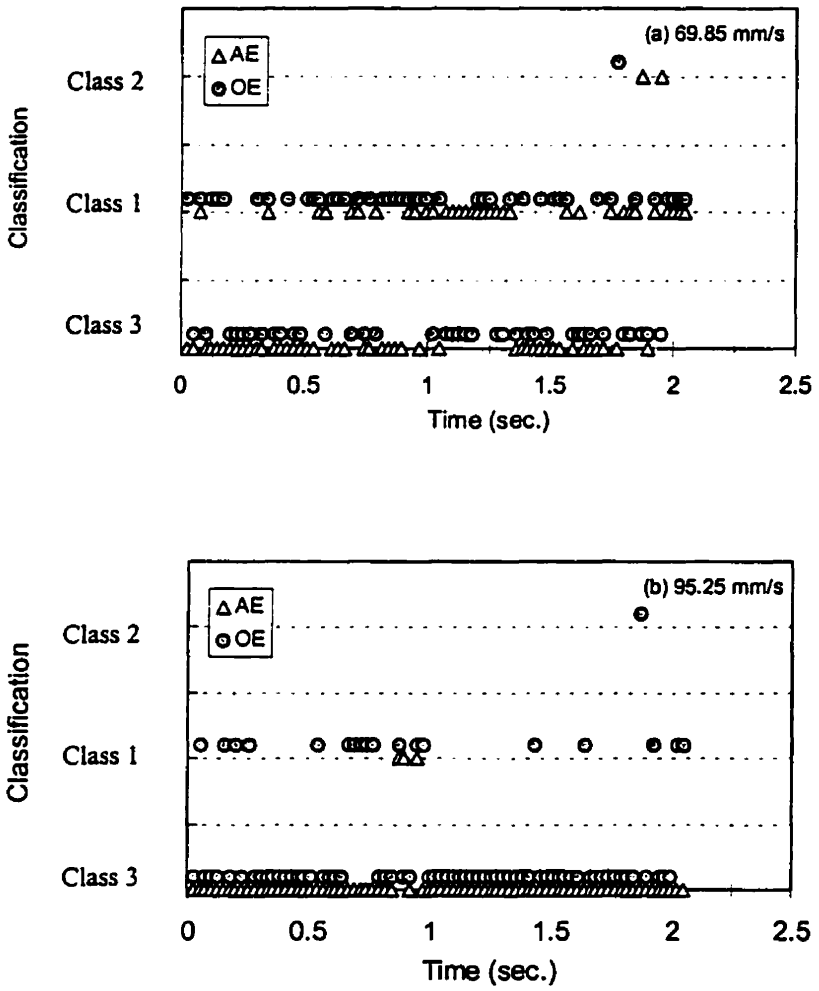


Figure 3.10 Graphic illustration of weld classification for two welding runs using acoustic and optical signal data. Laser power is about 1.6 kW.

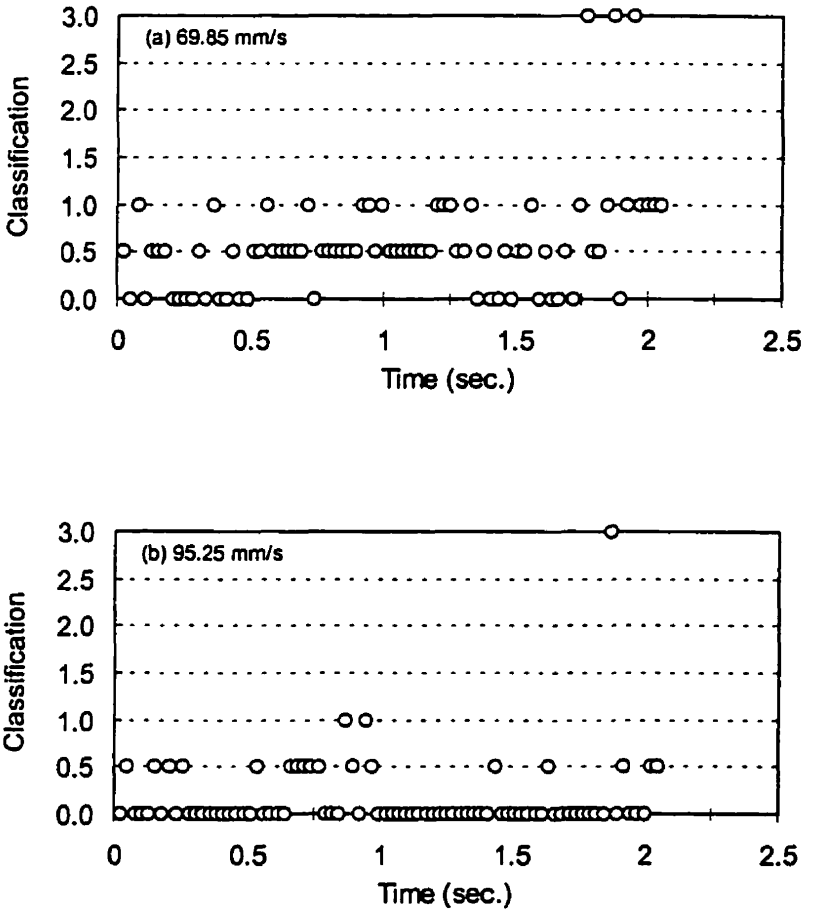


Figure 3.11 Graphic illustration of weld classification from data of combining acoustic and optical signals, which are the same set of data in Fig.3.10. The classes are denoted by numbers:

0 – class 3
1 – class 1
2 – class 2

The intermediate classes are defined:

0.5 – class between class 1 and class 3
1.5 – class between class 1 and class 2

value 3 represents a data of unclear class.

data are well grouped corresponding to each class and individual groups are reasonably separated in this discriminant space.

The classification performance of welds by a set of acoustic signals sampled at few hundred locations is listed in table 3.3. The prediction result is encouraging although the accuracy is not very high since some of the data from class 3 are mis-classified into class 2 and vice versa. The classification performance from a set of optical signals is also listed in table 3.3. The optical data were recorded simultaneously with the acoustic data. In comparison, the performance of the optical data is close to that from acoustic data.

Weld classification from emission signals can be represented graphically as class vs. time. In Fig.3.10, the results of weld classification from acoustic and optical signals are given during two welding runs, in which welds were performed at constant speeds of 69.85 mm/s and 95.25 mm/s, respectively. The condition of first weld is in between class 1 and class 3 according to the described definition, while the second belongs to class 3. In each run, the whole data are recorded and denoted by the signal data (count) in the figure. The assigned classes by weld classification are labeled on the left side. It can be noticed that for the weld, which belongs to class 3, most of the classification results fall into class 3 as expected, while for the weld between the two defined classes, the classification results are scattered between these two classes. Also, not all the data at the same count from acoustic and optical signals are assigned to the same class. This indicates that the acoustic signal and the optical signal may reflect different aspects of the weld properties.

Combination of the two signals could then give a better weld classification. The strategy is that if two signals are classified into the same class, then assignment to this class is confirmed; while if the two signals are classified into two neighboring classes (for example, class 1 and class 3), a between-class is defined. For instance, when the optical signal is classified into class 1 and the acoustic signal is identified to be class 3, we denote this weld to class A, which is the class with penetration condition between full penetration and partial penetration. Therefore the welding condition needs to have a small step adjustment toward optimal full penetration. If the acoustic signal and the optical signal are classified into two non-neighboring classes, this weld is considered to be unconfirmed (class C) and this result is discarded. In this way, class A represents a class between class 1 and class 3, and class B denotes a class between class 1 and 2. Fig.3.11

shows a classification of welds by combination of acoustic and optical signals. It can be seen that a more reliable description is made. Table 3.4 lists the result of a set of weld classification. Using this technique, the mis-classification of class 2 into class 3 or class 3 into class 2 is greatly reduced.

The effect of data sampling rate of the signals on the performance of weld classification can also be examined. When the data sampling rate is increased from 40 kHz to 50 kHz, two sets of spectra were obtained from the same welds (this can be realized by recording the emission signals in a VCR and then playing them back and processing them with a FFT). Using this set of data weld classification is calculated and listed in table 3.5. The overall performance of the acoustic signals taken at a sampling rate of 50 kHz is poorer than that at a sampling rate of 40 kHz. This result suggests that when the emission signals are taken in a shorter time interval, less information about the weld is contained in each signal.

3.3.4 Discussion

Acoustic emission signal contains frequency components over the complete audible range 20 Hz - 20 kHz, and the relative distribution of these components provides a good indicator of weld quality. The average accuracy of prediction of weld characteristics is as high as ~80%, as demonstrated above. This way of analyzing acoustic signals can lead to a way of developing a practical approach for real-time quality monitoring, although the calculation involved in the signal analysis is much more than a way of just looking at the emission intensity. However, the sampling rate cannot be increased since the signals recorded over a shorter time may not contain enough information for accurate predictions.

When this approach is applied to the optical emission signal, we have a performance of prediction of weld quality that is close to that of acoustic signals. This suggests that information on the dynamic variation of the keyhole carried by acoustic and optical signals are almost the same on average. In fact, there is a close relationship between acoustic and optical signals[57] through the driving force for acoustic emission. In detail, we found that the information reflected in these two signals are not completely

Speed(mm/s)	class 1	class 2	class 3	class1-2	class1-3	unconfirmed	Total	Error
12.70	5	38	1	33	0	3	80	1
19.05	3	43	0	29	1	4	80	1
25.40	1	61	0	15	1	2	80	1
31.75	10	36	2	30	1	1	80	3
38.10	16	22	0	37	5	0	80	
44.45	47	9	0	10	11	3	80	
50.80	41	3	0	15	21	0	80	
57.15	55	0	2	2	20	1	80	
63.50	36	0	10	1	31	2	80	1
69.85	19	0	21	0	37	3	80	0
76.20	15	0	38	0	22	5	80	0
82.55	12	0	38	0	26	4	80	0
88.90	4	0	44	0	31	1	80	0
95.25	2	0	60	0	17	1	80	0
101.60	1	0	57	0	22	0	80	0

Table 3.4 Classification of laser welds by combination of acoustic and optical signals. The definition of classes is as the same as that in table 3.3 and laser power is about 1.6 kW.

	Sampling rate 50 kHz				
	class 1	class 2	class 3	Total	Accuracy(%)
Overheated	37	152	21	210	72.4
Full penetration	164	14	32	210	78.1
Partial penetration	33	41	136	210	64.8
	Sampling rate 40 kHz				
	class 1	class 2	class 3	Total	Accuracy(%)
Overheated	19	180	11	210	85.7
Full penetration	174	10	26	210	82.9
Partial penetration	29	18	163	210	77.6

Table 3.5 Comparison of performances of weld classification by acoustic signals that are taken at two different sampling rates.

identical as the classification result sometimes differs, especially when the welding condition is in between two defined classes. One of the causes for this may be the difference in propagation time from the source to the detectors.

When these two signals are combined, weld classification performance is improved. However, this involves more calculation and will slow down the overall sampling rate.

3.4 Analysis of acoustic signals detected from different locations

3.4.1 Features of acoustic signals

Acoustic sensors can be placed at different locations around the weld spot, but the simplest solution is to mount the sensor on the laser beam weld head. Acoustic emission is generated due to rapid expansion of the metal vapor in the keyhole. The vapor atoms have a peak moment in the upward direction. This may result in different distributions of acoustic signals detected at different locations. Therefore, acoustic signals detected from various locations have been analyzed. Information contained in the acoustic signals, which can be used to identify or classify the welds, is assessed by means of information measure and the statistical pattern recognition technique applied to quantitative classification of welds.

As illustrated in Fig.3.12, three microphones of the same kind were mounted at specific locations. The distance between the weld spot and the microphones were all about 10 cm. Microphone #1 was on the laser head at an angle of −15 degrees with respect to the normal direction of the working surface. Microphone #2 was at an angle of 10 - 15 degrees with respect to the working surface, while microphone #3 was set under the work surface.

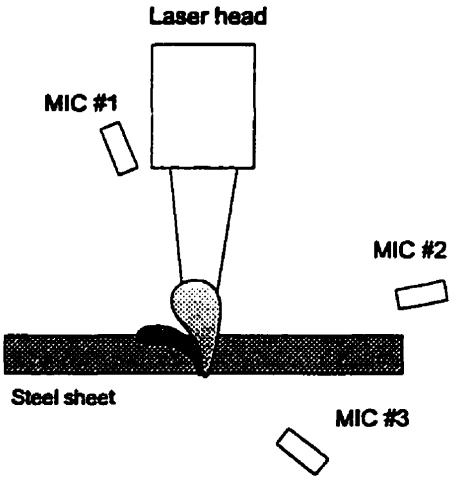
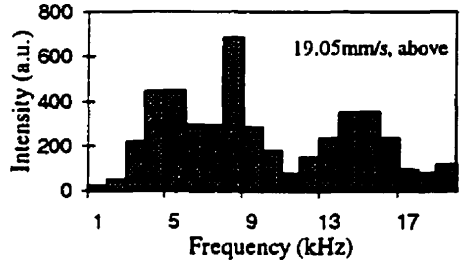


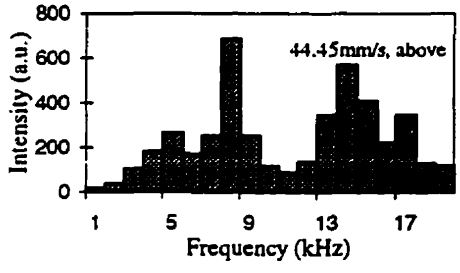
Figure 3.12 Schematic illustration of experimental setup for laser beam welding and multi-position acoustic detection.

Fig.3.13 gives a set of acoustic signals detected under various welding speeds and a constant laser power (1.6 kW) during laser beam lap welding of mild steel sheet of 1.1-mm thick. For comparison, a difference in intensity distribution among the features is apparent, and forms the base for classifying the welds by acoustic emission. The acoustic signals shown in Fig.3.13 correspond to three classes of welds defined above.

Fig.3.14 shows a set of acoustic signals detected under the working surface (location #3) during laser welding of the same steel sheet. These signals have different distribution pattern compared to those in Fig.3.13. These two sets of signals were recorded simultaneously from the same weld. Using Eq.3.5 the average mutual information for these two sets of signals are calculated and listed in Table 3.6. It can be seen that the frequency components above 16 kHz have relatively low information measures, which indicates that these components contribute little to the identification of different welds, i.e. the inclusion of these components in the input signals would not improve the distinctiveness of signals. Also from this table we know that the information measure of the acoustic signals as a total detected under the working surface is larger than the one above the working surface. From this result, therefore, we can expect that the classification of welds by the acoustic signals detected under the working surface will have a better performance than for the signals above the working surface.

Fig.3.15 and Fig.3.16 show two sets of acoustic signals detected at location #1 and #2, respectively, during laser beam lap welding of steel sheets when the focal position is changed. At the start position, the focal position was adjusted slightly below the surface (which is the optimal focal position). When the focal position moves down or up, the weld pool gets shallower. Photographs of the corresponding weld cross sections are shown in Fig.3.17. Acoustic signals in Fig.3.15 and Fig.3.16 are different in emission intensity as well as in energy distribution of frequency components. Information measures calculated using Eq.3.6 are listed in Table 3.7. The calculated results show that the total information measure of the acoustic signals at location #2 is higher than that at location #1. Furthermore, the total information measure in this case is higher than in the case of changing welding speed. This result suggests that acoustic signals during laser welding are more efficient in recognizing a change in focal position than in the penetration condition of the welds.





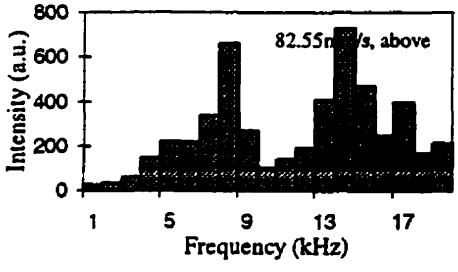
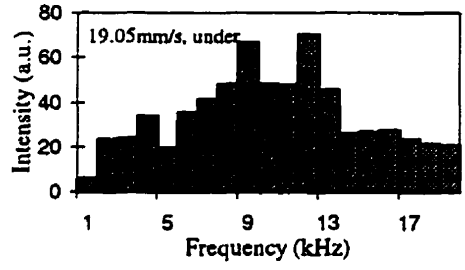
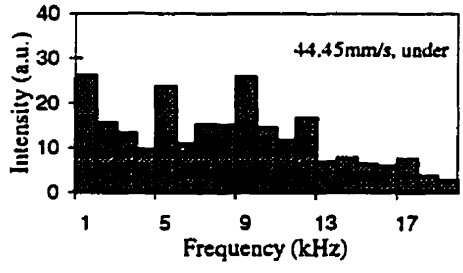


Figure 3.13 Acoustic spectra from laser lap welding of mild steel sheet at three welding speeds. The signals were recorded above the work-piece surface with the detector at location #1.





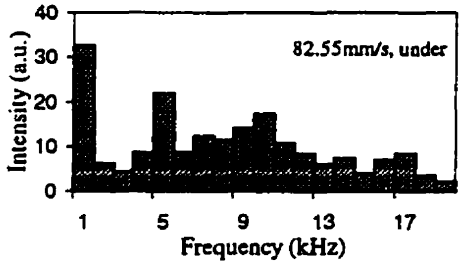


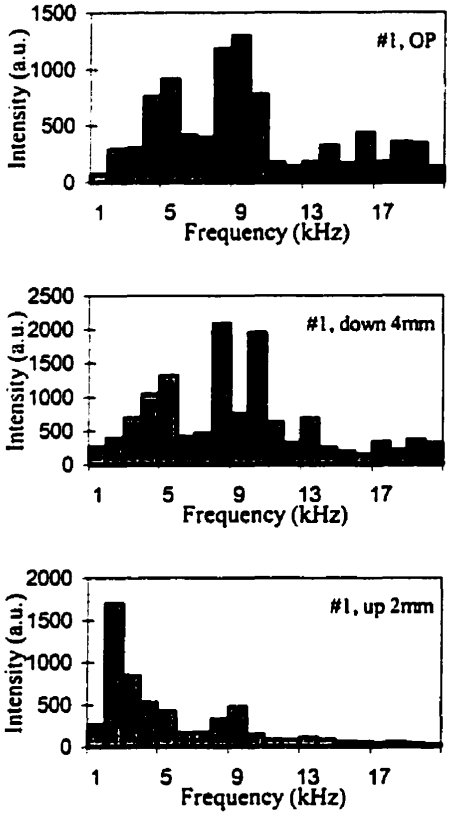
Figure 3.14 Acoustic spectra from laser lap welding of mild steel sheet at three welding speeds. The signals were recorded under the work-piece surface with the detector at location #3.

	Information measures	
Features	above	under
1	0.702	0.651
2	0.178	0.307
3	0.419	0.396
4	0.507	0.434
5	0.335	0.523
6	0.221	0.373
7	0.291	0.382
8	0.538	0.422
9	0.487	0.534
10	0.169	0.475
11	0.168	0.385
12	0.212	0.421
13	0.331	0.382
14	0.454	0.262
15	0.477	0.451
16	0.383	0.237
17	0.324	0.254
18	0.164	0.207
19	0.114	0.309
20	0.196	0.506
Total	6.671	7.909

Table 3.6 Information measures of acoustic signals from lap weld with changing welding speed.

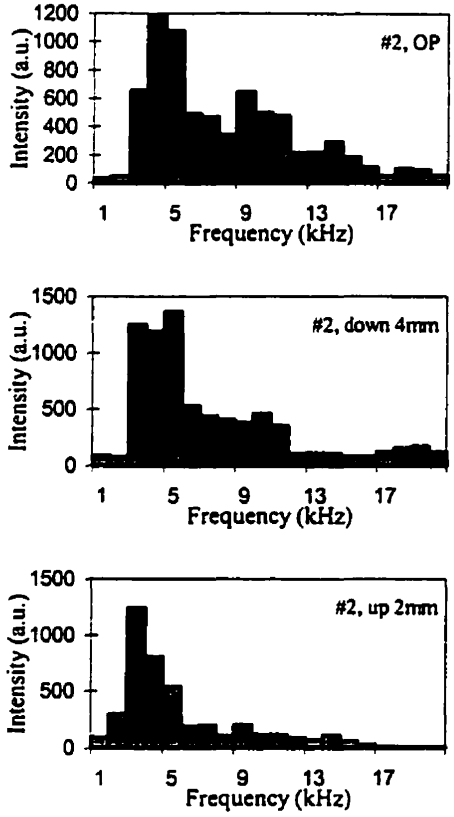
	Information measure	
Features	#1	#2
1	0.296	0.184
2	0.621	0.420
3	0.604	0.663
4	0.502	0.518
5	0.468	0.511
6	0.241	0.406
7	0.368	0.337
8	0.608	0.339
9	0.455	0.264
10	0.668	0.460
11	0.460	0.490
12	0.297	0.340
13	0.405	0.309
14	0.214	0.332
15	0.258	0.220
16	0.378	0.445
17	0.270	0.787
18	0.259	0.619
19	0.311	0.575
20	0.444	0.473
Total	8.126	8.689

Table 3.7 Information measures of acoustic signals from lap weld with changing laser beam focal position. Welds were carried out at a power of 1.6kW and a speed of 38.1 mm/s.



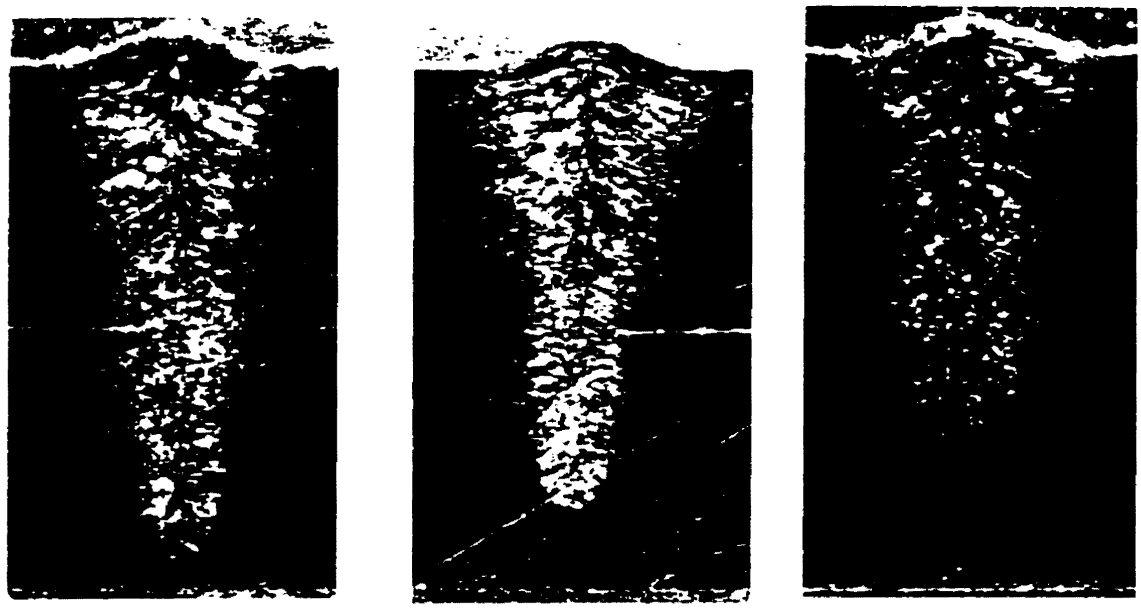
(a)

Figure 3.15 Acoustic spectra of laser welding of mild steel sheet at fixed speed (50.8 mm/s) and laser power (1.6 kW) and with changing focal position. The detector was at location #1.



(b)

Figure 3.16 Acoustic spectra of laser welding of mild steel sheet at the same process condition as that in Fig.3.15, but the detector was mounted at location #2.



(a) (b) (c)

Figure 3.17. Photographs of weld cross section. The welds are produced with a laser power 1.6 kW and at speed of 50.8 mm/s. The focal position are (a) optimal position, (b) move-down 4 mm, and (c) move-up 2 mm with respect to the optimal position.

3.4.2 Analysis of signals

The definition of weld classes for changing welding speed has been described in section 3.3. For the case of changing laser beam focal position at the optimal welding speed, optimal focal position is considered to be slightly below the sheet surface. Welds obtained at this condition are defined as class f1. When the focal position is moved down 4 mm, welds produced are taken as class f2. While welds performed when the focal position moves up 2 mm with respect to the start position are considered as class f3. The classification performance for welds is listed in Table 3.8 and Table 3.9. As expected, overall performance by the acoustic signals detected under the working surface is better than that by signals from above the work surface, while acoustic signals recorded at location #2 have a higher classification accuracy than those signals from location #1. All the results show that the signal set with the greater information measure has a better classification performance.

3.4.3 Discussion

Acoustic emission spectra, which have components in the 0 - 20 kHz range, do not have the same distribution pattern when they are detected at the same welding condition but at different locations around the welding spot. However diagnostic information is buried in the spectrum. Individual components, therefore, are not sufficient to be used as a monitoring signal. Only the relative differences among the frequency components are important. Furthermore, the experimental results obtained above show that the ability to distinguish optimal welds from those with various defects or under different process conditions is not the same. Location #1 is the ideal position to mount the microphone, but the performance of the signals detected at that position is poorer than that at other locations. However, as this difference is not large, one can still mount the microphone at this location without affecting the overall performance too much.

	Acoustic signal detected above working surface				
	class 1	class 2	class 3	total	Accuracy(%)
overheated	69	288	3	360	80.0
full penetration	273	126	51	450	60.7
partial penetration	64	39	257	360	71.4
	Acoustic signal detected under working surface				
	class 1	class 2	class 3	total	Accuracy(%)
overheated	22	338	0	360	93.9
full penetration	311	82	57	450	69.1
partial penetration	67	29	264	360	73.3

Table 3.8 Acoustic classification of laser welds of mild steel sheet. The welds are produced with a constant power 1.6 kW and at changing speed.

class 1: v35 - v45
class 2: v10 - v20
class 3: v57 - v65

MIC	Focal position	Class f1	Class f2	Class f3	Total	Accuracy(%)
#1	OFP	74	4	2	80	92.5
	-4mm	0	72	8	80	90.0
	+2mm	3	1	76	80	95.0
#2	OFP	80	0	0	80	100.0
	-4mm	0	79	1	80	98.8
	+2mm	2	0	78	80	97.5

Table 3.9 Acoustic classification of lap welds of mild steel sheet. Welds were produced with a laser power 1.6 kW and welding speed of 50.8 mm/s and with changing focal position. Signals were recorded at locations: "-" refers to move-down and "+" denotes move-up.

The acoustic signals shown above give additional evidence that acoustic signal emitted during laser beam welding mainly comes from the vapor or plasma plume expansion out of the keyhole. The microphone at location #1 senses the acoustic wave driven by the expanding front of the plume. Thus this acoustic signal contains many high frequency components. Conversely, the microphone at location #2 records the acoustic waves that are caused by the volume expansion of the vapor in the direction transverse to the keyhole. This volume expansion contains information about the keyhole oscillation which occurs in the low frequency range[53].

To conclude, acoustic signals sensed from various locations all contain diagnostic information related to weld quality and welding conditions, but the predictive accuracy differs with location. The acoustic signal detected under the work surface has a high probability of recognizing the weld penetration condition, whereas the acoustic signal detected almost perpendicular to the laser beam more accurately senses any changes in focal position. For practical purposes, it is most convenient to mount the microphone on the laser head and accept slightly poorer performance. These sensors can be incorporated into a system for real-time quality monitoring. However, in view of the classification results, it seems that acoustic monitoring alone has difficulty in identifying the change of keyhole penetration depth with high accuracy, but it is sensitive enough to identify welds from various focal positions.

3.5 Weld classification using a neural network

A neural network can realize mapping of data or patterns from high-dimension input space to low-dimension output space. It has the ability to learn, recall, and generalize from training patterns or data, and can be applied to weld classification.

3.5.1 Basic structure and learning rules of the neural network

Many models of neural networks have been developed[81,82]. Each has been designed for application in solving a particular problem which covers robot control, pattern recognition and process optimization. Basically, models of neural networks are

specified by three entities: models of the processing element, models of synaptic interconnections and structures, and training or learning rules. Multi-layer perceptron (or feedforward) networks are most popular, and have been successfully used in many areas such as pattern recognition and image processing. This kind of neural network is suitable for weld classification and so only this network is addressed in detail here. The structure of the feedforward neural network is presented in Fig.3.18. Generally, the processing element (PE) receives combined input to generate an output. Associated with the input of a PE is an integration function *net* that serves to combine information, activation, or evidence from an external source or other PEs into a net input to the PE. This is usually a linear function of the inputs x_j to the processing element in the form:

$$net_i = \sum_{j=1}^{m} w_{ij} x_j - \theta_i \tag{3.15}$$

where θ_i is the threshold of the *ith* processing element and w_{ij} is the weight that connects neuron j (source) to neuron i (destination). The weight represents the strength of the link. The processing element outputs an activation value as a function of its net input through an activation function or transfer function *a(net)*. The most frequently used activation function is the unipolar sigmoid function:

$$a(net_i) = \frac{1}{1+\exp(-\lambda \cdot net_i)} \tag{3.16}$$

where the constant $\lambda > 0$ determines the steepness of the continuous function *a(net)* near *net=0*. The non-linear feature of this integration function of the input allows the complex partitions of the input space and construction of arbitrary continuous regions. Thus the network has the ability to recognize complex patterns.

The neural network consists of highly interconnected processing elements such that each PE output is linked, through weights, to other PEs. Several PEs are combined with each other to make a layer of these nodes. Several layers can be further interconnected to form a multi-layer feedforward network, as shown in Fig.3.18. The front layer that receives inputs is the *input layer* and typically performs no function other than buffering of the input signals. The outputs of the network are generated from the *output layer*. Any layer between the input and output layers is a *hidden layer*, which is internal to the network and has no direct contact with the external environment. The

feedforward network characterizes its connections that originate and terminate the processing elements in specific layers. In this network, no PE output is an input to a node in the same layer or in a preceding layer.

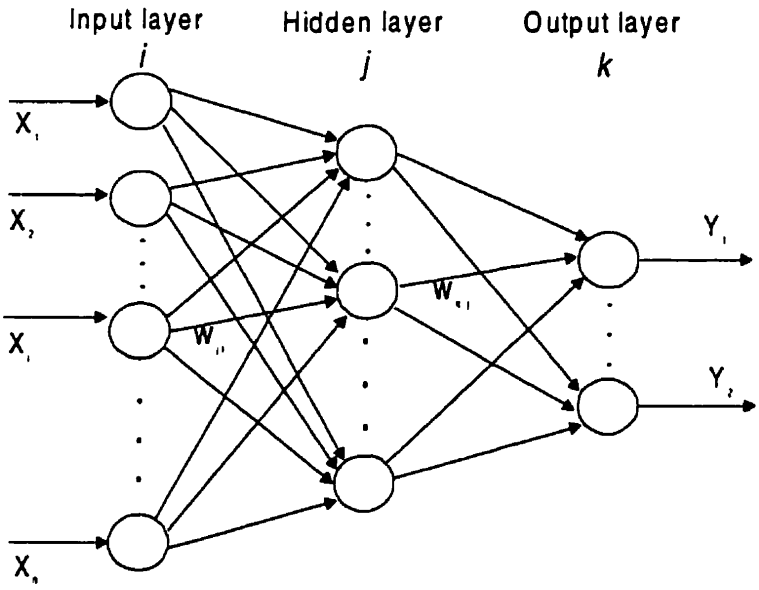


Figure 3.18 Structure of a feedforward neural network.

Learning rules are the third important element in constructing a neural network. The supervised back-propagation learning algorithm enables the network to adapt all the weights in the network efficiently. This learning algorithm is applied to multi-layer feedforward networks consisting of processing elements with continuous differentiable activation functions. The basis for this weight update algorithm is simply the idea of Hebbian learning law[83] and the gradient-descent method[84]. For a given input-output pair $(\mathbf{x}^{(p)},\mathbf{d}^{(p)})$, $p=1, 2, \ldots, N$ (data pairs), the back-propagation algorithm performs two phases of data flow. First, the input pattern $\mathbf{x}^{(p)}$ is propagated from the input layer to the output layer and, as a result of this forward flow of data, it produces an actual output $\mathbf{y}^{(p)}$. Then the error signals resulting from the difference between $\mathbf{d}^{(p)}$ and $\mathbf{y}^{(p)}$ are back-propagated from the output layer to the previous layers to update their weights.

Suppose we have m nodes in the input layer, l nodes in the hidden layer, and n nodes in the output layer. Let us consider an input-output training pair $(\mathbf{x},\mathbf{d})$, where the

superscript p is omitted for notation simplification. A node receives a net input from the previous layer nodes[80]

$$net_j = \sum_{i=1}^{m} w_{ji} x_i \tag{3.17}$$

where w_{ji} is the weight connecting *ith* node in the previous layer to the *jth* node in the particular layer. This produces an output

$$z_j = a(net_j) = [1 + \exp(-\lambda \cdot net_j)]^{-1} \tag{3.18}$$

The output from an output node is given by

$$y_k = a(net_k) = a(\sum_{j=1}^{l} w_{kj} z_j) \tag{3.19}$$

The output error vector for *pth* pair training data is

$$\mathbf{e} = \mathbf{d} - \mathbf{y} \tag{3.20}$$

The scalar measure of the output error (cost function) is[80]

$$E(\mathbf{w}) = \frac{1}{2} \sum_{k=1}^{n} (d_k - y_k)^2 \tag{3.21}$$

Thus, according to the gradient-descent method, the weights in the hidden-to-output connection are updated by

$$\Delta w_{kj} = -\eta \frac{\partial E}{\partial w_{kj}} \tag{3.22}$$

where η is the learning rate. Using the chain rule

$$\frac{\partial E}{\partial w_{kj}} = \frac{\partial E}{\partial net_k} \frac{\partial net_k}{\partial w_{kj}} \tag{3.23}$$

and

$$\frac{\partial E}{\partial net_k} = \frac{\partial E}{\partial y_k} \frac{\partial y_k}{\partial net_k}$$

and Eqs.(3.19)-(3.21), we can obtain

$$\frac{\partial E}{\partial w_{kj}} = (d_k - y_k)[a'(net_k)]a(net_k) \tag{3.24}$$

By defining an error signal

$$\delta_{ok} = -\frac{\partial E}{\partial net_k} = -(d_k - y_k)[a'(net_k)] = -(d_k - y_k) y_k (1 - y_k) \tag{3.25}$$

in which $a'(net_k) = y_k(1 - y_k)$, we have the weight update rule

$$\Delta w_{kj} = \eta \delta_{ok} a(net_k) \tag{3.26}$$

For the weight update on the input-to-hidden connections, we use the chain rule

$$\frac{\partial E}{\partial w_{ji}} = \frac{\partial E}{\partial z_j} \frac{\partial z_j}{\partial net_j} \frac{\partial net_j}{\partial w_{ji}} \tag{3.27}$$

and obtain the weight update on the link weight connecting node i in the input layer to node j in the hidden layer,

$$\Delta w_{ji} = \eta \sum_{k=1}^{n} [(d_k - y_k) a'(net_k) w_{kj}][a'(net_j) x_i] \tag{3.28}$$

Similar to Eq.(3.26), the above equation can be rewritten as

$$\Delta w_{ji} = \eta \delta_{hj} x_i \tag{3.29}$$

where δ_{hj} is the error signal of node j in the hidden layer and is defined as

$$\delta_{hj} = -\frac{\partial E}{\partial net_j} = a'(net_j) \sum_{k=1}^{n} \delta_{ok} w_{kj} \tag{3.30}$$

It can be observed that the error signal δ_{hj} of a hidden node j can be determined in terms of the error signals δ_{oi} of the nodes of the output layer, and therefore the error signals (δ_{oi}) are propagated backward instead of propagating signals forward.

The learning process of a neural network is actually a process in which the weights in the network are adjusted according to the pattern of the source data so that the input space can be mapped into the output space with a minimum squared error.

3.5.2 Performance of weld classification

A three-layer neural network with 20 input nodes, 10 hidden nodes and 3 output nodes is constructed for classifying welds into three classes. The 20 input nodes receive 20 input components of an acoustic spectrum with the last component replaced by the total intensity of the acoustic spectrum. Output node 1 is assigned to class 1 (full penetration), node 2 to class 2 (overheated), and node 3 to class 3 (partial penetration). When the output value of a node is high (above 0.6) and the other two nodes have a low

output value (below 0.4), the data is classified into the class of this node, otherwise the class of the data is not confirmed.

The same sets of training data and testing data that are used in producing the results in Table 3.3 are used here for training and testing the neural network. After training for several hours, the performance of classification for the testing data is given in Table 3.10. In comparison with the results in Table 3.3, the accuracy of classification of welds into three classes by neural network is not satisfactory; especially accuracy for the class of full penetration is very low. The performance of classification of a neural network may change when the number of nodes in the hidden layer changes. However, in our case, when larger or smaller numbers of nodes were used, the performance of the neural network had no significant change after training by the same sets of data.

Since the neural network did not generate satisfactory results for acoustic classification into three classes, the neural network was re-designed to classify welds into two classes: full penetration or partial penetration. The welds that are produced at speeds below 50.8 mm/s are defined as full penetration weld; while welds at speeds above 63.5 mm/s are defined as partial penetration. This neural network has two output nodes, each of them assigned to one of the classes. The same classifying logic is used as in the three-class case. After training, the network gives the performance of classification listed in table 3.11. It is apparent that the accuracy of classification is improved but that overall performance is still not satisfactory.

3.5.3 Discussion

A neural network has the ability to partition the feature space into regions of complex shape and can be trained to recognize patterns that are separable in its feature space. Acoustic signals generated during different welding conditions are distinguishable in principle (identified by the human ear), and mathematically separable using linear discriminating functions as discussed in section 3.3. However, the accuracy of weld classification of acoustic signals by the neural network is not satisfactory compared to the results of linear discriminating functions. There may be several reasons for this limitation. One of the reasons may be that the designed neural network here is not the

Table 3.10 Classification of welds into three classes by neural network

Output of classifier	Input samples		
	Overheated	Full penetration	Partial penetration
Overheated	240	105	29
Full penetration	54	152	34
Partial penetration	14	46	213
Not confirmed	12	17	44
Performance (%)	75	47.5	66.6

Table 3.11 Classification of welds into two classes by neural network

Output of classifier	Input samples	
	Full penetration	Partial penetration
Full penetration	536	99
Partial penetration	163	454
Not confirmed	21	7
Performance (%)	77.4	81.1

best one for acoustic signal classification and a better network could be found for weld classification. As a reference, the classification results for the training data are shown in Table 3.12. It is noticed that the performance for the training data is satisfactory with accuracy up to 96%. The training data of each class contain acoustic data from welding at

Output of classifier	Input samples	
	Full penetration	Partial penetration
Full penetration	231	13
Partial penetration	8	227
Not confirmed	1	0
Performance (%)	96.3	94.6

Table 3.12 Weld classification of the training data by a three-layer neural network.

three different speeds. If welding was carried out at two fixed welding speeds to produce full and partial penetration welds respectively, an even better performance of classification would be expected.

The second reason is related to the acoustic signals themselves. The distribution of acoustic signal data may be scattered in its feature space. There are considerable overlapped regions between data from different welding conditions. The neural network may find the boundaries for efficiently separating the training data, but these boundaries do not give a good separation for test data.

In comparison, a neural network takes several hours to be trained, while the linear discriminate function can be constructed using training data in a few seconds. For this reason, a statistical pattern recognition algorithm is more suitable for weld classification using acoustic signals.

Chapter 4
Characteristics of Optical Emission and Detection Techniques

4.1 Variation of optical emission

During keyhole welding with the CO_2 laser, the metal under the laser beam undergoes melting and vaporization that may result in plasma generation provided sufficient power is absorbed. The dynamics of keyhole formation and maintenance is very complicated, and is a process in which the vaporization of the material brings a change in momentum and a recoil force at the surface compensates this change. The recoil pressure that depresses the molten material in the melt pool and the material loss due to the vaporization together results in keyhole formation. This keyhole confines the incident beam causing increased beam absorption so that high vapor pressure is maintained inside the keyhole resulting in a sustained keyhole. By further absorption of laser radiation, hot metal vapor is partially ionized resulting in a luminescent vapor plasma. For a thin plasma (in the initial stage of plasma evolution), the laser beam can directly reach the metal surface and is partially absorbed by Fresnel absorption. When the vapor density builds up, electrons inside the plume absorb photons from the laser beam by inverse Bremsstrahlung. This process raises the electrons to higher quantum states which may be sufficient to ionize the ambient gas or material vapor further and thus increase the number of electrons by avalanche ionization. In extreme cases, rapid

ionization occurs and there is a shock wave driven into the material. As a result of this shock wave and rapid ionization, a high-pressure region is formed within the plasma that causes the plasma to expand radially to the cool surrounding atmosphere.

Due to rapid ionization and the accompanying significant rise in temperature, a high-pressure region is formed within the plasma inside the keyhole. This high pressure causes the plasma to expand into the cool surrounding atmosphere, thus producing a plume above the melt pool. This plume contains ionized atoms, electrons, neutral atoms and excited species. Further absorption of laser energy by this plume is possible. Thus its temperature remains high and it becomes luminous. The core of this plume is adjacent to the keyhole opening.

The keyhole is in a state of dynamic balance where matching forces are all related to the absorbed laser power. Since the vapor expands rapidly, beam absorption is rarely constant and the contribution of vapor plasma absorption and direct heating on the keyhole wall interchanges. This alone may cause variations in plume shape and weld properties. It has been observed[60] that there is a strong correlation between plasma fluctuation and the dynamics of the molten metal in the weld pool, but this may also arise from power fluctuations and variations in surface quality. As a result, all the parameters involved in the keyhole dynamics continuously fluctuate. Even during a smooth welding process, the molten metal surrounding the keyhole is known to oscillate around the radius where the evaporation recoil force and the surface tension are balanced. The oscillating frequency is found both theoretically and experimentally to be in the kilohertz range for laser welding of steel sheets[53, 58]. For this reason, it has been observed that vapor plasma is ejected out of keyhole on an intermittent basis[59].

In a simple physical model, the plasma plume can be described as a hot core surrounded by a luminous cloud, as shown in Fig.4.1, where the hot core is near the keyhole opening. Its interaction with the laser beam affects the melt pool. When its absorption of laser energy is increased either due to increased laser power or reduced welding speed, more heat is available to be transferred to the keyhole wall near the opening, leading to a large melt pool.

The radiation from the welding site is very strong and the spectral emission is very complicated. It contains a continuous spectrum as well as spectral lines from the

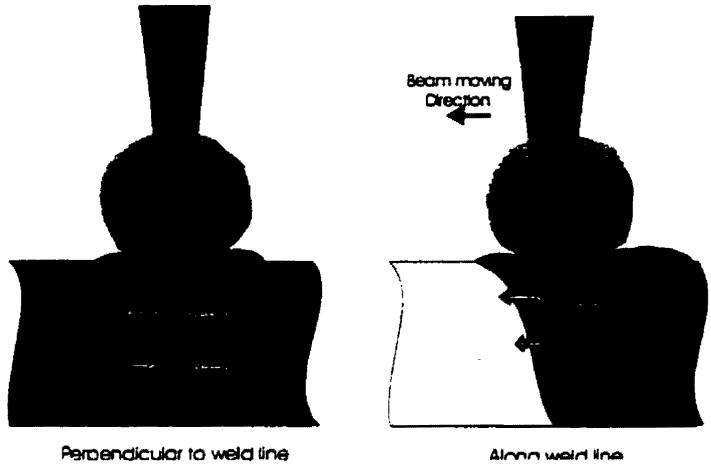


Figure 4.1 Physical model of plasma plume emission during laser beam interaction with metals.

infrared to the ultraviolet, as described in chapter 1. The main sources of radiation during laser beam welding are the metal vapor plasma, the hot melt and the hot ejecta. These sources have different characteristic lifetimes, spectral and spatial distributions. The plasma decay time ranges from hundreds of nanoseconds to microseconds[61, 62]. While for the hot ejecta its radiation decay time is determined by size and hydrodynamic motion, and typically ranges from microseconds to hundreds of microseconds. The intensity of the thermal radiation originating from the hot melt has a corresponding characteristic decay time and is basically that of a blackbody. The radiant power at any particular wavelength and temperature follows the Planck's law:

$$w_{b\lambda}d\lambda = \frac{2hc^2}{\lambda^5}(e^{hc/kT} - 1)^{-1}d\lambda \qquad (4.1)$$

where λ is the wavelength being emitted, h Planck's constant, k Stefan-Boltzmann constant, and c the speed of light. T is absolute temperature and $w_{b\lambda}d\lambda$ denotes the emission of unpolarized radiation per unit area in all directions in the wavelength range of $d\lambda$. It is obvious that at a given waveband there is an almost exponential rise in radiative energy with temperature. For this kind of radiation, the peak spectral emission occurs at (Wein's law):

$$\lambda_{max} = 2891 / T\,(^{\circ}\mathrm{K}) \qquad (4.2)$$

where λ_{max} is the wavelength in μm at the peak of the energy distribution. Radiation from the hot melt lies in the region of near infrared to infrared radiation. Since

the melt pool is only at the temperature between melting point and boiling point in steel, the optical emission contains little UV radiation. The radiation intensity and wavelength depend on the temperature of the surface of the material.

The short wavelength radiation (UV) is mainly from plasma emission and originates from the combination of a high temperature blackbody, Bremsstrahlung, and the optical breakdown or atomic and ionic transitions of the gas atoms. The plasma vapor also emits a significant amount of infrared radiation due to its high temperature. A spectrum of the radiation in the range of UV to visible from the plasma plume is shown in Fig.4.2. This spectrum was taken during laser beam welding of galvannealed steel sheet. The sensitivity of the spectrometer has been calibrated using a standard light source. But the transmission of the optical fiber has not been corrected. This spectrum contains rich UV radiation with many strong lines originating from iron atomic transitions. Several Zn lines appear in the visible range.

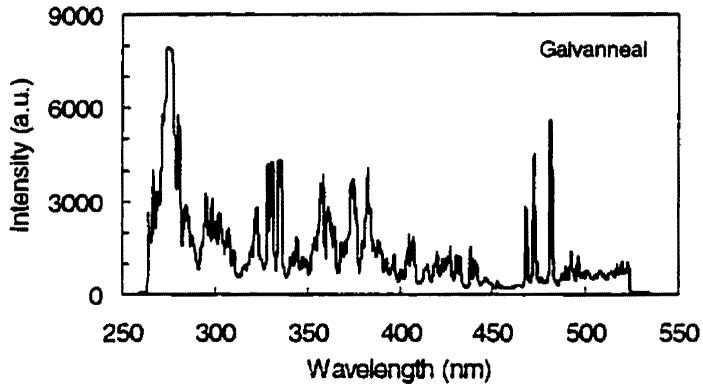


Figure 4.2 Optical emission spectrum of the plasma plume recorded during CO_2 laser beam welding of galvannealed steel sheet. The optical sensing range of the spectrometer is 259.25 – 534.69 nm.

4.2 Statistical characteristics of emission signals

As described above, keyhole dynamics induce a corresponding variation in the plasma plume, and emission signals will reflect this fluctuating behavior. A typical radiation signal during laser welding is shown in Fig.4.3 where signal data were sampled at a rate of 2 kHz. A high fluctuation in intensity during a period of time is common for

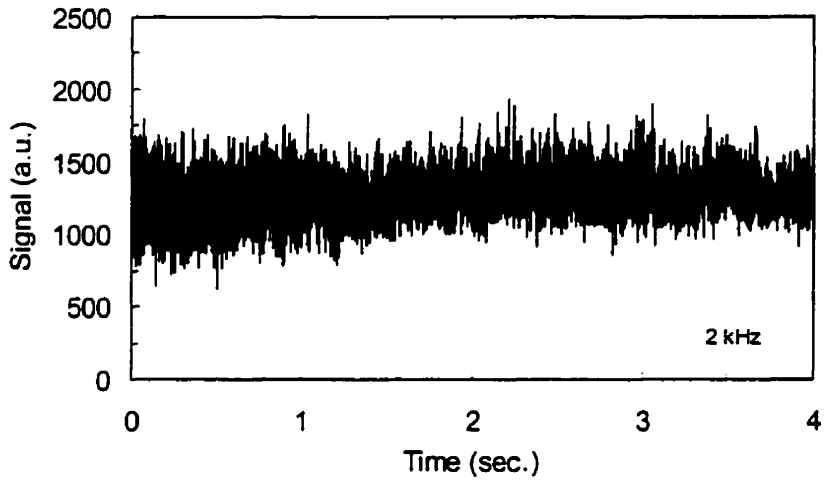


Fig.4.3 A typical optical emission signal of plasma plume recorded during laser beam welding of steel sheet.

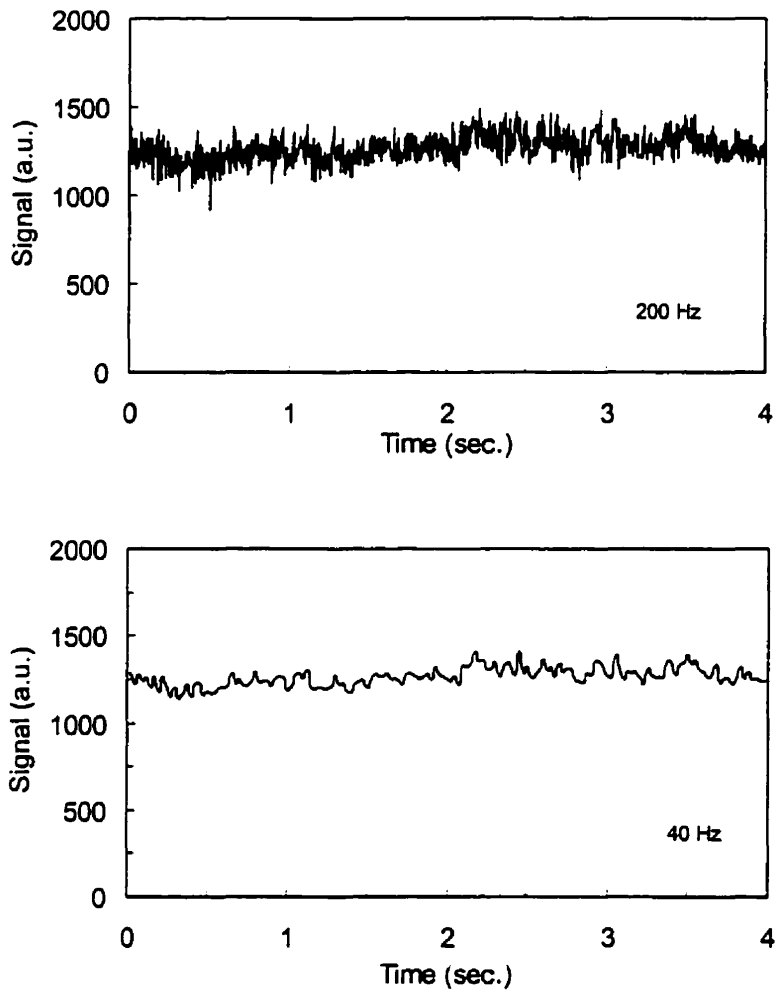


Fig.4.4 (a) Averaged emission signals of Fig.4.3. The average is calculated over 10 data points. (b) Averaged emission signal in (a). The average is calculated over 50 data points, thus the overall sampling rate is reduced to 40 Hz.

this kind of radiation signal. In order to reduce the signal fluctuation, an average over every 10 data points was calculated. This is shown in Fig.4.4(a). The average is still fluctuating significantly since the dominant fluctuation components are in the low frequency range. A further average of these data to bring the overall sampling rate down to 40 Hz still gives a fluctuating curve (Fig.4.4(b)).

In order to study the emission signal behavior, a statistical description can be utilized. The statistical mean (M) indicates the overall emission intensity level and the standard deviation (σ) describes the variation of the signal. These two parameters are defined as

$$M = \frac{1}{N}\sum_{i=1}^{N} x_i \tag{4.3}$$

and

$$\sigma^2 = \frac{1}{N}\sum_{i=1}^{N} (x_i - M)^2 \tag{4.4}$$

in which $\{x_i,\ i = 1, 2, \ldots, N\}$ is a set of signal data. In table 4.1, a set of statistical means and standard deviations of three UV, VIS and IR radiation signals are given. These signals were collected from the plasma plume during laser welding at different welding speeds with which welds from full penetration to partial penetration were produced. It can be noted that the fluctuation amplitude (standard deviation) is large relative to the mean amplitude.

Table 4.1 Statistical data of emission signals from the center of the plume.

Speed (mm/s)	Mean			Standard Deviation		
	UV	VIS	IR	UV	VIS	IR
38.1	496.44	22.89	1135.3	150.35	4.82	127.14
63.5	463.7	17.31	1001.3	185.7	4.52	153.21
19.1	428.2	21.45	1215.1	165.86	5.58	172.31

In order to analyze the characteristics of the optical emission data, a statistical distribution of the emission data can be used. The density function $p(x)$ can be estimated by means of the Parzen window estimation[63]. With this method, the density function is constructed by interpolating from N window functions centered on the N sample data. For one-dimensional space, the window function defines a region, R_N, and is constructed so that the width of the window $h_N \to 0$ as $N \to \infty$. The window function can be defined as

$$\varphi(u) = \begin{cases} 1 & |u| \le 1/2 \\ 0 & otherwise \end{cases} \tag{4.6}$$

where u is a variable. With a change of variables we obtain:

$$\varphi(\frac{x - x_i}{h_N}) = \begin{cases} 1 & if(x \in R_N) \\ 0 & else \end{cases} \tag{4.7}$$

This window centered on the *ith* sample data, x_i. Using the window as a counting function, the density estimate can be obtained by

$$p_N(x) = \frac{1}{N}\sum_{i=1}^{N}\frac{1}{h_N}\varphi(\frac{x - x_i}{h_N}) \tag{4.8}$$

By the Parzen window estimation approach, the calculated signal intensity distributions are shown in Fig.4.5. For different welds (full penetration or partial penetration), these distributions of the signals in three wavebands almost overlap each other. For a given signal intensity, it is impossible to identify the undergoing weld condition. As a result, the emission signals from center of the plume are non-separable in a sense with respect to weld penetration conditions.

The capability of emission signals to discriminate full penetration from partial penetration can be described by a separability parameter ζ, which is defined as

$$\zeta = \frac{|M_1 - M_2|}{SD_1 + SD_2} \tag{4.9}$$

where M_1 and M_2 are means of two signals; SD_1 and SD_2 are the standard deviations of these signals. A high value of ζ means that the two signals have a large difference in mean value or the total standard deviation of these signals are small. In this case, detected signals under one welding condition have little or no overlapping data with those located in the data region of another welding condition.

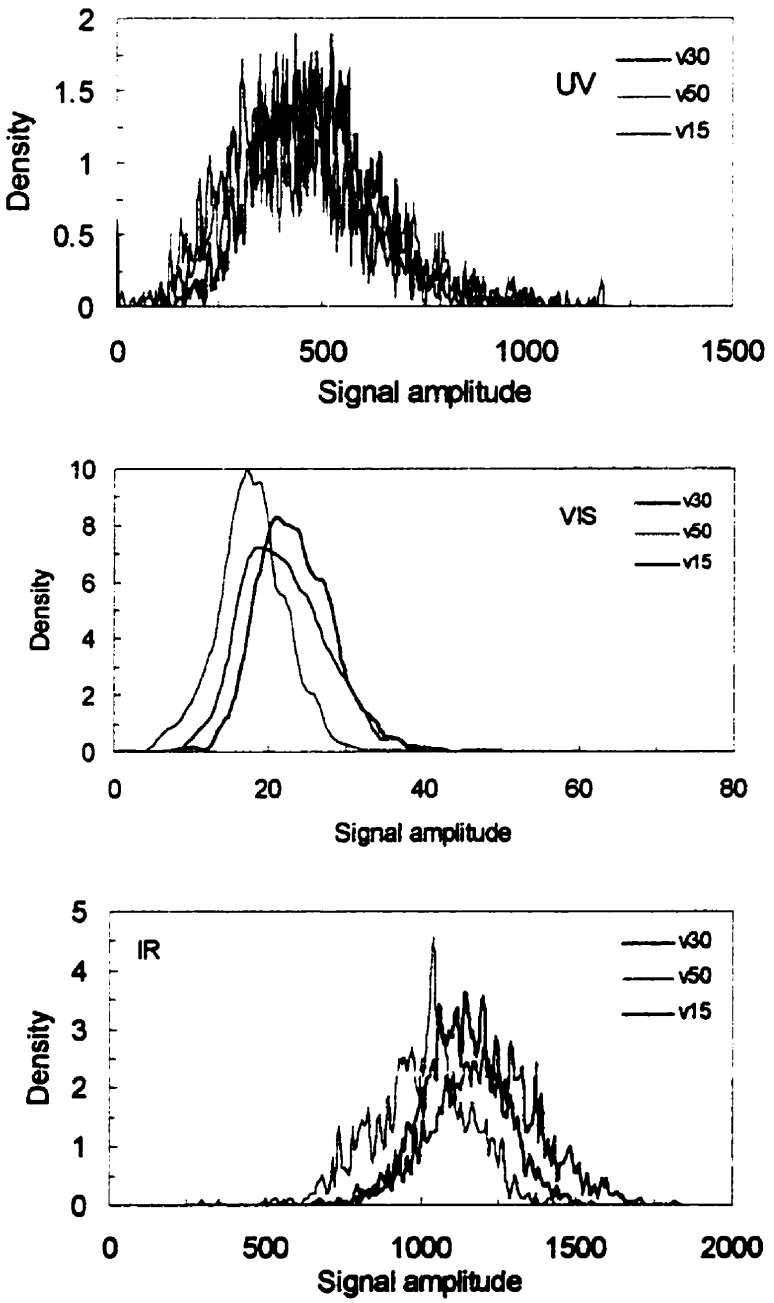


Figure 4.5 Density distributions of the emission signals from the plasma plume. The signals were recorded by photodiodes during laser beam welding of galvanneal steel sheet (1 mm thick) at laser power 1.5 kW and at three welding speeds: v15 = 19.05 mm/s, v30 = 38.1 mm/s and v50 = 63.5 mm/s.

Using the statistical data listed in Table 4.1, the separability ζ between full penetration and partial penetration can be calculated. At a welding speed of 63.5 mm/s, welds are partially penetrated, while those at 19.1 mm/s are full penetration. Separability parameters for these two welding conditions are listed in Table 4.2. For all the waveband, the parameters ζ have a small value. In referring to Fig.4.5, they are not separable.

UV	VIS	IR
0.1	0.41	0.66

Table 4.2 Separability of the emission signals from the plume.

To describe the separability quantitatively, a criterion can be introduced: where if $\zeta > 1$, then the signals are separable, while if $\zeta < 1$, then the signals are not separable. At $\zeta = 1$, the two signals are marginally separated. According to this criterion, emission signals collected from the center of the plume fail to distinguish the penetration condition.

However, radiation away from the center of the plume may exhibit different behavior. In Fig.4.6, two possible detecting spots are illustrated. These two spots are located in the weld pool or close to it: one is beside the keyhole (spot 1) and the other behind the keyhole (spot 2). Infrared radiation signals were collected and signal density distributions are given in Fig.4.7. It can be seen that when the detecting spot is viewed at

Spot 1	Spot 2
2.5	0.9

Table 4.3 Separabilities of IR signals from weld pool.

spot 1 there is a large difference in the emission signal intensities from full penetration weld and partial penetration weld. For spot 2, the emission signals have a considerable portion overlapped. Using Eq.4.9, the separability of the emission signals for these two detecting spots can be calculated. The results are listed in Table 4.3. According to the

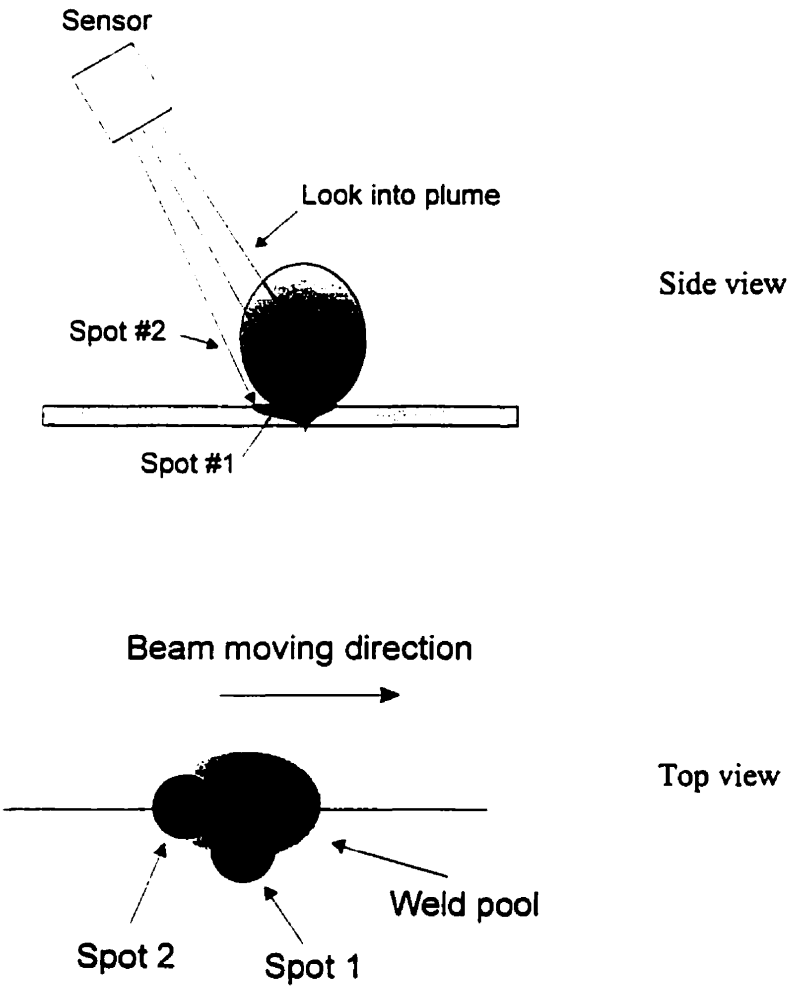


Figure 4.6 Illustration of side and top views of different detection spots.

separability criteria, the IR radiation signal from spot 1 is separable, while the signal from spot 2 is barely separable.

4.3 Running average filtering

As has been described in the previous sections, emission signals exhibit strong fluctuations. This is intrinsic to a dynamic welding process and only applying an average over a considerable number of data points can smooth these signals. However, such averaging will bring the overall-sampling rate down significantly. As shown in Fig.4.4(b), the signal is smoothed significantly when the sampling rate is reduced to 50 Hz so that this approach to signal processing is not suitable for real-time application.

In order to filter out the significant fluctuation and maintain the overall-sampling rate, a running average filtering algorithm can be applied. Suppose that at time t_k, the recorded signal is $x(k)$. During the process, we keep a series of data: $x(k), x(k-1), x(k-2), ..., x(k-n)$ in a buffer, in which $x(k-i)$ is the signal data acquired at a previous time $t_k - i \cdot \delta t$. Every time a data point is acquired, all the data in the buffer shift one sample towards the previous time and the newly acquired data point stored at the latest position. An average over this set of data is calculated and the result serves as the new data signal for process control. The reasonable size of the buffer is about 5 to 10. When applying this algorithm, the visual sampling rate or updating rate remains the same, but the signal would be greatly smoothed.

After applying the running average filtering algorithm to the signal in Fig.4.4(a), the resultant signal is plotted in Fig.4.8. Although the size of averaging data is only 5, the effect is dramatic. It can be seen that the filtered signal maintains the main feature while the noise level is much lower.

Furthermore, additional benefits can be obtained when applying the run-time filtering algorithm to emission signals. After filtering of the signals in Fig.4.7, the density distributions of the signals have been re-calculated and are presented in Fig.4.9. In comparison to the density distributions in Fig.4.7, filtered signals now have a narrow distribution. The separabilities of the treated signals are calculated to be 3.55 (spot 1) and 1.0 (spot 2) which are higher than those listed in table 4.3.

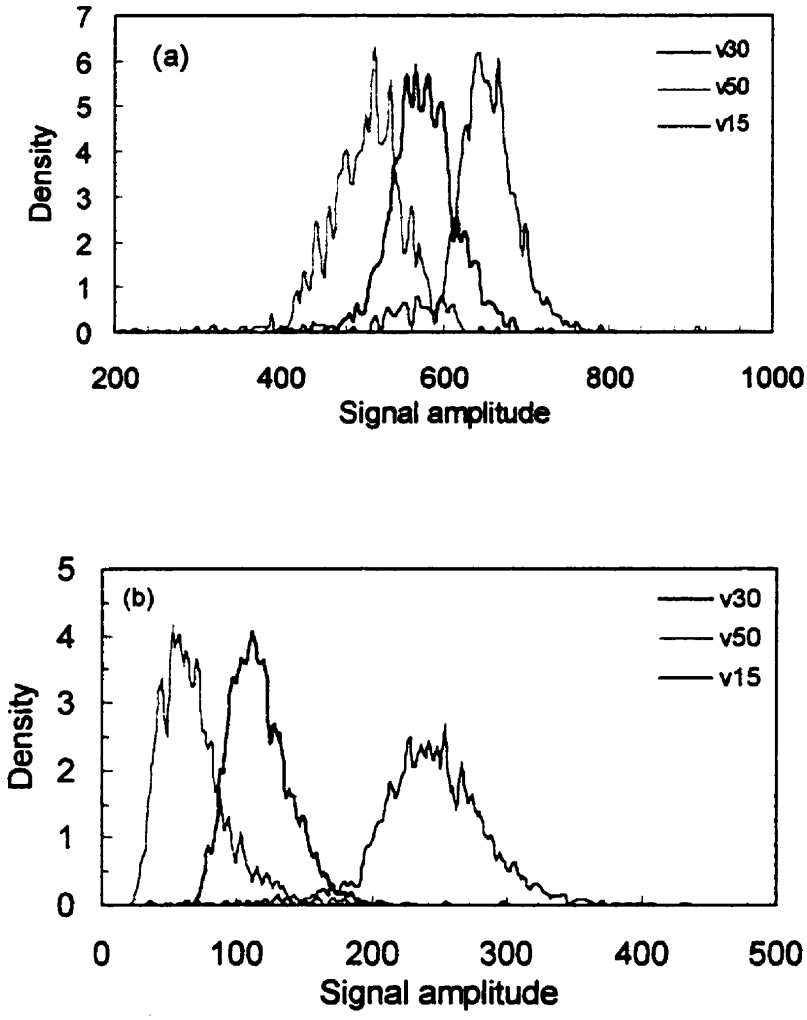


Figure 4.7 Density distributions of IR radiation signals from the melt pool at two detecting spots: (a) behind the keyhole, (b) beside the keyhole. The three distributions in each plot represent welds at different welding speeds.

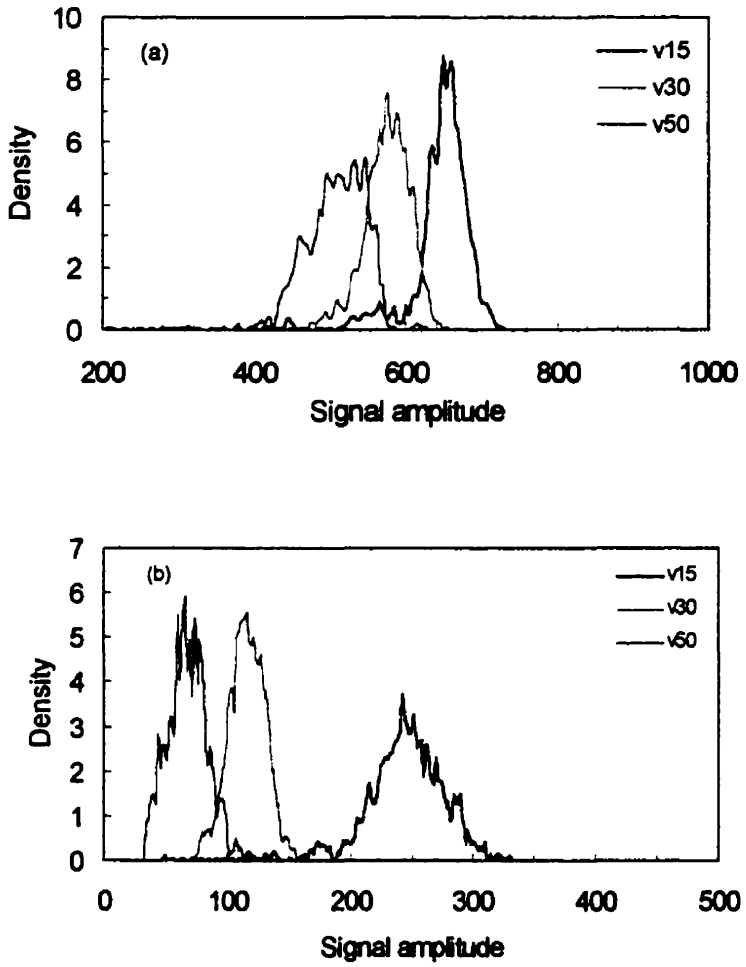


Figure 4.9 Density distributions of IR signals after run-time filtering. The signal source is the same as that in Fig.4.2-6. (a) behind the keyhole, (b) beside the keyhole.

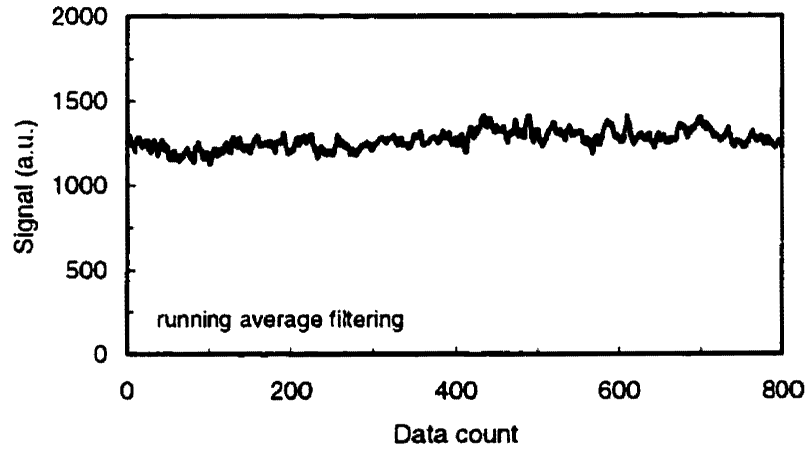
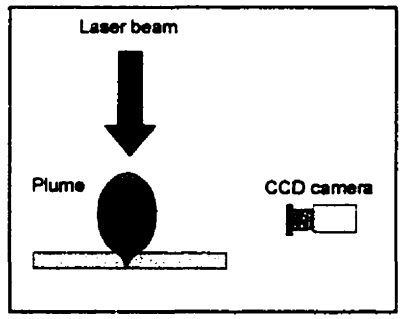


Figure 4.8 Smoothed emission signal of that in Fig. 4.3 using running average filtering.

4.4 Spatial distribution of plasma radiation

It is important to have an idea about the spatial distribution of plasma plume radiation. Due to plasma fluctuation, no unique description of a plasma plume is possible. However, there is always a dense core, which is located adjacent to the keyhole opening and a cloud of luminous plume that surrounds this core.

In general, the size of the keyhole opening and the dimension of the plasma plume are related. The radius of the keyhole at its mouth is similar to the laser beam radius in optimal full penetration welding. However, the radius of the keyhole will be larger than the laser beam at low welding speed or under higher energy deposition condition, since strong inverse Bremsstrahlung absorption has enough energy to heat the surrounding metal or the plasma plume is hot enough to defocus the laser beam. Imaging studies of the weld pool[64] show that at full penetration at medium speed the weld pool has a tear drop shape and the size of the pool does not change appreciably with changing processing parameters. However, at very low speed, the weld pool is elliptical in shape and this shape will become large with decreasing speed. At higher speed, where penetration is lost, the weld pool becomes longer and the sides of the pool are more parallel. In this case, an increase in speed results in a large decrease in weld pool length and slight



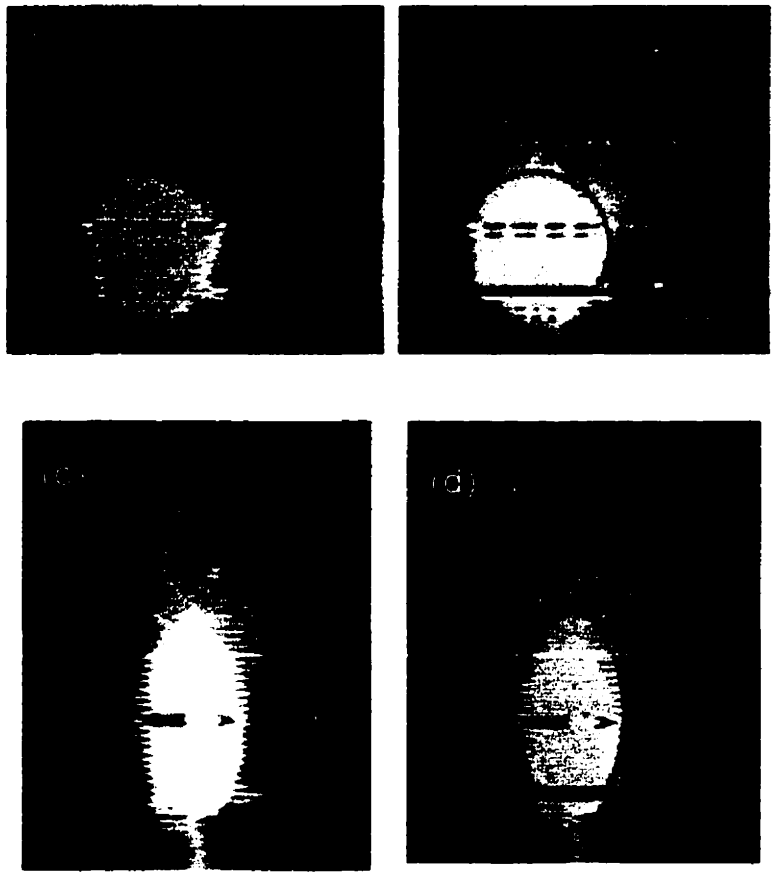


Figure 4.10 Schematic drawing of imaging system with a CCD camera and the horizontal view of images of the plasma plume.

narrowing. Therefore, infrared emission from the weld pool will show a different spatial distribution when processing parameters are changed.

Under normal welding conditions, the metal vapor expanding from the narrow keyhole is immediately spread out over a much greater area. This is due to the high radial velocity of the shielding gas at the surface. Consequently, the plasma ejected from the keyhole expands very rapidly and its pressure quickly decreases. The vapor pressure changes significantly from partial penetration to full penetration and if there is an opening at the keyhole bottom, the pressure drops considerably. This effect results in a different spatial distribution of the plasma plume above the work-piece surface, which has been observed using streak photograph imaging technique[65]. Fig.4.10 shows a photograph of the plasma plume taken with a CCD camera during laser beam welding of steel sheet. The red line represents the sheet surface. The shape of this typical plasma plume is semi-spherical (Fig.4.10(a)) with the center on the metal surface. It should be noticed that this shape is not constant during real time welding. It frequently varies. Sometimes, the shape is elongated (Fig.4.10(c). However, the high intensity region is located adjacent to the keyhole opening and will have a relative constant shape.

Fig.4.11 shows three images of the plasma plume during laser beam welding taken with a CCD camera attached to the laser head. The view angle of the camera toward to the weld spot was about 45 degrees with respect to the work-piece surface, and they show the plasma plume at three different welding speeds. At low speed, the luminous plasma plume occupies a wider region. With an increase in welding speed, the plume size becomes smaller. It can be seen that at high welding speed the plume is much smaller than that at low speed. These images suggest that the size of the luminous plasma

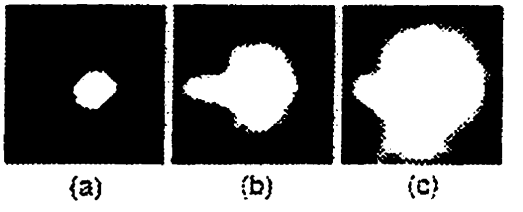


Figure 4.11 Images of CO_2 laser beam interaction with steel sheet.

plume be indirectly related to the weld penetration condition. Although the emission signal collected from the center of the plume is not a good indicator of weld penetration, optical emission from the plume away from the center will reflect the weld penetration condition.

The spatial distribution of the plasma plume has been measured by shifting the detecting spot across the plume in two perpendicular directions. The results are given in Fig.4.12. In this measurement, the detector is mounted behind the laser head. The UV radiation has a bell-like shape, while the IR radiation has a wider distribution. Significant IR radiation can still be detected far away from the welding spot along the weld line. This IR radiation must be from the hot melt. The data given in Fig.4.12 is averaged over a whole welding run. So the plot represents an average distribution. The exact shape and dimension of the distribution is not important here. It is important to note the emission distribution of the plume and that detection spot is not restricted to the center of the plume.

The general distribution of optical emission from the plume agrees with the measured electron temperature and density distribution of the plasma plume[32]. This distribution is also similar to the density of vapor atoms in the vapor plume that was generated by laser ablation of metal surface[66]. The similarity implies that the dense vapor generated by laser beam at a spot expands rapidly to form the plasma plume. Such a plasma plume will have a hemispherical shape.

Suppose the plasma plume has a semi-sphere shape with the center located at the keyhole opening. A vapor density $\rho_v(r)$ is assumed since the plasma vapor expands radially into the surrounding environment. During its expansion, the density and the temperature decrease. Then, the density of the excited species of the plasma plume is assumed to be

$$\rho(r) = D \cdot \exp(-\alpha r) \tag{4.10}$$

where D and α are two constants. α determines the decay of the plume density with distance r from the center. It is assumed that optical emission is proportional to $\rho(r)$.

With assumption that plume radiation is in a thin cyclinder with a cross section area ds as given in Fig.4.13. the radiation intensity detected with a photodiode is

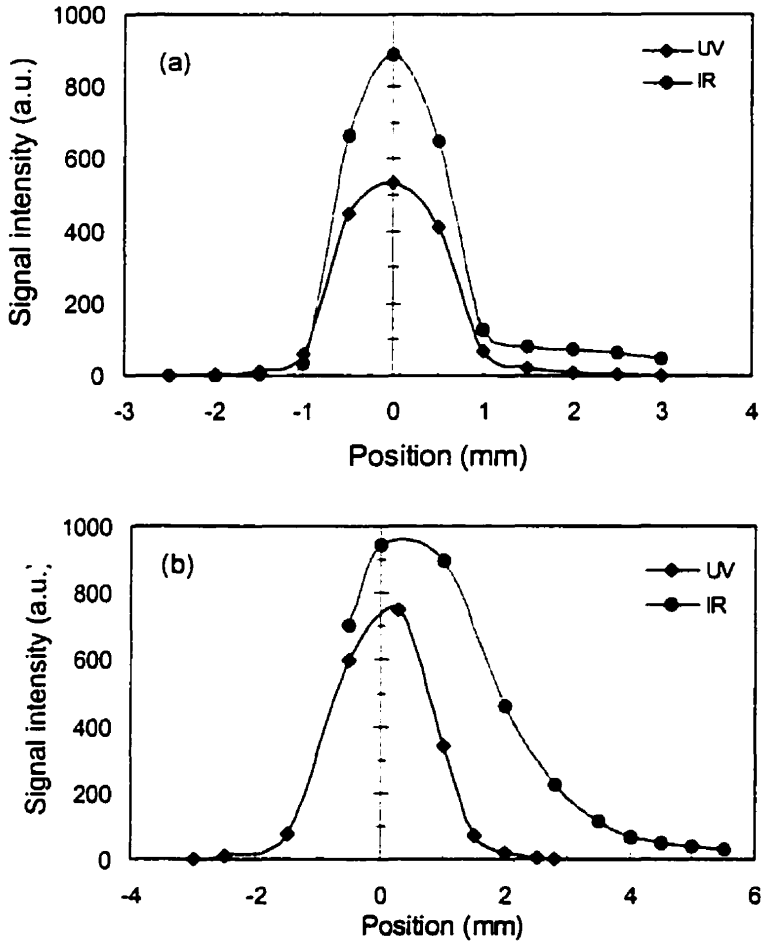


Figure 4.12 Spatial distributions of plasma plume emission. (a) Signals were measured across the weld, (b) Signals were measured along the weld with the detector behind the laser head.

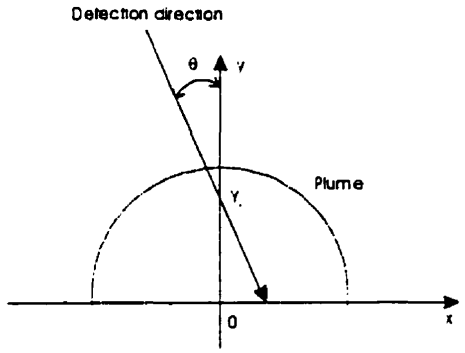


Figure 4.13 Schematic illustration of the position of the detection spot relative to the plasma plume.

$$I = const \int \rho(r) dl \tag{4.11}$$

where $dl = \sqrt{dx^2 + dy^2}$. In a XY cordinate scheme, the detection line can be expressed as linear equation:

$$y = -x / \tan(\theta) + y_0 \tag{4.12}$$

in which θ is the observation angle. Integration of expression (4.11) at various x value produces a distribution of radiation detected by a photodiode, as shown in Fig.4.14.

The calculated shape of the detectable emission intensity along the weld line is similar to that observed experimentally. Therefore this simple model shows that the density of the luminant plasma vapor decreases radially out of the keyhole opening and that the signal intensity is very sensitive to the position of the detection spot in the plume.

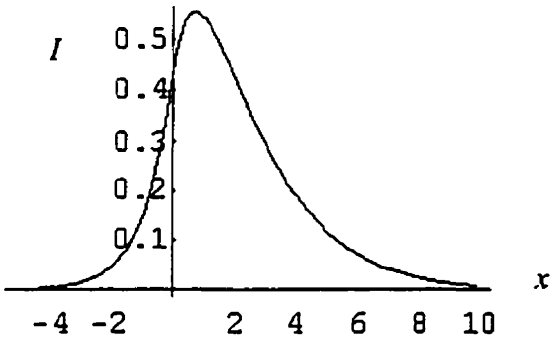


Figure 4.14 Calculated plume radiation with changing detection spot along the weld line.

4.5 Frequency domain analysis

4.5.1 Characteristics of FFT spectrum

Characteristics of variations or fluctuations in the optical signals can be analyzed in the frequency domain. The fast Fourier transform (FFT) algorithm is commonly used to generate the frequency spectrum. This algorithm has a high processing speed that allows it to analyze a large number of data samples in a short time.

With a sampling frequency of 40 kHz, a spectrum of frequency range 0 – 20 kHz is obtained using the data acquisition board. The optical emission spectrum contains two parts: one is a very strong DC component while the other is a distribution over a broad frequency range. In order to see details of the frequency distribution, the DC component is subtracted from the spectrum. Fig.4.15 shows two sets of frequency spectra of optical emission signals that were detected from the plasma plume and the weld pool beside the keyhole (spot 1 in Fig.4.6). Optical emission from the weld pool was filtered with an IR transmission filter. These two sets of spectra represent the full penetration and partial penetration welding conditions. As a whole, the frequency components are mainly located at low frequency with a distribution which decays with increasing frequency. This is typical distribution representing unsteady motion of the fluid with slow variation. This spectrum indicates that the plasma plume fluctuates mainly at low frequency, especially for IR emission from the weld pool. However, the emission spectrum under full penetration welding conditions shows a strong band of frequency components in the range of 2 - 5 kHz. This band of frequency components would be generated by keyhole oscillations[53, 40] and is characteristic of full penetration welding.

Under partial penetration welding conditions, plume emission loses this characteristic distribution and shows approximately the same pattern as IR emission from the weld pool. IR spectra, on the other hand, show that the distribution of the frequency component shifts to low frequencies under partial penetration welding condition.

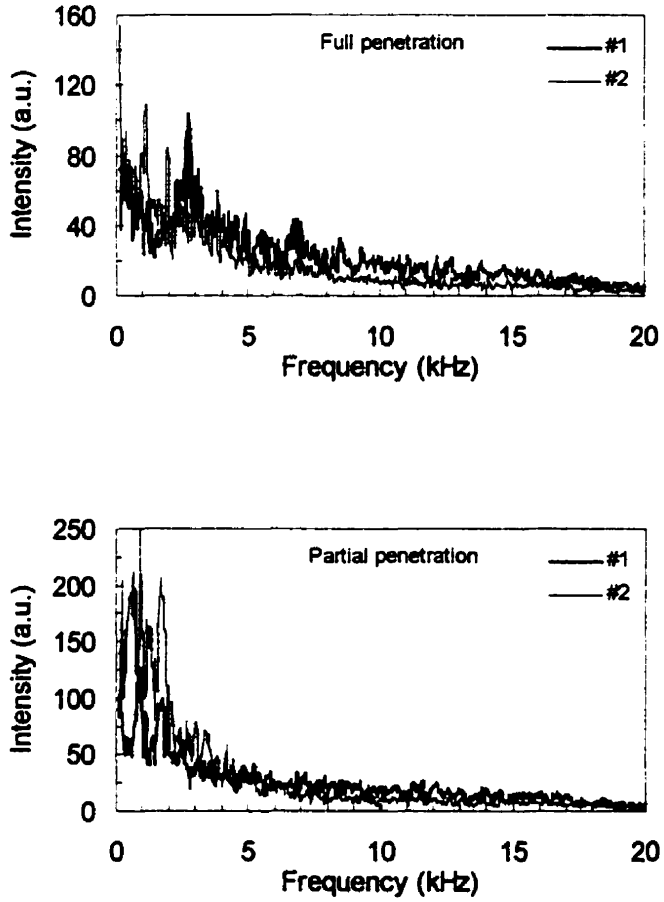


Figure 4.15 FFT spectra of optical emission signals of broad band emission from plasma plume (#1) and IR emission from weld pool beside the keyhole(#2). Laser power is 1.6 kW and the welding was performed on bead-on-plate.

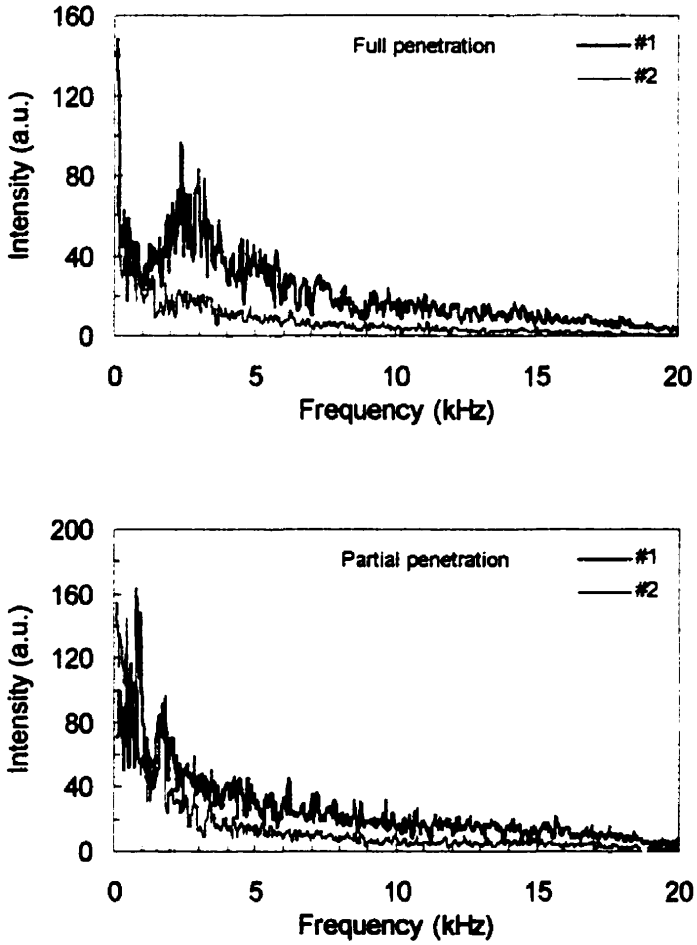


Figure 4.16 FFT spectra of optical signals of broad band emission from the plume (#1) and IR emission from the weld pool behind the keyhole (#2).

Another pair of spectra is given in Fig.4.16. These are IR emission from the weld pool behind the keyhole and broad band emission from the plasma plume. As before, spectra representing full penetration and partial penetration welding conditions are shown in this figure. There is no sign of characteristic frequency components in the IR emission from the weld pool. The main energy distribution of the IR emission is at low frequency.

It can be seen from optical emission spectra that the frequency distribution pattern changes as one goes from full penetration welding to a partial penetration weld. With a proper classification algorithm, this pattern variation could provide enough information for weld quality monitoring. In next section, the feedforward neural network is utilized to classify welds based on optical emission spectra.

4.5.2 Weld classification by neural network

As for acoustic signal processing, optical emission spectra are combined into 20 spectral bins using integration and normalized to a total intensity of the spectra to value between 0 and 1. These final spectral bins are used as the inputs to the neural network. Since optical signals have an energy distribution in the low frequency range, below 10 kHz (Fig.4.15 and 4.16), only ten spectral bins for each spectrum need to be considered as inputs. Combining two signals detected from two spots, we obtain 20 spectral bins in total as inputs. In addition to these spectral bins, the total intensity of the optical emission signals can be included. From section 4.2, we know that IR signals are separable under different welding conditions. Therefore the IR signal intensity is available as an additional input to the neural network. In constructing a three-layer neural network, 21 input nodes are used, and 10 nodes of hidden layer and one output node are considered here for classification of welds between full penetration and partial penetration.

The constructed feedforward network was trained using 40 sets of data recorded during welding, in which 20 sets of data were from a full penetration welding condition while 20 sets were from the partial penetration condition. After training, the network was fed into 100 sets of data for each welding condition for testing. Test results are summarized in tables 4.4 and 4.5. Welds at speeds of 25.4 and 38.1 mm/s are full

Classification results	Input signals			
	Full penetration		Partial penetration	
(mm/s)	25.4	38.1	63.5	76.2
Full penetration	50	44	0	0
Partial penetration	0	1	50	53
Not confirmed	0	5	0	1
Total	50	50	50	54
Accuracy (%)	94		99.04	

Table 4.4 Results of weld classification by neural network. Input data are the optical emission spectra from plasma plume emission and IR emission from the weld pool beside the keyhole.

Output results	Input signals			
	Full penetration		Partial penetration	
(mm/s)	25.4	38.1	63.5	76.2
Full penetration	41	28	0	0
Partial penetration	2	7	49	49
Not confirmed	7	15	1	1
Total	50	50	50	50
Accuracy (%)	69		98	
Error rate (%)	9		0	

Table 4.5 Results of weld classification by neural network. Input data are the optical emission spectra from plasma plume emission and IR emission from the weld pool behind the keyhole.

penetration welds, while those at 63.5 and 76.2 mm/s produces partial penetration welds. With optical signals from the plasma plume and weld pool beside the keyhole, overall performance is quite satisfactory and has an accuracy of 99% for classifying partial penetration welds and of 94% for identifying full penetration welds (table 4.4). Classified welds labeled 'not confirmed' refer to those that are not identified as full penetration or partial penetration.

For the classification using the emission signals from the plasma plume with IR from the weld pool behind the weld pool, results (table 4.5) are not as good as those of the first case, especially for identifying full penetration welds. However, the mis-classified welds are located under the 'not confirmed' category. In this case, the error rate, which is defined as the ratio of the number of welds incorrectly classified to the total number, is still not high. Therefore, the performance of the neural network-based classifier using dual optical signals is generally satisfactory.

4.6 Multi-spot and multi-color detection technique

The conventional detection method is to adjust the detection spot as close as possible to the center of the plume, so that the sensing system can get the strongest plume emission. Information on the spatial distribution of the plume radiation has not yet been incorporated into a control system.

One idea is to use information on spatial distribution to locate the vertical position of weld spot relative to the laser head. As described in section 4.4, the detected emission signal is very sensitive to any change in the detecting spot. If the detector is mounted on the laser head, a change of height of the laser head above the work-piece surface corresponds to a shift of the detection spot along the surface, as is shown in Fig.4.17.

To implement this technique, a dual-view detection technique has been developed. Under proper focusing conditions, the twin spots on the surface are adjusted to lie on either side of the plasma plume. The separation between these two spots depends on the laser focal radius and power level, so that both channels have a good signal intensity. When the work-piece surface shifts upward, one of the detectors gradually gets

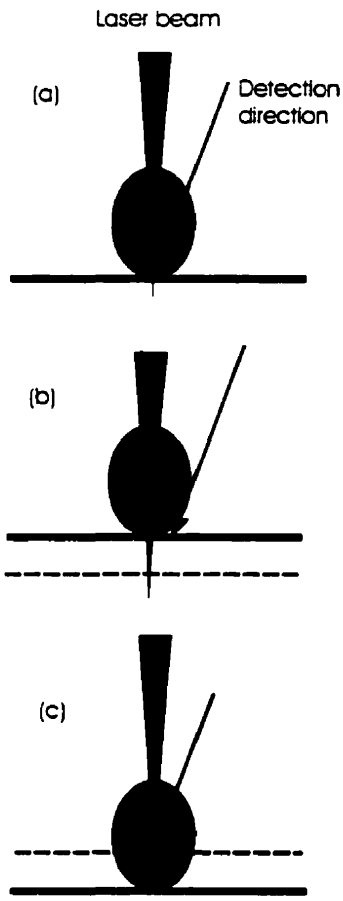


Figure 4.17 Principle behind detection of focal position.

a stronger signal. If the surface shifts downward, the other detector senses a stronger emission signal. The difference in signal intensity between these two detectors indicates the focus position change required and the direction of this change.

Another idea is to consider the shift of the hot core of the plasma plume across the welding seam. In laser beam butt welding of dissimilar steel sheets, part of the laser beam should be located on the thin sheet side and another part of the beam is incident on the thick sheet side. If there is a shift of the laser beam across the seam, the hot core of the plasma plume shifts up or down accordingly. Using three or four spot detection, this kind of shifting could be sensed.

Furthermore, as infrared radiation from the weld originates from the hot plasma vapor as well as from the melt pool, in the center of the plume the major contribution is the hot plasma vapor. However, away from the center, the contribution of the melt pool becomes dominant. As shown in Fig.4.6, the distribution of infrared radiation from behind and beside the melt pool can be separated for full penetration and partial penetration welds. Radiation from beside the weld pool is more easily separated. For this reason, the multi-spot detecting system can identify the welding penetration condition.

4.7 Inverse filtering and weld fault identifier

Good welds can be achieved when the process runs smoothly and regularly. However, transient disturbance can occur interrupting the steady welding process. As a result, welds may be irregular. These transient processes are usually caused by defects on the welding edge, material impurities and changes in processing parameters such as a variation in laser power. Such unexpected factors result in disturbances of laser beam coupling into the work-piece. One example is when edges are prepared using a shear, where it is inevitable that some degree of mis-match will occur in volume production. As a result, laser-welded seams are not always perfect and ripples, pinholes and other surface defects can be observed.

Fluctuation in acoustic and plume emission accompanying these irregularities and emission signals from the weld site contains information that may indicate weld stability. Transient processes are not the only reason for fluctuation in the plasma plume, as part of

this fluctuation is intrinsic to the welding process itself. Generally, the keyhole fluctuates strongly and these fluctuations must be reflected in the dynamics of the plasma expanding from the keyhole. This expansion also results in pressure variations in the keyhole that can damp or cause new fluctuations. Variations of pressure in the keyhole and changes of the keyhole capillary geometry can also modify the absorption of the laser beam in the keyhole resulting in a higher or lower evaporation rate at the walls of the keyhole. Thus, the fluctuating plasma can disturb the coupling of laser radiation into the material, causing instability in the welding process.

A fluctuation in the plasma plume corresponds to a change in the evaporation rate of metal vapor from the keyhole wall or to an oscillation in the keyhole shape. So the plasma plume has an instantaneous response to transient disturbance. The response of the molten metal pool is however slow in comparison with the plume vapor since it takes time to form a molten pool. Therefore IR emission from the weld pool and the UV radiation from the metal vapor plasma have a different response time to fluctuations. In experiments[7] certain regular and characteristic bands in power spectra of fluctuating plasmas have been identified for various welding conditions, and constitute a basis for monitoring and controlling penetration depth and pore formation during the welding process. From the experimental data, it can be seen that power spectra of plasma fluctuations are very rich and are broad band and noisy, and thus in these spectra almost any frequency can be found. Moreover, characteristic frequencies vary slightly with the uncontrolled variations of welding parameters such as pre-heating of the weld seam, the focus position and the total laser power [58].

Knowing the fluctuating nature of the plasma, we can devise an algorithm to inversely filter out the intrinsic portion of the fluctuation. The filtered signals could indicate the occurrence of the disturbance or other transient processes.

In order to filter normal fluctuations, an algorithm for signal processing has been developed. Suppose in a time interval $t \rightarrow t+\Delta t$, two sets of optical emission data are collected

$$\begin{aligned} \{x_i\} &= \{x_1, x_2, \cdots, x_n\} \\ \{y_i\} &= \{y_1, y_2, \cdots, y_n\} \end{aligned} \tag{4.13}$$

These two sets of data represent UV and IR radiation signals. Let x_o and y_o be the mean values of these two data set:

$$x_0 = \frac{1}{n}\sum_i^n x_i$$
$$y_0 = \frac{1}{n}\sum_i^n y_i \tag{4.14}$$

So that

$$x_i = x_0 + \Delta x_i$$
$$y_i = y_0 + \Delta y_i \tag{4.15}$$

where Δx_i and Δy_i are fluctuation amplitudes around the mean value. As for the calculation of the cross correlation of two sets of discrete signals, a normalized coefficient η can be defined

$$\eta = \frac{\sum_{i=0}^n x_i y_i}{(\sum_{i=0}^n x_i^2 \sum_{i=0}^n y_i^2)^{1/2}} \tag{4.16}$$

Summation terms in the above expression can be written as

$$\sum_{i=0}^n x_i y_i = \sum_{i=0}^n (x_i + \Delta x_i)(y_i + \Delta y_i) = n x_0 y_0 + \sum_{i=0}^n \Delta x_i \Delta y_i$$
$$\sum_{i=0}^n x_i^2 = \sum_{i=0}^n (x_0 + \Delta x_i)^2 = n x_0^2 + \sum_{i=0}^n \Delta x_i^2 \tag{4.17}$$
$$\sum_{i=0}^n y_i^2 = \sum_{i=0}^n (y_0 + \Delta y_i)^2 = n y_0^2 + \sum_{i=0}^n \Delta y_i^2$$

So that equation (4.16) can be expressed as

$$\eta = \frac{1+\alpha}{(1+\beta)^{1/2}(1+\gamma)^{1/2}} \tag{4.18}$$

Where

$$\alpha = \frac{\sum_{i=0}^n \Delta x_i \Delta y_i}{n x_0 y_0}$$

$$\beta = \frac{\sum_{i=0}^{n} \Delta x^2{}_i}{n x_0{}^2} \tag{4.19}$$

$$\gamma = \frac{\sum_{i=0}^{n} \Delta y_i{}^2}{n y_0{}^2}$$

For a constant deep penetration welding condition, the plasma radiation has a regular dynamic fluctuation. The signals have a mean value larger than the fluctuation amplitude. For this reason, the values of α, β and γ are very small. Thus η can be simplified

$$\eta = (1+\alpha)(1-\frac{\beta}{2})(1-\frac{\gamma}{2}) = 1-\delta \tag{4.20}$$

where

$$\delta = \frac{\beta+\gamma}{2} - \alpha \tag{4.21}$$

For plasma emission, α is approximately equal to zero due to chaotic fluctuations. Thus, $\delta>0$. If the welding process is constant, the correlation coefficient η is close to 1.

However, when disturbance occurs, large spikes or extremely low signals appear. Some of the Δx_i or Δy_i become large, so that β and γ could be large compared to x_o and y_o. In this case, the coefficient drops considerably. Large disturbances or significant transients, therefore, cause larger drop in η. In this way, η could be expected to indicate various weld faults, from rough beads, ripples to pinholes, large concavities and failed welds.

Chapter 5
Optical Monitoring and Optical Data Analysis

5.1 Gap detection

A seam gap is one of the main causes of weld defects, however, early detection allows proper corrective action such as defocusing or moving of the laser beam to avoid production of weld defects.

5.1.1 Gap and weld quality

A seam gap has a significant effect on the welding process and weld quality. A good fit between two sheets is a guarantee of sound welds if other processing parameters are within the operating windows. Although it is experimentally verified that a small gap, if used properly, can benefit the welding process, the difficulty of maintaining a small gap is a problem in production. For this reason, good fit up of sheets in welding is always desired.

There are a number of factors that may cause a gap: thermal distortion, edge damage during material handling and an improper cut. An improper cut makes a curved edge, and as a result, a gap is produced at some point of the weld line. During transfer from the shear to the welding table, edge damage can occur. This damage causes dips and warps along the edge, and at the damaged locations the two sides of the sheet cannot be fitted properly. Thermal distortion, on the other hand, occurs during the laser welding

process. During welding when clamping cannot withstand the distortion force, a gap gradually opens up. In all cases, the two sides of the material are not in good contact so that some portion of the laser beam may pass through, causing improper laser beam coupling, or melt depletion and a poor weld.

If the gap is not too big, an adjustment in welding parameters may compensate the defects in the joint by producing enough melt to fill the gap, thus making an acceptable weld. For this reason, an efficient and sensitive gap detection technique is essential.

5.1.2 Gap detection technique

During laser keyhole welding, the front of the keyhole always has a molten metal layer, which moves along with the laser beam. If a gap opens, this molten metal layer may or may not be broken depending on the width of the gap and the size of the weld pool. In the case of a small gap, the melt layer is thick enough to fill this gap and it is not broken. The melt is always at high temperature (at least at melting pointing of the metal), and there is a considerable amount of infrared radiation from this part of the melt which appears through the gap. With an increase in gap width, more melt is exposed to the air in the gap, and IR emission through the gap will get stronger. If the melt layer is broken, the plasma vapor inside the keyhole will expand out through the opening in the gap. This process produces much stronger IR radiation and radiation at other wavelengths. By

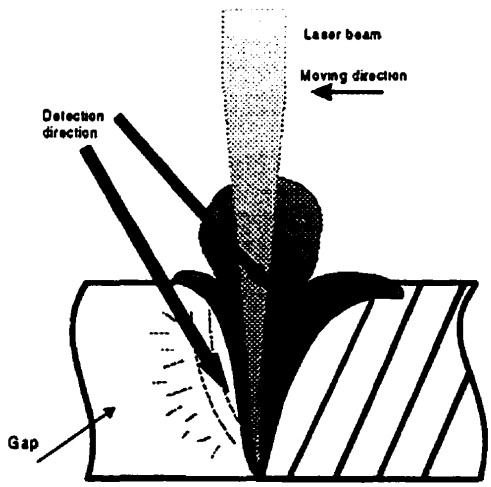


Figure 5.1 Schematic illustration of gap detection technique.

collecting IR radiation through the gap in front of the keyhole, it is possible to measure gap width.

A schematic illustration of the gap detection scheme is shown in Fig. 5.1. A twin-spots detection technique is employed where one views the plasma plume, while the other looks at the gap in front of the weld pool at such an angle as to see the keyhole under the metal surface. The emission signal from the plasma plume is used as a reference, while the emission signal from the gap indicates the size of the gap. Its intensity is related to the width of the gap.

5.1.3 Experimental data

A wedge shaped gap was purposely introduced during CO_2 laser butt welding, so that a gap is gradually increased along the welding seam. Fig.5.2 shows two sets of emission signals using such a twin-spot detection technique. These two signals are from welding processes at two different speeds. The sheets used in this experiment were about 25 cm long. And at one end, a 0.225 mm thick shim was used to create a gap. As can be seen from the data, a strong emission from the plume is observed at the beginning of welding, but after some distance, the emission signal starts to decrease gradually. After a certain distance, the signal intensity becomes very low. At the beginning, the IR signal detected in front of the weld pool is almost at noise level and gradually increases with distance. At the point when the emission from the plume is very low, the IR intensity reaches its highest level. These effects happening are related to changes in the gap width.

It was found that changes in laser power causes a change in emission intensity, however, the signal from the gap is not affected (Fig.5.3), and emission through the gap has the same characteristics as above.

The viewing spot on the seam is much larger than the laser beam diameter and covers the entire gap at the viewing position. The IR intensity reflects the gap width so that the wider the gap, the more radiation can be detected. When welding along the wedged gap seam, the gap width increases continuously from 0 to 0.225 mm in this

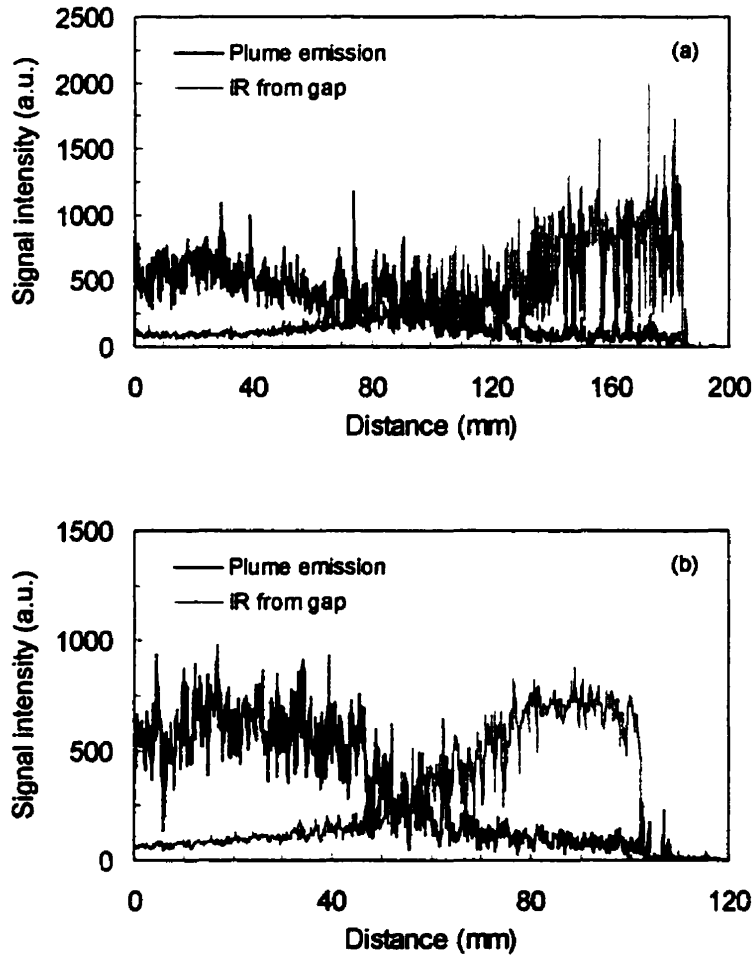


Figure 5.2 Emission signals acquired using twin-spot detection technique. These signals represent two welding speeds: (a) 38.1 mm/s, (b) 63.5 mm/s.

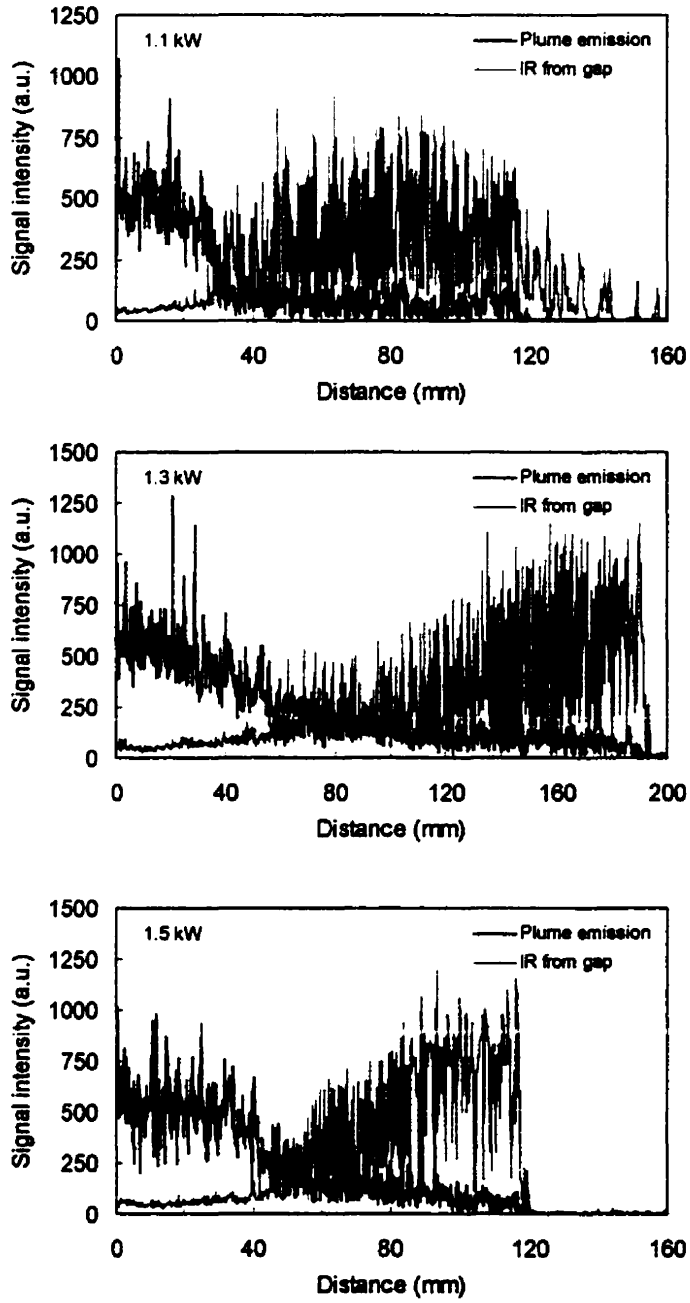


Figure 5.3 Emission signals detected by twin-spot technique at different laser powers.

experiment. At the point when noticeable IR signal is detected, the gap width is estimated to be less than 0.1 mm.

It is important to verify that the IR signal is mainly dependent on the gap width and not on welding speed. A number of welding trials was performed at welding speeds so that partial penetration and full penetration welds were produced. From the observed emission signals, the position at which the IR signal intensity is close to that of the plume emission can be found. The results are shown in Fig.5.4. In this figure, position is represented as a fraction of the total welding length. From the measurement, the relative positions for all the welding speeds are around 0.4, which corresponds to a gap width of 0.09 mm. It is evident that signal intensity does truly reflect gap width.

This technique is also capable of detecting pinholes existing on the edge of the sheet, as such pinholes act as a light guide through which infrared radiation leaks from the weld pool. Fig.5.5 shows signals detected during butt joint welding when dips on the edge of one of the sheets were created. The sharp peaks in the IR signal indicate the location of these pinholes.

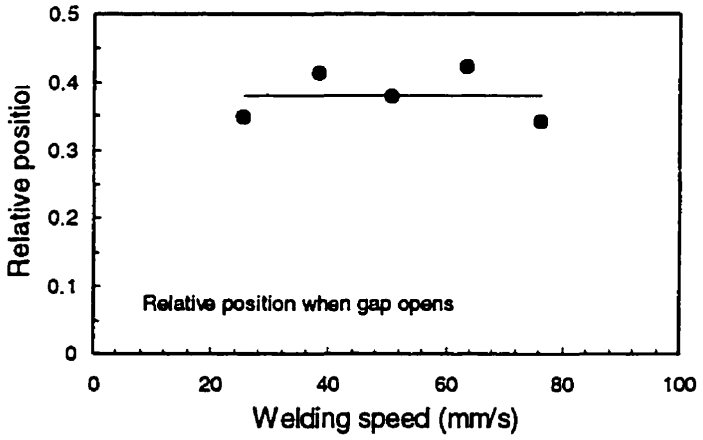


Figure 5.4 Relative positions at which a significant IR signal was detected through the gap.

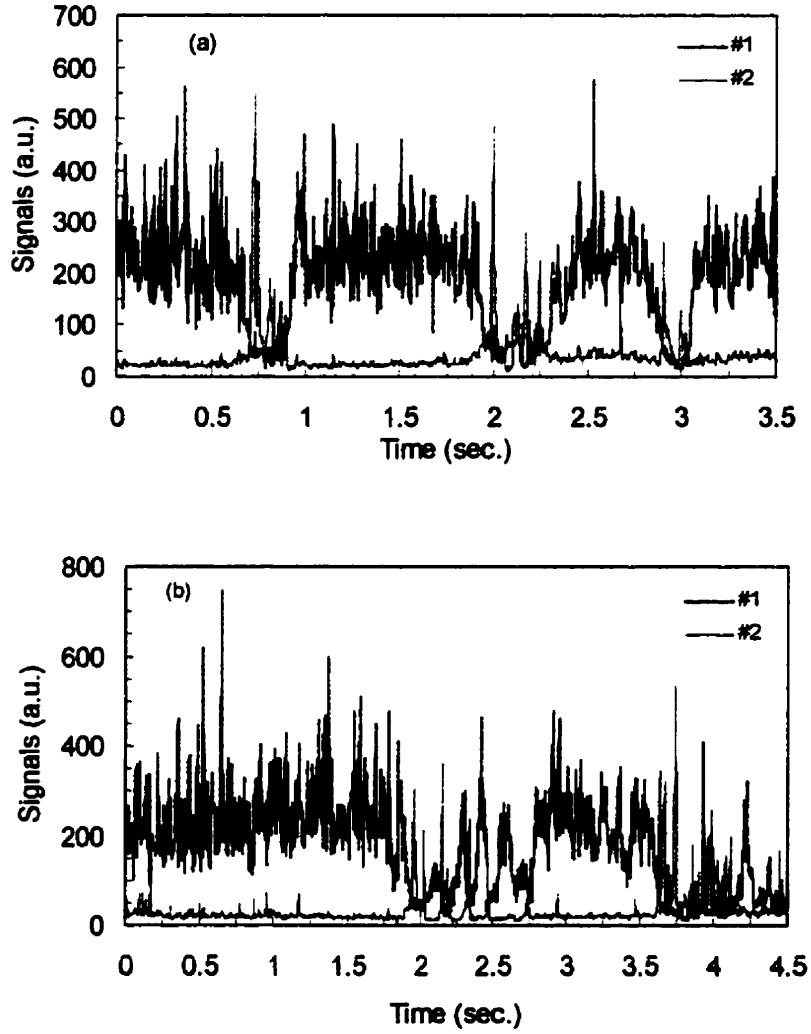


Figure 5.5 Emission signals corresponding to pinhole detection acquired by twin-spot detection technique. #1 signal is the UV radiation from plume. #2 signal is the IR in front of the weld pool.

5.1.4 FFT analysis of UV and IR signals

Several sets of FFT spectra of the UV and IR signals are shown in Fig.5.6. In the UV spectra, there is a relatively strong band of frequency components in the range of 3 – 5 kHz when at optimized full penetration welding conditions. This band of components is coincident with the low frequency band of frequency components in the acoustic emission spectra[53] where these components come from keyhole oscillations. For comparison, these band of components are absent in the IR spectra and only very low frequency components (< 1 kHz) appear in the IR spectra. These data suggest that IR detected through the gap does not originate from the vapor since the vapor fluctuates at frequencies in the kilohertz region and must come from the hot melt. The melt in the outer boundary oscillates at low frequencies.

5.2 Weld fault detection

In laser welding, the relationship between process parameters and ultimate weld quality is complex. In-process monitoring of the welding process to identify acceptable, marginal and bad welds is important to avoid a time consuming post-process analysis of all welds, and facilitates in quality control.

5.2.1 Nature of weld faults

There are many weld faults which may occur in laser welds. Common faults can be categorized as rough beads or ripples, pinholes, large concavity and drop down. Some weld defects, such as bubbles in the welds, cannot be observed from the surface. However, those weld detects that are unobservable are process related and usually exist in partial penetration or excessively overheated welds, so they can be prevented when proper process parameters are chosen.

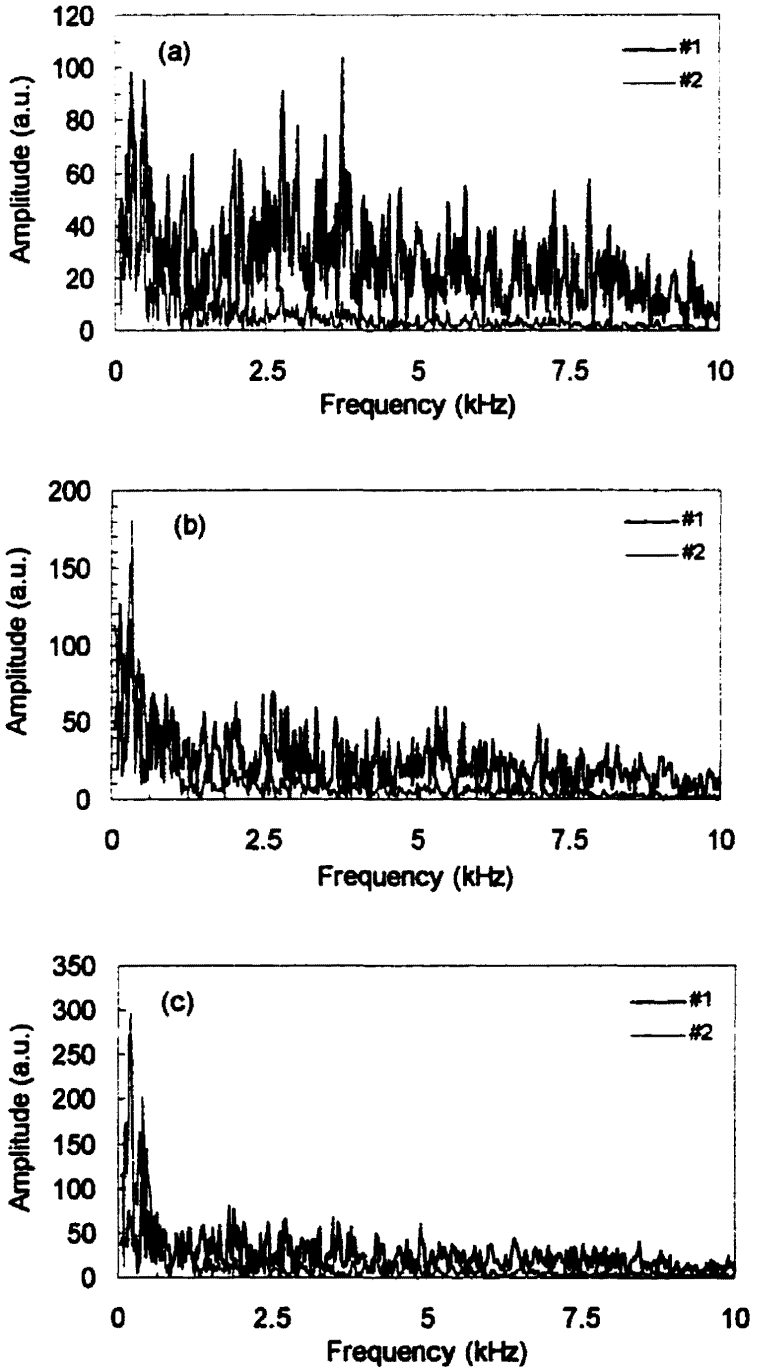


Figure 5.6 FFT spectra of emission signals from laser beam butt welding of a wedge seam. #1 signal is UV radiation from the plume; #2 is the IR from the gap ahead of weld pool. From (a) to (c) the gap gradually opens up so that the IR signal increases.

Good welds can be achieved when the process is uniform. However, the stability of a welding process can be disturbed by transient effects or material defects such as impurities. As a result, a weld irregularity will occur. Such transients are governed by the specific shape of the welding edge, and may also be caused by variations in processing parameters such as the finish of the surface and fluctuations in laser power. All these transient effects result in a disturbance of laser beam coupling into the work-piece. Fluctuations in acoustic emission and optical radiation emitted by the plasma plume above the keyhole mouth can be noticed during these irregularities. Therefore emission signals from the weld site contain information that indicates weld stability.

In order to detect weld faults, several kinds of weld defects were artificially introduced. These can be produced in two ways. One is to create damage on the sheet edge for butt welds by means of filling the seam edge, while the other is to maintain a mechanical gap in the weld seam. In this way, weld defects such as rough beads or ripples, pinholes and large concavities are generated.

Two photographs are shown in Fig.5.7 and Fig.5.8 of welds in which faults exist. In these experiments, the welding speed was kept at a value with which full penetration could be achieved. Visually, good welds have a smooth, uniform weld bead, while unacceptable welds are welds with rough bead, ripples, pinholes, and large concavities. Ripples and large concavities appear in butt welds with a gap. As the laser beam hits the gap, part of the power is lost because it passes through the gap. As a result, not enough melt is produced. A fluctuating melt buildup occurs if the gap is small and causes ripples. When the gap is relatively large, the front layer of melt is broken and no plasma vapor can be confined in the keyhole to enhance laser beam absorption so that large concavities occur. It can be seen in Fig.5.7 that the weld is good at the beginning while ripples are present in the middle of the weld. At the end, the weld shows a large concavity. In Fig.5.8, there are four pinholes in the weld which are accompanied by changes in plume emission.

In experimental data[15], regular and irregular emissions of plasma plume are noticed in accordance with certain welds, but the measured signal intensity has been the main basis for process monitoring and control. Experimental data show that the emission signals have a broad band with many frequencies. Detailed analysis shows that

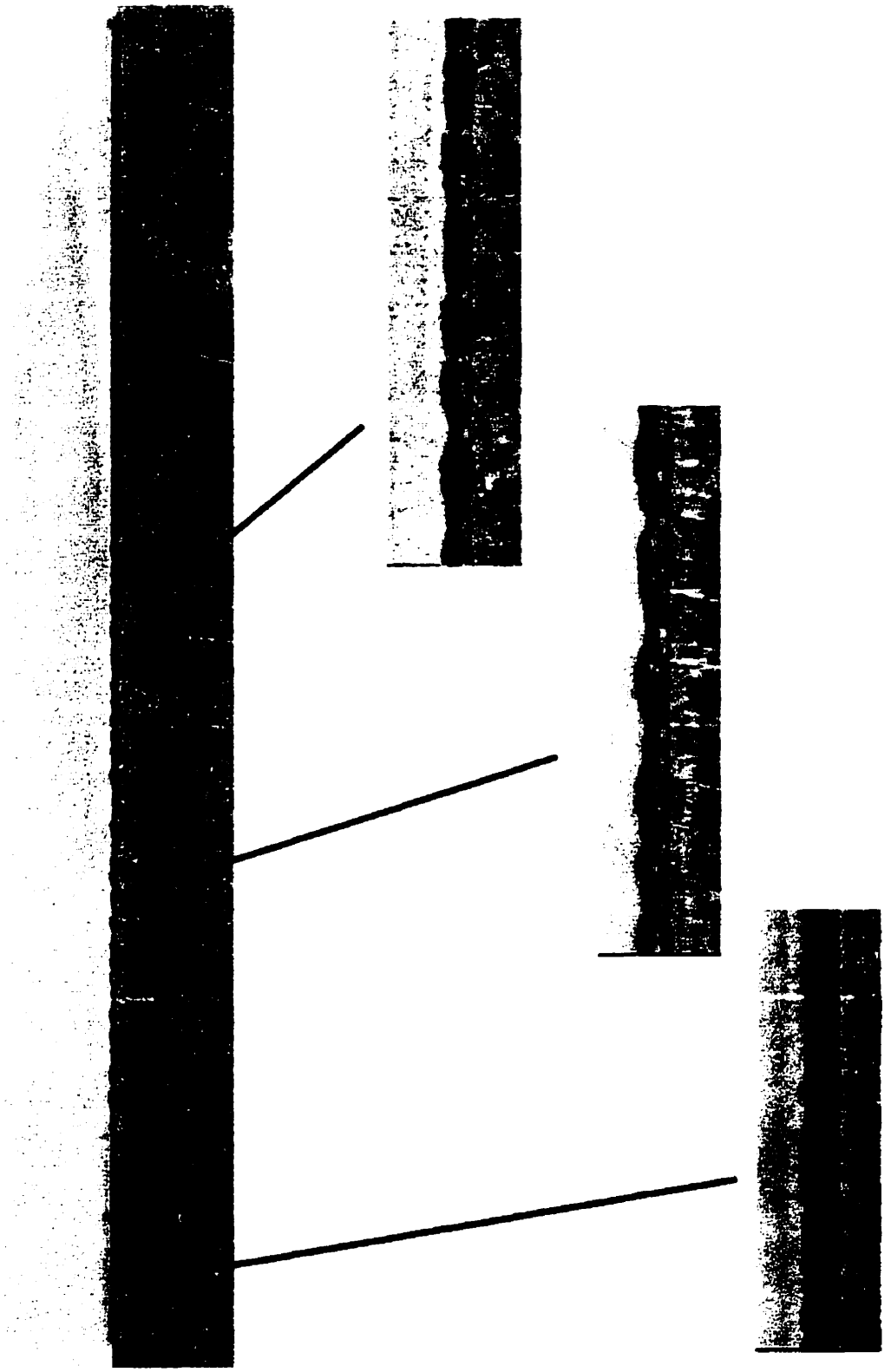


Figure 5.7 Photograph of a weld produced on a seam of gradual gap.



Fig.5.8 Photograph of a weld with pinholes in it.

characteristic frequencies vary slightly with uncontrolled variations of welding parameters such as pre-heating of the weld seam, focal position and total laser power[15].

Plasma plume emission is an immediate indication of variations in the evaporation rate of the metal vapor from the keyhole wall or oscillations of the keyhole shape. It responds instantaneously to any transient disturbances. But the response of the molten metal pool to the disturbance is relatively slow since the plasma vapor is a direct cause of laser beam interaction with metal and the molten pool is an indirect result of this interaction. It is not difficult to see that IR emission from the weld pool and UV radiation from the metal vapor plasma has different transient responses.

5.2.2 Signal variation with weld quality

Optical emission from the plasma is an instant indication of the state of the welding process, and associated fluctuations are inherent to the process itself. For a smooth weld, radiation from the fluctuating plasma has a characteristic spectral distribution and most energy lies in the range 0 – 10kHz. Within a specific band, all the components occur chaotically, and it is impossible to describe the behavior of a fixed component because the variation is so high, although the mean amplitude of the radiation signal depends on the deposited laser beam power and penetration condition. As shown in Fig.4.3 and 4.4, the fluctuation amplitude is large so that an absolute value at a sampling point could not be related to any particular process. However, if the signal is averaged over a long time scale, the mean value does correspond to the laser power, welding speed and focal position. But, this approach is not suitable for real-time monitoring or control.

When a disturbance or interruption occurs, the beam coupling into material is altered and the plasma will respond rapidly to this change. Emission signals corresponding to the welds in Fig.5.7 and Fig.5.8 are shown in Fig.5.9 and Fig.5.10. It is found that the UV radiation signal changes rapidly, while the IR radiation signal (which comes from the hot plasma as well as hot melt pool) will have a slower variation. This response time depends on the source of IR radiation, since the main portion of the signal energy is from the hot plasma, then the variation will have the same behavior as the UV radiation. Otherwise, any change is smaller and less significant.

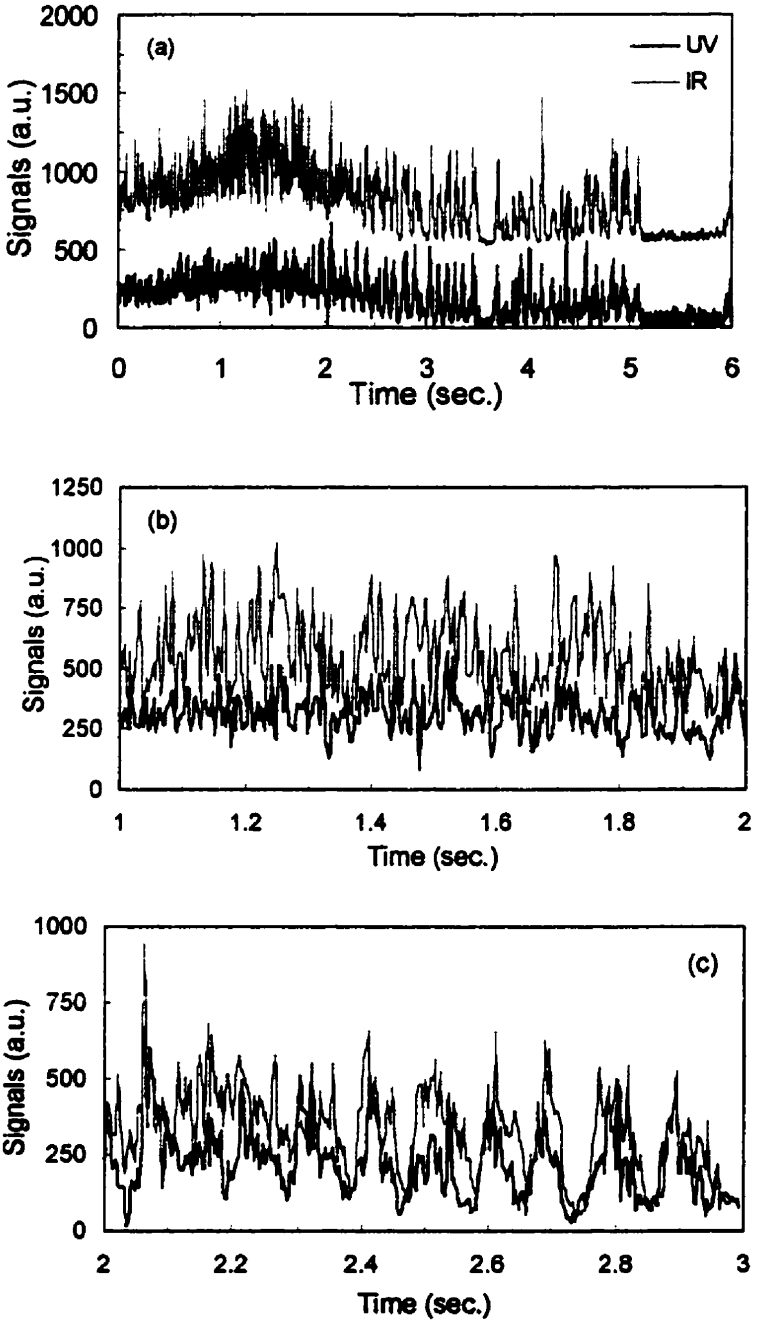


Figure 5.9 UV and IR radiation from laser beam butt welding of a wedge-gap seam. In (a), the IR signals are shifted to avoid overlap in the plot. (b) and (c) are subsections of signals in (a).

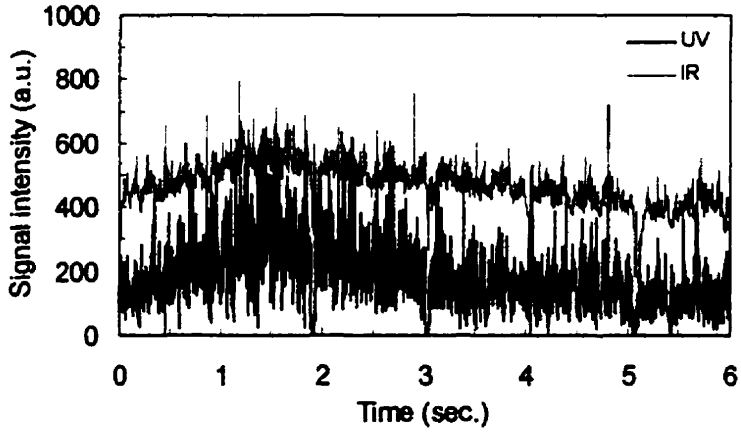


Figure 5.10 UV and IR radiation during laser beam butt welding with pinholes in the weld. The emission signals are obtained using a twin-spot detection technique.

5.2.3 Implementation of inverse filtering

For a smooth welding process, plume radiation exhibits regular fluctuations with a mean value which depends on laser power and welding speed. The mean value calculated in a time interval will also vary from period to period due to its dynamic nature. Emission signals resulting from the disturbance or the transient process are therefore buried in this dynamic fluctuation. The inverse-filtering algorithm developed in chapter 4.5 can be used to implement real-time weld fault detection.

To use the inverse-filtering algorithm, two independent signals are needed. If these two signals are closely related (for instance $x \approx \sigma y$) the coefficient η is always close to 1. For this reason, a twin-spot detection technique is used with which two signals are acquired from different sources. In the current experiments, the signals used in Eq.4.16 are taken from the emission of the plume as well as from the weld pool. From the plume UV radiation is obtained, while from the weld pool IR radiation is taken. These two signals will show different responses to a sudden change in welding conditions and are not completely correlated. From Eq.4.19, the running average coefficients for the two sets of signals in Fig.5.9 and Fig.5.10 are shown in Fig.5.11 and Fig.5.12. In Fig.5.11, the coefficient η is close to 1 at the beginning of the weld, and at about one third of the way along the weld, it starts to decrease. At the end of the weld, η is much smaller than 1. Referring to Fig.5.7, $\eta \approx 0.8$ denotes ripples or rough beads on the weld, while $\eta \approx 0.6$ welds have a large concavity. Pinholes, on the other hand, have sharp peaks with a coefficient $\eta \leq 0.5$ for a significant pinhole. When the pinhole is not obvious, the peak is small.

Several more weld trials were performed to make butt joints between dissimilar steel sheets to simulate tailored blank welding. The coefficients η calculated from the emission signals are presented in Fig.5.13. It can be seen that for a smooth weld, the correlation coefficient η is above 0.9. When a weld fault occurs, the η changes significantly. In detail, pinholes correspond to a sharp spikes; surface roughness and ripples have η in the range of 0.6 –0.85; while any sharp decrease in η indicates welds

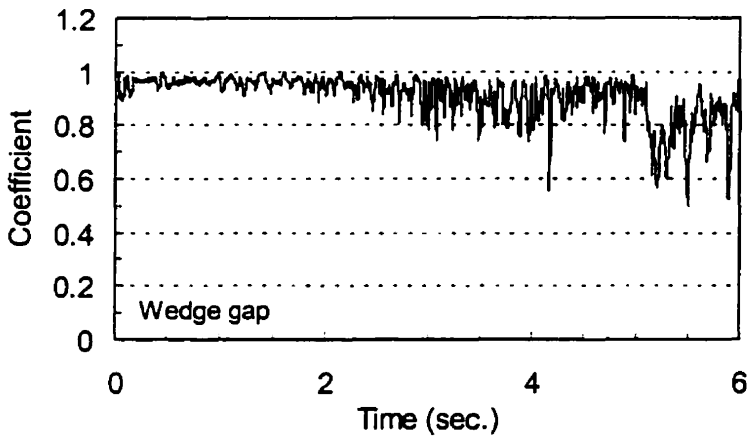


Figure 5.11 Coefficient calculated by inverse filtering algorithm using the emission signals in Fig.5.9.

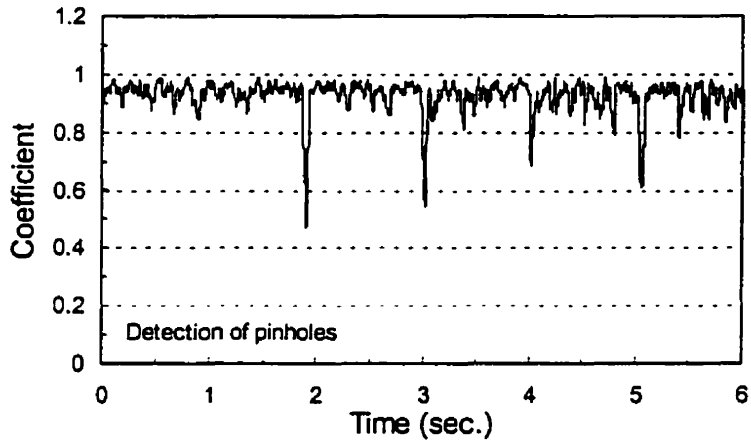


Figure 5.12 Coefficient calculated by inverse filtering algorithm. The emission signals are related to the weld in Fig.5.10.

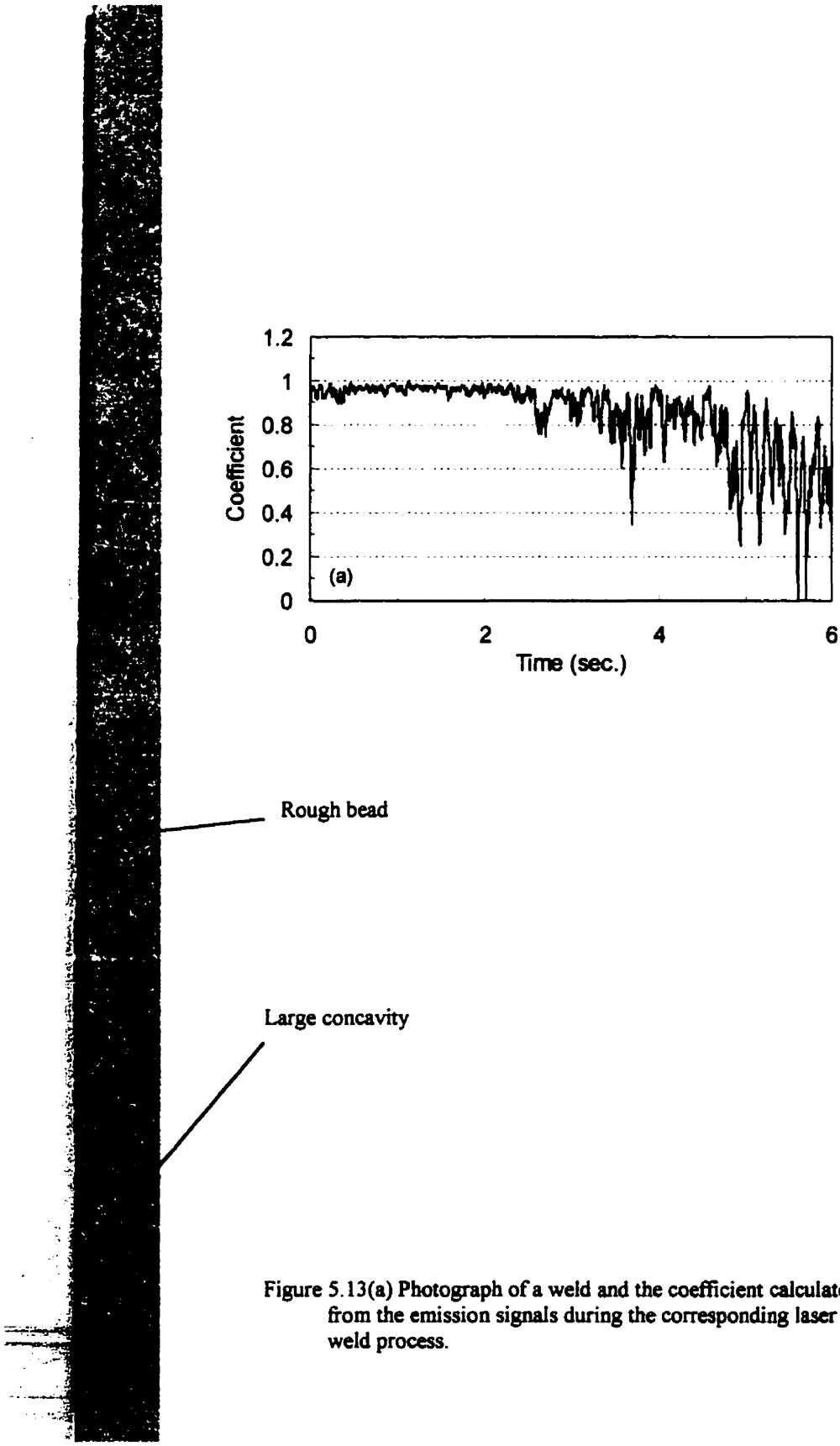


Figure 5.13(a) Photograph of a weld and the coefficient calculated from the emission signals during the corresponding laser weld process.

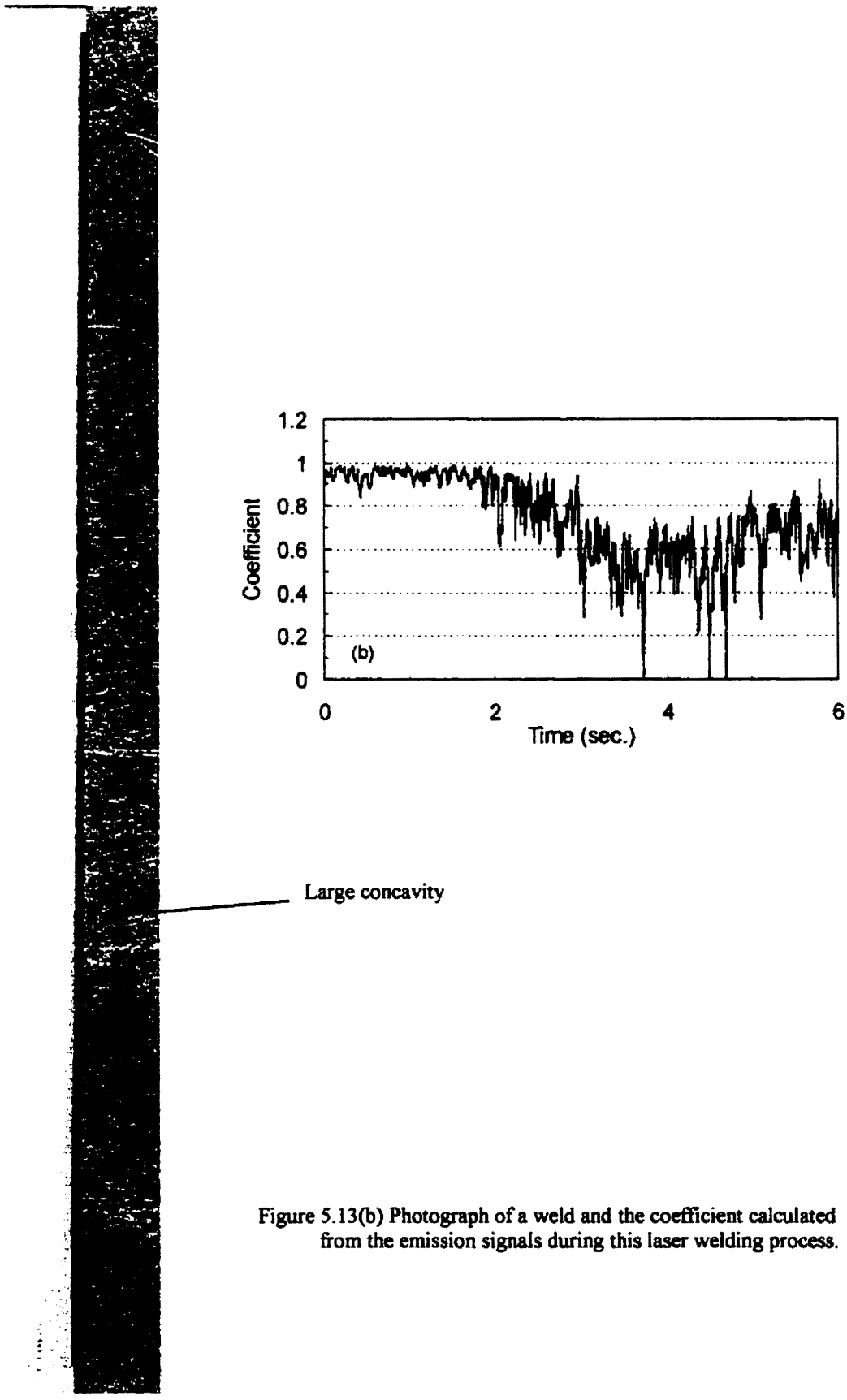


Figure 5.13(b) Photograph of a weld and the coefficient calculated from the emission signals during this laser welding process.

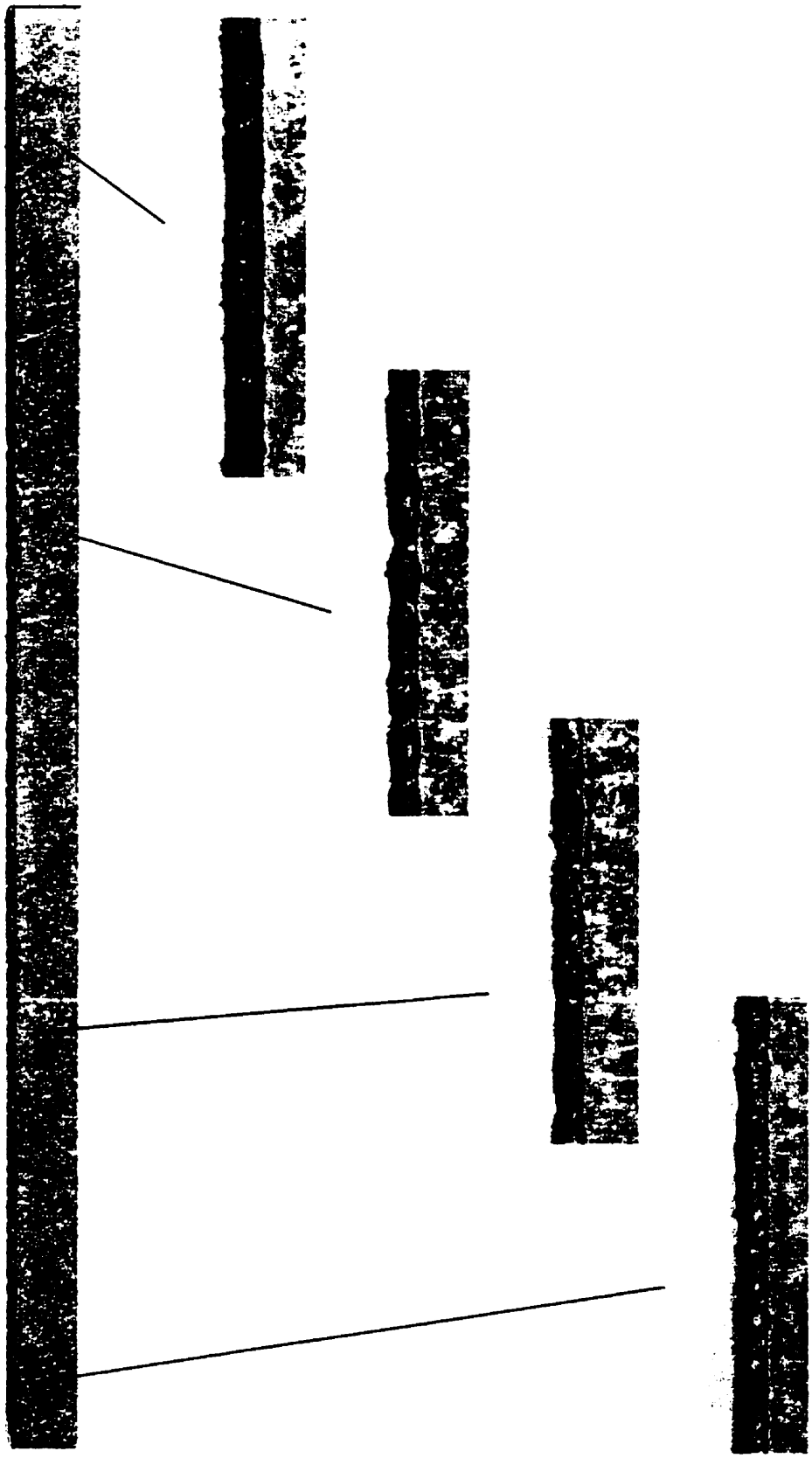


Figure 5.14 Photograph of laser weld with defects.

with a large concavity. When $\eta = 0$, the weld has completely failed. Therefore, $\Delta\eta = 1 - \eta$ is representative of the degree of weld fault.

It is interesting to look at the performance of inverse-filtering algorithm for the emission signals detected at the same spot. For a typical weld with weld defects in Fig.5.14, the calculated coefficient by Eq.4.16 from the recorded signals is plotted in Fig.5.15. Minor weld faults such as rough beads or ripples are not reflected in the output signal. A modification of Eq.4.16 can be used to improve the performance in this case.

A time shift in one of the emission signals can be introduced:

$$\eta_s = \frac{\sum_{i=0}^{n-s} x_i y_{i+s}}{(\sum_{i=0}^{n-s} x_i^2 \sum_{i=s}^{n} y_i^2)^{1/2}} \qquad (5.1)$$

in which s is a shifting count (relating to a time interval Δt) and η_s is the modified coefficient. The s can be adjusted to change the sensitivity. Using Eq.5.1, we can re-calculate the inverse-filtering coefficient of the emission signals for Fig.5.15. Some results are given in Fig.5.16 and it is apparent that the shifting of data reveals such weld faults.

This time-shift scheme also can be applied to emission signals acquired with the twin-spot detection technique. Fig.5.17 gives the inverse-filtering coefficients of the same data used for calculating η in Fig.5.11. For comparison, we can see that using the shifting scheme η_s has a larger variation when weld faults occur. On the other hand, coefficients corresponding to a good weld are not affected by the time shift scheme. Therefore, the time shift scheme makes the detection more sensitive.

The beauty of using the correlation coefficient η to describe the welds is its simplicity and effectiveness. Interpretation is also straightforward. Furthermore, the η description is universal and is not affected by different systems such as laser power, welding speed, and the gain of the signal detection device. In addition, precise optical alignment is not required for the detecting system.

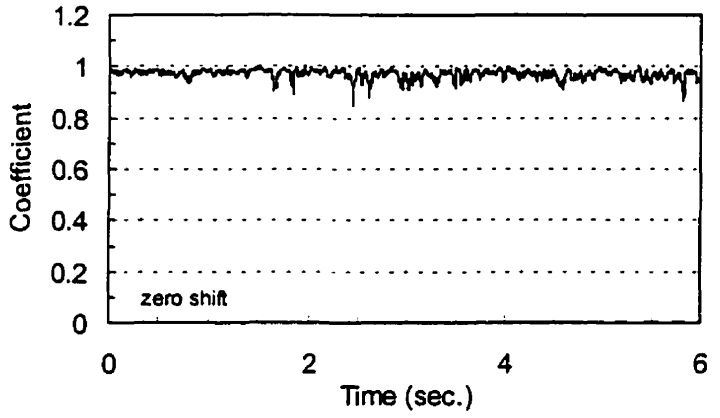


Fig.5.15 The inverse-filtering coefficient of the UV and IR emission signals from the welding plume. A small gap is maintained in the seam so that the weld has defects in it.

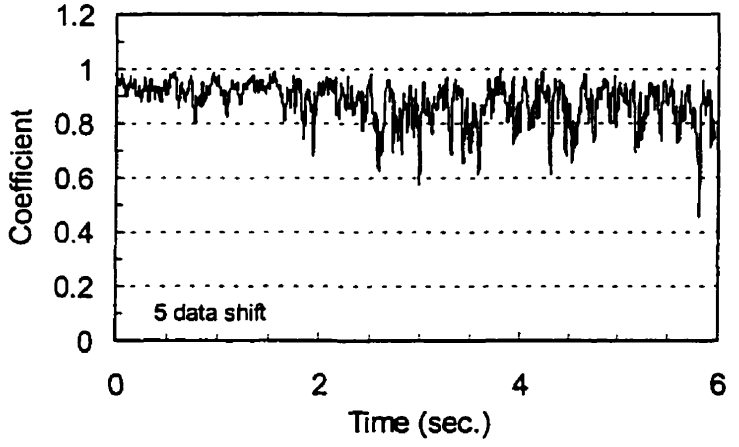


Fig.5.16 The modified inverse-filtering coefficient of the emission signals in Fig.5.15 by shifting 5 data points.

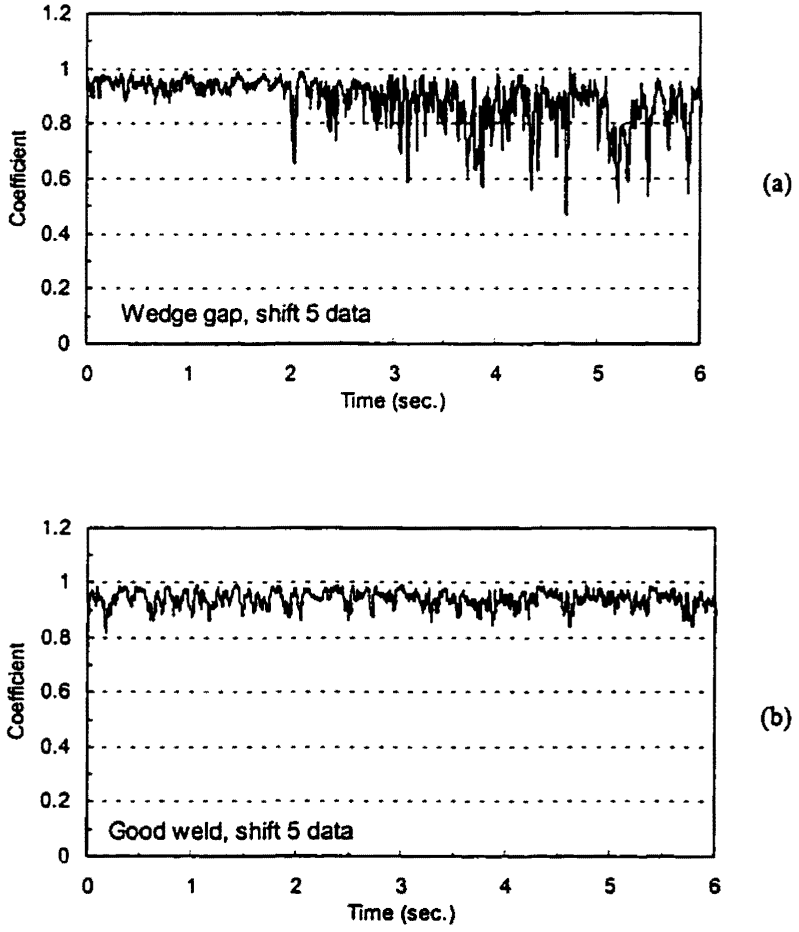


Figure 5.17 (a) Coefficient of the emission signals relating to weld in Fig.5.7. A data-shifting scheme is applied. (b) Calculated coefficient of a good weld. Data shift does not change the overall data value.

5.3 Analysis of weld quality using FFT technique

5.3.1 Technique of separate-signal detection

Optical emission signals from the plasma plume contain information about weld quality. However, intensity alone is not a good indicator of the processing condition or weld quality, as the signal intensity varies with equipment setup, sensitivity of the detector system and various processing conditions. One solution to this problem is to consider multiple signals and the intensity relationship between these signals. Another approach is to study the Fourier spectrum of the signal and use the intensity distribution among different frequency bands.

In order to seek a possible technique for monitoring weld quality, FFT (fast Fourier Transform) spectra of optical emission signals viewed in two directions were analyzed under varying welding conditions. As illustrated in Fig.5.18, a beam splitter was inserted in the laser beam to collect the optical emission from the weld plume along the beam direction. The laser spot on the work-piece was imaged on a photodiode window, so that the light emission from the keyhole could be detected. This photodiode is

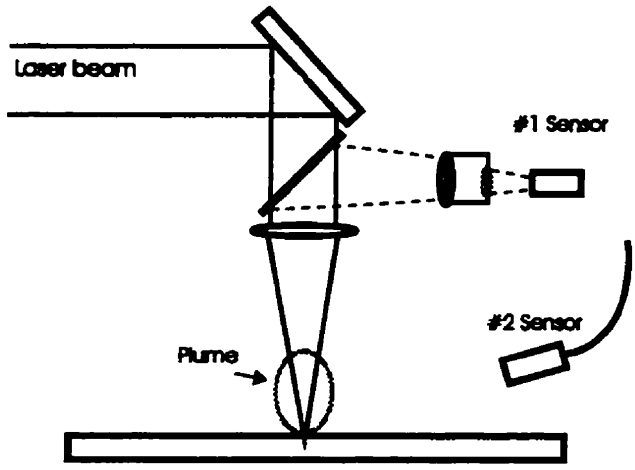


Figure 5.18 Schematic illustration of laser beam welding and signal detection system.

labeled as #1 sensor. Another optical focusing system aimed at 60 degree to the laser beam (sensor #2) also detected light from laser welding. This sensor only detects light emission from the plume.

5.3.2 Experimental data and analysis

The intensity of light emission from the plume in laser welding is primarily distributed in the frequency range less than several kHz[53, 67]. Fig.5.19 shows spectra of the optical emission signal detected by the photodiode (#1 sensor) looking into the keyhole during CO_2 laser welding. Welds were produced at varying speeds between 12.7 and 101.6 mm/s. At low speed, excessive heat is deposited in the material and the welds are wider; while at the high speed end, only partial penetration is produced. In our experiments, full penetration high quality welds were produced at a travel speed near 38 mm/s. From the data given, several trends are obtained: (1) The low frequency component decreases with increasing speed, or in other words, decreases with a decease in penetration depth. (2) Under good full penetration welding conditions, a strong narrow band signal is detected. (3) A more complex spectrum is present during partial penetration welding. These results are somewhat different from those obtained in previous experiments when the photodiode looked sideways into the plume[53]. On the other hand, the presence of a strong emission band during full penetration welding is in agreement with the observation reported by Miyamoto *et al.*[13] that the mean square value lies in the 2-4 kHz range, when the signal was detected at a large angle and was greatly increased under full penetration welding condition.

When the time derivative of the optical signals is taken, the variation of vapor pressure or vapor density in the keyhole or in the plume can be analyzed. Fig.5.20 shows a set of FFT spectra of the time derivative of optical signals detected by sensor #1. For partial penetration welding, i.e. at higher travel speed, spectral components are enhanced in the high frequency range and the overall signal fluctuations are stronger than in the case of full penetration welding. For full penetration welding, i.e. at moderate travel speed, a strong well-defined signal band between 2 - 5 kHz is observed. These results indicate that according to the optical emission, the keyhole is oscillating at relatively

stable frequencies in the range of 2 - 5 kHz under full penetration welding conditions. For comparison, a set of FFT spectra of the time derivative of the optical emission signals detected with sensor #2 is given in Fig.5.21. The signal from the plume contains a broad band of spectral components which extend over 20 kHz and which has been shown to be closely related to the acoustic emission[57]. Although the shift of the spectral components to a higher frequency range is noticeable in this signal set, a well-defined spectral band is not observed.

At low laser power, penetration decreases when the welding speed is kept at 38 mm/s. Fig.5.22 shows FFT spectra of the time derivative of the optical emission detected by #1 sensor. In comparison to Fig.5.20(a), the narrow band near 3kHz becomes broader as laser power decreases. In the limit of low penetration, as seen in Fig.5.22(b), the frequency components extend over 20 kHz which is similar to the case (Fig.5.20(c)) of high speed welding with a laser power of 1.7 kW. Therefore, it is clear that light emission signals from partial penetration welding contain rich spectral components in the high frequency range. An explanation for this effect is that within a shallow keyhole, the flow rate of the vapor gas is higher and the keyhole itself is not stable.

In order to analyze the frequency components that are present in these spectra, modulated laser beam welding was performed. The laser beam was programmed to have a square output waveform. A resonant component within the keyhole oscillation band is expected[53] in optical emission from the plasma with a modulated laser beam welding. For reference, a FFT spectrum of the modulated laser beam radiation is given in Fig.5.23. The modulation frequency is 1.5656 kHz and the modulation depth is 50%. The modulated laser beam is seen to have a third harmonic component at 4.6967 kHz. This component is within the keyhole oscillation band (2 - 5 kHz). Optical emission spectra in Fig.5.24 show that the third harmonic component is observed as a strong resonant component in the signals detected by both sensors. Even the fourth harmonic component is present in the spectrum from #1 sensor. Acoustic signals were also recorded simultaneously with the optical signals and the acoustic spectrum is given in Fig.5.25. In the acoustic spectra, the same resonant peak is present. In addition, the overall profile of the acoustic spectrum is roughly close to that of the optical spectra detected by #2 sensor.

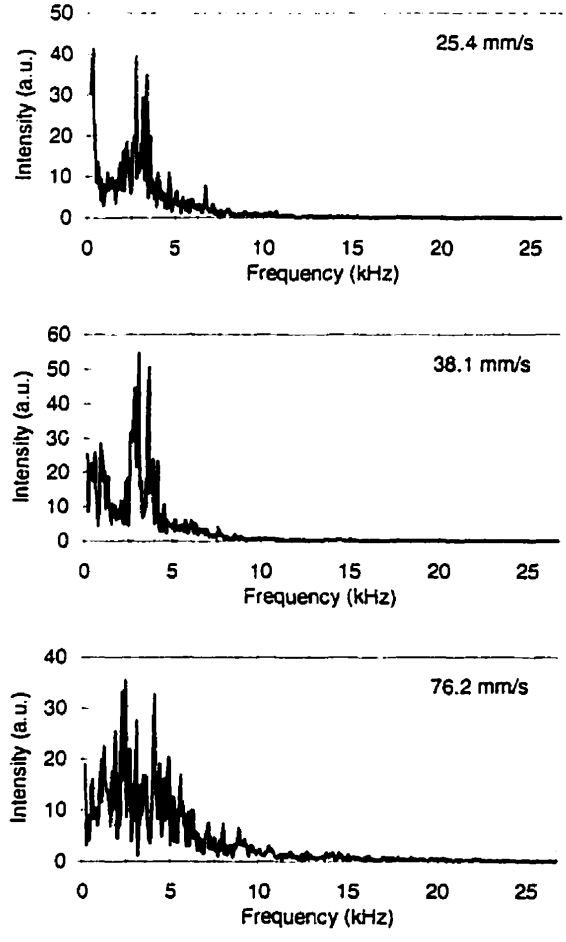


Figure 5.19 FFT spectra of optical emission detected by #1 sensor. Laser power is 1.7 kW. At speed of 38.1 mm/s, good full penetration welds were produced on a steel sheet of 1.1 mm thick.

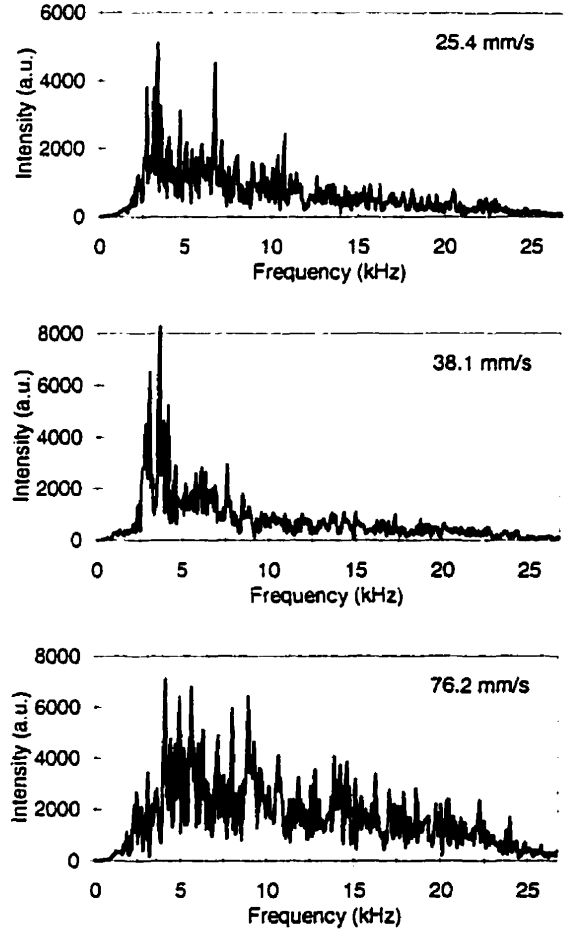


Figure 5.20 FFT spectra of the time derivative of optical emission signals detected by #1 sensor. The spectra are corresponding to that in figure 3.19.

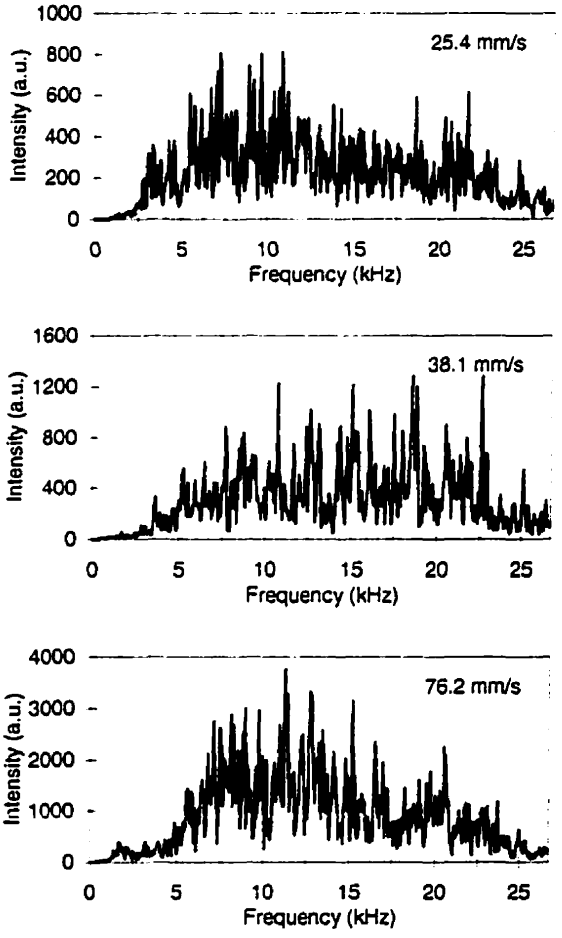


Figure 5.21 FFT spectra of optical emissions from laser welding plume that are detected by #2 sensor. Laser power is 1.7 kW.

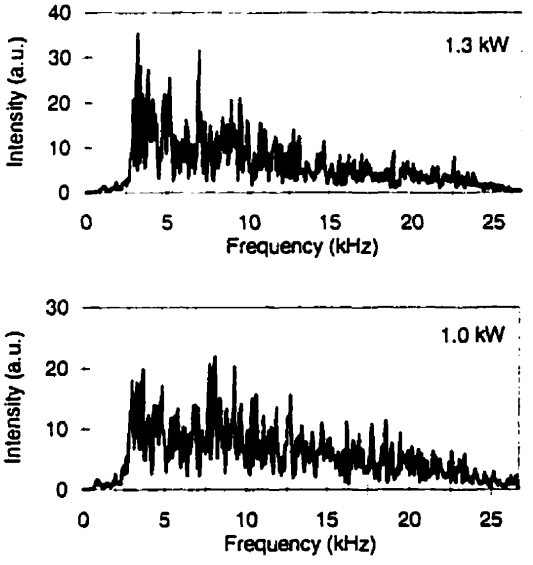


Figure 5.22 FFT spectra of the time derivative of optical signals detected by sensor #1. The welding speed is kept at 38.1 mm/s and the laser power is lowered so that partial penetration welds were produced.

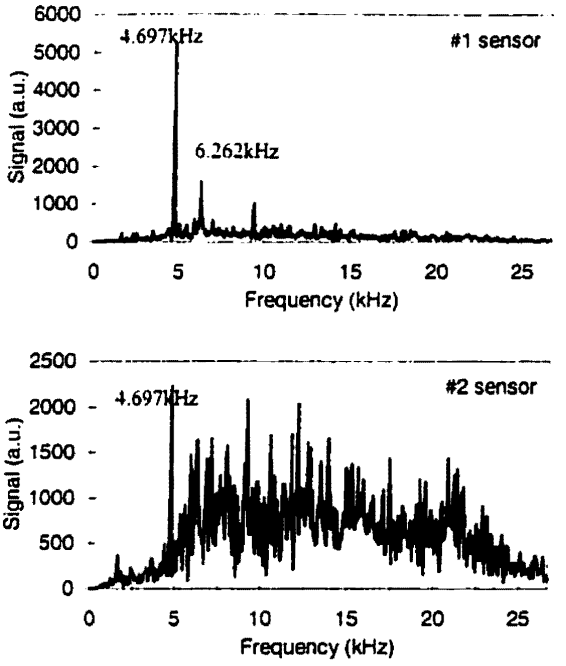


Figure 5.24 FFT spectra of optical signals from modulated laser beam welding at a travel speed of 50.8 mm/s. The averaged laser power is 1.38 kW.

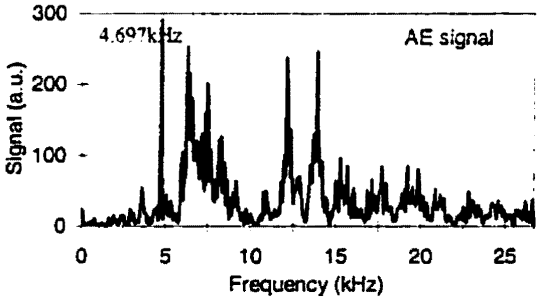


Figure 5.25 FFT spectrum of acoustic emission from modulated laser beam welding. Laser average power is 1.38 kHz and travel speed is 50.8 mm/s.

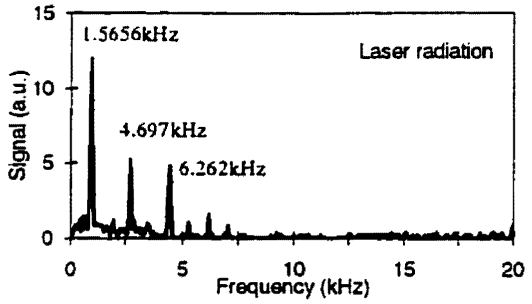


Figure 5.23 FFT spectrum of the modulated laser beam radiation that was sensed by a pyroelectric detector.

The optical emission signal from the keyhole plasma contains spectral components mostly in the low frequency range. However, the FFT frequency distribution of its time derivative extends to a wider range. The time derivative of the optical signals can be related to the density variation of the vapor or plume. For this reason, a degree of correlation exists between the acoustic signal and the time derivative of the optical signal[57].

Imaging into the welding keyhole allows the keyhole oscillation to be directly detected. Under good full penetration welding conditions, an oscillation band of 2 - 5 kHz was observed in our laser welding system. We believe the laser beam shape used for welding could affect the band size and central frequency. And signals from different laser beam welding system will exhibit some difference in the keyhole oscillation frequencies. Expansion of the spectral distribution under partial penetration welding conditions makes this signal a useful indicator of weld quality.

The experimental data presented here indicate that a noticeable difference exists in the FFT spectra of the time derivative of the optical emission signals detected by vertically imaging into the keyhole when the weld shifts from full penetration to partial penetration. Proper use of this kind of signal could provide an effective way of monitoring the laser welding process. Furthermore, in the present system, stable keyhole oscillations in the frequency range between 2 and 5 kHz could be induced during full penetration welding. The variation in optical signal and acoustic signal at high frequencies can be associated with vapor expanding out of the keyhole opening. .

Chapter 6
Implementation of Closed Loop Control

In addition to in-process monitoring, closing the loop to give real-time process control of some welding parameters has the ability to correct or avoid the occurrence of weld fault. This will greatly aid the development of reliable and flexible automated systems.

6.1 Basic concept of feedback control

During a closed loop controlled process, the control system cannot only generate specific commands to manipulate the machine and process actuators, but also has the capability of comparing a desired set of results with actual results and taking corrective action. In this system, proper sensors are required to obtain feedback data on the current state of the process. Fig.6.1 depicts a computer control system. In a control loop, the role of the computer is to collect operating data from sensors in the process, accept desired reference states or the set points from an operator, and close the control loop by establishing manipulation commands that cause specific changes in the process outputs. Usually, the control system performs two basic operations. It calculates the difference or error between the operating point and the set point or error from an equation

$$Error = Set\ point - Actual\ output.$$

And then it determines a corrective action by solving an equation or set of equations that have been established as characterizing a desirable way to control the process. The law

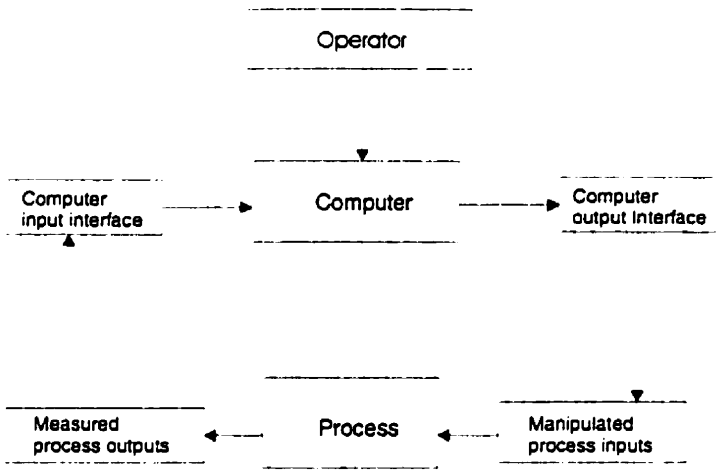


Figure 6.1 Schematic diagram of computer close-loop control.

governing determination of this manipulation can be referred to as the control algorithm. To realize feedback control, the sensing data and the control algorithm are the most important elements in the system.

The main feature of computer feedback control system is its digital operation. The computer operates with specific sets of numbers at discrete points in time. The computer is programmed to sample values of the process output variables at certain instants in time. Calculation then proceeds in such a way as to establish the error and the desired manipulation corresponding to that error, using an appropriate control law or algorithm. The manipulation is then applied to the process. The process outputs are again sampled after a predetermined interval called the sample period, and the procedure is repeated. Clearly, the speed at which the computer can perform many operations relative to the speed at which the process can respond is a significant factor in how well the process can be kept under control. The response time of the sensors and the computing power of the computer limit the sampling rate. Control algorithms can be designed according to specific process and its complexity.

In laser welding, the process is too complex to develop a model to allow a direct estimation of weld quality and there are no governing equations that exist between various sensing signals and processing parameters. The observed parameters have to be correlated to resultant quality using an empirical database for the process. The relations between signals and processing parameters are, therefore, established by knowledge from

experiments. For different welding systems, there exist different correlations between processing parameters and final weld quality.

If the relation between the feedback signal and the processing parameter is well established, a PID (Proportional plus Integral plus Derivative) control action can be used. PID control action combines the effects of each action (proportional to the error, to the time integral of the error, and to the difference of errors) to obtain a composite control manipulation according to the equation[76]

$$\Delta m_n = m_n - m_{n-1} = K_0 e_n + K_1 e_{n-1} + K_2 e_{n-2} \qquad (6.1)$$

where n is the time index, m_n is the process parameter at time index n, e_n is the current error value, e_{n-1} and e_{n-2} are previous errors, K_i's are constants or gains. The gains determine the stability of the system and should be chosen properly.

During laser beam welding, the sensed signals are always fluctuating due to its dynamic nature. The measured errors never will be zero even for a stable welding process. The control action (Eq.6.1), thus, should be modified. In considering the fact that the process parameters for laser beam welding have their operating windows, the welding parameters do not need to be controlled precisely at a specific value for producing good welds. Therefore, quantization of the correction signal is applied.

6.2 Auto focusing system

Focal position is one of the important factors that affects laser weld quality. If the laser spot is not at its optimum focal position, the efficient keyhole-welding regime may be lost, resulting in conduction limited welding or poor penetration through the material. Focus control is especially valuable in operation on non-planar work-pieces, where there is a need for the laser focus to follow the contours of its surface. Focus control will also ease the requirement on the work-piece clamping arrangement. Development of a fast and efficient system for automatic focus position control will expand the use of laser welding techniques.

6.2.1 Laser beam focusing ability and working regime

The dominant parameter in laser welding is the laser intensity. In order to generate sufficiently high intensity to produce deep penetration welds, a laser beam needs to be brought to a tight focus on the work-piece surface. A focusing lens or a spherical or parabolic mirror is usually utilized to focus this beam. The focusability of a laser beam is determined by its spatial profile, or its mode. A laser beam in the fundamental mode has true diffraction limited beam divergence and can be brought to a tight focus by a lens system. High mode laser beams are accompanied by large beam divergence. For a fundamental mode laser beam, a specific distribution of laser intensity exists across the output beam. This is the Gaussian distribution:

$$I(r) = I_0 \exp(-\frac{r^2}{w^2}) \tag{6.2}$$

where w is the radius of the beam at the radial distance for which $I=I_0e^{-1}$. r is a radial coordinate, and I_0 is the intensity at $r=0$. At the focal plane, the beam has a minimum diameter, $2w_0$. The minimum beam radius w_0, called the beamwaist, is directly related to the beam divergence. However, the beam divergence can be changed with a suitable optical system. Thus different sizes of focal spot can be produced using different lens systems.

For a Gaussian beam, the spot size at a position z relative to the position with the beamwaist is

$$w^2(z) = w_0^2[1 + (\frac{\lambda z}{\pi w_0^2})^2] \tag{6.3}$$

The beam divergence angle is

$$\theta = \tan^{-1}(\frac{\lambda}{\pi w_0}) \tag{6.4}$$

After focusing by a lens, the new beam waist is very close to the focal point of the lens. It can be shown[77] that in general the minimum spot size of a Gaussian beam focused by a lens is

$$w_f = \frac{f\lambda}{\pi w_1}[(1 - \frac{f}{R_1})^2 + (\frac{f\lambda}{\pi w_1})^2]^{-1/2} \tag{6.5}$$

where w_l and R_l are the laser beam spot size and radius of curvature at the input face of the lens. If the lens is placed very close to or very far away from the beam waist of the beam being focused, the minimum spot size can be simplified to

$$w_f = f\theta_B \tag{6.6}$$

where θ_B is the beam divergence at the input face of the lens.

In order to focus a laser beam to a small spot, we must use either a lens of very short length or a beam of small divergence. There is a limitation to the reduction in the focal length of the focusing lens. When the focal length does not satisfy $f<<w_0$, w_l, the relatioship in Eq.6.6 no longer holds and the lens ceases to satisfy the definition of a thin lens. However, there are means to obtain a laser beam of small divergence by expanding and recollimation of the beam.

Another important characteristic of a focused beam is the depth of focus. This parameter denotes an estimate of the distance over which the lens-image distance can be varied without a substantial increase in spot size. The depth of focus can be approximated as

$$\delta = \pm\frac{w_f}{\lambda} \tag{6.7}$$

in which the ± sign appears since the depth of focus applies for motions toward and away

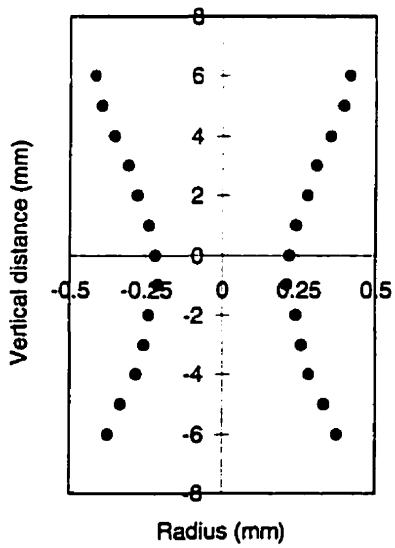


Figure 6.2 Measured spot size of the CO_2 laser beam as a function of vertical distance.

from the lens. If the beam is tightly focused, the depth of focus will be small and this is not an optimal case for many weld applications since the laser intensity varies considerably through the work-piece. In reality, this range for the depth of focus allows production of good welds, which eases the requirements for focal position control.

In our system, the output laser beam has a spatial distribution close to that of a Gaussian beam. Measured beam spot size as a function of vertical distance shift is plotted in Fig.6.2. It can be seen that the spot size has no noticeable change within ±0.5 mm around the focal point.

6.2.2 Dual-view detection technique

As described in chapter 4, the information of spatial distribution of the plasma plume emission can be used to detect the vertical distance shift of the work-piece surface relative to the laser head. This idea forms the basic for the automatic focal position control system. In Fig.6.3, a schematic illustration of the focal position detection system is shown. The optimal focal position can be independently set according to the nature of laser process. For laser welding of sheet materials, the focal point is usually maintained slightly below the work-piece surface for best performance. At the optimal focal position, the dual spots on the surface are adjusted on both sides of the keyhole opening. When the surface moves up, viewing spot #1 shifts close to the hot core and viewing spot #2 moves

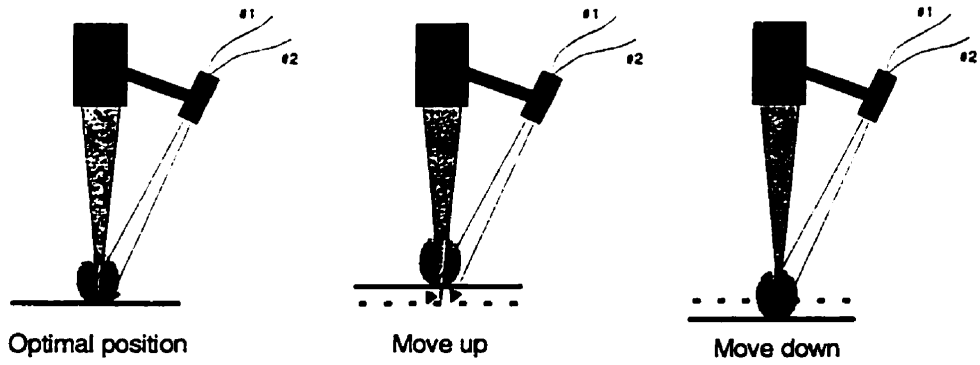


Figure 6.3 A schematic illustration of the focal position detection technique.

away from the hot core. Thus the detected signal from spot #1 increases and signal from spot #2 decreases. In the opposite case when the surface moves down, viewing spot #2 approaches the hot core and viewing spot #1 shifts away from the hot core. As a result, the signal from spot #1 increases and signal from spot #2 decreases. Simply combining these two signals generates an error signal to indicate the focus error.

The optical focusing system for collecting plume emission is a standard focusing device, which consists of two or more lenses. Its function is to image the detection spot onto the entrance of the fibers. The design of the focusing system must consider the mounting distance and the magnification of the focusing lenses.

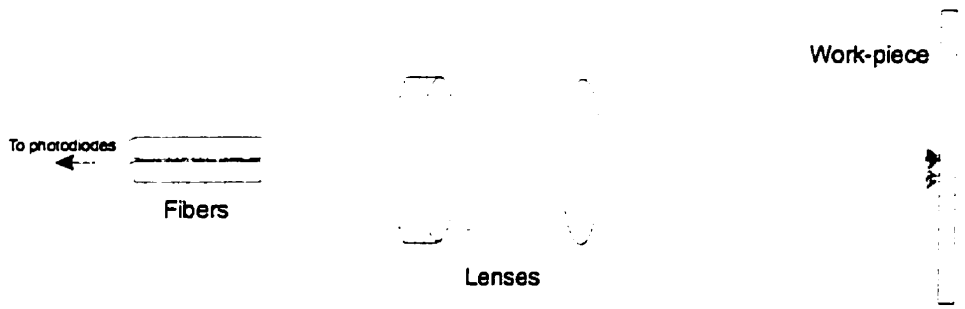


Figure 6.4 Diagram of the light-collection focus system.

The optical fiber is a specially constructed fiber bundle. It is consist of two multi-mode fibers. Fig.6.4 shows the ray diagram of this system. At one end where the fiber is connected to the focusing system, the two fibers are housed in a standard fiber connector with a proper separation between the two fibers, which is compatible with the design of the focusing system. In this structure, a single focusing lens system could focus the two detection spots on the fibers. Light is transmitted independently through each fiber. Using this structured fiber bundle, the separation of the detecting spots on the work-piece surface is about 2 mm. At the other two ends, they are then connected to photodiodes to generate electric signals. Before the light reaches the photodiode, it can be filtered to select the desired wavelength band. Any wavelength band filters can be used for this focus position control system except for infrared light, since the hot melt behind the keyhole emits strong IR and this radiation makes the spatial distribution asymmetrical.

The output from each photodiode is pre-amplified and fed into a multi-channel A/D board in a computer, which calculates the corresponding focus error and adjusts the laser head position. The sampling rate is about 200 Hz. In this work, the converted electric signals from the photodiodes were not filtered with an electronic low-pass filter. Since a low-pass filter could remove significant parts of the high frequency components the signals could be smoothed and this might improve the performance of this system.

6.2.3 Signal response

To investigate the effect of focus error, bead-on-plate welds were made by translating the work-piece beneath the laser head. The work-pieces were flat plates that were tilted at an angle of 4 degrees relative to the traverse direction in order to generate a constantly changing focus error. The zero error or optimal focal position was set in the center of the plate, so that at the beginning of the weld the focal position was above the work-piece surface.

Typical emission signals from the two channels in open-loop tests are plotted in Fig.6.5. These signals were obtained during the production of a bead-on-plate weld across a 1.1 mm thick angled mild steel plate at a traverse speed of 38.1 mm/s at a laser power of 1.6 kW. For this weld, one of the signals decreases monotonically and the other increases continuously over a limited range. These signals were found to be highly repeatable. In addition, the point at which two signals have the same intensity can be adjusted by simply tuning the viewing angle.

Taking the difference of the signals from two fibers then results in an error signal relating to the error in focal position. This error signal is given in Fig.6.6. There is a large region in which the error signal is a linear function of the height, and in the central region close to the optimal focal position, the signal fluctuation is much less than in the outer region. This feature facilitates high-resolution position control.

It is seen that the error signal exhibits a large fluctuation and this fluctuation will affect the resolution of focal position control. However in the optimal focal position region the fluctuation is much smaller than that of larger position deviation, so that focal

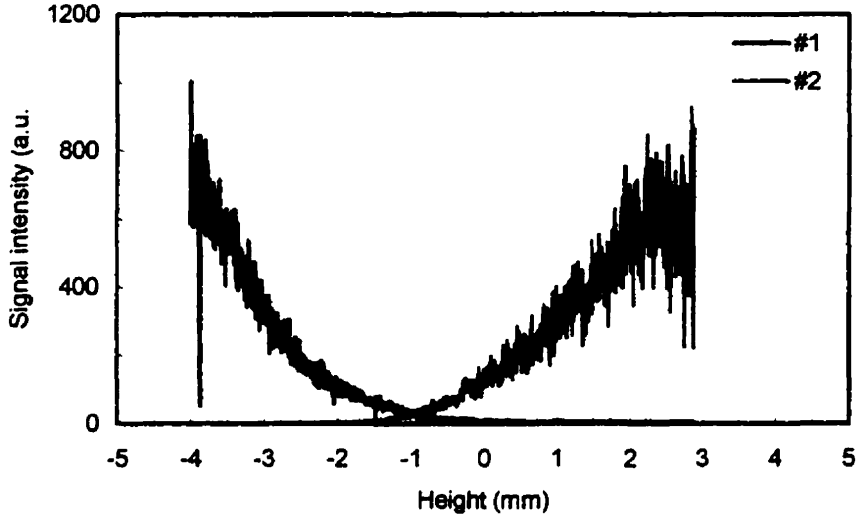


Figure 6.5 Emission signals by two-spot detection during laser welding of a slope surface. Laser power was 1.6 kW and welding speed was 50.8 mm/s. Laser beam moves in horizontal plane.

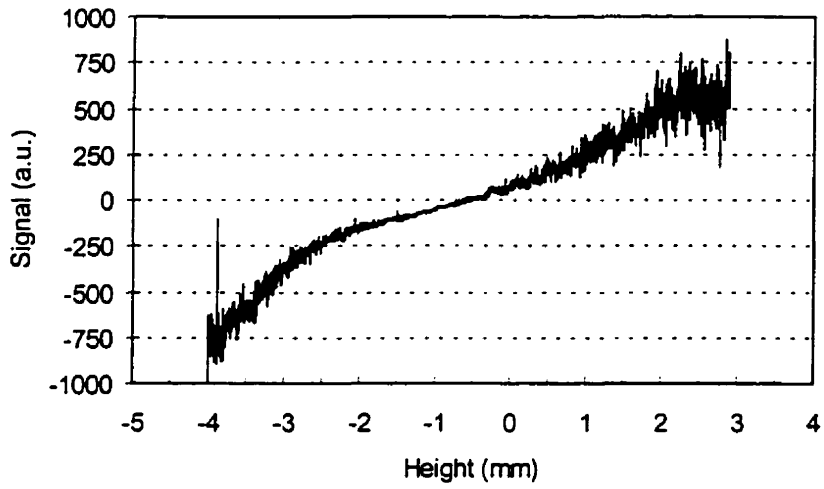


Figure 6.6 Differential signal intensity recorded using the dual-view technique.

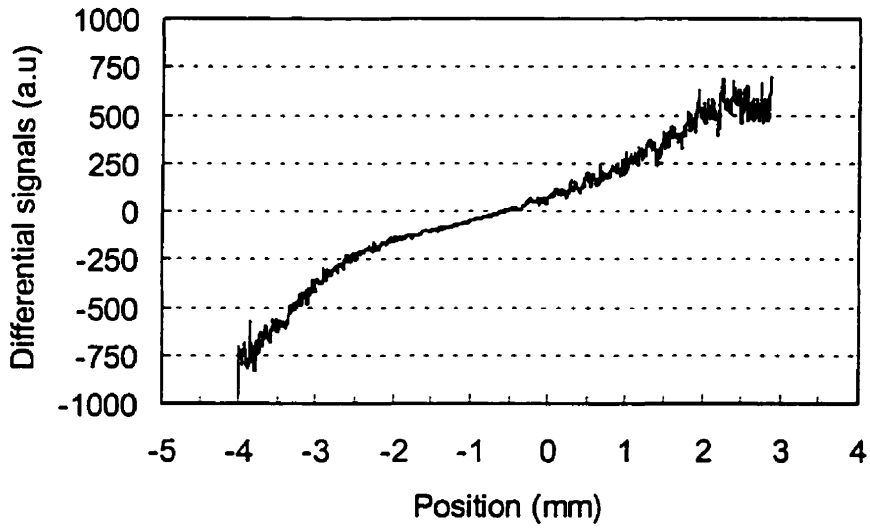


Figure 6.7 Differential signal intensity of that in Fig.6.6 after filtered using running average filtering algorithm.

position can be satisfactorily controlled. Furthermore, after filtering with running average filtering, the signal is greatly smoothed, as shown in Fig.6.7.

The total focal position region controllable by this system depends on the viewing angle and the separation of the two spots on the surface. A small viewing angle with respect to the laser beam will give a larger control range, but the resolution is reduced. In this system, the total control range is about 8 mm. This is quite a significant result compared to other systems[20].

6.2.4 Closed-loop welding

On closing the loop, the control of focus gave excellent welds across the entire plate with a tilted angle for a range of welding speeds. Welds on a surface of a single slope were first successfully tested at various traverse speeds. In the test, a simple proportional algorithm is used. The adjustment in position is proportional to the error signal:

$$\varepsilon = \alpha \cdot \delta I + \beta \tag{6.8}$$

where α *is* a proportional constant, which is dependent on the amplifier setting and fiber structure; β is constant which is determined by the zero focal position error. Both α and β are determined by experiment, while δI is the error signal.

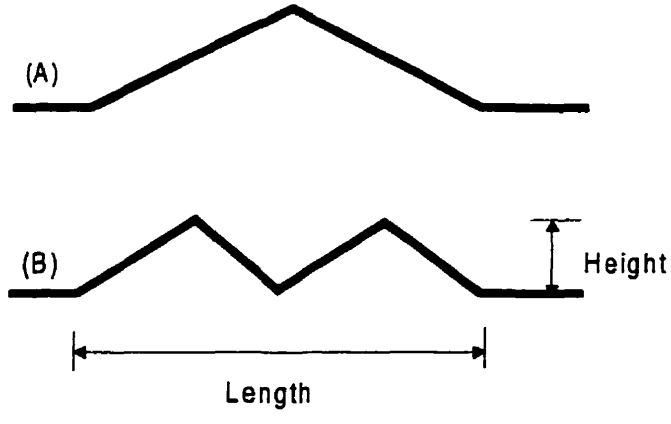


Figure 6.8 Weld contours tested in experiment. (a) Triangular shape, (b) Double-triangular shape.

More complicated tests were carried out by welding along a contoured steel sheet, as shown in Fig.6.8. The first test was on a triangular shape with the peak as high as 15 mm and a horizontal length of 152 mm, while the second test is a double triangular shape with almost the same height and length. For all those samples, excellent welds across the entire weld length were produced. Fig.6.9 presents a photograph of two welds for the first kind of shape. One of the welds was with the control loop open, and the other was with a control loop closed. It is obvious that with the control loop open some portion of the weld loses penetration. But, when the control loop was closed, the entire weld is uniform.

For the second shape (double triangular), the test result was satisfactory and a photograph of this weld with closed loop control is shown in Fig.6.10. Several more welds of this kind of contour were make at different welding speeds, with excellent results.

The range over which focus can be maintained is limited only by the traverse range of the motorized z-axis stroke, provided that there are no sudden jumps in height of more than 8 mm or the focus distance changes at a speed within the capabilities of the z-axis motion. Focus resolution is limited by noise. Since in optical emission signals the oscillation or fluctuation is intrinsic to the welding process itself, the instability due to this noise source is always present. The oscillation spectrum is broad and the main oscillation frequency of the keyhole is in the kHz range. Efficient low-pass filtering could reduce this instability but cannot eliminate it. However, the laser beam has a certain value of focus-of-depth (Eq.6.6) and the focal point change within this range will not actually affect the weld penetration condition. Therefore, focal position control into a certain resolution is enough to produce perfect welds.

6.3 Seam tracking

Seam tracking is the control of the laser spot relative to the seam in order to make a consistent and uniform weld bead.

The multi-spot fiber detection system has the ability to sense the position of the laser irradiation spot across the weld seam. This technique only applies to butt welding of sheet metals of dissimilar gauges. Unlike the vision system which extracts information on

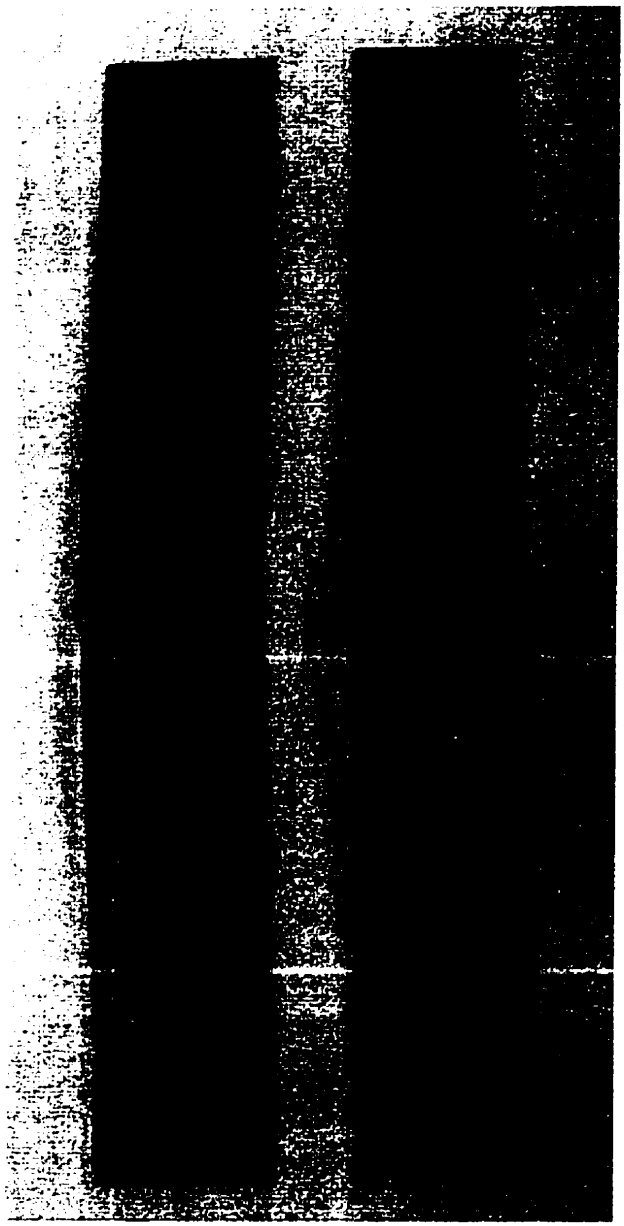
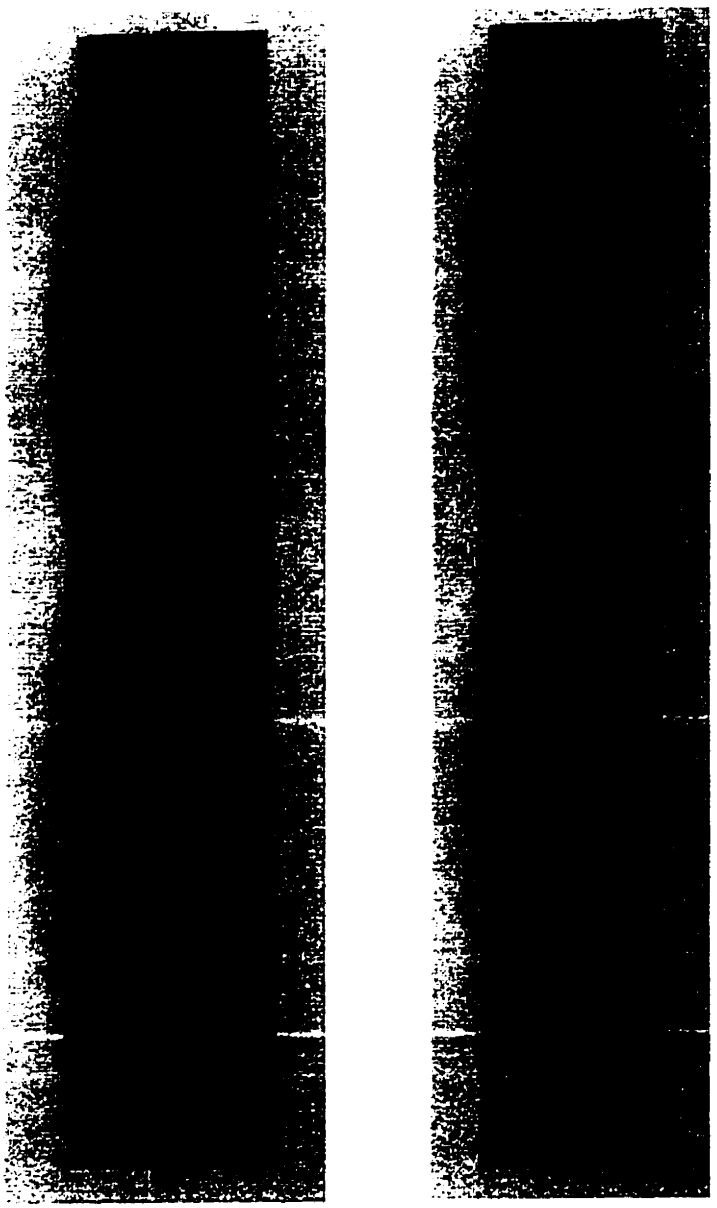


Figure 6.9 Photographs of bead-on-plate welds with and without closed loop focus control.



(a) (b)

Figure 6.10 Photographs of welds that were produced under closed loop control and at two speeds: (a) 63.5 mm/s and (b) 76.2 mm/s.

joint position from images of an externally projected light, the multi-spot fiber detection system senses emission from the welding process.

The main principle relies on the fact that the hot core of the luminescent plume during laser welding will move up or down as the irradiation spot of the laser beam shifts across the seam joint. As shown in Fig.6.11, part of the laser beam is incident on the thick sheet and the other is on the thin sheet. The position of the hot core above the surface is dependent on the percentage of the beam on one of the sheets. In extreme cases, if the entire beam is incident on the thin sheet, the hot core is close to the thin sheet surface. On the other hand, when the entire laser beam is on the thick sheet, the hot core is located on the thick sheet surface. In this case the hot core is high above the thin sheet surface, and during welding, the optimal condition is to keep a little more than half of the beam on the thick sheet side. Metal vapors are generated both from the thin sheet and thick sheet. The hot core is located in the center between the two extreme cases. When there is a deviation from this location, a shift in emission can be detected.

6.3.1 Optical fiber sensing system

The sensing system has a three-spot detection configuration, as shown in Fig.6.12. The optical sensor is mounted behind the laser head, viewing the welding site at an angle of about 30 – 40 degrees with respect to the laser beam. Two of the three spots are aligned along the weld line while the other is on the thin sheet side. The function of two-spot sensing is similar to that of focal position detection, and involves the detection of an up and down motion of the hot core. The third sensor measures the evaporation at the interface between the two sheets during laser irradiation.

If the optical sensing system is mounted on the thin sheet side with a viewing direction perpendicular to the welding direction, the sensitivity will be higher than that of the previous setting. Due to the space limitation this kind of configuration has not been utilized.

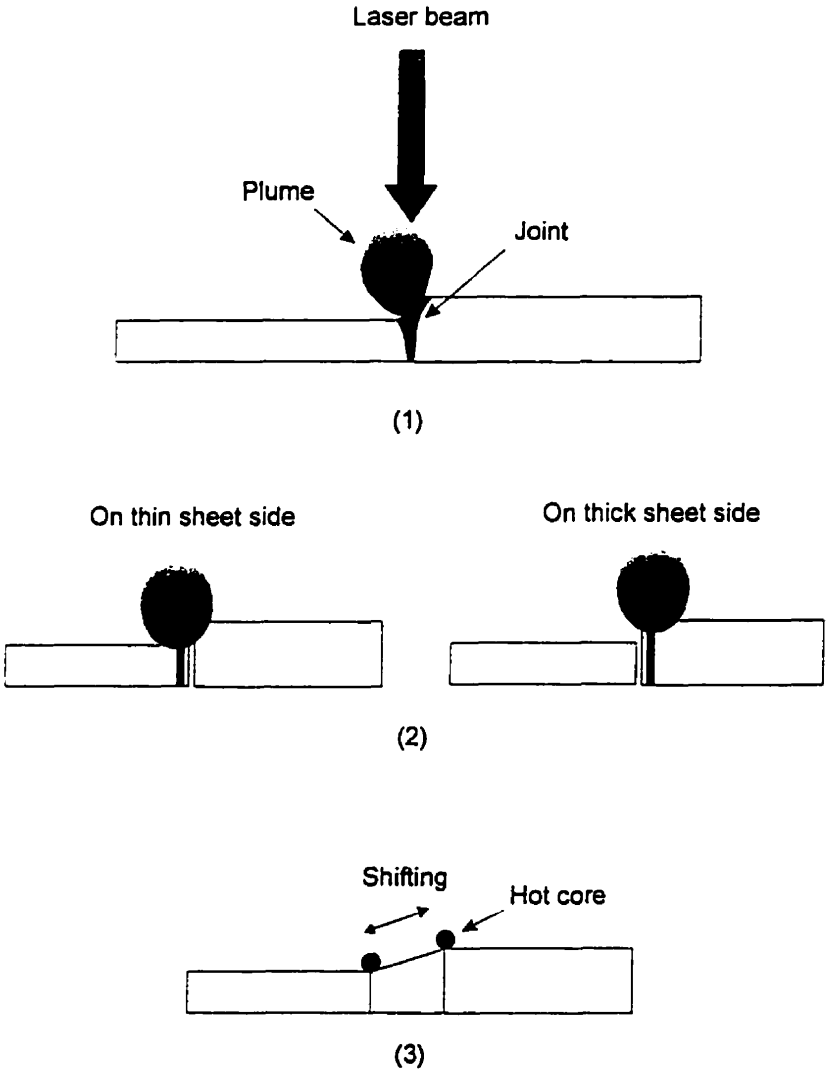


Figure 6.11 Schematic illustration of the relation between the laser spot and the center of the source of emission.

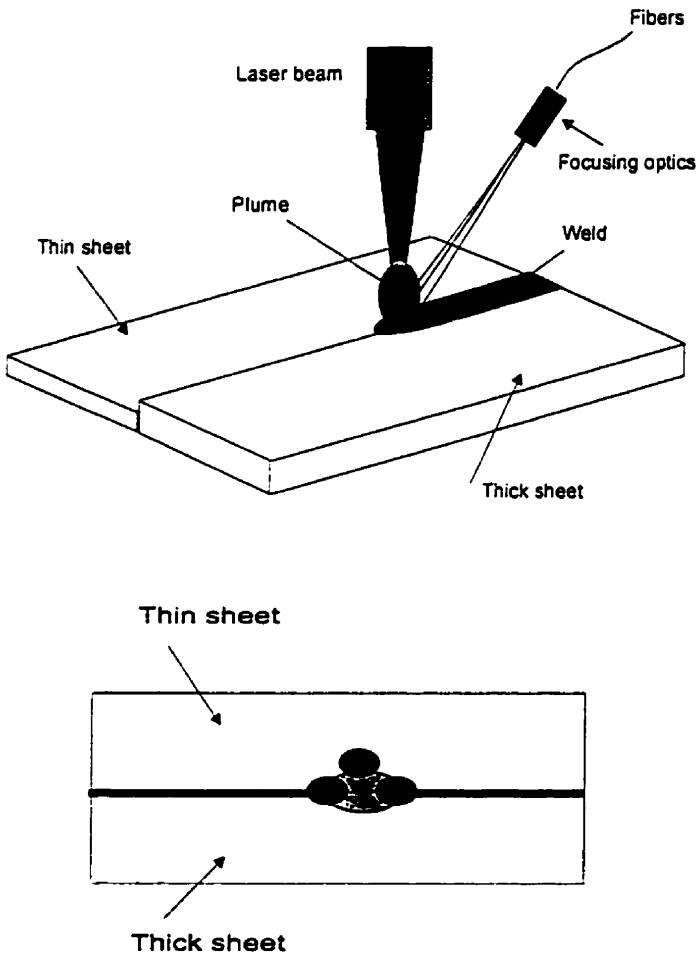


Figure 6.12 Schematic illustration of seam position detection.

6.3.2 Signal response

To test the detection system, butt joints between steel sheets of 0.8 mm and 1.6 mm in thickness were made. In an initial test, welding was carried out along the seam at a constant speed, but after every weld the laser beam was shifted in a direction perpendicular to the seam by a distance of 0.127 mm. The weld started with the beam on the thin sheet. At the end of welding, the beam was on the thick sheet side. A total of nine welds were carried out. Emission from the welding was recorded at a sampling rate of 200 Hz using the three-spot detection technique, and the data were averaged (Fig.6.13). It is clear that there is significant change in the emission signals when the laser beam shifts from one side of the seam to another. It should be noted that relative intensities of the signals are important in description of the beam position change.

For the second test, laser welding was carried out along a tilted seam. In this test, the weld line was purposely aligned to be not parallel to the seam so that at the beginning of the weld the beam spot was on one of the sheets so that the weld ended with the beam

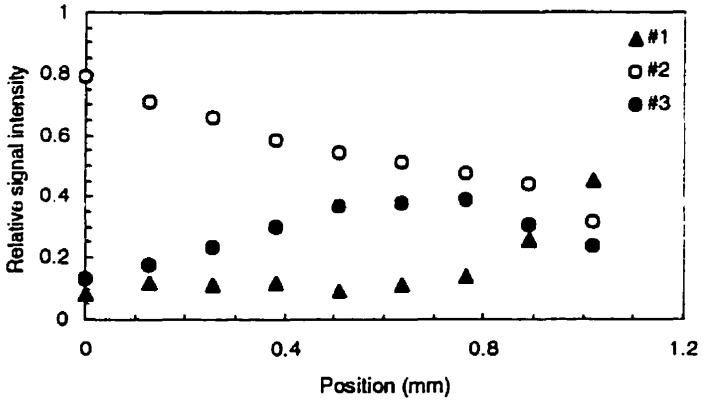
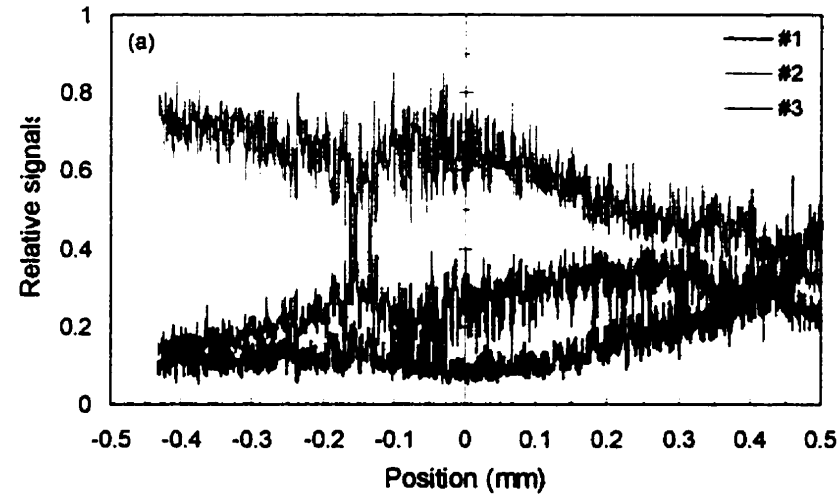


Figure 6.13 Relative optical signals of plume emission recorded using the multi-spot detection technique. Welds of butt joint of different gauge metal sheets were made. The laser beam irradiated spot shifted from the thin sheet side to the thick sheet side.

spot on the other sheet. The beam spot gradually covers the seam during welding. In the middle of the weld process the weld crosses the seam. Emission signals from this process were recorded and are shown in Fig.6.14. These signals represent welding processes in which a laser beam starts at either the thin sheet ending on the thick sheet or starts on the



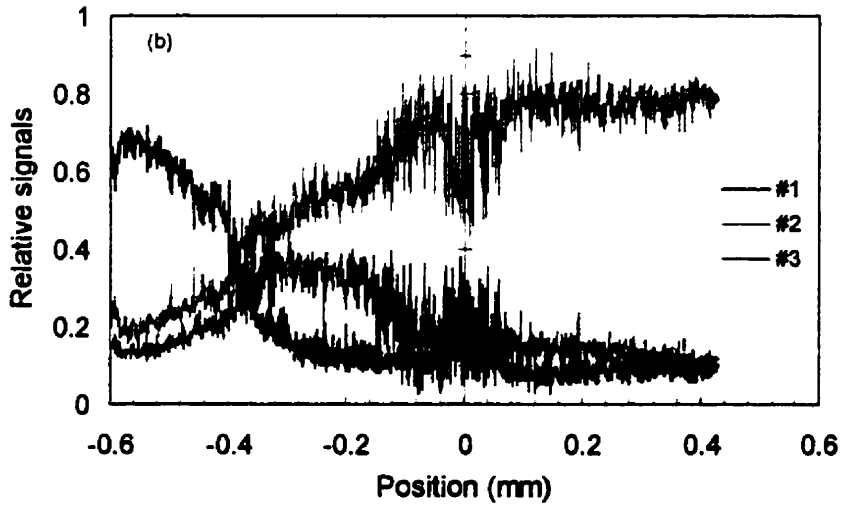


Figure 6.14 Real-time optical emission signals detected using the multi-spot detection technique. Welds were performed on a tilted seam of butt joint of different gauge metal sheets. (a) At the start of weld the laser beam was located on the thin sheet and at the end of weld the beam shifted to the thick sheet. (b) Beam position shift in reverse direction.

thick sheet ending on the thin sheet. Real-time signals reflect the shift from one sheet to other, and can be implemented into a closed loop control.

6.3.3 Linear combiner and position error signal

The output of the sensing system has three individual signals. In order to generate a position error signal, an adaptive linear combiner (a simple neural network called Adaline) is used (Fig.6.15). Its output is a linear combination of its inputs. At time k, this element receives an input signal vector or input pattern vector:

$$\mathbf{x}_k = [x_{0_k}, x_{1_k}, x_{2_k}, \cdots, x_{n_k}]^T \tag{6.9}$$

The components of the input vector are weighted by a set of coefficients, the weight vector:

$$\mathbf{w}_k = [w_{0_k}, w_{1_k}, w_{2_k}, \cdots, w_{n_k}]^T \tag{6.10}$$

The sum of the weighted inputs is then computed, producing a linear output, the inner product $s_k = \mathbf{x}_k^T \mathbf{w}_k$. The components of x_k may be either continuous analog values or binary values. The weights are essentially continuously variable and can take on negative as well as positive values. In a digital implementation, a desired response d_k, a special input, is used to effect learning.

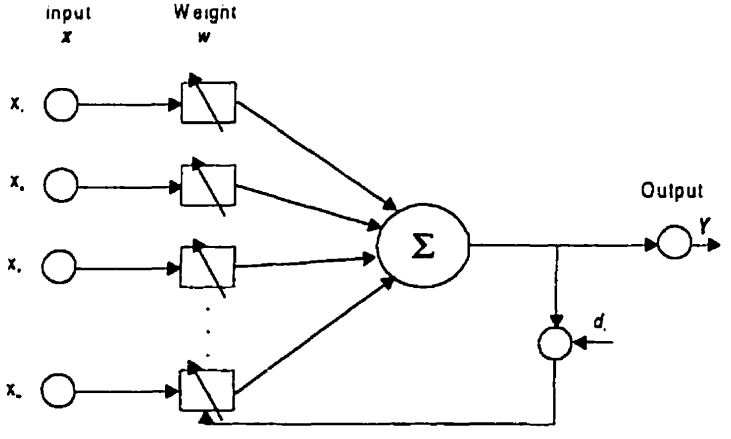


Figure 6.15 Structure of a linear combiner.

During the training process, input patterns and corresponding desired responses are presented to the linear combiner. An adaptation algorithm automatically adjusts the weights so that the output responses to the input patterns will be as close as possible to their respective desired responses. In signal processing applications, the most popular method for adapting the weights is the simple LMS (least mean square) algorithm. This algorithm minimizes the sum of squares of the linear errors over the training set. The minimum mean square error algorithm can, therefore, be employed to extract the output signal from the linear combiner. At the *kth* sample, let input pattern $\boldsymbol{x}_k$ and the associated desired response d_k, which can be determined by the experimental setting or be drawn from a statistically stationary population. The linear error ε_k is defined to be the difference between the desired response d_k and the linear output $s_k = \mathbf{w}_k{}^T\mathbf{x}_k$ during the *kth* presentation:

$$\varepsilon_k = \mathbf{w}_k{}^T\mathbf{x}_k - d_k \tag{6.11}$$

For N input patterns ($k = 1, 2, \ldots, N$), the error equation (6.8) can be written as a vector format:

$$\mathbf{e} = \mathbf{Y}\mathbf{w} - \mathbf{D} \tag{6.12}$$

where

$$\mathbf{e} = \begin{bmatrix} \varepsilon_1 \\ \varepsilon_2 \\ \cdot \\ \cdot \\ \cdot \\ \varepsilon_N \end{bmatrix}, \qquad \mathbf{Y} = \begin{bmatrix} \mathbf{x}_1{}^T \\ \mathbf{x}_2{}^T \\ \cdot \\ \cdot \\ \cdot \\ \mathbf{x}_N{}^T \end{bmatrix}, \qquad \mathbf{D} = \begin{bmatrix} d_1 \\ d_2 \\ \cdot \\ \cdot \\ \cdot \\ d_N \end{bmatrix}$$

$\boldsymbol{Y}$ is an $N \times n$ matrix with the ith sample vector as the ith row, and $\boldsymbol{D}$ is the vector of the desired responses $\{d_i\}$. Usually, the dimension of the input patterns $\boldsymbol{x}_i$ are small compared to the number of input patterns for training. Thus, the minimum squared magnitude of the error vector can be found.

The purpose of training is to find a weight vector $\boldsymbol{w}$ such that the mean square error is minimized. The mean squared error can be expressed as

$$J(\mathbf{w}) = |\mathbf{e}|^2 = |\mathbf{Y}\mathbf{w} - \mathbf{D}|^2 = \sum_{i=1}^{N} (\mathbf{w}^T\mathbf{x}_i - d_i)^2 \tag{6.13}$$

The gradient of the mean square error function is obtained by differentiating Eq.6.10 with respect to the weight vector w:

$$\begin{aligned}\nabla J(\mathbf{w}) &= \frac{\partial}{\partial \mathbf{w}} J(\mathbf{w}) \\ &= \frac{\partial}{\partial \mathbf{w}} \sum_{i=1}^{N} (\mathbf{w}^T \mathbf{x}_i - d_i)^2 \\ &= \sum_{i=1}^{N} 2(\mathbf{w}^T \mathbf{x}_i - d_i)\mathbf{x}_i \\ &= 2\mathbf{Y}^T(\mathbf{Y}\mathbf{w} - \mathbf{D})\end{aligned} \tag{6.14}$$

This is a linear function of the weights. The optimal weight vector is obtained from the minimum error. At a minimum, the gradient is set to zero

$$Min(J(\mathbf{w})) = \nabla J(\mathbf{w}) = 0 \tag{6.15}$$

Therefore, we have

$$\mathbf{Y}^T\mathbf{Y}\mathbf{w} = \mathbf{Y}^T\mathbf{D} \tag{6.16}$$

If the $n \times n$ matrix has an inverse, the solution vector is

$$\mathbf{w} = [\mathbf{Y}^T\mathbf{Y}]^{-1}\mathbf{Y}^T\mathbf{D} \tag{6.17}$$

Defining the vector P as the cross-correlation between the desired response and the x vector then yields

$$\mathbf{P} = \frac{1}{N}\mathbf{Y}^T\mathbf{D} = \frac{1}{N}\sum_{i=1}^{N} d_i\mathbf{x}_i \tag{6.18}$$

The input auto-correlation matrix R is defined in terms of the average over all the samples:

$$\mathbf{R} = \frac{1}{N}\mathbf{Y}^T\mathbf{Y} = \frac{1}{N}\sum_{i=0}^{N} \mathbf{x}_i\mathbf{x}_i^T \tag{6.19}$$

Therefore, the weight vector can be simply expressed as

$$\mathbf{w} = \mathbf{R}^{-1}\mathbf{P} \tag{6.20}$$

For a stationary system, the output signal of the linear combiner is simply $s_k = \mathbf{w}^T\mathbf{x}_k$.

For a dynamic system, the weight vector needs to be adaptively adjusted at a given time k. The Widrow-Hoff delta rule could be applied to the adaption of the linear combiner to the dynamic environment. In this case, the initial weights can be obtained

using the above algorithm by a set of training data. The weights then can be updated using the following algorithm[78]:

$$\mathbf{w}_{k+1} = \mathbf{w}_k + \alpha \frac{\varepsilon_k \mathbf{x}_k}{|\mathbf{x}_k|^2} \tag{6.21}$$

where k is the time index or adaption cycle number, w_{k+1} is the next value of the weight vector, w_k is the present value of the weight vector, and x_k is the present input pattern vector. The present linear error ε_k is defined to be the difference between the desired response d_k and the linear output of the form in Eq.(6.11). It can be shown that after adaptation, the error is reduced by a factor of α as the weights are changed while the input pattern is fixed:

$$\Delta\varepsilon_k = -\alpha\varepsilon_k \tag{6.22}$$

The choice of constant α controls stability and significance of the adaptation. A practical range for α is $0.1<\alpha<1.0$.

For seam tracking, emission signals acquired from a complete welding process along a tilted seam are used to train the linear combiner. The desired outputs are the positions away from the center of the seam, which can be measured after welding. After training, a stationary weight vector is determined. Using the signals in Fig.6.14 as the inputs of a linear combiner, the output signals are shown in Fig.6.16. These output signals are in reality position error signals. Since the signals are close to linear function, a simple PID controller could be constructed for closed loop control.

By applying the running average filtering, a smoother position error signal can be obtained. Fig.6.17 shows the filtered error signals corresponding to the signals in Fig.6.16.

6.3.4 Closed-loop seam tracking experiment

Fig.6.18 shows photographs of welds. These welds were from closed loop seam tracking welding. The straight line weld (Fig.6.18(a)) is a tilted seam weld. It can be seen that the weld is very uniform since the seam tracking continuously corrects the position error. For non-straight line welds (Fig.6.18(b) and (c)), part of the weld is unstable, which

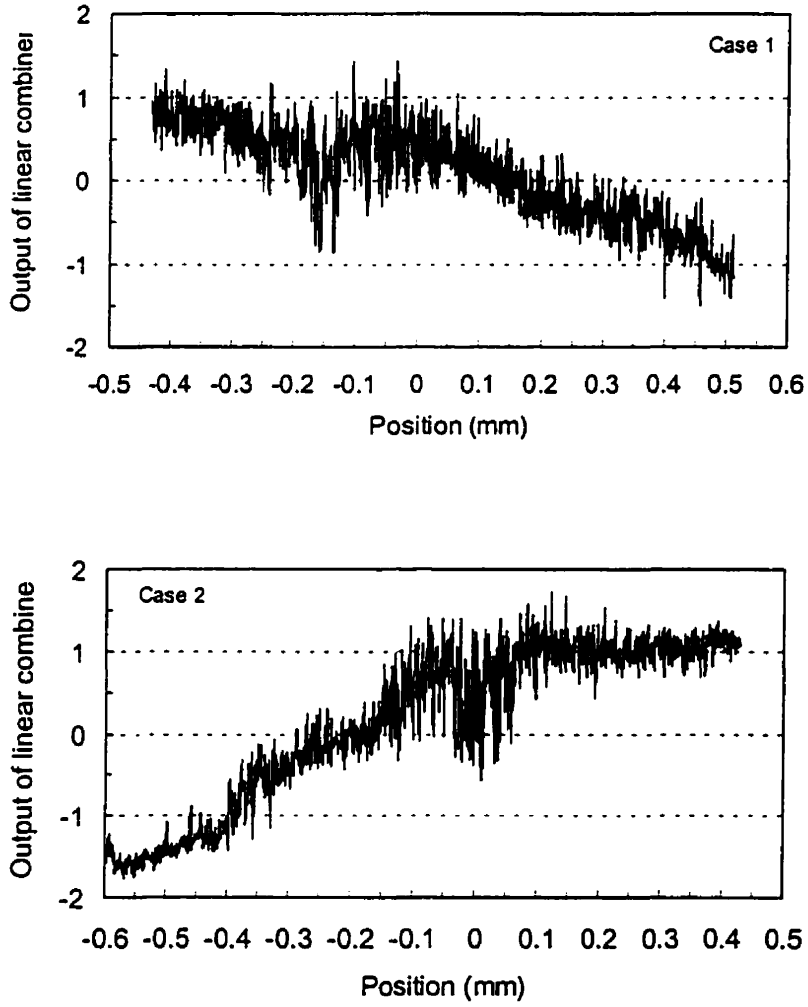


Figure 6.16 Error signals of the beam position off the seam which are the output from a linear combiner. Case 1: from thin to thick; Case 2: from thick to thin.

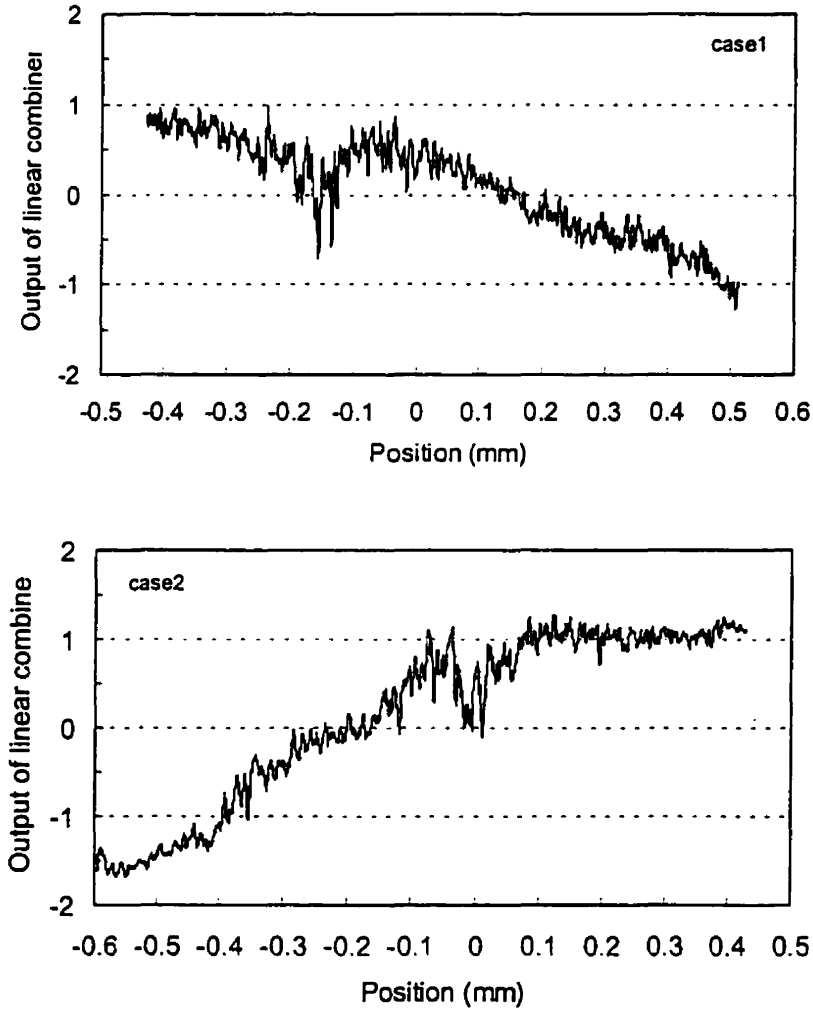


Figure 6.17 Position error signals of those in Fig.6.16 after applying running average filtering.

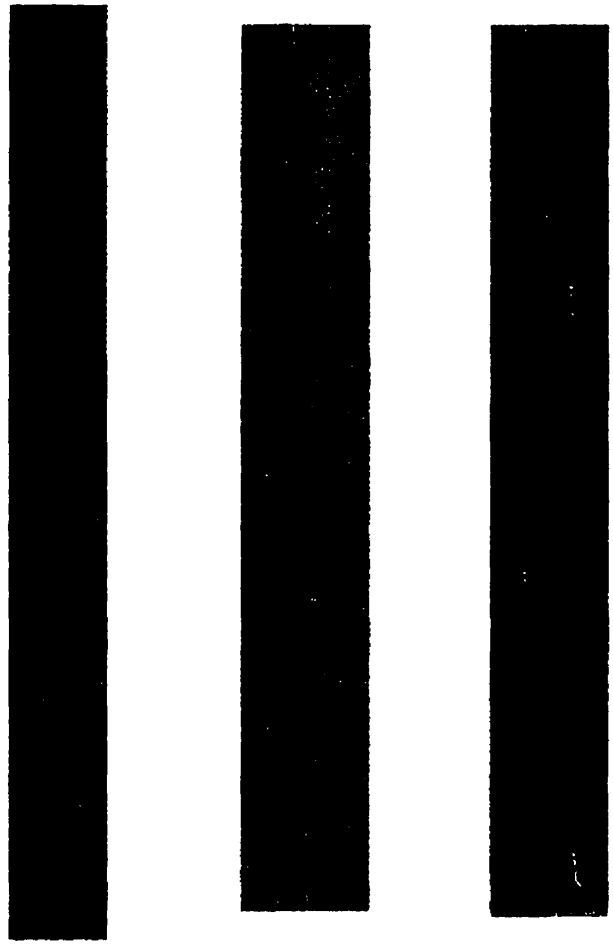


Figure 6.18 Photographs of welds that were made under closed loop seam tracking. (a) A titled straight line joint, (b) and (c) bending seam.

is originated in part from the fluctuation in the emission signals. Since only a simple proportional control algorithm is utilized in this controller, it does not have the capability of uncertainty tolerance. By employing proper signal filtering such as running average filtering, the instability could be improved, but this cannot be eliminated due to the intrinsic fluctuation in the emission signals. Another reason is that for efficient seam tracking one needs to rotate the laser head and the sensor in such a way that the viewing direction is always along the direction of motion. In our system, the laser head and the sensor are fixed.

This sensor is inferior to a vision sensor[79] in that it looks ahead so that it predicts the position change. In addition, in a vison sensor system, an external light source is used to illuminate the joint with a line pattern projected across the seam. The patterns of illuminated lines are then observed by a CCD camera and the seam profile can be obtained by analyzing the image recorded by the CCD camera. The positions of the joint are then extracted from these images. Since information on the seam position is obtained using a stable light source and the illuminated image area, the signal to noise ratio can be relatively high and position control stability is high. However, since the vison sensor system involves image processing sampling rates are relatively low.

In spite of these difficiencies of the seam tracking system developed here, this technique could be satisfactorily used as a monitoring device for identifying the partial penetration caused by the shifting of laser beam towards the thick sheet side. This kind of weld defect can be observed frequently on the production line since the thermal distortion causes the alignment pins to shift.

The performance of the sensing system could be improved by changing the device setup. If the sensor is mounted in such a way that it views the plume from side, the sensitivity will be increased. In addition, for a tilted laser beam welding, the sensitivity is expected to increase.

6.4 Adaptive speed control

If the penetration condition varies during welding, adaptive speed control is needed to maintain a weld with constant overall full penetration and highest possible speed.

6.4.1 Principle of sensing weld penetration

In laser beam welding with constant power, penetration depth can be adjusted using the welding speed. Penetration depth cannot be measured directly in a real time process. However, there are several phenomena relating to different weld penetration conditions. For instance, the spectral distribution of acoustic signals[53] emitted during laser beam welding and plume images[11] recorded by a CCD camera during the welding process contain information indicating weld penetration conditions. These data can, in principle, be incorporated into a control system to achieve adaptive speed control.

There are two key factors that affect the performance of a digital controller: frequency and stability. The frequency (or sampling rate) determines how fast the system responds to the change in process. Stability avoids erratic behavior in real processing control. In addition, the controller should be robust so that it can withstand a harsh production environment. The use of optical emission signals as feedback is an immediate response to the process variation if proper emission signals are detected, since data acquisition and processing with more than mega bytes per second is achievable with commercially available hardware. The cost of the system is very low compared to the CCD camera sensing system. Therefore, observation of optical emission from weld process is ideal in terms of speed and cost.

A combination of multi-radiation signals provides a strong indication of weld penetration. For keyhole welding with a known laser source and sheet thickness, the welding speed directly determines the penetration depth. At low speed, more laser energy is deposited in the material, and accordingly, more material is melted. In the direct interaction region, the material is raised to a higher temperature, resulting in strong

infrared radiation. With an increase in welding speed, less laser power per unit volume is introduced and the IR emission is relatively low. As shown in chapter 4, the IR signal detected from the melt pool is quite different in full and partial penetration welds. It has a high intensity at low speed. On the other hand, the UV radiation from the excited elements in the vapor behaves differently. For full penetration, the keyhole opens at both ends and vapor pressure is relatively low. The plume expands out of the keyhole radially thus it has a large cloud (Fig.4.11). When the bottom opening of the keyhole is closed or the penetration is getting sharrow, the pressure inside the keyhole is relatively higher than for full penetration case. The vapor expands upwards with more directionality. Although the plume size is small, UV radiation will increase slightly due to the high pressure. It will be shown in the following that UV radiation from the plume increases slightly from low to high speed. The combination, therefore, is a good indication of weld penetration.

A multi-spot sensing technique is used for adaptive speed control (Fig.6.19). Four or three spot detection technique can be used and detection spots are imaged on to the weld pool with two spots beside the keyhole and the other in front of and behind the keyhole. Radiations from these spots can be filtered individually with a proper selection of waveband to best reflect the penetration condition.

In order to obtain the relationship between the radiation signals and weld speed, bead-on-plate welds were carried out with changing speed. Optical emission signals were recorded for each welding run. Fig.6.20 shows relative signals recorded by a four-spot detection technique. In one weld, the process speeds up continously from 12.7 to 101.6 mm/s. In the other, the speed decreases from 101.6 to 12.7 mm/s. With this sensing system, infrared radiation is sensed from spot #1. Spots #2 and #3 detect blue and green light, respectively, while UV radiation is obtained from spot #4. From Fig.6.20, it can be seen that the IR and UV signals are dominant. IR intensity decreases significantly with increase of speed, while UV radiation increases with acceleration. Thus, the differential signal between IR and UV signals is a good indication of weld penetration. As given in Fig.6.21, the differential signal decreases monotonically with an increase of weld speed.

Broadband signals using the three-spot detection technique are given in Fig.6.22 with same condition of acceleration and deceleration as in Fig.6.20. The spot #1 and #2 detect the radiation from the weld pool beside the keyhole. The spot #3 senses the plume

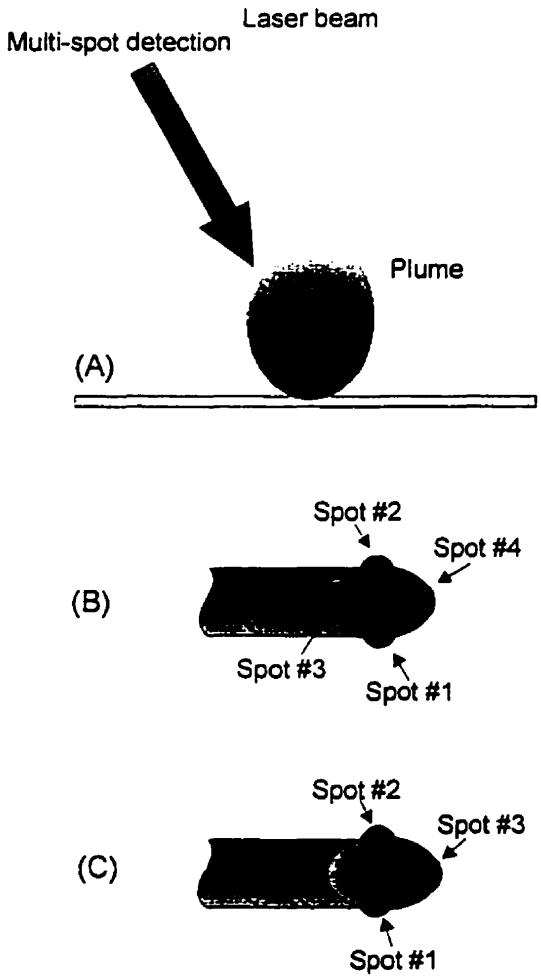


Figure 6.19 Multi-spot detection technique used for adaptive speed control.

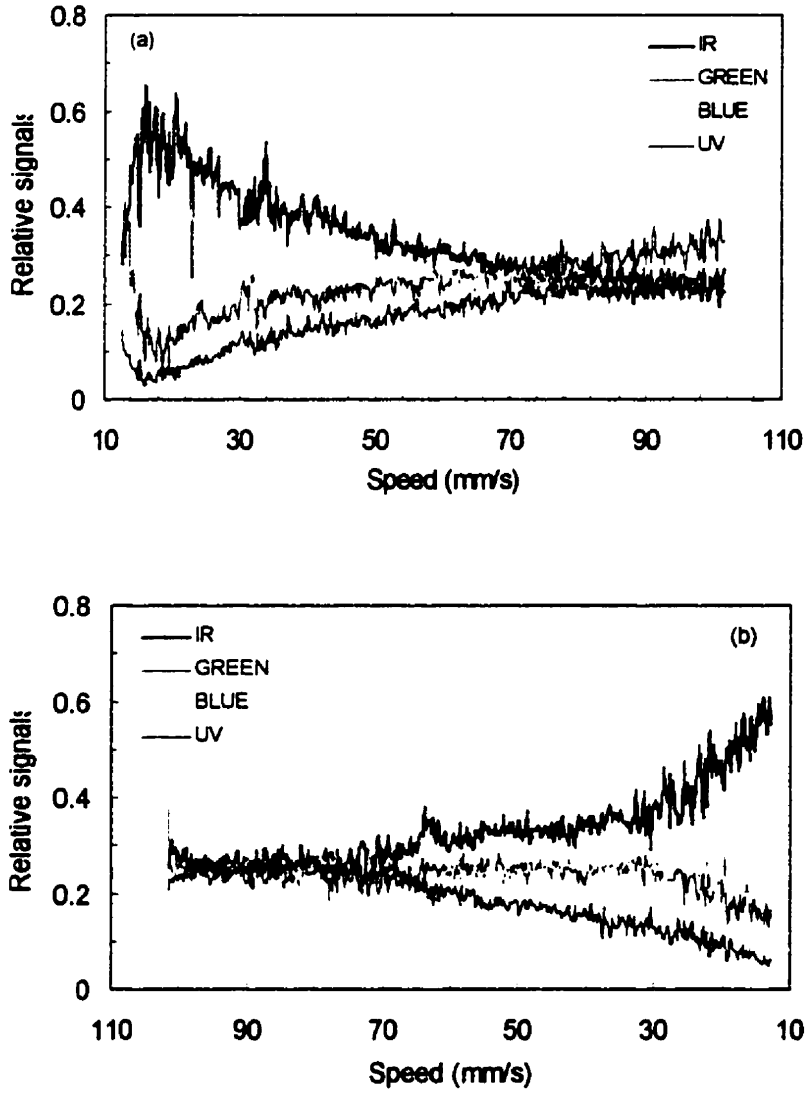


Figure 6.20 Optical signals detected using the multi-spot detection technique during laser beam welding at changing speed: (a) acceleration and (b) deceleration. Laser power was 1.6 kW.

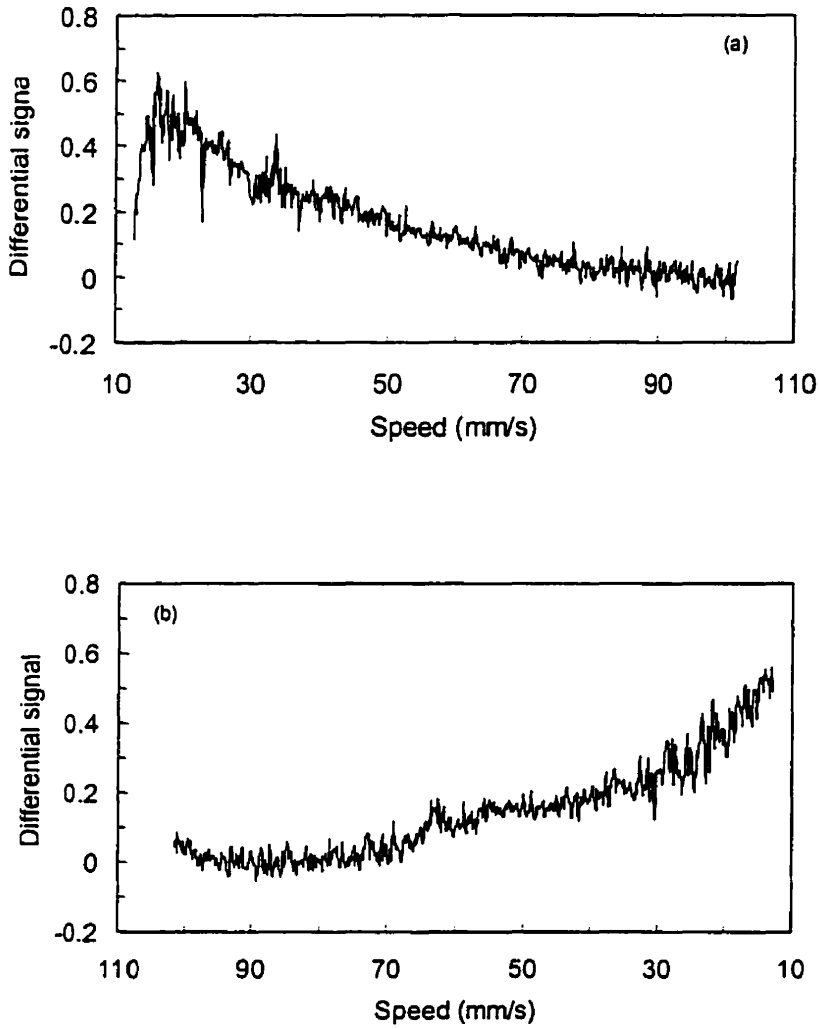


Figure 6.21 The differential signals between IR and UV radiation from Fig.6.20.

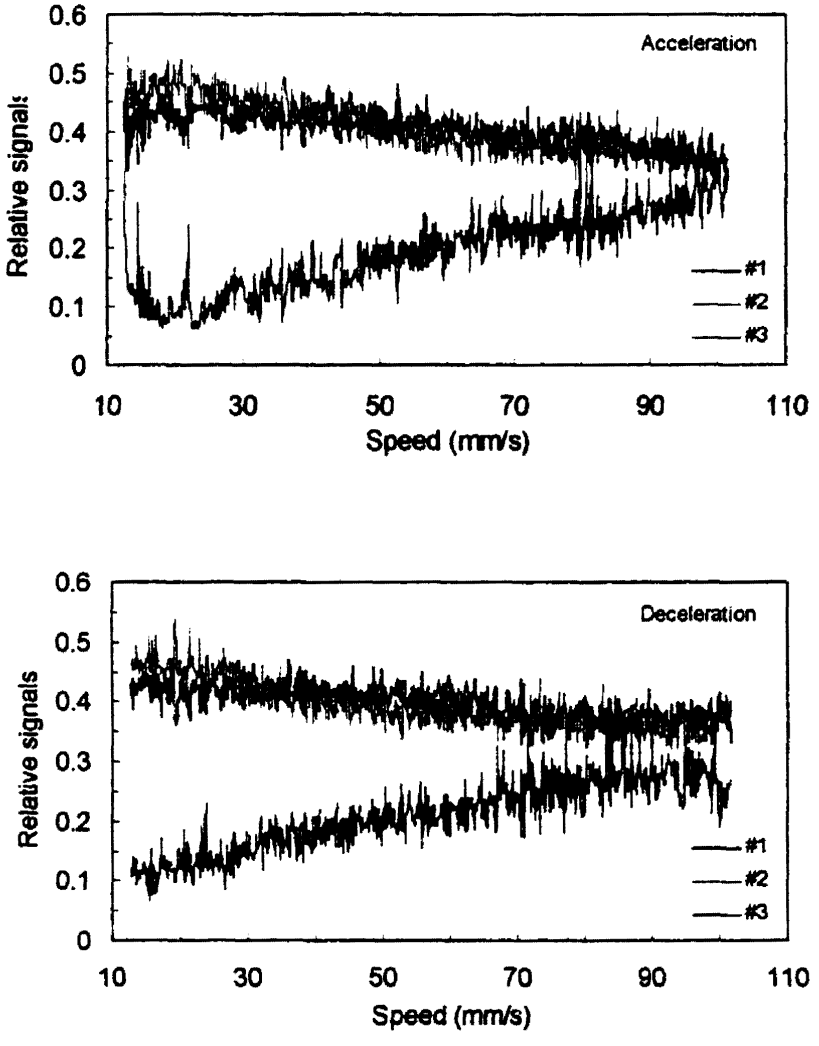


Figure 6.22 Relative signal intensities of plume emission using the three-spot detection technique. All the signals were broad-band light. (a) Acceleration, (b) Deceleration. #1 and #2 spots are beside the weld pool. #3 spot is at the center of weld pool.

emission. These data demonstrate the capability of detection of penetration condition using the multi-spot detection technique.

6.4.2 Closed loop welding with a PID controller

Implementation of adaptive speed control with a PID controller is straightforward using the differential signal as the feedback signal. The relative differential signal has a nearly linear relation with welding speed if there is absence of disturbance. This linear relation can be used as the base of a PID controller. For the purpose of demonstration, a "hard" control action was utilized. In this experiment, welding speed is completely determined by the emission signals:

$$V_t = \alpha(S_d - S_0) + V_0 \tag{6.23}$$

where V_t is command speed, V_0 is the speed according to the set point. S_d is the differential signal, S_0 is the set point of the signal, and α is a proportionality constant. Parameters are determined from experiment. Here, $S_0 = 0.2$ and $\alpha = 63.5$ *(mm/s)*.

Fig.6.23 shows weld speeds during two feedback control welding processes. One process starts at very low speed, while the other starts at high speed. The computer controller is capable of adjusting the welding speed quickly to the set value using the feedback signals, although there are oscillations in the actual speeds. This oscillation stems from the strong fluctuation of emission signals. Therefore, it could be reduced, but cannot be eliminated using this control law.

In pratical welding, this "hard" control action cannot be adopted and continuous speed adjustment is not necessary. For laser beam welding with a specific laser power, there is an operational range of the weld speed within which good welds will be produced. In the control algorithm, we can set a minimum and maximum limit of speed and start run the process at an optimal speed that is known from experience or knowledge base. The feedback signal is only used to modify the speed in case of significant transient process happening. This control method is called "soft" control action.

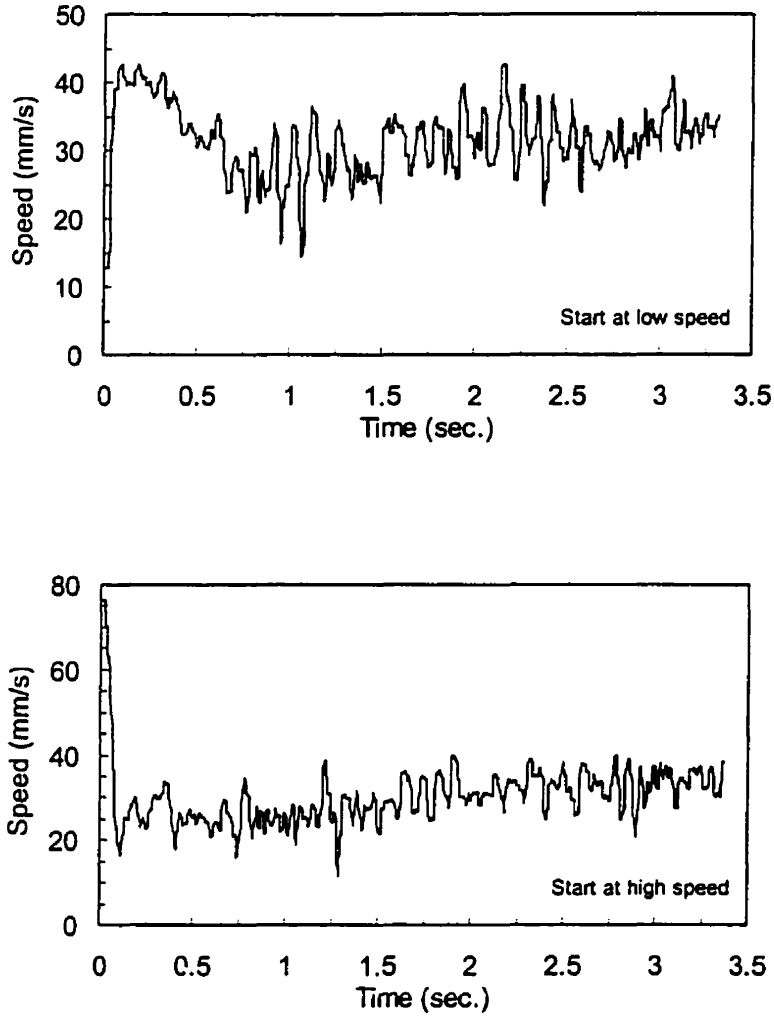


Figure 6.23 Velocity profile of bead-on-plate welding under close-loop control. Laser power was 1.5 kW. Two initial speeds are given: (a) low speed and (b) high speed.

Chapter 7
Improvement of Control Action Using A Neuro-fuzzy Controller

The PID controller works only if one knows the mathematical relation between the control parameter and the feedback signal. In the previous chapter, it has been shown that since the difference of the relative signals between UV and IR from three or four spot detection has a nearly linear function of welding speed, the proportional control algorithm (Eq. 6.21) can be applied to speed control. However, the emission intensity is subject to a continuous variation, and in certain situations this linear relationship may be affected. As an example, during laser welding of a long butt joint, various transient effects such as a slight shift in position of the laser spot on the seam, material defects and thermal deformation can occur. In such cases, the PID controller is unable to handle these disturbances and may not function properly. Using a fuzzy logic controller could improve the performance of this kind of feedback control.

7.1 Structure of rule based fuzzy logic controller

The fuzzy controller embodies concepts necessary to realize control algorithms in the presence of uncertainty. Its structure includes an input interface called the fuzzification module, an output interface (the defuzzification block) and the processing module (the inference engine). The underlying architecture of the fuzzy controller comes

with its rule-based organization. Its key premise is that the available control knowledge can be easily structured into rules linking the current state of the system with the relevant control action.

The fuzzy logic controller (FLC) can be understood as a processing module that maps a system state linguistic input to a control output. This mapping is accomplished by a collection of fuzzy control rules (If-Then rules) which use linguistic variables rather than a complicated dynamic mathematical model. The typical architecture of a FLC is shown in Fig.7.1, which consists of four principal components, as mentioned above: a fuzzifier, a fuzzy rule base, an inference engine, and a defuzzifier. In the fuzzifier, the measured crisp data are transformed to probability values for suitable linguistic states. The inference system works with the predetermined rules to calculate the probability value for the linguistic output states. The inference system has the capability of simulating human decision making by performing approximate reasoning to achieve a desired control strategy. These rules determine the behavior of the controller in the closed loop system. In the fuzzy rule base, it stores the empirical knowledge of the operation of the process of the domain experts. Through the defuzzifier, the linguistic states are transformed to output signals for process control.

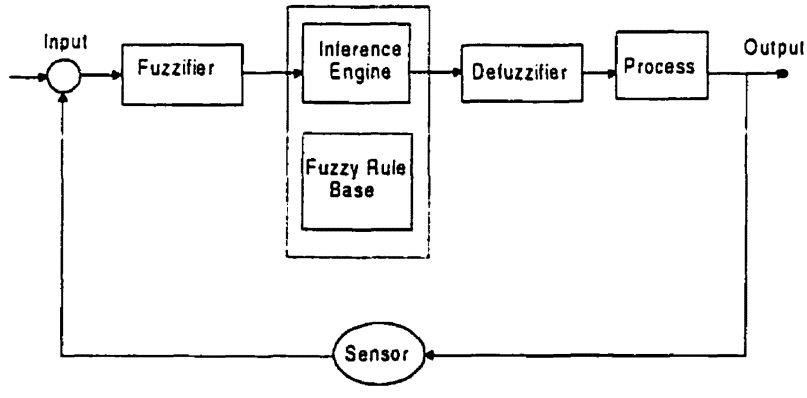


Figure 7.1 Basic architecture of a fuzzy logic controller.

The fuzzifier transforms the measured variables to the linguistic states. This is done by defining membership functions (MF) for each linguistic state. With a membership function the connection between a physical state with respect to a probability of membership to a linguistic state is specified. Proper fuzzy partitioning of

input and output spaces and a correct choice of membership functions play an essential role in achieving a successful FLC design. The number of MFs and their shape varies. More membership functions result in smoother control action, but then it will take longer time to calculate the result. The popular shapes of MFs are triangular, trapezoidal and Bell-shaped functions.

Based on the probabilities of the different linguistic states there are inference rules specifying the desired closed loop behavior. The inference rules are characterized by a collection of fuzzy IF... THEN rules. The IF-part refers to the linguistic input states, and the THEN-part concerns the linguistic output states. The rules are usually drived from the expert's knowledge and from experimental data. The rules include different linguistic expressions in the IF part and at least one linguistic output in the THEN part. The fuzzy logic expressions are combined via fuzzy operators. The fuzzy AND and OR operators are used, in which AND is calculated as the minimum or product, the OR as the maximum of the contributed fuzzy expressions. The output of each rule is a probability for at least one linguistic output variable. To generate an output signal these variables have to be condensed. In the current work, this is done by a max-product operation[80].

The defuzzifier transforms the calculated probabilities of different linguistic outputs to output signals which are required to actuate the control. A defuzzification strategy is aimed at producing a nonfuzzy control action that best represents the possibility distribution of an inferred fuzzy control action. There are many defuzzification methods[80], but the most common one is the center of area (COA) method. The COA strategy generates the center of gravity of the possibility distribution of a control action. If the universe of discourse is continuous, this method yields

$$z_{COA}^{\bullet} = \frac{\int_z \mu_c(z) z dz}{\int_z \mu_c(z) dz} \tag{7.1}$$

where $\mu_c(z)$ represents its membership value in the output fuzzy set C.

The above described fuzzy inference system is Mamdani's method[80]. Another fuzzy reasoning method is Sugeno type, in which the consequent of a rule is a function of input linguistic variables. For instance, assume the controller has two fuzzy control rules as follows:

R^1: IF x is A_1 AND y is B_1, THEN z is $f_1(x, y)$

R^2: IF x is A_2 AND y is B_2, THEN z is $f_2(x, y)$

When the input variables x and y are x_0 and y_0, the inferred values of the control action from the first and second rules are $\alpha_1 f_1(x_0, y_0)$ and $\alpha_2 f_2(x_0, y_0)$, respectively. Consequently, a final control action is given by

$$z_0 = \frac{\alpha_1 f_1(x_0, y_0) + \alpha_2 f_2(x_0, y_0)}{\alpha_1 + \alpha_2} \tag{7.2}$$

where α_1 and α_2 are firing strengths of the first and second rules which are expressed as $\alpha_1 = \mu_{A_1}(x_0) \cdot \mu_{B_1}(y_0)$ and $\alpha_2 = \mu_{A_2}(x_0) \cdot \mu_{B_2}(y_0)$, where $\mu_{A_1}(x_0)$ *et al.* are the membership value and indicate the degrees of partial match between the user-supplied data and the data in the fuzzy rule base.

For complex systems (high nonlinearity), construction of membership functions and selection of control rules are difficult. Usually, the parameters of the membership functions need to be tuned properly to yield satisfactory control action. Neural networks can be used in learning or tuning membership functions and fuzzy rules of fuzzy system. This system is called neuro-fuzzy controller (NFC), which provides fuzzy systems with automatic tuning abilities. In this system, neural network learning techniques can susbtantially reduce development time and cost while improving the performance of fuzzy systems.

An ANFIS (adaptive network-based inference system) neural fuzzy controller can be used in control of laser beam welding. An ANFIS neuro-fuzzy system uses the network nodes to represent the functions of fuzzy logic. Consider the parameter learning of NFCs with fuzzy logic rules whose consequents are fuzzy singletons. The fuzzy logic rules are in the following form:

R^j: IF x_1 is A_1^j AND x_2 is A_2^j AND ... AND x_n is A_n^j, THEN y is w_j,

where x_i is an input variable, y is the output variable, A_i^j are linguistic terms of the precondition part with membership functions $\mu_{A_i^j}(x_i)$, w_j is a real number of the consequent part, $j=1, 2, ..., M$ and $i=1, 2, ..., n$. When product inference and a centroid defuzzifier are used, the final output y_{cd} of this system is calculated by

$$y_{cd} = \frac{\sum_{j=1}^{M} \mu_j w_j}{\sum_{j=1}^{M} \mu_j} = \sum_{j=1}^{M} \bar{\mu}_j w_j \tag{7.3}$$

where

$$\mu_j = \mu_{A_1^j}(x_1)\mu_{A_2^j}(x_2)\cdots\mu_{A_n^j}(x_n) \tag{7.4}$$

and

$$\bar{\mu}_j = \frac{\mu_j}{\sum_{j=1}^{M} \mu_j} \tag{7.5}$$

μ_j are firing strengths of R^j and $\bar{\mu}_j$ are normalized firing strengths. The ANFIS architechture of a two-input and one-output system is shown in Fig.7.2, where node functions in the same layers are of the type described below[80].

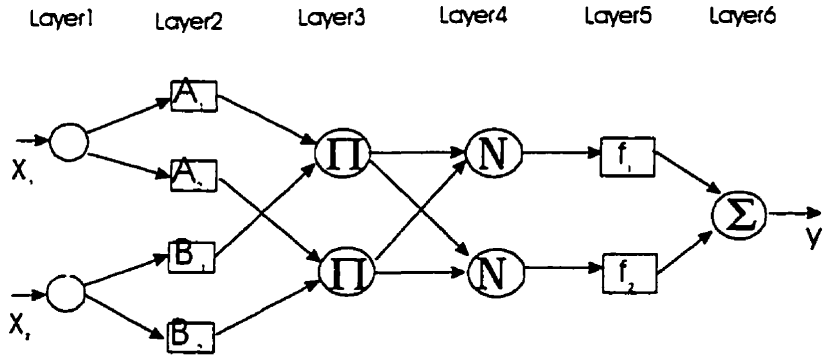


Figure 7.2 Architechture of an ANFIS fuzzy controller.

Nodes in layer 1 are input nodes that simply pass external signals to the next layer. Nodes in layer 2 act as membership functions $\mu_{A_i^j}(x_i)$, and their outputs specify the degree to which the given x_i satisfies the quantifier A_i^j. Here Gaussian membership functions $\mu_{A_i^j}(x_i, a_i^j, b_i^j) = \exp[-\frac{(x_i - a_i^j)^2}{2(b_i^j)^2}]$ are used, in which a_i^j and b_i^j are parameters of the functions to be tuned. Each node in layer 3 multiplies the incoming signals (Eq.7.4) and sends the product out, which represents the firing strength of a rule. Each node in layer 4 calculates the normalized firing strength (Eq.7.5) of a rule. In layer

5, each node calculates the weighted consequent value $\bar{\mu}_j w_j$. Parameters in this layer are referred to as consequent parameters. The node in layer 6 sums all incoming signals to obtain the final inferred result for the whole system.

The back-propagation algorithm of the deepest descent method is used during training for membership function parameter tuning. Assume that y_d is the desired output for an input set (x_i). The objective function to be minimized is defined as

$$E = \frac{1}{2}(y_{ca} - y_d)^2 \tag{7.6}$$

The learning rule for tuning the parameters can be derived as follows:

$$a_i^j(t+1) = a_i^j(t) - \eta_a \frac{\partial E}{\partial a_i^j} \tag{7.7}$$

$$b_i^j(t+1) = b_i^j(t) - \eta_b \frac{\partial E}{\partial b_i^j} \tag{7.8}$$

$$w_j(t+1) = w_j(t) - \eta_w \frac{\partial E}{\partial w_j} \tag{7.9}$$

where the derivatives can be written as

$$\frac{\partial E}{\partial a_i^j} = (y_{ca} - y_d)\frac{(w_j - y_{ca})}{\sum_{j=1}^{M}\mu_j}\frac{\partial \mu_j}{\partial a_i^j} \tag{7.10}$$

$$\frac{\partial E}{\partial b_i^j} = (y_{ca} - y_d)\frac{(w_j - y_{ca})}{\sum_{j=1}^{M}\mu_j}\frac{\partial \mu_j}{\partial b_i^j} \tag{7.11}$$

$$\frac{\partial E}{\partial w_j} = \frac{\mu_j}{\sum_{j=1}^{M}\mu_j}(y_{ca} - y_d) \tag{7.12}$$

Eqs.(7.7 - 7.9) are the update rules for tuning the parameters a_i^j, b_i^j and w_j of membership functions. η_a, η_b and η_w are learning rates for the each parameter, respectively.

For implemetatiing FLC in laser welding, input values to the system are emission signals collected using the multi-spot detection technique. The signals are pre-processed to estabilish an array which could include total emission intensity, differential relative

intensity and change of total intensity. The total emission intensity indicates the soundness of the welding process. If the intensity is too low, the beam may not be properly coupled into the material, while if the intensity is higher than the usual level a drift in beam position may be occurring. The differential relative intensity relates to the penetration depth, beam position, etc. The intensity change reflects the stability of the welding process. A supervisory fuzzy logic controller can be used to assign the control task to specific controller of the next step to determine individual control action. The fuzzy if-then rules for these signals are then articulated by an expert from their experience. Through the design of membership functions consisting of a set of fuzzy set values, each input signal has a certain value which is correlated to a linguistic value. With these signals, the controller is capable of adjusting the welding speed to maintain a constant penetration when the emission is within the correct intensity range. When transient processes occur, the controller will first try to correct the process for example through a change in beam position, then to maintain the satisfactory penetration condition. In the following, a fuzzy logic controller and a hybrid neural fuzzy controller is designed to implement control of welding speed and beam position.

7.2 A fuzzy logic controller for welding speed control

A PD-like fuzzy logic controller can be designed to control welding speed. In this controller, two crisp input variables are required: the sensed signal and the rate of change in the signal. The sensed signal is the difference of the relative optical signals from two channels. The output variable is the adjustment of speed.

Fig.7.3 shows a block diagram of the basic structure of the controller. In the fuzzification step, the signal (S) and the rate of change in the signal (ΔS) are transformed into fuzzy variables through fuzzy membership functions. The membership functions determine the conditional instructions to be initialized so that they allow choosing the most effective control actions. The system performances will be affected by the shapes and the number of membership functions. As seen in chapter 4, the statistical distribution of optical emission signals are Bell-shaped functions. For this reason, Gaussian membership functions are constructed for the optical signal input and trapezoidal

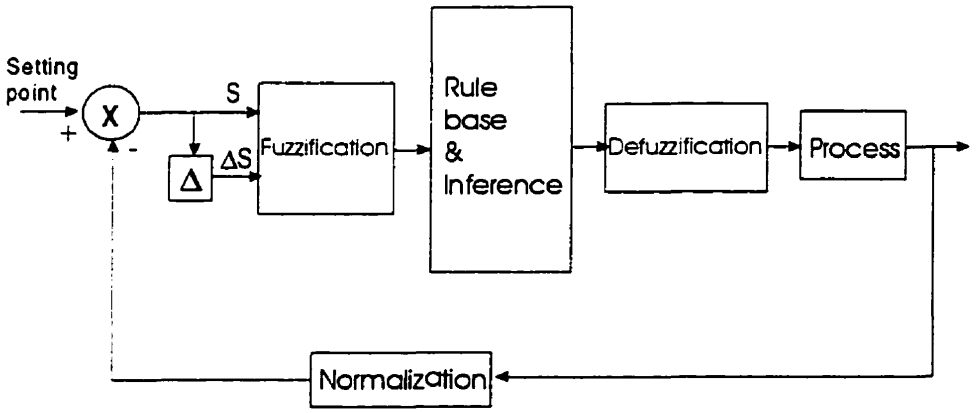


Figure 7.3 Block diagram of a PD-like fuzzy logic controller for welding speed control.

functions are used for the rate of change in these signals. Output membership functions are triangular and trapezoidal. The use of the trapezoidal function for the 'no change' membership permits the controller to allow input variable variation within the operating window.

Membership functions for this speed control system are shown in Fig.7.4. A linguistic value has been attributed to every level of the input signal in the following way: NL is negative large, NS negative small, AZ approximately zero, PS positive small and PL positive large. The linguistic variables for change of signal are positive (P), negative (N) and zero (Z).

In the fuzzification process, the input data is applied to the input membership functions to determine the degree to which S and ΔS is, for example, positive and either big or small. The values resulting from the fuzzification process correspond to the antecedents in the rule base which are then ANDed together using product function to form the strength of the rule. This strength is then applied to each of the rule outputs. If an output has already been assigned a rule strength during the current inference pass, a maximum function is used to determine which strength should apply. The defuzzification process completes the mapping from the input fuzzy sets to the output fuzzy set of weld speed values. The center-of-area method is used here to evaluate the defuzzification to produce a control action.

The collection of control rules is one of the most important steps in construction of a fuzzy logic controller. Since the final feedback is quasi-linear with welding speed,

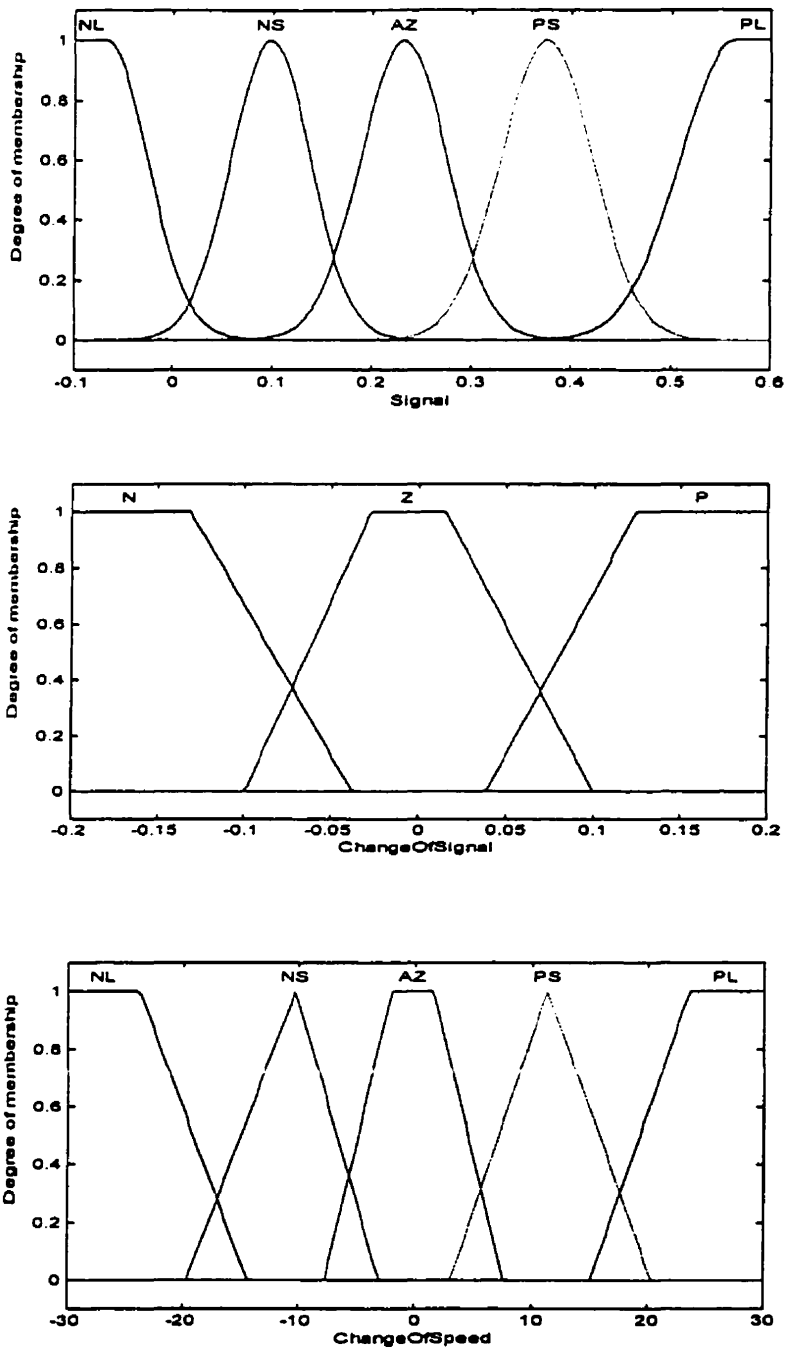


Figure 7.4 Input and output membership functions of a fuzzy logic controller for speed adjustment.

extracting rules is not very difficult. Some of the most obvious rules can be rationalized in the following manner. When good penetration is achieved, no change in welding speed should occur. During welding of good penetration conditions, the corresponding signal S has been given the linguistic value of AZ. If the fluctuation is small (Z), then the steady state (no change) rule is

If S is AZ and ΔS is Z, then ΔV is NC.

When the welding speed is too fast or poor beam coupling happens due to gap or change of material surface finish, poor weld penetration is occurring or about to occur and correction in weld speed is required. In this case, the signal S is small (negative large or small) and ΔS may be also zero, thus the rule is written as

If S is NL and ΔS is zero, then ΔV is NL.

In the same way, the complete set of linguistic control rules can be extracted from welding experience and the characteristics of the optical signals. The rules are listed in Table 7.1. With these rules and the membership functions, the control surface of this FLC can be constructed, which is plotted in Fig.7.5.

ΔS \ S	NL	NS	AZ	PS	PL
N	NS	NC	NC	PS	PL
Z	NL	NS	NC	PS	PL
P	NL	NS	NC	NC	PS

Table 7.1 Control rules of a fuzzy logic controller for welding speed control.

To simulate the performance of the controller, the experimental data in Fig.6.21 were fed into the system to evaluate the output (control action). Fig.7.6 gives the corresponding control action. It can be seen that there is good linear response of the control action to the feedback signals. In the optimal welding regime, very little adjustment incurs.

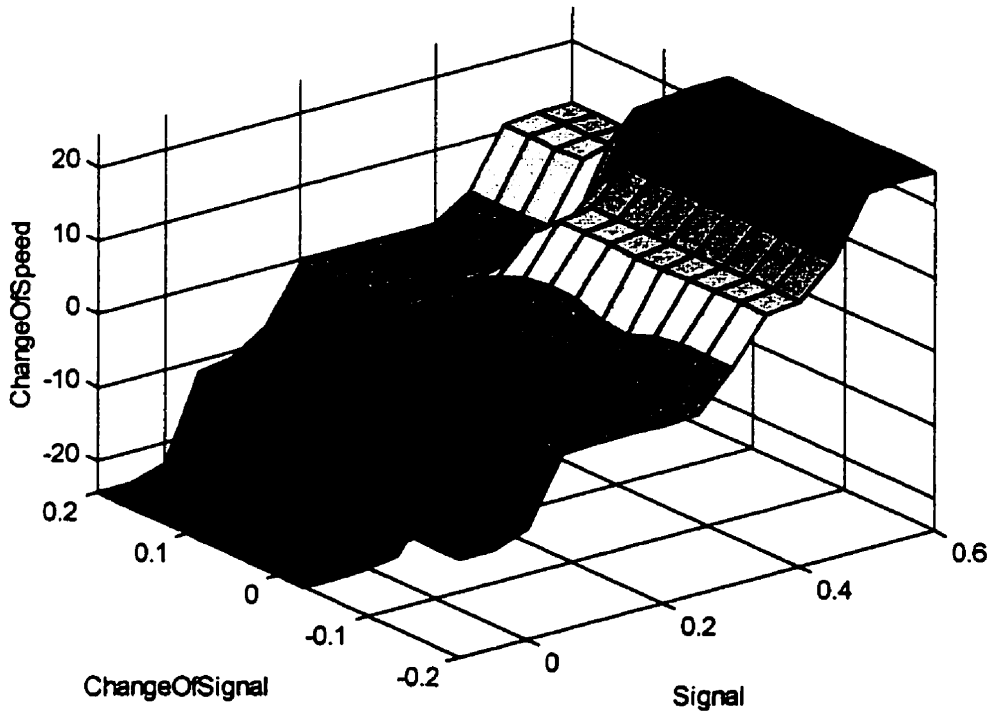


Figure 7.5 Control surface of the fuzzy logic controller for welding speed.

When a conventional PID controller is used, the overall control action is represented by Eq.6.21 and is plotted in Fig.7.7. This control action is similar to the fuzzy logic controller, but the fuzzy controller has a better performance than this one in the range of high speed. In addition, when the process is in a steady state, the fluctuation of the emission will cause the PID controller to adjust the process around the set point significantly, while the FLC will keep the process more steady since the fuzzification of the rate of change in signal will eliminate small fluctuations.

7.3 A hybrid neuro-fuzzy controller for seam tracking

In order to ease the burden of constructing proper membership functions and control rules for multi-input signals/data, a hybrid neural fuzzy system is proposed to first map the multi-input data into data in one-dimensional space and then to construct an ANFIS for the mapped data. The basic structure of the hybrid neural fuzzy system is shown in Fig.7.8. In this system, an Adaline based network is used to achieve three-to-one mapping. The output signal from the Adaline and its rate of change are used as the inputs to the ANFIS fuzzy controller. The rate of change in signal is obtained by taking the difference of the signal and the delayed signal (signal of previous time step). Inclusion of this signal can improve the stability of the control action in order to account for fluctuations in optical signals. This system is designed for sensing with multiple input signals such as seam tracking in butt welding of different thickness sheets, in which three signals are used to indicate shift in beam position. This hybrid neuro-fuzzy system needs two-step training. The first step is to train the Adaline to obtain the weight matrix and the second step is to train the ANFIS to get proper membership functions.

For training the Adaline, raw optical signals and the corresponding desired beam positions are presented to this network. An adaptation algorithm (LSM algorithm described in Chapter 6) is used to adjust the weight elements so that the output from this network is as close as possible to the desired values.

The next step is to construct the membership functions in the ANFIS fuzzy controller. To train the ANFIS is to adjust the parameters of the membership functions. In the ANFIS, the functions of fuzzy logic are represented using network nodes. Since the

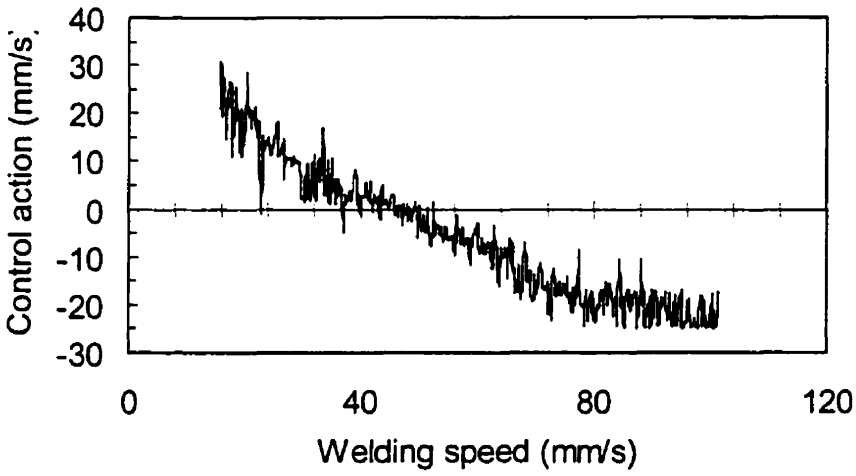


Figure 7.6 Control action of the fuzzy logic controller for speed adjustment when optical signals are presented to the system.

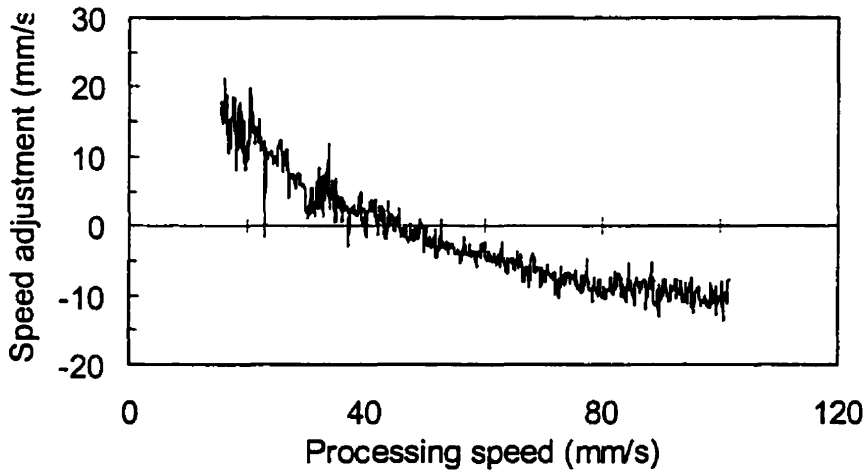


Figure 7.7 Control action incurred from a proportional controller in response to the input differential optical signal.

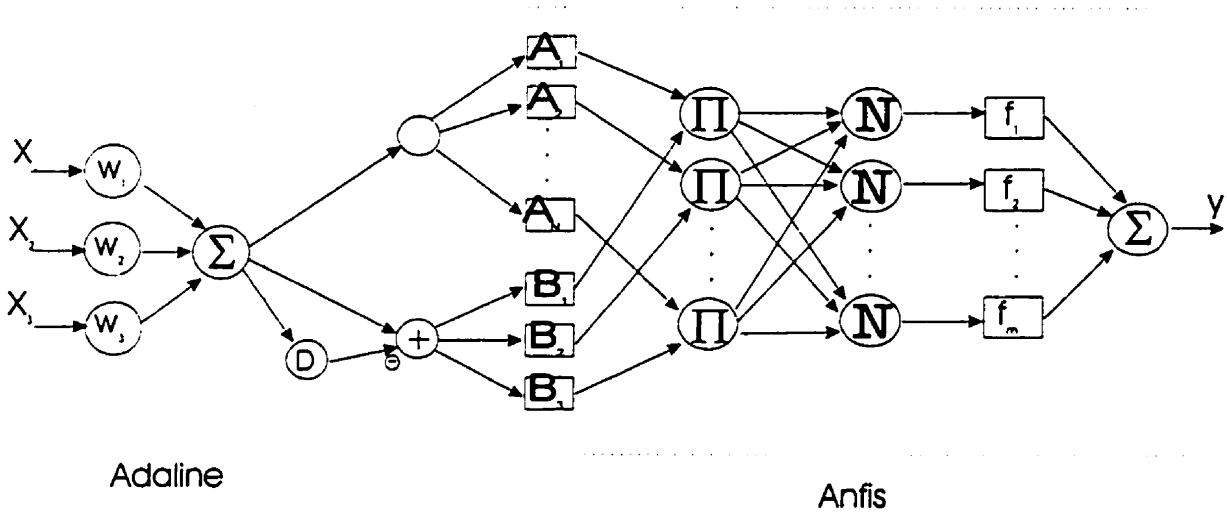


Figure 7.8 Basic structure of a hybrid neural fuzzy control system for seam tracking during laser beam welding.

output from the Adaline is a monotonic function of the beam position, initial membership functions can be constructed in Fig.7.9, in which Gaussian membership functions are used for inputs of optical signals and trapezoidal membership functions are used for rates

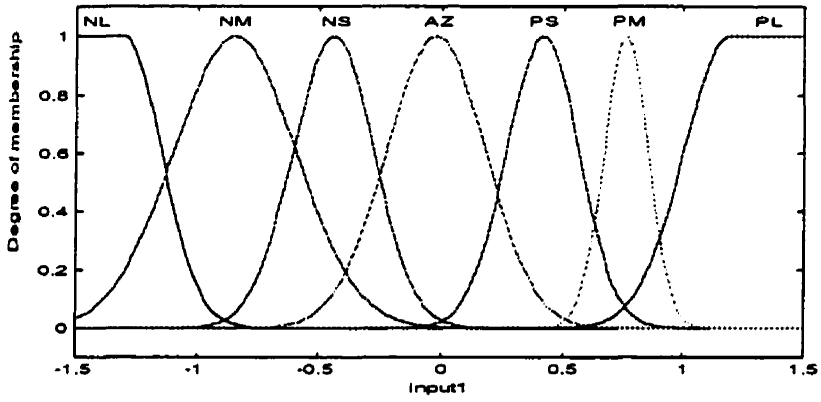


Figure 7.9 Initial membership functions of the optical signal from the Adaline, which are constructed for the input of ANFIS controller.

of signal change. From the output of the Adaline (Fig.6.17), it is known that if the input signal is large and the rate of signal change is small then the beam position should move a little to negative direction, that is, to the thin sheet side. So the control rule can be stated as

IF S is positive small AND ΔS is zero, THEN Δd is negative small (NS).

When the signal is positive small and the rate of signal change is positive, the signal

ΔS \ S	NL	NM	NS	AZ	PS	PM	PL
N	PM	PS	NC	NC	NS	NM	NL
Z	PL	PM	PS	NC	NS	NM	NL
P	PL	PM	PS	NC	NC	NS	NM

Table 7.2 Control rules of the fuzzy controller in a hybrid neuro-fuzzy system for seam tracking.

change may caused by fluctuation rather than a shift in real position. In this case, the beam position should not move. Thus, a complete set of control rules can be established (Table 7.2). In this table, linguistic values have been attributed to all levels of input signal in the following way:

NL Negative large

NM Negative medium

NS Negative small

AZ Approximately zero

PS Positive small

PM Positive medium

PL Positive large

The same concepts are applied to a shift in beam position. However, for the rate of signal change, only three levels are used, which are as follows:

N Negative

Z Zero

P Positive

Based on the update rules (Eqs.7.7-7.12), tuning of the parameters of membership functions in the premise part and consequent part can be performed separately, that is,

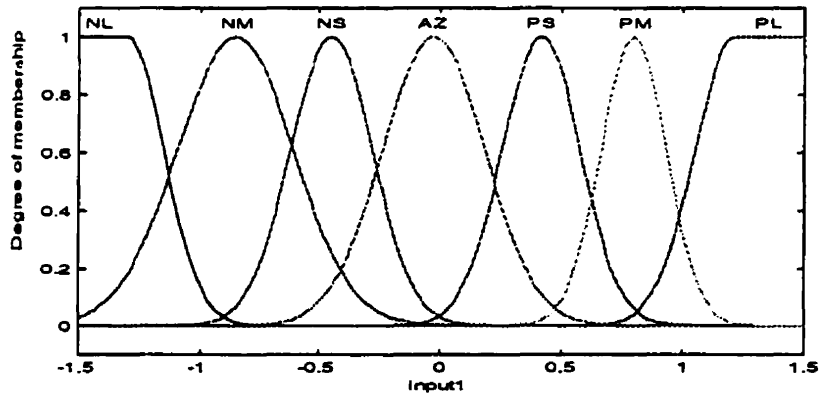


Figure 7.10 Membership functions of figure 7.9 after parameter adjustment through a training process with the experimental data.

each time value w_i and parameters of a_i and b_i are adjusted in different steps. The tuning process is repeated until that the change of the objective function (Eq.7.6) is less than a desired threshold value with respect to its value in the previous step.

In reality, the training process only takes a few epochs. In the current case, about 10 sets of training data were selected from the output of the Adaline. The entire training process runs 8 – 10 epochs. After training, the membership functions of the input signal are shown in Fig.7.10 and the constants of the consequent part in a Sugeno inference system are given in Table 7.3.

Symbol	Values
PL	0.4987
PM	0.3084
PS	0.1672
NC	0.0485
NS	-0.1625
NM	-0.2532
NL	-0.483

Table 7.3 Constants of the consequent part in a Sugeno inference system after trained.

The performance of this hybrid neuro-fuzzy controller can be simulated. In doing so, a set of experimental data (Fig.6.14) is input to the system and the outputs from the controller are the proper control action. Since this set of experimental data represent a linear shift in beam position from one side of the seam to the other, the satisfactory control action should have an approximately linear response. In Fig.7.11, the simulated control action is presented. As is seen in this figure, the control action is very satisfactory. In a range around the set point, adjustment of the controller is proportional to the desired position shift. The set point is adjustable by selecting proper training data or by tuning the membership function manually.

With properly trained input membership functions, a Mamdani's inference system[80] can be used for the fuzzy controller part in this hybrid neuro-fuzzy system. The membership functions in Fig.7.12 are constructed for the consequent part. The same control rules as the above Sugeno system are used. The performance of the controller is

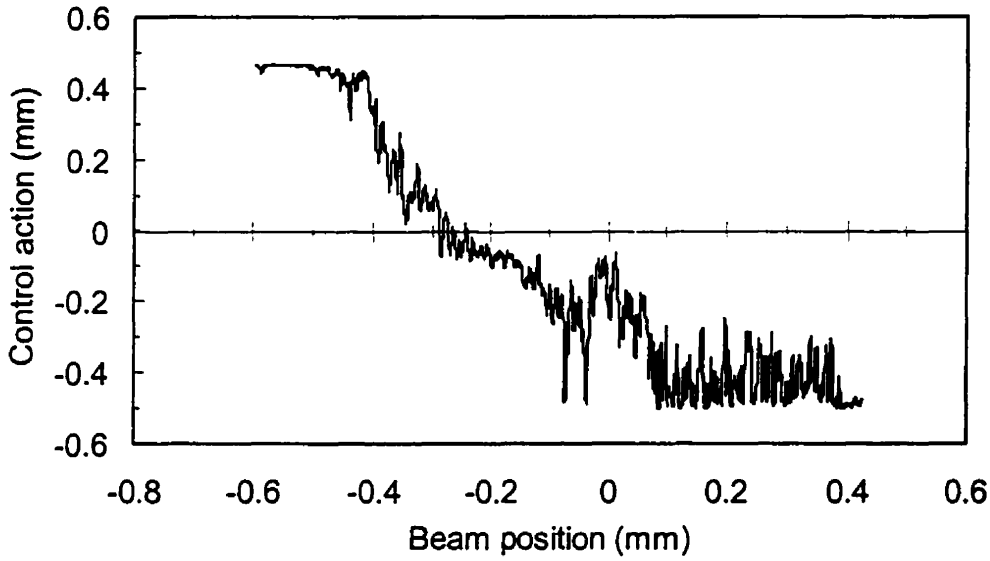


Figure 7.11 Control action of the hybrid neural fuzzy controller when the three optical emission signals are presented to the system.

tested by using the same experimental data and the result is given in Fig.7.13. From the simulation, it can be seen that satisfactory control action is reached by this system.

When implementing the fuzzy control system into a closed loop control of seam tracking, an improvement of the control system performance can be expected.

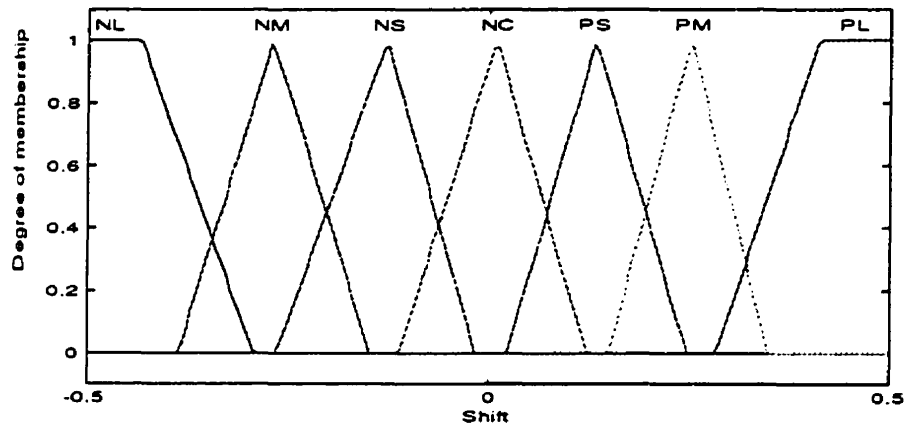


Figure 7.12 Membership functions of the consequent part of a Mamdani type fuzzy controller for seam tracking in the hybrid neuro-fuzzy system.

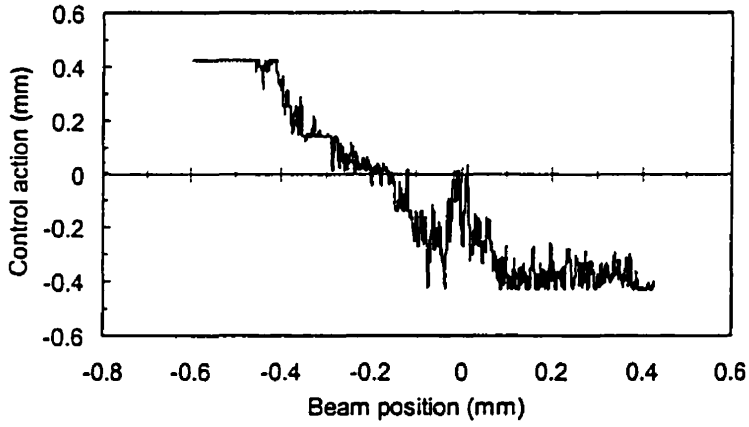


Figure 7.13 Control action of the Mamdani type fuzzy controller in the hybrid neuro-fuzzy system when three optical signals are fed into the system.

Chapter 8

Discussion and Conclusion

In-process weld quality monitoring and adaptive process control during laser beam welding is not straightforward. This is because the quality of laser welds cannot be directly measured in the process. Welds of good quality are those that have a proper weld nugget or shape and are free from defects such as bubbles and pinholes. Most of the defects can only be seen through post-process inspection. However, defects or bad welds are usually produced when improper laser beam interaction with materials occurs. Poor beam-material interaction during laser welding may be caused by defects in or on the material, a shift of the welding spot, variations in laser beam power etc. Emission signals closely reflect the status of laser beam interaction with materials and follow the variation of the process of beam-material interaction. Therefore, optical and acoustic emission signals could be monitored to indirectly measure weld quality.

As regards to feedback control, sensor signals as a function of processing parameters need to be determined. Description of this function may change from one system to another. Sometimes the relation between sensor signals and processing parameters is complicated and thus feedback control is a challenge.

In this work, the possibilities of acoustic and optical monitoring have been explored and an efficient optical sensing system has been developed to implement closed-loop control of welding process.

8.1 Acoustic monitoring

Acoustic monitoring is based on the fact that weld quality is related to acoustic signals of different distinctive patterns in the frequency domain. In particular, the difference in acoustic emission accompanying full penetration and partial penetration welding is distinguishable from the frequency distribution. When improper fit up occurs in the butt joint, the acoustic spectrum also changes significantly. However, the details of frequency distribution of the acoustic signals are subject to severe fluctuation and a constant frequency distribution is not seen even with a well-controlled welding process. . If monitoring a specific component in the spectrum, its reproducibility is poor. The acoustic emission contains lots of spike-like transients in the high frequency region. For this reason, a normalized power spectrum is used to give a clearer picture of relative spectral changes in response to weld quality variation.

Using a normalized acoustic spectrum, a statistical approach of weld monitoring and linear pattern recognition for weld classification as well as neural network classification has been developed. In the statistical approach, a comparison between the acoustic spectrum of welding and the special spectrum corresponding to the optimal welding condition is made. The optimal spectrum is derived by averaging the acoustic spectra from a welding run under optimized processing conditions. A fitness function, the total squared deviation, of the comparison is defined to indicate the welding condition. It has been demonstrated that when the welding condition is at or close to the optimal condition the total squared deviation is low, otherwise the total squared deviation value increases as the welding condition deviates away from the optimal welding condition. Poor welds correspond to a large deviation value. This technique could be very useful for detecting unexpected deviations from optimal welding condition in production.

A pattern recognition algorithm has shown its ability to classify the various welds that include full penetration, partial penetration and overheated welds. With proper training of a classifier, the performance of weld classification can reach an accuracy of 80 – 90 %. When using combined signals of acoustic emission and optical emission, the total performance can be improved. Furthermore, welds produced under conditions which are close to the optimal condition could be identified.

A neural network has been designed for weld classification and is trained using acoustic emission signals from three classes of welds. However, the classification accuracy was not as good as the performance of the statistical pattern recognition classifier. It has been shown that the neural network classifier is more suitable for classification of welds into two classes, that is full penetration or partial penetration.

8.2 Optical monitoring

Optical monitoring signals in the time domain are successfully used to detect gap width and various weld faults with a two-spot detection technique. For gap width detection, one spot is placed in front of the weld pool and another is in the plume. The light that is transmitted through the gap from the weld keyhole indicates the width of the gap. When the gap opens up from zero, the intensity of the emission signal detected through the gap increases up to the point that the keyhole disappears, while the intensity of emission from the plasma plume decreases with increase of the gap width. Combining these two signals, the gap width can be measured very efficiently with a sensitivity of detecting gap width ≤ 0.09 mm.

For weld fault detection, one viewing spot is located in the weld pool behind the keyhole and another is in the plume. In this way, infrared radiation from the weld pool and UV radiation from the plasma plume are sensed at the same time. An inverse filtering algorithm has been developed to resolve the information contained in these two signals. It has been proved that with the two-spot detection technique the inverse-filtering algorithm is efficient to detect weld faults such pinholes, ripples, excessive concavity and failed weld.

With the multi-spot detection technique, the recorded optical emission signals are highly separable with regards to different penetration conditions. When these signals are fed into a neural network that is used to classify the welds via acoustic signals, the classification accuracy reaches up to 98%.

8.3 Adaptive control of welding process

Closed-loop controls of laser beam focus, seam tracking and adaptive speed adjustment have been realized during welding process using the multi-spot and multi-color detection technique. The multi-spot and multi-color detection technique uses an imaging system that consists of a structured optical fiber bundle and focusing lenses to sense emissions from plasma plume and weld pool. This detection technique has the ability of sensing a shift in (i) focal position, (ii) beam spot on the seam and (iii) weld penetration condition.

A linear response of the difference signal to the focal position shift has been obtained using the two-spot detecting technique. This linear response signal can be easily incorporated into a proportional controller to adjust the beam focal position.

Three signals from the four-spot detection configuration are used to construct the control signal. A linear combiner (Adaline) has been adopted for signal processing. These three emission signals were fed into the linear combiner and the output signal is a monotonic function of the beam position across the seam. With this signal, control of the beam spot on the seam has been successfully demonstrated during laser welding of tilted seam butt joint.

Speed control is based on the different responses of the infrared radiation from the weld pool and the UV radiation from the plasma plume to penetration conditions. With optimized detection, the infrared radiation increases with deposited laser beam energy, while UV or visible radiation from the plume decreases with deposited laser beam energy in a processing range that involves transition between full penetration and partial penetration. A simple PID controller for speed control has been implemented although the transition action of this controller is not very smooth.

A neuro-fuzzy control system has been constructed for improving control action of speed adjustment and seam tracking. Performance of the neuro-fuzzy controller is simulated using the experimental data. From these simulation data, it is seen that the controller has a satisfactory performance. Further development of a neural-fuzzy controller is the next step to integrate all the control signals into a unit system to achieve systematic control of the welding process.

References

[1] W. M. Steen, *Laser Material Processing*, (Springer-Verlag, London, 1991), Chapter 4

[2] Dieter Radaj, *Heat Effect of Welding*, (Springer-Verlag, Berlin, 1992)

[3] J-c. Mombo-Caristan, V. Lobring, W. Prange, and A. Frings, "Tailored Welded Blanks: A New Alternative in Automobile Body Design" in *The Industrial Laser Handbook*, ed. by David Belforte and Morris Levitt, (Springer-Verlag, 1993)

[4] L. Li, W. M. Steen, K. Shi and D. J. Brookfield, "Sensor Development for In-process Quality Inspection and Optimization of High Speed Laser Can Welding Process", *Proc. LAMP'92*, Nagaoka (June, 1992), pp415-420

[5] L. Li, D. J. Brookfield and W. M. Steen, "Plasma charge sensor for in-process, non-contact monitoring of the laser welding process", Measurement Science Technology, 7(1996), 615-625

[6] H. B. Chen, L. Li, D. J. Brookfield, K. Williams and W. M. Steen, "Laser Process Monitoring with Dual Wavelength Optical Sensors", Proc. ICALEO'91, pp113-122

[7] Maischner D, Drenker A, Seidel B, Abels P and Beyer E, 1991, "Process control during laser beam welding", ICALEO'91 Proc. SPIE vol.1722, pp150-155

[8] M. C. Jon, "Noncontact Acoustic Emission Monitoring of Laser Beam Welding", Welding Journal, Sept. 1985, pp43-48

[9] Hongping Gu and W. W. Duley, "Acoustic emission and optimized CO_2 laser welding of steel sheets", Proc. ICALEO'94, pp77-85

[10] D. Maischner, A. Drenker, B. Seidel, P. Abels, E. Beyer, "Process Control During Laser Beam Welding", Proc. ICALEO'91, pp150-155

[11] G. Kinsman and W. W. Duley, "Fuzzy Logical Control of CO_2 Laser Welding", Proc. ICALEO'93, pp160-167

[12] E. Beyer, D. Maischner, Ch. Kratzsch, "A Neural Network to Analyze Plasma Fluctuations with the Aim to Determine the Degree of Full Penetration in Laser Welding", Proc. ICALEO'94, pp51-57

[13] I. Miyamoto and K. Mori, "Development of In-process monitoring system for laser welding", Proc. ICALEO'95, Vol.81 (1995), LIA, pp.759-767

[14] I. Miyamoto, K. Kamimuki, H. Maruo, K. Mori and M. Sakamoto, "In-process monitoring in laser welding of automotive parts", ICALEO'93, 413-424

[15] F. M. Haran, D. P. Hand, S. M. Ebrahim, C. Peters and J. D. C. Jones, "Optical signal oscillations in laser keyhole welding and potential application to lap welding", Measurement Science Technology, 8(1997), 627-633

[16] P. G. Sanders, J. S. Keske, G. Kornecki and K. H. Leong, "Capabilities of infrared weld monitor", ICALEO'97

[17] E. Nava-Rudiger and M. Houlot, "Integration of real time quality control systems in a welding process", Journal of Laser App. 1997, Vol.9, pp95-102

[18] J. Beersiek, R. Poprawe, W. Schulz, Hongping Gu, R. Mueller, W. W. Duley, "On-line monitoring of penetration depth in laser beam welding", ICALEO'97

[19] Ji-Liang Doong, Ching-Shang Wu and Jiun-Ren Hwang, "Infrared temperature sensing of laser welding", Int. J. Mach. Tools Manufact. Vol.31, No.4, 1991, 607-616

[20] F. M. Haran, D. P. Hand, C. Peters, J. D. C. Jones, "Real-time focus control in laser welding", Meas. Sci. Technol. 7(1996), 1095-1098

[21] L. Li, W. M. Steen and P. Modern, "Meltpool Behavior Monitoring and Adaptive Control of Laser Surface Treatment through Machine Vision", Proc. ICALEO'93, pp372-375

[22] D. Racko, "Acoustic Emission from Welds as Indicator of Cracking", *Materials Science and Technology*, December, 1987, Vol.3. pp1062-1066

[23] C. E. Hartbower, W. G. Reuter, C. F. Morais, and P. P. Crimmins, "Use of Acoustic Emission for the Detection of Weld and Stress Corrosion Cracking", *Acoustic Emission*, ASTM STP 505, Philadelphia, 1972, pp187-221

[24] C. K. Fang, E. Kannatey-Asibu, Jr., and J. R. Barber, "Acoustic Emission Investigation of Cold Cracking in Gas Metal Arc Welding of AISI 4340 Steel", Welding Journal Vol.74(6), 1995, pp177s-184s

[25] M. A. Saifi and J. Vahaviolos, "Laser Spot Welding and Real-time Evaluation", IEEE J. Quant. Electr. Vol.QE-12, 1976

[26] J. W. Whittaker, T. M. Mustaleski and K. D. Nicklas, "In-process Acoustic Emission Monitoring of Laser Welds", *The Second International Conference on Acoustic Emission*, 1993

[27] Y-L. Mao, G. Kinsman, W. W. Duley, "Real-time Fast Fourier Transform Analysis of Acoustic Emission during CO_2 Laser Welding of Materials", J. Laser Applications, Vol.5, 1993, pp17-22

[28] W. W. Duley and Y. L. Mao, "The Effect of Surface Condition on Acoustic Emission during Welding of Aluminum with CO_2 Laser Radiation", J. Phys. D: Appl. Phys. 27(1994), pp1379-1383

[29] D. Farson, K. Hillsley, J. Sames and R. Young, "Frequency-Time Characteristics of Air-Borne Signals from Laser Welds", Proc. ICALEO'94, pp86-94

[30] D. Farson, Y. Sang and A. Ali, "Relationship between airborne acoustic and optical emissions during laser welding", Journal of laser Appl. 1997, Vol.9, pp87-94

[31] R. Ducharme, P. Kapadia, M. H. Glowachi, J. M. Dowden, K. Williams and W. M. Steen, "The welding of thin sheets of various metals with a continuous CO_2 laser and a variety of shielding gases investigated by means of an integrated mathematical model", ICALEO'93, pp233-241

[32] Z. Szymanski and J. Kurzyna, "Spectroscopic measurements of laser induced plasma during welding with CO_2 laser", J. Appl. Phys. 76(12), 1994, pp7750-7756

[33] Y. Arata, "Challenge of Laser Advanced Materials Processing", *Proc. Conf. Laser Advance Material Processing LAMP'87*, (Osaka Publ.: High Temperature Soc. Japan, 1987), pp3-11

[34] W. W. Duley, M. Olfert, P. M. Bridger, J. Bird and R. E. Mueller, "Basic Physical Phenomena during Laser Processing of Materials", *Proc. LAMP'92*, Nagaoka (Osaka: High Temperature Soc. Japan, 1992), pp261-268

[35] M. Olfert, P. M. Bridger, I. Dunn and W. W. Duley, "Physical Processes during Laser Drilling in the Presence of a Liquid", High Temp. Chem. Processes, 1994

[36] P. G. Klemans, "Heat Balance and Flow Conditions for Electron Beam and Laser Welding", J. Appl. Phys. Vol.47, 1976, pp2105-2114

[37] J. Dowden, N. Postaciogulu, M. Davis and P. Kapadia, "A Keyhole Model in Penetration Welding with a Laser", J. Phys. D: Appl. Phys. Vol.20, 1987, pp36-44

[38] P. E. Denney and E. A. Metzbower, Proc. ICALEO'91, San, Jose CA. Nov. 1991

[39] J. Trappe, C. Tix, J. Kroos and G. Simon, "On the Shape and Location of the Keyhole in Laser Beam Welding", J. Phys. D: Appl. Phys. Vol.27, 1994

[40] T. Klein, M. Vicanek, J. Kroos, I. Decker and G. Simon, "Oscillations of the Keyhole in Penetration Laser Beam Welding", J. Phys. D: Appl. Phys. Vol.27, 1994, pp2023-2030

[41] B. R. Finke and G. Simon, "On the Gas Kinetics of Laser-Induced Evaporation of Metals", J. Phys. D: Appl. Phys. Vol.23, 1990, pp67-74

[42] T. Iida and R. I. L. Guthrie, *The Physical Properties of Liquid Metals*, (Oxford: Clarendon, 1988), p88

[43] J, Kroos, U. Gratzke and G. Simon, "Towards a Self-consistent Model of the Keyhole in Penetration Laser Beam Welding", J. Phys. D: Appl. Phys. Vol.26, 1993, pp474-480

[44] I. Miyamoto, H. Maruo and Y. Arata, "The Role of Assist Gas in CO_2 Laser Welding", L.I.A. Vol.44, ICALEO'84, pp68-75

[45] A. Poueyo-Verwaerde, R. Fabbro, and G. Deshors, "Experimental Study of Laser-induced Plasma in Welding Conditions with Continuous CO_2 Laser", J. Appl. Phys. Vol.74, 1993, pp5773-5780

[46] E. Beyer, G. Herziger, A. Gasser, W. Sokolowski, "Plasma Fluctuations during Laser Machining with CW-CO_2-lasers", SPIE. Vol.801, 1987, pp178-184

[47] J. Richter, in *Plasmas Diagnostics*, edited by W. Lochte-Holtgreven (North Holland, Amsterdam, 1968)

[48] Joseph T. Verdeyen, *Laser Electronics*, (Prentice Hall, Englewood Cliffs, New Jersey, 1995)

[49] D. Farson, Y. Sang and A. Ali, "Relationship between airborne acoustic and optical emissions during laser welding", J. Laser Appl. Vol.9, 1997, pp87-94

[50] P. Kapadia, R. Ducharme and C. Trayner, "Radiative emissions in the laser welding of thin metal sheets", ICALEO'92, pp209-218

[51] A. P. Dowling and J. E. Ffowcs-Williams, *Sound and sources of sound*, Chichester UK: Ellis-Horwood Pullishers, 1983

[52] W. W. Duley, *Laser Processing and Analysis of Materials*, (Plenum, 1983), p47

[53] H. Gu and W. W. Duley, "Resonant acoustic emission during laser welding of metals", J. Phys. D: Appl. Phys. 29(1996), pp550-555

[54] P. R. Krishnaiah, L. N. Kanal, *Classification, pattern recognition, and reduction of dimensionality*, (Amsterdam, North-Holland Pub. Co.), 1982

[55] M. Nadler and E. P. Smith, *Pattern recognition engineering*, (John Wiley and Sons Inc. Toronto, 1st editions), 1993

[56] R. A. Jonson and D. W. Wichern, *Applied multivariate statistical analysis*, (Englewood Cliffs, NJ: Prentice Hall), 1992

[57] D. Farson, A, Ali, Y, Sang, "Overview of emission-based laser process sensing", Proc. ICALEO'96, Vol.82, 1996, ed. By F. DiPietro et al. (Detroit, MI" LIA), pp72-79

[58] T. Klein, M. Vicanek and G. Simon, "Forced oscillations of the keyhole in penetration laser beam welding", J. Phys. D: Appl. Phys. 29(1996), pp322-332

[59] W. Sokolowski, G. Herziger, E. Beyer, "Spectroscopic study of laser-induced plasma in the welding process of steel and aluminum", SPIE Vol.1132, *High power lasers and laser machining technology*, 1989, pp288-295

[60] R. Fabbro, D. Bermejo, J. M. Orza, L. Sabatier, L. Leprince and V. Granier, "Absorption measurements in continuous high-power CO_2 laser processing of materials", SPIE, Vol.1276, 1990, pp461-467

[61] C. Tix and G. Simon, "A transport theoretical model of the keyhole plasma in penetration laser welding", J. Phys. D: Appl. Phys. 26(1993), pp2066-2074

[62] V. V. Semak, M. H. McCay and T. D. McCay, "Comparison of IR Emittance distributions along Steel and aluminum surface during CO_2 laser welding", Proc. ICALEO'93, pp777-782

[63] R. Schalkoff, *Pattern recognition: Statistical, structural and neural approaches*, (John Wiley & Sons, New York, 1992)

[64] K. Williams, W. M. Steen, R. Ducharme, P. Kapadia, J. Dowden, "On laser welding meltpool dynamics", Proc. ICALEO'93, pp168-176

[65] W. Gatzweiler, D. Maischner, F. J. Faber, C. Derichs, E. Beyer, "Model of dynamic behavior in laser beam welding", SPIE, Vol.1132, *High power lasers and laser machining technology*, 1989, pp157-165

[66] T. P. Duffey, T. G. McNeela, and J. Mazumder, A. L. Schawlow, "Absorption spectroscopic measurement of atomic density in laser-induced vapor plume", Proc. ICALEO'93, pp127-134

[67] Werner Kluft, Peter Boerger, Reinhold Schwartz, Prometec GmbH, "On-line Monitoring of laser welding of sheet metal by special evaluation of plasma radiation", Proc. ICALEO'96, Vol.82, ed. by F. DiPietro, F. Kuepper, LIA, 1996, pp.62-71

[68] I. Miyamoto, H. Maruo and U. Arata, "The role of assist gas in CO_2 laser welding", Proc. ICALEO'84, Vol.44, pp.68-75

[69] J. H. P. C. Megaw, M. Hill and S. J. Osbourn, "Girth welding of X-60 pipeline with a 10 kW laser", SPIE, Vol.650, *High power lasers and their industrial applications*, 1986, pp.311-117

[70] W. M. Steen, "Adaptive control of laser material processing", Proceedings of LAMP'92, Nagaoka (June 1992), pp.439-444

[71] P. Kapadia, R. Ducharme and J. Dowden, "The theory of radiative transfer in the plasma of the keyhole in penetration laser welding", Proc. ICALEO'91, pp.53-62

[72] A. Kaplan, "A model of deep penetration laser welding based on calculation of the keyhole profile", J. Phys. D: Appl. Phys. Vol.27, No.9, 1994, pp.1805-1814

[73] J. Mazumder, *Laser materials processing*, ed. M. Bass (North-Holland, Amsterdam, 1983)

[74] Andreas Otto, Gunter Deinzer and Manfred Geiger, "Control of transient processes during CO_2-laser beam welding", SPIE, Vol.2207, 1994, pp.282-288

[75] Mark Faerber, "The position of the laser welding gas supply nozzle is the crux", Body Assembly & Manufacturing, IBEC'97, pp.14-16

[76] Karl J. Astrom and Bjorn Wittenmark, *Computer-controlled systems*, (Prentice Hall, Englewood Cliffs, New Jersey, 1990)

[77] Christopher C. Davis, *Lasers and electro-optics: fundamentals and engineering*, (Cambridge University Press, 1995)

[78] Bernard Widrow and Eugene Walach, *Adaptive inverse control*, (Prentice Hall P T R, Upper Saddle River, New Jersey, 1996)

[79] Zhigang Qu, Antti Salminen and Tapani Moisio, "Seam tracking for laser welding using vision sensors", The Third International Conference on Automation, Robotics and Computer Vision (ICARCV'94), Singapore, November 9-11, 1994, pp.1668-1672

[80] Chin-Teng Lin and C. S. George Lee, *Neural fuzzy systems*, (Prentice Hall P T R, Upper Saddle River, New Jersey, 1996)

[81] J. J. Hopfield, "Neural networks and physical systems with emergent collective computational abilities", Proc. Nat. Acad. Sci. USA, Vol.79, 1982, pp.2554-2558

[82] D. E. Rumelhart, G. E. Hinton, and R. J. Williams, "Learning representations by back-propagation", In D. E. Rumelhart, J. L. McClelland, et al., eds., *Parallel distributed processing*, Vol.1, (Cambridge, MA: MIT Press.), 1986

[83] D. O. Hebb, The organization of behavior: A neuropsycholoical theory, (New York, John Wiley, 1949)

[84] B. Widrow and M. E. Hoff, Jr., "Adaptive switching circuits", Proc. 1960 IRE West. Elect. Show Conv. Rec. Part 4, New York, 1960, pp.96-104